

UNDERSTANDING THE FORMATION AND IMPACTS OF ATMOSPHERIC AEROSOLS

A Dissertation

by

YIXIN LI

Submitted to the Graduate and Professional School of  
Texas A&M University  
in partial fulfillment of the requirements for the degree of

DOCTOR OF PHILOSOPHY

Chair of Committee,	Renyi Zhang
Committee Members,	Natalie M. Johnson
	Simon W. North
	David H. Russell
Head of Department,	Simon W. North

August 2021

Major Subject: Chemistry

Copyright 2021 Yixin Li

## ABSTRACT

Atmospheric aerosol, liquid or solid particles suspended in air, has profound implications for air quality, climate, and human health. Secondary organic aerosol (SOA) formed from photochemical oxidation of volatile organic compounds (VOCs) represents the dominant constituent of tropospheric fine aerosols. However, the chemical complexity relevant to gaseous oxidation and subsequent gas-to-particle conversion poses enormous challenges in elucidating the formation and impacts of atmospheric particles.

In the first part of this dissertation, we performed experiments by exposing sub-micrometer seed particles to glyoxal or methylglyoxal in the presence/absence of ammonia and formaldehyde inside an environmental chamber. We show significantly more efficient growth and browning of aerosols upon exposure to methylglyoxal than glyoxal under atmospherically relevant concentrations, and non-volatile oligomers and light-absorbing nitrogen-heterocycles are identified as the dominant particle-phase products. The distinct aerosol growth and optical properties are attributed to carbenium ion-mediated nucleophilic addition, interfacial electric field-induced attraction, and synergetic oligomerization involving organic/inorganic species.

Second, we investigate multi-generation SOA production from toluene and *m*-xylene by simultaneously tracking the evolutions of gas-phase oxidation and aerosol formation in a reaction chamber. The results reveal that aerosol growth and browning are mainly attributed to earlier generation products consisting of the di-carbonyl and carboxylic functional groups. We conclude that toluene/*m*-xylene contribute importantly to SOA formation via primarily dicarbonyls and

organic acids resulting from their prompt and high yields from oxidation as well as their unique functionalities for participation in particle-phase reactions.

Third, to assess the role of respiratory aerosols in the transmission of infectious diseases, the pandemic trends during the earlier COVID-19 pandemic in several epicenters worldwide and in the United States were analyzed. The transmission and intervention jointly shape the pandemic trends from January to May 2020, showing that airborne transmission and face covering play the dominant role in spreading the virus and flattening the total infection curve, respectively.

Our findings explain atmospheric measurements of rapid SOA formation especially under polluted urban conditions and highlight the importance for functionality-reactivity relationship for SOA production from condensable oxidized organics. Additionally, we show that aerosols play an important role in transmission of infectious diseases.

## DEDICATION

To my family and friends

## ACKNOWLEDGEMENTS

I would like to acknowledge my research advisor and committee chair, Dr. Renyi Zhang, for the opportunity to work with him closely and accomplish these challenging yet interesting projects. I wish to thank my committee members, Dr. Natalie M. Johnson, Dr. Simon W. North, Dr. David H. Russell, and Dr. Don Collins for their guidance and support during my graduate studies. I also wish to thank Dr. Charles E. Kolb, Dr. Mario J. Molina, Dr. Yuemeng Ji, Dr. John H. Seinfeld, Dr. Manish Shrivastava, Dr. Yuan Wang, and Dr. Yuxuan Wang for their inspiring suggestions and kind help during our collaborations.

I wish to acknowledge several funding agencies, including Texas A&M University Dissertation Fellowship, Hagler Institute for advanced study HEEP Graduate Fellowship, and the Robert Welch Foundation, for their financial support. Additional support from both the Department of Chemistry and Department of Atmospheric Sciences is also acknowledged.

Special thanks also go to my friends, previous and current members in our group, for their help and support. I also wish to thank the staff members from both the Chemistry and the Atmospheric Sciences Departments for their patience and kind helps, which make my study at Texas A&M University a great experience.

Finally, I would like to thank my family for their encouragement and support.

## CONTRIBUTORS AND FUNDING SOURCES

### **Contributors**

#### *Part I, faculty committee recognition*

This work was supervised by a dissertation committee consisting of Professors Renyi Zhang (Chair), Simon W. North, and David H. Russell from the Department of Chemistry, Professor Natalie M. Johnson from the School of Public Health, and Professor Don Collins from Chemical and Environmental Engineering, Center for Environmental Research & Technology in University of California, Riverside.

#### *Part 2, student/collaborator contributions*

The molecular dynamic simulation and quantum calculation in Chapter II were conducted in part by Professor Yuemeng Ji and her student Qiuju Shi from Institute of Environmental Health and Pollution Control, Guangdong University of Technology, Guangzhou, China and were published in 2020. In Chapter II, aerosol growth measurements for direct exposure to methylglyoxal were performed by Jianfei Peng and Yuying Wang. Part of the aerosol growth in the presence of formaldehyde were conducted together with Jiayun Zhao and Chunyu Wang. The data analysis for global aerosol budget in Chapter II was conducted in collaboration with Dr. John H. Seinfeld from Division of Chemistry and Chemical Engineering, California Institute of Technology, Dr. Yuan Wang from Division of Geological and Planetary Sciences, California Institute of Technology, Dr. Yuxuan Wang from Department of Earth and Atmospheric Sciences, University of Houston, and Dr. Fang Zhang from College of Global Change and Earth System Science, Beijing Normal University, Beijing, China.

All other work for the dissertation was completed by the student independently.

### **Funding Sources**

Graduate study was supported by the Texas A&M University Dissertation Fellowship and Hagler Institute for Advanced Study HEEP Graduate Fellowship.

This work was also made possible in part by Robert A. Welch Foundation under Grant Number of A-1417. The contents of this dissertation are solely the responsibility of the authors and do not necessarily represent the official views of the Welch Foundation.

## NOMENCLATURE

ABS	Ammonium Bisulfate
ACI	Aerosol-Cloud Interaction
APM	Aerosol Particle Mass Analyzer
ARI	Aerosol-Radiative Interaction
AS	Ammonium Sulfate
AVOC	Anthropogenic Volatile Organic Compound
$b_{\text{abs}}$	Light Absorption Coefficient
$b_{\text{ext}}$	Light Extinction Coefficient
$b_{\text{sca}}$	Light Scattering Coefficient
BrC	Brown Carbon
BVOC	Biogenic Volatile Organic Compound
CDC	Centers for Disease Control and Prevention
CA	California
CH <sub>2</sub> O	Formaldehyde
<sup>+</sup> CH <sub>2</sub> OH	Formaldehyde Carbenium Ion
CH <sub>4</sub>	Methane
CIMS	Chemical Ionization Mass Spectrometry
CPC	Condensation Particle Counter
CRDS	Cavity Ring-Down Spectrometer
COOs	Condensable Oxidized Organics



CO <sub>2</sub>	Carbon Dioxide
COVID-19	Coronavirus Disease 2019
CT	Connecticut
DMA	Differential Mobility Analyzer
$D_0$	Particle Initial Diameter
$D_p$	Particle Diameter After Exposure
FL	Florida
FTIR	Fourier-Transform Infrared Spectrometer
G1	First Generation
G2	Second Generation
G3	Third Generation
GA	Georgia
GF	Growth Factor
GL	Glyoxal
GLTD	Glyoxal Trimer Dihydrate
H <sub>2</sub> SO <sub>4</sub>	Sulfuric Acid
H <sup>+</sup>	Proton
H <sub>2</sub> O <sub>2</sub>	Hydrogen Peroxide
H <sub>3</sub> O <sup>+</sup>	Hydronium Ion
HO <sub>2</sub>	Hydroperoxy Radical
HOMs	Highly Oxidized Multi-Functional Organics
H/C	Hydrogen Carbon Ratio
ID-CIMS	Ion Drift - Chemical Ionization Mass Spectrometer

IEPOX	Isoprene-Epoxydiols
IL	Illinois
IPCC	Intergovernmental Panel on Climate Change
LA	Louisiana
LVO	Low-Volatility Polyhydroxy Organic
MA	Massachusetts
MD	Maryland
MDS	Molecular Dynamic Simulation
MERS-CoV	Middle East Respiratory Syndrome Coronavirus
MG	Methylglyoxal
MI	Michigan
NaCl	Sodium Chloride
N <sub>2</sub>	Nitrogen
nm	Nanometer
Na <sub>2</sub> SO <sub>4</sub>	Sodium Sulfate
NBO	Natural Bond Orbital
NCO	Nitrogen-Containing Organics
n-heterocycles	Nitrogen-heterocycles
NH <sub>3</sub>	Ammonia
NH <sub>4</sub> <sup>+</sup>	Ammonium Ion
NH <sub>4</sub> HSO <sub>4</sub>	Ammonium Bisulfate
(NH <sub>4</sub> ) <sub>2</sub> SO <sub>4</sub>	Ammonium Sulfate
NJ	New Jersey

NO	Nitric Oxide
NO <sub>2</sub>	Nitrogen Dioxide
NO <sub>x</sub>	Nitrogen Oxides (NO + NO <sub>2</sub> )
NPF	New Particle Formation
NY	New York
NYC	New York City
O <sub>2</sub>	Oxygen
O <sub>3</sub>	Ozone
OH	Hydroxyl Radical
OHs	Ohio
O/C	Oxygen to Carbon Ratio
P1	First Generation Oxidation Products
P2	Second Generation Oxidation Products
P3	Third Generation Oxidation Products
PA	Pennsylvania
PM	Particulate Matter
PM <sub>0.1</sub>	Ultrafine Particles with Diameters Less than 0.1 Micrometers
PM <sub>2.5</sub>	Fine Particulate Matter with Diameters Less than 2.5 Micrometers
PM <sub>10</sub>	Coarse particulate matter with Diameters Less than 10 Micrometers
P <sub>2</sub> O <sub>5</sub>	Phosphorus pentoxide
ppb	Parts Per Billion
ppm	Parts Per Million
PTR-MS	Proton Transfer - Reaction Mass Spectrometer

R <sub>0</sub>	Basic Reproduction Rate
RCOOH	Organic Acids
RH	Relative Humidity
RI	Relative Intensity on TD-ID-CIMS spectrum
RO·	Alkoxy Radical
RO <sub>2</sub> ·	Organic Peroxy Radical
SARS-CoV-1	Severe Acute Respiratory Syndrome Coronavirus-1
SARS-CoV-2	Severe Acute Respiratory Syndrome Coronavirus-2
sccm	Standard Cubic Centimeters Per Minute
SMPS	Scanning Mobility Particle Sizer
slpm	Standard Liter Per Minute
SO <sub>2</sub>	Sulfur Dioxide
SO <sub>4</sub> <sup>2-</sup>	Sulfate Ion
SOA	Secondary Organic Aerosol
SSA	Single Scattering Albedo
TD-ID-CIMS	Thermal Desorption-Ion Drift-Chemical Ionization Mass Spectrometer
Tg a <sup>-1</sup>	Tera-grams Per Year
TgC a <sup>-1</sup>	Tera-grams Carbon Per Year
TMB	1,3,5-Trimethylbenzene
TX	Texas
U. S.	United States
UV	Ultraviolet
VA	Virginia

VOC	Volatile Organic Compound
WHO	World Health Organization
$\mu\text{L}$	Microliter
$\mu\text{m}$	Micrometer
$\gamma$	Uptake Coefficient

## TABLE OF CONTENTS

	Page
ABSTRACT.....	ii
DEDICATION.....	iv
ACKNOWLEDGEMENTS.....	v
CONTRIBUTORS AND FUNDING SOURCES .....	vi
NOMENCLATURE .....	viii
TABLE OF CONTENTS.....	xiv
LIST OF FIGURES .....	xvi
LIST OF TABLES.....	xix
CHAPTER I INTRODUCTION.....	1
CHAPTER II SECONDARY ORGANIC AEROSOL FORMATION FROM SMALL A- DICARBONYLS .....	6
Introduction .....	6
Experimental.....	8
Results and Discussion .....	18
Atmospheric Implications.....	45
CHAPTER III MULTI-GENERATION PRODUCTION OF SECONDARY ORGANIC AEROSOL FROM TOLUENE PHOTOOXIDATION.....	47
Introduction .....	47
Experimental.....	49
Results and Discussion .....	53
Atmospheric Implications.....	84
CHAPTER IV FUNCTIONALITY-BASED SECONDARY ORGANIC AEROSOL FORMATION FROM M-XYLENE PHOTOOXIDATION.....	87

	Page
Introduction .....	87
Experimental .....	88
Results and Discussion .....	91
Atmospheric Implications .....	110
CHAPTER V UNDERSTANDING THE ROLE OF AEROSOL IN THE TRANSMISSION FOR THE COVID-19 PANDEMIC .....	112
Introduction .....	112
Methods .....	115
Results and Discussion .....	118
Conclusions .....	141
CHAPTER VI SUMMARY AND CONCLUSIONS .....	144
REFERENCES .....	147

## LIST OF FIGURES

FIGURE	Page
Figure 1 Emissions, photooxidation, lifecycles, and impacts of VOCs from biogenic and anthropogenic sources.....	4
Figure 2 Experimental schematic for SOA formation from $\alpha$ -dicarbonyls.....	9
Figure 3 TD-ID-CIMS calibration using purified methylglyoxal liquid.....	10
Figure 4 SOA growth from methylglyoxal .....	20
Figure 5 Time-dependent GF of seed particles exposed directly to methylglyoxal vapor.....	21
Figure 6 Weak RH-dependence of GF for AS exposed to products from photochemical oxidation of TMB and OH.....	21
Figure 7 Carbenium ion-mediated pathways leading to oligomeric products.....	22
Figure 8 Carbenium ion-mediated pathways leading to imidazoles and n-heterocycles .....	23
Figure 9 SOA growth from glyoxal .....	27
Figure 10 Synergetic oligomerization in the presence of $\text{NH}_3$ and $\text{CH}_2\text{O}$ .....	28
Figure 11 Dependence of relative volume growth ( $\text{GF}^3-1$ ) of AS particles on gas-phase $\text{NH}_3$ concentration exposing to TMB oxidation products.....	29
Figure 12 Particle growth factor when exposure to glyoxal vapor in the presence of $\text{CH}_2\text{O}$ ..	30
Figure 13 Distinct reactivity and light absorption between methylglyoxal and glyoxal.....	30
Figure 14 Carbenium ion-mediated, interfacial electric field-enhanced, and synergetic SOA and BrC formation .....	34
Figure 15 Oligomerization from multi-functional hydroxycarbonyl .....	36
Figure 16 Surface- and volume-limited uptake of $\alpha$ -dicarbonyls .....	40
Figure 17 Unaccounted contributors to global SOA production.....	41
Figure 18 Mutually promoted inorganic and organic aerosol formation .....	44



Figure 19 Schematic representation of the experimental setup.....	52
Figure 20 Temporal evolution of gaseous products and particle properties .....	55
Figure 21 Multi-generation products from toluene-OH photooxidation.....	56
Figure 22 Temporal evolutions in products and reactants from toluene oxidation.....	56
Figure 23 Pathways for oligomerization .....	58
Figure 24 Pathway for BrC formation.....	59
Figure 25 Variation in SOA growth with seed particles .....	65
Figure 26 Size growth with NH <sub>3</sub> .....	68
Figure 27 Variations in size growth and composition with NH <sub>3</sub> .....	68
Figure 28 RH dependence of SOA formation.....	70
Figure 29 Temporal evolution in SOA density .....	71
Figure 30 Variations in size growth and composition with NH <sub>3</sub> .....	74
Figure 31 The effects of NO <sub>x</sub> on SOA formation from toluene oxidation.....	78
Figure 32 Variations in particle growth with reactants .....	80
Figure 33 Multi-generation SOA and BrC formation from toluene-OH oxidation .....	81
Figure 34 SOA formations versus O/C ratio and volatility.....	84
Figure 35 Temporal evolution of gaseous products .....	92
Figure 36 Multi-generation products from <i>m</i> -xylene-OH photooxidation.....	93
Figure 37 Temporal evolutions of P2 and P3 concentrations from <i>m</i> -xylene oxidation.....	93
Figure 38 Temporal evolutions of <i>m</i> -xylene under photooxidation.....	94
Figure 39 Multigeneration SOA formation from <i>m</i> -xylene photooxidation.....	95
Figure 40 Variation in SOA growth with seed particles and NH <sub>3</sub> concentration.....	99
Figure 41 RH dependence of SOA formation .....	103

Figure 42 The effects of NO <sub>x</sub> on SOA formation from toluene oxidation.....	105
Figure 43 Functionality-based SOA formation from <i>m</i> -xylene photooxidation .....	107
Figure 44 Distinct global trends of the COVID-19 pandemic .....	119
Figure 45 Cumulative confirmed COVID-19 cases in the top-fifteen infected states of U.S..	123
Figure 46 Initial sub-exponential growth in the total infections .....	124
Figure 47 Initial sub-exponential growth in the total infections .....	125
Figure 48 The evolving epicenter from Wuhan, to Italy, to NYC .....	127
Figure 49 Linear correlation of the number of confirmed infections for using 15-day .....	128
Figure 50 Transmission of COVID-19.....	130
Figure 51 RH and PM <sub>2.5</sub> amid COVID-19 outbreaks in Wuhan, Rome, and NYC. ....	132
Figure 52 Mingling of coronavirus COVID-19 with regional haze in Wuhan, China.....	133
Figure 53 Mitigation paradigm.....	136

## LIST OF TABLES

TABLE	Page
Table 1 Peak assignments for oligomeric products detected by TD-ID-CIMS .....	24
Table 2 Peak assignments for n-heterocycles detected by TD-ID-CIMS .....	25
Table 3 Measured uptake coefficient ( $\gamma$ ) for methylglyoxal (MG) and glyoxal (GL) on different seed particles .....	31
Table 4 Diffusion coefficients for monomer and trimer of glyoxal and methylglyoxal.....	40
Table 5 Global budgets of species involved in cation-mediated, interface-enhanced, and synergetic SOA formation. ....	42
Table 6 Measured mass fractions of SOA and AS in major urban cities.....	45
Table 7 Density of identified major SOA components by TD-ID-CIMS.....	59
Table 8 The percent contributions of condensable organic species from toluene-OH oxidation to the particle-phase mass intensity .....	60
Table 9 Mass peak assignments for nitrogen-containing organics (NCO) from $\alpha$ -dicarbonyls n-heterocycles and $\gamma$ -carbonyls n-chains detected by TD-ID-CIMS.....	61
Table 10 Mass peak assignments for organic acids and LVO detected by TD-ID-CIMS.....	62
Table 11 Mass peak assignments for oligomeric products detected by TD-ID-CIMS.....	63
Table 12 Relative contributions of condensable oxidized organics with each type of functionality to SOA formation .....	72
Table 13 Oxygen to carbon (O/C) ratio for identified SOA components and saturation vapor pressures ( $P_s$ ) of condensable oxidized organics.....	73

Table 14 Comparison of measured gaseous concentrations of condensable oxidized organics from toluene-OH oxidation between 10% and 90% RH.....	75
Table 15 Measured uptake coefficient ( $\gamma$ ) for condensable oxidized organics on ammonium sulfate seed particles in the presence of ammonia.....	76
Table 16 The percent contributions of condensable organic species from <i>m</i> -xylene-OH oxidation to the particle-phase mass intensity .....	97
Table 17 SOA mass yield (%) from <i>m</i> -xylene-OH oxidation.....	99
Table 18 Relative contributions of condensable oxidized organics to SOA formation on (NH <sub>4</sub> ) <sub>2</sub> SO <sub>4</sub> seed particles with 19 ppb NH <sub>3</sub> and at 10% - 70% RH.....	102
Table 19 Measured uptake coefficient ( $\gamma$ ) for condensable oxidized organics on ammonium sulfate seed particles in the presence of ammonia.....	109
Table 20 COVID-19 pandemic trend and projection of the difference in total infections by face covering in the fifteen top-infected states of U.S.....	122

# CHAPTER I

## INTRODUCTION

Atmospheric aerosol, also known as particulate matter (PM), is a suspension of particles in the air. Although atmospheric aerosols can be defined or classified in a number of ways, aerodynamic diameter is one of the main criteria to describe its transport ability in the atmosphere and through the respiratory tract. The size of ambient particles ranges from a few nanometers (nm) to 10 micrometers ( $\mu\text{m}$ ).<sup>1</sup> Types of atmospheric particles include coarse particulate matter ( $\text{PM}_{10}$ ) with an aerodynamic diameter of 10  $\mu\text{m}$  or less, fine particulate matter ( $\text{PM}_{2.5}$ ) with an aerodynamic diameter of 2.5  $\mu\text{m}$  or less,<sup>2</sup> and ultrafine particles ( $\text{PM}_{0.1}$ ) with an aerodynamic diameter of less than 0.1  $\mu\text{m}$ .<sup>3</sup>

In particular, fine particulate matter has profound impacts on air quality, climate, and human health.<sup>4</sup> For example,  $\text{PM}_{2.5}$  in the air can reduce visibility and cause the air to appear hazy when levels are elevated.<sup>2</sup> The aerosol effects on climate include modification of the Earth's radiative balance, by directly absorbing/scattering the incoming solar radiation and indirectly by influencing cloud formation and precipitation processes, relevant to the aerosol-radiative interaction (ARI) and aerosol-cloud interaction (ACI), respectively.<sup>5</sup> Currently, the aerosol radiative effects on climate correspond to the largest uncertainty in prediction of future anthropogenic influence, which is partially attributed to the lack of understanding of their formation, transformation, and physicochemical properties (such as hygroscopicity and optical properties).<sup>5</sup> Also, high levels of fine aerosols have been unequivocally identified to exert large adverse health effects on human.<sup>6</sup> Particles in the  $\text{PM}_{2.5}$  size range are able to travel deeply into the respiratory tract, reaching the lungs.<sup>7</sup> Exposure to fine particles can not only cause short-term

health effects such as eye, nose, throat and lung irritation, coughing, sneezing, runny nose, shortness of breath but also affect lung function and worsen medical conditions such as asthma and heart disease.<sup>8</sup> Globally, exposure to fine PM has been identified as the cause of more than 7 million premature deaths a year.<sup>9</sup> Recent studies have shown that maternal exposure to ultrafine particles results in pulmonary immunosuppression, birth defects and fatalities.<sup>10,11</sup> Additionally, previous experimental and observational studies on interhuman transmission have indicated a significant role of aerosols in the transmission of many respiratory viruses, including influenza virus, severe acute respiratory syndrome coronavirus-1 (SARS-CoV-1), and Middle East Respiratory Syndrome coronavirus (MERS-CoV).<sup>12-14</sup>

Atmospheric aerosol is emitted directly into the atmosphere (primary) or formed in the atmosphere through gas-to-particle conversion (secondary).<sup>15,16</sup> In the troposphere, secondary organic aerosol (SOA) constitutes a major component of the global fine particulate matter (typically the largest mass fraction) and is produced from photochemical oxidation of biogenic and anthropogenic volatile organic compounds (VOCs).<sup>4,17</sup> VOCs are organic compounds that have high vapor pressure and low water solubility at room temperature. Based on their sources, VOC can be classified into biogenic and anthropogenic VOC. Although most VOCs in earth's atmosphere are biogenic (BVOCs) and emitted by plants, anthropogenic VOCs (AVOCs) from vehicular emissions, oil and gas operations, industrial processes, evaporation of volatile organic solutions, and consumer products (comprised alkanes, alkenes, and aromatics) have received increasing attention because of their contribution to high wintertime ozone levels and urban PM pollution.<sup>4,18,19</sup>

Photochemical oxidation of VOCs represents one of the most critical and challenging topics in atmospheric chemistry research.<sup>4,5,20</sup> VOC oxidation proceeds via various pathways and

steps, leading to the production of tropospheric ozone (O<sub>3</sub>), carbon dioxide (CO<sub>2</sub>), and condensable oxidized organics (COOs); the latter contribute to SOA formation via gas-to-particle conversion and cloud-processing (Figure 1).<sup>21</sup> Gas-to-particle conversion includes new particle formation (NPF), condensation/partitioning, and particle-phase reactions.<sup>22,23</sup> The gas-to-particle conversion of COOs also produces light-absorbing brown carbon (BrC), representing one aerosol type that scatters and absorbs solar radiation relevant to ARI.<sup>1,5,24</sup> In addition, while SOA serves as cloud condensation nuclei for cloud formation relevant to ACI, evaporation of cloud droplets leads to regeneration of SOA and COOs.<sup>4,25</sup> There are two ultimate fates for VOC oxidation, i.e., conversion to CO<sub>2</sub> and SOA. The organic carbon from VOC oxidation is believed to be predominantly converted to CO<sub>2</sub>, with a minor fraction (less than 10%) to SOA.<sup>26</sup> Currently, the global SOA budget is consistently underpredicted in atmospheric models,<sup>27</sup> and there is growing recognition of the important role of multiphase chemistry in the SOA growth.<sup>28-30</sup> In addition, the differences between experimental conditions (e.g., the concentration of precursors and other coexisting gases) and real atmospheric conditions might greatly affect the oxidation processes and multiphase processes in smog chamber.<sup>31-33</sup> In view of the low concentration of precursors in the atmosphere, it is necessary to use the laboratory results cautiously to model prediction applied for the real atmospheric ambient. Until now, the enormous chemical complexity of VOC oxidation and subsequent gas-to-particle conversion poses significant challenges in elucidating the fundamental chemical mechanisms for SOA formation and in assessing the impacts on human health and climate.<sup>4,5,34</sup>

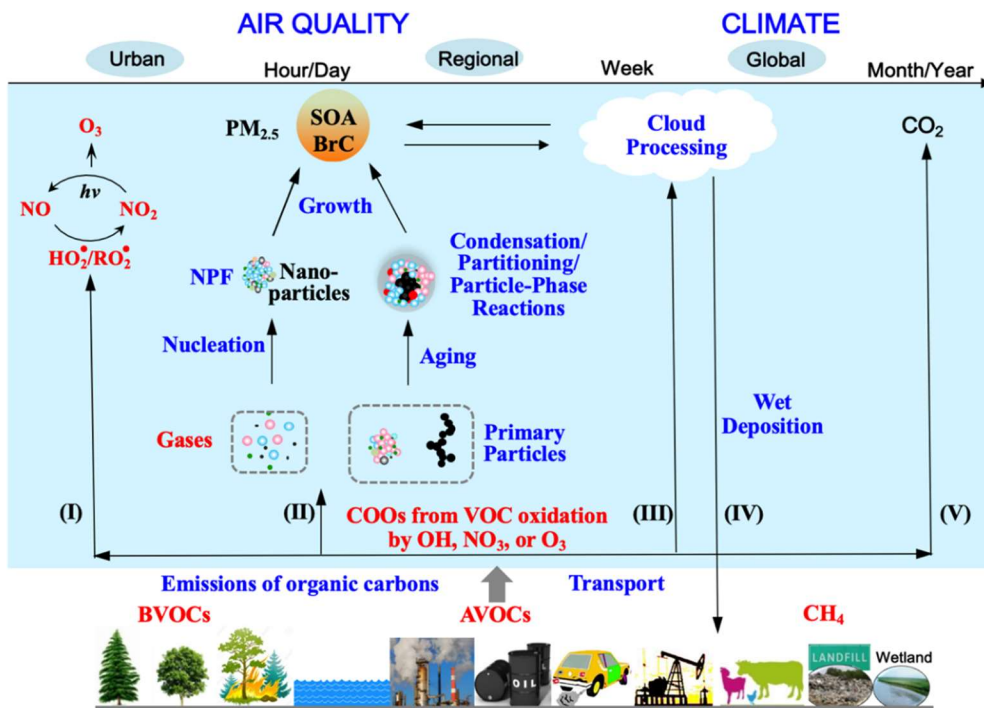


**Figure 1. Emissions, photooxidation, lifecycles, and impacts of VOCs from biogenic and anthropogenic sources.** Paths I to V correspond to O<sub>3</sub> production, gas-to-particle conversion, cloud-processing, dry/wet deposition, and CO<sub>2</sub> formation, respectively. SOA formation includes paths II and III.

This dissertation attempts to investigate the fundamental mechanism for the formation of SOA via the multiphase reactions of VOC oxidation products in Chapter II, III, and IV.

Specifically, in Chapter II, we conducted combined experimental and theoretical study to elucidate the reaction mechanism of glyoxal/methylglyoxal in aqueous phase. We probe and quantify the SOA formation from glyoxal and methylglyoxal via the growth, light absorption, and chemical composition of monodispersed submicron nanoparticles exposed to glyoxal/methylglyoxal vapors or 1,3,5-trimethylbenzene (TMB) oxidation products in an environmental chamber. Glyoxal and methylglyoxal represent one key type of COOs (i.e., dicarbonyls) that can engage in aqueous reaction. The effects of various atmospheric conditions including ammonia (NH<sub>3</sub>), formaldehyde (CH<sub>2</sub>O) concentrations, relative humidity (RH), particle acidity, and particle surface charge separation on SOA formation are also evaluated.



Chapter III and IV discuss the SOA production from toluene and *m*-xylene photooxidation, respectively. Toluene and *m*-xylene represent dominant aromatic hydrocarbon in urban atmosphere and important contributors to urban PM pollution. We simultaneously track the temporal evolutions in the gaseous products and aerosol properties when monodisperse sub-micrometer seed particles are exposed to toluene/*m*-xylene oxidation products. We quantify the contributions of COOs to SOA according to their unique functionality and aim to establish a functionality-based method for the estimation of SOA formation from VOC oxidation.

Chapter V assesses the role of respiratory aerosol in transmission of infectious diseases as well as the effectiveness of mitigation measures. We analyze the trend and mitigation measures for COVID-19 pandemic in several epicenters (Wuhan, Italy, New York City, and fifteen states in the U. S.) from January to May 2020. Chapter VI summarizes the results from Chapter II-V, offering some perspective for future research directions.

## CHAPTER II

### SECONDARY ORGANIC AEROSOL FORMATION FROM SMALL $\alpha$ -DICARBONYLS\*

#### Introduction

An annual amount of  $\sim 2000$  tera-grams ( $\text{Tg a}^{-1}$ ) of VOCs is emitted into the atmosphere from natural and anthropogenic sources.<sup>1,4</sup> Photochemical oxidation of VOCs has profound implications for air quality, human health, and climate.<sup>5,35</sup> Notably, there exist two distinct fates for the organic carbon from VOC oxidation, i.e., conversion to carbon dioxide or SOA, with drastically different atmospheric lifetimes of 5–200 years and about one week, respectively.<sup>1</sup> Although long-lived  $\text{CO}_2$  is unequivocally linked to global warming,<sup>5</sup> short-lived SOA often represents the dominant constituent of tropospheric fine aerosols.<sup>23,27,29,36,37</sup> The products from VOC oxidation contribute to tropospheric aerosol loading via new particle formation, condensation, equilibrium partitioning, particle-phase reactions, and cloud processing.<sup>22,38,39</sup> The enormous chemical complexity of VOC oxidation and the subsequent gas-to-particle conversion pose major challenges in assessing the atmospheric impacts for SOA.<sup>5,35</sup> Atmospheric models have consistently underestimated SOA mass concentrations measured in field studies.<sup>27</sup>

Small  $\alpha$ -dicarbonyls, i.e., glyoxal and methylglyoxal, are ubiquitous in the atmosphere.<sup>4,40</sup> Specifically, the oxidation of aromatics (toluene, xylenes, or trimethylbenzenes) and diketones from traffic and industrial sources and biogenic isoprene leads to significant production of

---

\* Part of this chapter is reprinted with permission from Li, Y.; Ji, Y.; Zhao, J.; Wang, Y.; Shi, Q.; Peng, J.; Wang, Y.; Wang, C.; Zhang, F.; Wang, Y.; Seinfeld, J. H.; Zhang, R. Unexpected Oligomerization of Small  $\alpha$ -Dicarbonyls for Secondary Organic Aerosol and Brown Carbon Formation. *Environ. Sci. Technol.* **2021**, 55 (8), 4430–4439. Copyright 2021 American Chemical Society. Part of this chapter is reprinted with permission from Ji, Y.; Shi, Q.; Li, Y.; An, T.; Zheng, J.; Peng, J.; Gao, Y.; Chen, J.; Li, G.; Wang, Y.; Zhang, F.; Zhang, A. L.; Zhao, J.; Molina, M. J.; Zhang, R. Carbenium Ion-Mediated Oligomerization of Methylglyoxal for Secondary Organic Aerosol Formation. *Proc. Natl. Acad. Sci.* **2020**, 117 (24), 13294 – 13299. Copyright 2020 National Academy of Sciences.

methylglyoxal on urban, regional, and global scales.<sup>17,23,41</sup> A modeling study predicted the global sources of 45 Tg a<sup>-1</sup> for glyoxal and 140 Tg a<sup>-1</sup> for methylglyoxal, with an estimated global SOA production of 11 TgC a<sup>-1</sup> from both species.<sup>40</sup> Currently, the chemical mechanisms for oligomer and BrC formation from small  $\alpha$ -dicarbonyls are highly uncertain.

The conventional view is that methylglyoxal is less reactive than glyoxal because of the unreactive methyl substitution.<sup>42</sup> A field-modeling study indicated that glyoxal from anthropogenic sources contributes to rapid and high SOA formation.<sup>43</sup> Oligomerization of methylglyoxal was postulated based on the observation of high-molecular-weight polymers from OH oxidation of TMB in an environmental chamber.<sup>44</sup> However, experimental studies on nano- to sub-micrometer particles showed negligible size growth upon exposure to methylglyoxal vapor<sup>45-47</sup> but large size growth upon exposure to glyoxal vapor under similar experimental conditions.<sup>38,45,46</sup> For example, significantly different growth factors of  $(1.93 \pm 0.04)$  and  $(1.01 \pm 0.01)$  were measured on sulfuric acid nanoparticles (20 nm) exposed to elevated glyoxal and methylglyoxal vapors (about 4 parts per million or ppm), respectively, at 20% RH.<sup>46</sup> The reactive uptake of glyoxal on sulfuric acid nanoparticle was indicated to be via a hydration mechanism as the measured growth factor of the particles decreased with decreasing RH and size (4–20 nm).<sup>46,47</sup> On the other hand, comparable reactive uptake of glyoxal and methylglyoxal was measured on bulk sulfuric acid solution,<sup>48,49</sup> and the difference in the uptake measurements between bulk solutions and nano/sub-micrometer particles implicated a profound interfacial effect. Also, surface browning was detected on ammonium/amine-containing particles exposed to methylglyoxal despite negligible particle growth,<sup>50</sup> and nitrogen-heterocycles (n-heterocycles) were identified as light-absorbing BrC with low single-scattering albedo (SSA) in bulk mixtures consisting of methylglyoxal and amines.<sup>51</sup> Moreover, previous studies hinged on measurements of direct

exposure to high levels of glyoxal and methylglyoxal vapors, i.e., from hundred parts per billion (ppb) to parts per million (ppm) levels, or using bulk samples,<sup>38,42,46,47</sup> for which their applicability to atmospheric conditions requires validation. Currently, available experimental results on the multiphase chemistry of  $\alpha$ -dicarbonyls are conflicting, casting doubt on their role in SOA formation.

## Experimental

To elucidate the mechanisms leading to SOA and BrC formation from small  $\alpha$ -dicarbonyls, we performed laboratory measurements by exposing seed particles to glyoxal and methylglyoxal in the absence/presence of gaseous  $\text{CH}_2\text{O}$  and  $\text{NH}_3$  using a 1 m<sup>3</sup> reaction chamber (Figure 2). Seed particles consisting of ammonium bisulfate (ABS), ammonium sulfate (AS) in the presence/absence of gaseous  $\text{NH}_3$ , sodium chloride (NaCl), or sucrose were chosen to represent distinct acidity and interfacial charge separation.<sup>52</sup> The size increase after exposure was measured by a differential mobility analyzer (DMA) and quantified by a growth factor,  $\text{GF} = D_p/D_o$ , where  $D_p$  is the diameter after exposure and  $D_o = 100$  nm is the initial diameter. The chemical composition of exposed particles was monitored by a thermal desorption-ion drift-chemical ionization mass spectrometer (TD-ID-CIMS). The optical properties (i.e., extinction and scattering) at 532 nm were measured using a cavity ring-down spectroscope and an integrating nephelometer.

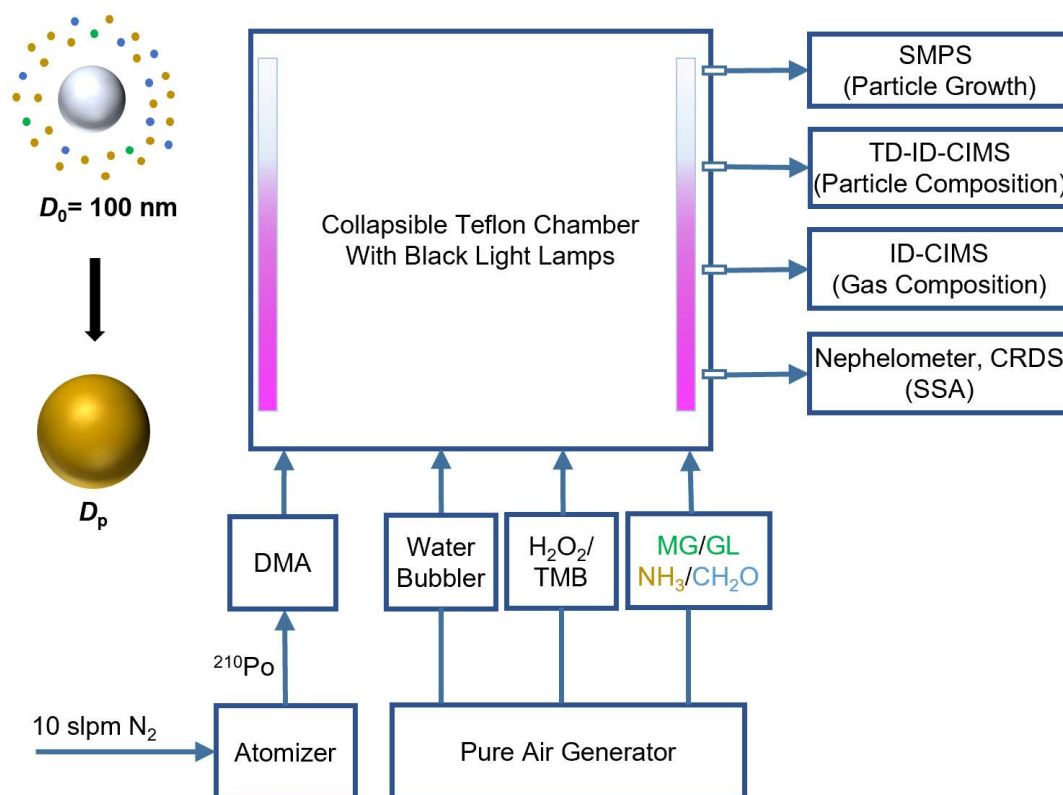


**Figure 2. Experimental schematic for SOA formation from  $\alpha$ -dicarbonyls.** MG for methylglyoxal; GL for glyoxal; TMB for 1,3,5-trimethylbenzene; DMA for differential mobility analyzer; ID-CIMS for ion drift – chemical ionization mass spectrometry; TD-ID-CIMS for thermal desorption - ion drift – chemical ionization mass spectrometry; and SMPS for scanning mobility particle sizer. Monodispersed seed particles consisting of different chemical compositions (i.e., ammonium bisulfate, ammonium sulfate, sodium chloride, and sucrose) were exposed to organic (MG, GL,  $\text{CH}_2\text{O}$ , and oxidation products of TMB by OH) and inorganic ( $\text{NH}_3$ ) vapors inside the reaction chamber, and the aerosol growth and chemical composition were simultaneously quantified by SMPS and TD-ID-CIMS, respectively. Single scattering albedo (SSA) was measured by a nephelometer and a home-built cavity ring-down spectrometer (CRDS).

Methylglyoxal solution was purified similarly to that previously described.<sup>48</sup> Briefly, commercial aqueous methylglyoxal solution (40%, Sigma-Aldrich Co. Ltd.) was used to obtain the unpolymerized and water-free form. About 5 mL of the methylglyoxal solution was pumped to remove water overnight in a flask covered with a black cloth. Phosphorus pentoxide ( $\text{P}_2\text{O}_5$ ) was

added to the resulting liquid, and the mixture was heated to 130°C. The distillate passed subsequently through a flask immersed in liquid nitrogen. The collected liquid consisted of dominant methylglyoxal monomer as shown by TD-ID-CIMS measurement (Figure 3).

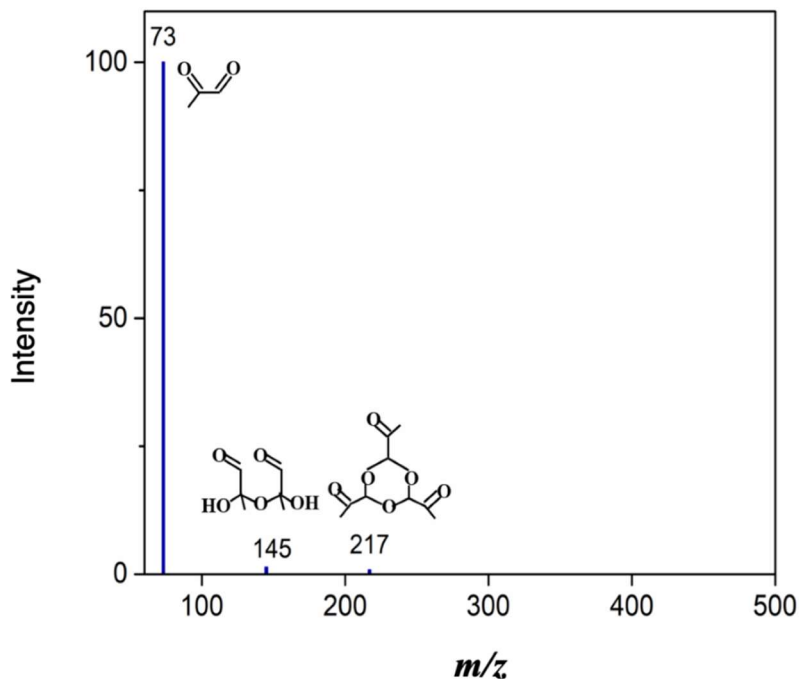


**Figure 3. TD-ID-CIMS calibration using purified methylglyoxal liquid.** TD-ID-CIMS scan from 75 to 500 amu: protonated methylglyoxal at  $m/z = 73$  represents the dominant peak, along with trace impurities of several methylglyoxal oligomeric products. About 1  $\mu\text{L}$  purified methylglyoxal was deposited on the platinum filament, and the analyte was evaporated and detected using  $\text{H}_3\text{O}^+$  reagent ions.

Three different approaches were employed to introduce methylglyoxal vapor to the chamber. First, purified methylglyoxal vapor was collected by a 1 L glass container, diluted in nitrogen ( $\text{N}_2$ ), and then flushed into the chamber. Seed particles were exposed to methylglyoxal vapor with an initial concentration of 100, 500 ppb, 1, or 5 ppm. Second, purified methylglyoxal vapor was continuously introduced into the chamber with a steady-state concentration of 500 ppb,

1, or 5 ppm throughout the experiments. Third, experiments were performed with seed particles exposed to methylglyoxal produced from oxidation of TMB and OH, which has a molar yield of ~90%.<sup>44</sup> On the other hand, to introduce glyoxal, 0.025 g of glyoxal trimer dihydrate (GLTD, Sigma Aldrich, 97%) was heated to 160°C, and glyoxal vapor was continuously introduced to the chamber by a flow of 0.5 standard liter per minute (slpm) N<sub>2</sub> during the experiment (~1.5 h); the remaining mass for GLTD was measured to be ~0.015 g. The gaseous concentrations of glyoxal and methylglyoxal were measured using an ion drift–chemical ionization mass spectrometer with hydronium ions.

The oxidation experiments between TMB and OH were performed similarly to our previous studies.<sup>53</sup> A 1 m<sup>3</sup> environmental chamber (Teflon® PFA) with eighteen black light lamps (18 × 30W, F30T8/350BL, Sylvania) was used in our experiments. A water bubbler at a temperature of 30 °C was used to humidify the chamber to 50% ~ 90% RH. A 5 slpm N<sub>2</sub> flow was used to atomize 0.06 M solution of ABS, AS, NaCl, and sucrose to produce seed particles. Particles were size-selected by a DMA to 100 nm, and the initial particle number concentration inside the chamber was 4 × 10<sup>4</sup> cm<sup>-3</sup>. The four different seed particles were used to represent distinct particle acidity and interfacial electric fields. AS particles have an estimated pH of 3~5 in the presence of gaseous NH<sub>3</sub> and a pH of 0~1 in the absence of gaseous NH<sub>3</sub>. ABS particles have a pH of -0.5. Particles containing NaCl and sucrose have a pH of 7. AS and ABS are interchangeable in our experiments, since addition of gaseous NH<sub>3</sub> converts NH<sub>4</sub>HSO<sub>4</sub> to (NH<sub>4</sub>)<sub>2</sub>SO<sub>4</sub>, dependent on the NH<sub>3</sub> concentration. Our measurements were performed on varying NH<sub>3</sub> to mimic the variable atmospheric conditions. Sucrose contains eight hydroxyl functional groups and was used in our experiments as a surrogate for hydroxycarbonyls, which have been shown to form with a significant yield from Isoprene oxidation.<sup>54</sup> Also, the electric field induced from net charge

separation of  $\text{NH}_4^+$  and  $\text{SO}_4^{2-}$  distributions is positive (pointing away from the interface) and the strongest for AS at the air-water interface, while the electric field is negligible, slightly negative (pointing to the interface), and absent for AB, NaCl, and sucrose, respectively.<sup>52</sup>

For experiments in the presence of gaseous  $\text{NH}_3$ ,  $\text{NH}_3$  with a concentration of 2000 ppm in  $\text{N}_2$  was injected into the chamber with a flow of 100 standard cubic centimeters per minute (sccm) for 2 min. To produce methylglyoxal from photooxidation of TMB and OH, 400  $\mu\text{L}$   $\text{H}_2\text{O}_2$  (35 wt%, Sigma-Aldrich) and 10  $\mu\text{L}$  1,3,5-trimethylbenzene (Sigma-Aldrich) were injected into a glass reservoir, which was then flushed into the chamber by a 10 slpm flow from a zero air generator (Aadco 737-11, Aadco Inc.) for 10 min. The gases were then mixed by a fan inside the chamber. Once a desired concentration was established, the black light lamps were turned on to initiate  $\text{H}_2\text{O}_2$  photolysis, and the oxidation reaction produced a constant methylglyoxal concentration. The black light lamps were turned off for direct exposure experiments to glyoxal and methylglyoxal. For experiments with  $\text{CH}_2\text{O}$ , 1.5 slpm  $\text{N}_2$  was blown through a flask containing 5 mL  $\text{CH}_2\text{O}$  aqueous solution (37%, Sigma-Aldrich) to introduce  $\text{CH}_2\text{O}$  vapor into the chamber for 10 min. A SMPS was used to continuously measured  $GF$  for 120 min. An ion drift - chemical ionization mass spectrometer (ID-CIMS) was used to analyze gas-phase concentrations of TMB, methylglyoxal, and glyoxal with a sample flow rate of 0.5 slpm from the chamber. The sample line was heated to 70°C to reduce wall loss. Gas-phase concentrations of methylglyoxal/glyoxal were detected and quantified by ID-CIMS according to Fortner et al.<sup>55</sup> Briefly, the concentration of species X (X = methylglyoxal or glyoxal) is determined by,

$$[\text{X}] = \frac{S_{\text{X}}}{k_{\text{PTR}}\Delta t S_{\text{RI}}} \quad (1)$$



where  $S_X$  and  $S_{RI}$  are the mass spectrum intensities for X and reagent ions, respectively.  $k_{PTR}$  is the proton transfer rate constant between X and  $H_3O^+$ .  $\Delta t = \frac{l}{U_i}$  is the retention time of ions in the drift tube, which is determined by the length of the drift tube  $l = 8$  cm and the ion drift velocity  $U_i$ . The ion drift velocity  $U_i$  is determined from,

$$U_i = u_0 \left( \frac{760 \text{ torr}}{p} \right) \left( \frac{T}{273 \text{ K}} \right) E \quad (2)$$

where  $u_0 = 2 \text{ cm}^2 \text{ V}^{-1} \text{ s}^{-1}$  is the reduced ionic mobility,<sup>56</sup>  $p = 5.0$  torr and  $T = 298$  K are the pressure and temperature in drift tube, respectively, and  $E = 37.5 \text{ V cm}^{-1}$  is the voltage gradient in the drift tube. The concentrations of TMB, methylglyoxal, and glyoxal determined from this method are  $(4.5 \pm 0.2) \times 10^{13}$ ,  $(3.7 \pm 0.8) \times 10^{10}$ , and  $(2.2 \pm 0.3) \times 10^{11} \text{ molecule cm}^{-3}$ , respectively.

To analyze the particle-phase chemical composition by TD-ID-CIMS, exposed particles after 30 min of photooxidation were collected for 2 h by a platinum filament in a 2.5 slpm flow from the reaction chamber, and the analytes were evaporated by heating the filament and detected using hydronium ions ( $H_3O^+$ ) as the reagent ions.

To measure the optical properties of exposed particles, a 1-srpm flow from the chamber was diluted by 4-srpm  $N_2$  and introduced into a commercial integrating nephelometer (TSI 3563) and a home-built cavity ring-down spectrometer (CRDS) after 1.5 h of exposure. Light scattering ( $b_{sca}$ ) and extinction ( $b_{ext}$ ) at 532 nm were determined by the nephelometer and CRDS, respectively.<sup>57</sup> The absorption coefficient ( $b_{abs}$ ) was determined from  $(b_{ext} - b_{sca})$ , and the SSA was calculated from  $b_{sca}/b_{ext}$ . To account for the size dependence of SSA, the nephelometer and CRDS were calibrated by measuring size-selected ammonium sulfate particles with the diameters of 100, 150, 200, 250, and 300 nm. The measured SSA for particles after exposure was corrected by that of ammoniums sulfate particles with the corresponding diameter.

### *Vapor Wall Loss Correction*

Loss of vapors to the chamber wall is estimated by the first-order wall-loss coefficient  $k_w$  ( $s^{-1}$ ) by considering gas-phase transport within the chamber according to Zhang *et al.*,<sup>58</sup>

$$k_w = \left(\frac{A}{V}\right) \frac{\alpha_w \bar{c}}{4 + \frac{\pi}{2} \left(\frac{\alpha_w \bar{c}}{\sqrt{k_e D_g}}\right)} \quad (3)$$

where  $A/V$  is the surface to volume ratio of the chamber (equal to  $6/L$  for a square chamber, where  $L = 1$  m is its dimension),  $\alpha_w$  is the mass accommodation coefficient of vapors onto Teflon chamber walls at RH = 90%,  $\bar{c} = \sqrt{\frac{8k_B T}{m}}$  is the mean thermal speed of the molecules,  $k_e$  is the coefficient of eddy diffusion,  $k_e$  is estimated to be 0.5 for a  $1 \text{ m}^3$  well-mixed chamber with a mixing time scale of  $\sim 5$  s based on the loss rate of particles,<sup>59</sup>

$$k_e = \frac{\left(\frac{\pi L \beta_0}{12}\right)^2}{D_b} \quad (4)$$

where  $\beta_0$  is the fractional loss rate of the particles,

$$\beta_0 = \frac{dN}{Ndt} = \frac{15000 \text{ cm}^{-3} - 7500 \text{ cm}^{-3}}{15000 \text{ cm}^{-3} \times 7200 \text{ s}} = 1.4 \times 10^{-5} \text{ s}^{-1} \quad (5)$$

$D_b = 6.75 \times 10^{-10} \text{ m}^2/\text{s}$  is the Brownian diffusion coefficient for particles.  $D_g$  is the gas-phase diffusion coefficient.

The average concentration  $c$  of a gas species is estimated by,

$$c = \frac{1 - e^{-k_w \Delta t_i}}{k_w \Delta t_i} c_0 \quad (6)$$

For NH<sub>3</sub>, the mass accommodation coefficient of vapors onto the chamber wall  $\alpha_w$  is taken to be 0.01.<sup>60</sup> Gas-phase diffusion constant  $D_g$  is  $1.98 \times 10^{-5}$ .<sup>61</sup> The mean thermal speed  $\bar{c}$  is calculated to be  $603 \text{ m s}^{-1}$ . The first-order wall-loss coefficient of NH<sub>3</sub> is  $1.20 \times 10^{-2} \text{ s}^{-1}$ ,  $\Delta t_i$  is about 30 min during the initial growth period. For initial injection of  $c_0 = 400 \text{ ppb}$  NH<sub>3</sub>, The average concentration of NH<sub>3</sub> is estimated to be  $\bar{c} = 19 \text{ ppb}$ .

The concentration of CH<sub>2</sub>O in the chamber was calculated from the evaporation rate according to a previously established method.<sup>62</sup> In our study, the N<sub>2</sub> flow over CH<sub>2</sub>O solution  $f$  is calculated by  $f = \frac{F'}{S}$ , where  $F'$  is the flow rate of N<sub>2</sub> over CH<sub>2</sub>O (1.5 slpm),  $S$  is the cross-sectional area of the flask  $S = \pi r^2$ ,  $r$  is the radius of the flask  $r = 0.025 \text{ m}$ , and  $f$  is  $0.05 \text{ m s}^{-1}$ . For 37% CH<sub>2</sub>O solution at 25 °C ambient temperature and alongside and crosswind puddle lengths of 0.025 m, the evaporation rate of CH<sub>2</sub>O is  $R = 2.24 \times 10^{-7} \text{ g s}^{-1}$ . The concentration of CH<sub>2</sub>O in the chamber is given by,

$$[\text{CH}_2\text{O}]_0 = \frac{R t_{inj} V_m}{V \cdot M_{\text{CH}_2\text{O}}} \quad (7)$$

where  $t_{inj} = 10 \text{ min}$  is the time of injection,  $V_m = 22.4 \text{ L mol}^{-1}$  is the molar volume,  $V = 1 \text{ m}^3$  is the volume of the chamber, and  $M_{\text{CH}_2\text{O}} = 30 \text{ g mol}^{-1}$  is the molar weight of CH<sub>2</sub>O. To correct wall loss, the mass accommodation coefficient  $\alpha_w$  is taken as 0.0001,<sup>63</sup> the gas-phase diffusion coefficient  $D_g$  is  $1.8 \times 10^{-5} \text{ m}^2 \text{ s}^{-1}$ , and the mean thermal speed  $\bar{c}$  is  $455 \text{ m s}^{-1}$ . The first-order wall-loss coefficient of CH<sub>2</sub>O,  $k_{w\text{CH}_2\text{O}}$ , is  $9.8 \times 10^{-3} \text{ s}^{-1}$ , yielding a CH<sub>2</sub>O concentration of 31 ppb.

### *Uptake Coefficient Calculation*

The measured initial particle growth (within 30 mins) is used to derive the uptake coefficient of methylglyoxal/glyoxal from,

$$\gamma = \frac{4FRk_1}{\bar{c}S} \quad (8)$$

where  $FR$  is the fraction of oligomeric and n-heterocycle products contributing to the growth of seed particles. In addition to methylglyoxal, other products from photo-oxidation of TMB (i.e., oxidation intermediates such as furanone products at  $m/z = 111$  and  $113$ ) also contributed to the growth of seed particles.  $FR$  is given by

$$FR = \frac{RI_{oli} + RI_{n-het}}{RI_{oli} + RI_{n-het} + RI_{by}} \quad (9)$$

where  $RI_{oli}$ ,  $RI_{n-het}$ ,  $RI_{by}$  are the relative intensities of oligomeric products, n-heterocycles, and other products.  $k_1$  is first order decay rate constant of methylglyoxal/glyoxal, and  $k_1$  is calculated from the measured growth rate of AS particles in the presence of  $\text{NH}_3$ ,

$$k_1 = \frac{\pi(D_p^3 - D_0^3)\rho NN_A}{6MW[X]dt} \quad (10)$$

where  $D_p$  and  $D_0$  are the final and initial diameters of the particles during the time-period of  $dt$ , respectively,  $\rho$  is the density of methylglyoxal ( $1.05 \text{ g cm}^{-3}$ ) or glyoxal ( $1.27 \text{ g cm}^{-3}$ ),  $N = 40000 \text{ cm}^{-3}$  is the measured particle number concentration,  $N_A$  is Avogadro constant,  $MW$  is the molar weight of methylglyoxal ( $72 \text{ g mol}^{-1}$ ) or glyoxal ( $58 \text{ g mol}^{-1}$ ), and  $[X]$  is the gas phase concentration.  $\bar{c}$  is the mean thermal speed of methylglyoxal/glyoxal.  $S$  is the average surface area of aerosols ( $\text{cm}^2 \text{ surface/cm}^3 \text{ air}$ ) during the time-period of  $\Delta t = 90 \text{ min}$ ,

$$S = \frac{\pi \int_{t=0}^{90 \text{ min}} D^2 HGf^2 N dt}{\Delta t} \quad (11)$$

where  $D$  is the time-dependent particle diameter,  $HGf$  is the hygroscopic growth factor of particles.

### *Molecular Dynamic Simulations*

Classic molecular dynamic simulation (MDS) was carried out using the package Nanoscale Molecular Dynamics (NAMD 2.11)<sup>64</sup> to investigate the interfacial kinetic process of methylglyoxal from gas to aqueous phases. The neutral solution is composed of about 500 water molecules.<sup>65</sup> The 500 ps equilibration is executed in the isothermal-isochoric ensemble ( $T=298\text{K}$ ) and then in isothermal-isobaric ( $NPT$ ) ensemble ( $P=1$  bar) to guarantee thermodynamic equilibrium of the neutral solution. Methylglyoxal and water are described by the OPLS-AA force field and TIP3P force, respectively.<sup>65</sup> The restrained electrostatic potential charge is used for methylglyoxal by Multiwfn program<sup>20</sup> with a box size of  $25\times 25\times 25$  Å.<sup>66</sup> The Lennard-Jones and real space Coulombic interactions were cut off at 12 Å. The coulomb term is determined by the Particle Mesh Ewald method<sup>21,22</sup> in an accuracy of 0.0001 kcal/mol. The time step of 0.5 fs is used to solve the Newton equations of molecular motion. The Gibbs free energy is obtained using the umbrella sampling and the Weighted Histogram Analysis Method based on the equilibrated MDS trajectories, and the reaction coordinate is calculated as the distance between the center of mass of the solute and center of mass of the solvent. A force constant of  $10 \text{ kcal} (\text{mol}\cdot\text{Å}^2)^{-1}$  water is applied to keep boundary potentials. The molecular dynamic simulation of 500 ps is run using the the isothermal-isochoric ensemble.

### *Diffusion coefficient calculation*

The diffusion coefficients for the oligomers of glyoxal and methylglyoxal are estimated using the Stokes–Einstein approach,

$$D = \frac{k_B T}{6\pi\eta a} \quad (12)$$

where  $k_B$  and  $T$  are the Boltzmann constant and temperature, respectively,  $\eta$  denotes the viscosity of the solvent, and  $a$  is the radius of the molecule.

## **Results and Discussion**

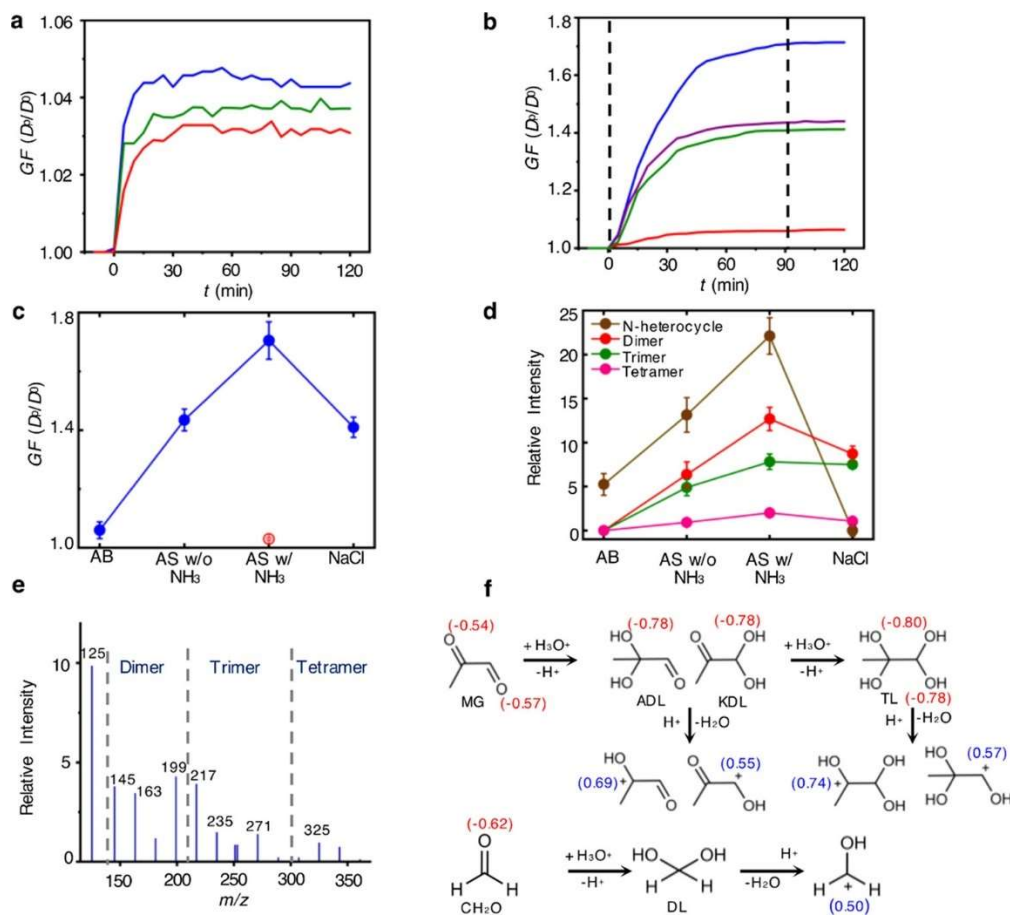
### *SOA and BrC Formation on Sub-Micrometer Aerosols*

Exposure of AS particles to methylglyoxal vapor in a concentration range from 100 ppb to 5 ppm results in a small growth, with a GF of 1.03–1.04 (Figures 4a and 5). The temporal evolution of the GF shows that the size increase occurs only during the initial time, i.e.,  $t < 10$ –20 min (each GF measurement took 5 min). Figures 4a and 5 show that the measured GF increases slightly with an increasing methylglyoxal concentration and similar growth occurs in the experiments with methylglyoxal either introduced initially or continuously into the chamber, with the GF values of  $(1.03 \pm 0.01)$  and  $(1.04 \pm 0.01)$ , respectively (Figure 5). The GF values measured in our work are comparable to those of the previous experimental studies,<sup>43,45,46</sup> which showed negligible particle growth upon exposure to methylglyoxal vapor (i.e., from  $0.99 \pm 0.01$  to  $1.02 \pm 0.01$  on sulfuric acid nanoparticles).

On the other hand, large particle growth occurs when methylglyoxal is produced from photooxidation of TMB by OH. In the latter experiments, methylglyoxal was continuously produced from TMB-OH oxidation, resulting in a steady-state mixing ratio of about 2 ppb

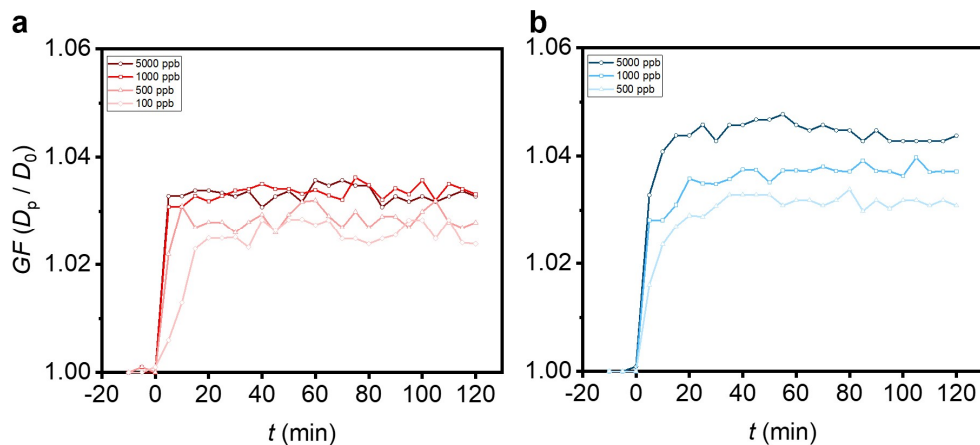
(Figure 4b,c) that closely replicates the atmospheric conditions. Figure 4b shows gradual and continuous particle growth throughout the experiments on different seed particles. The measured GF is dependent on seed particles, and the highest GF of  $1.70 \pm 0.06$  corresponds to AS particles in the presence of 19 ppb  $\text{NH}_3$  (Figure 4b,c).

Also, there is a weak dependence of GF on RH from 50 to 90% (Figure 6a). Measurements of chemical compositions of the exposed particles by TD-ID-CIMS reveal that the size increase results dominantly from formation of oligomers and *n*-heterocycles (Figures 4d, 7a and 8a, and Tables 1 and 2). Both oligomers and *n*-heterocycles are detected on ABS and AS, whereas only oligomeric products are identified on NaCl. Formation of oligomers and *n*-heterocycles varies with seed particles similarly as GF (Figure 4c) and decreases from *n*-heterocycles (except for NaCl), dimers, trimers, to tetramers (Figure 4e). The mechanism for the aqueous reactions involves the methylglyoxal carbenium ions as the key intermediates (Figure 4f), which subsequently undergo nucleophilic addition to yield oligomers and *n*-heterocycles.

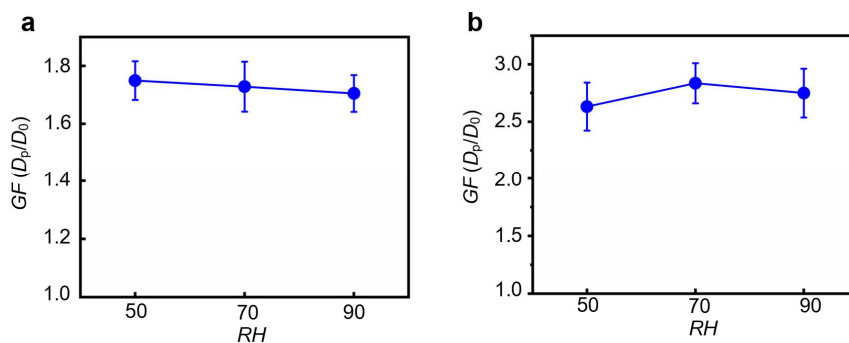


**Figure 4. SOA growth from methylglyoxal.** (a) Time-dependent growth factor ( $GF = D_p/D_0$ ) of AS seed particles exposed to methylglyoxal vapor continuously introduced to the chamber at steady-state concentrations of 5 ppm (blue), 1 ppm (green), and 500 ppb (red). (b) Time-dependent GF of seed particles consisting of AS in the presence (blue) and absence (purple) of 19 ppb NH<sub>3</sub>, NaCl (green), and ABS (red) exposed to the products from photochemical TMB-OH oxidation. The vertical dashed line at  $t = 0$  denotes the time for injection of methylglyoxal vapor or turning on the UV lights, and the vertical dashed line at  $t = 90$  min denotes the time for obtaining GF. (c) Measured GF after 90 min of direct exposure to methylglyoxal vapor (red circle) and to the products from TMB-OH photochemical oxidation (blue circle). For experiments with exposure to the products of OH-TMB oxidation, the initial concentrations of TMB and H<sub>2</sub>O<sub>2</sub> were 1.8 and 114 ppm, respectively, and the steady-state concentration of methylglyoxal was 2 ppb. (d) Single-ion monitoring of particle-phase  $n$ -heterocycles at 83 and 125  $m/z$ , dimers at 145, 163, 181, and 199  $m/z$ , trimers at 217, 235, 253, 271, and 289  $m/z$ , and tetramers at 307, 325, 343, 361, 379, 397, and 415  $m/z$ . Particles exposed to TMB-OH photooxidation products were collected by TD-ID-CIMS after 30 min of exposure, and the collection time was 2 h. (e) Mass spectral peaks of aerosol-phase products on AS in the presence of NH<sub>3</sub>. (f) Carbenium-ion formation from methylglyoxal (MG) and CH<sub>2</sub>O. ADL, KDL, TL, and DL denote aldehyde diol, ketone diol, tetrol, and diol, respectively. The numbers within parentheses denote the negative (red) or positive (blue) natural charge (in e). All experiments were performed at 298 K and RH = 90%. The uncertainty in measured GF corresponds to one standard deviation ( $1\sigma$ ) of 6 measurements for direct methylglyoxal exposure, and all other uncertainties correspond to  $1\sigma$  of at least 3 measurements. Each GF measurement took 5 min, corresponding to each DMA scan.

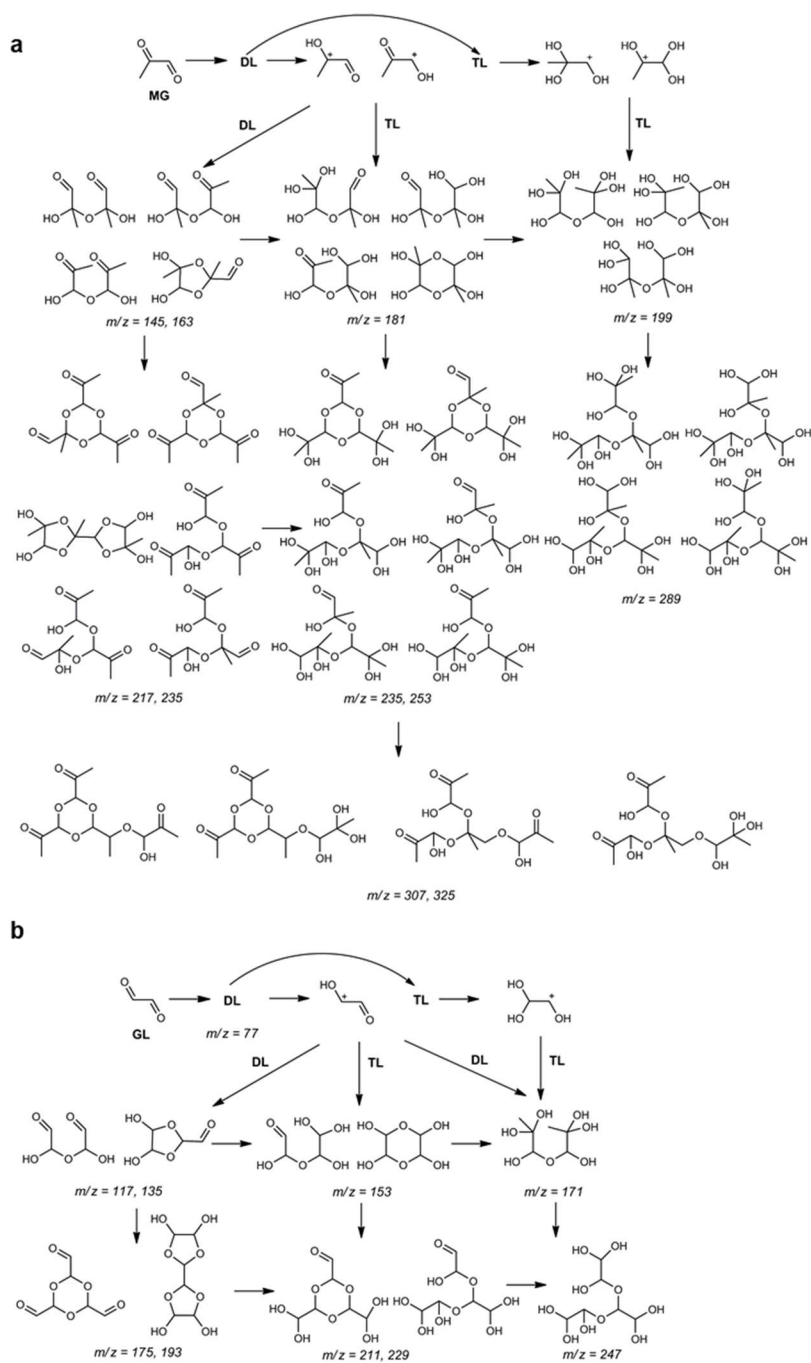




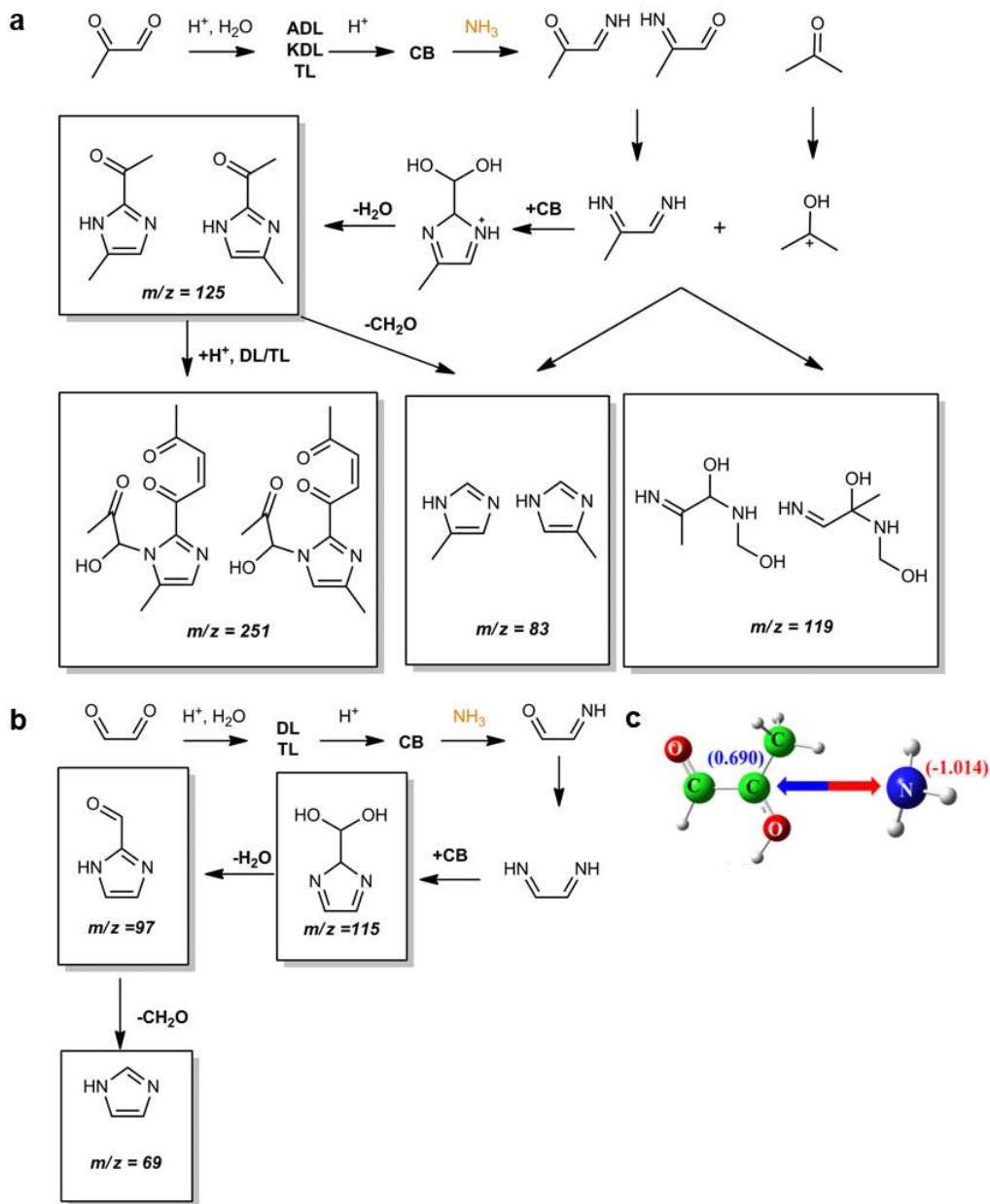
**Figure 5. Time-dependent  $GF$  of seed particles exposed directly to methylglyoxal vapor.** (a) Methylglyoxal was introduced to the chamber in the beginning of the experiment with an initial concentration of 100 ppb to 5 ppm. (b) Methylglyoxal was introduced continuously to the chamber during the experiment with a steady-state concentration of 500 ppb to 5 ppm. AS seed particles in the presence of 19 ppb  $\text{NH}_3$  were used in the experiments.  $t = 0$  denotes the time for injection of methylglyoxal vapor.



**Figure 6. Weak RH-dependence of  $GF$  for AS exposed to products from photochemical oxidation of TMB and OH (a) and glyoxal vapor (b) in the presence of 19 ppb  $\text{NH}_3$ .**



**Figure 7. Carbenium ion-mediated pathways leading to oligomeric products.** (a) Oligomerization pathways of methylglyoxal. (b) Oligomerization pathways of glyoxal. The  $m/z$  value corresponds to the protonated form. DL and TL denote diol and tetrol, respectively.

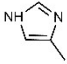
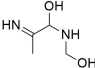
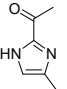
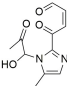
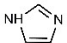
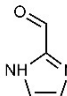
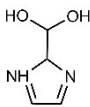


**Figure 8. Carbenium ion-mediated pathways leading to imidazoles and *n*-heterocycles.** (a) Formation of *n*-heterocycles and imidazole from methylglyoxal,  $\text{NH}_3$ , and  $\text{CH}_2\text{O}$ . The peaks at  $m/z = 83$  and  $119$  represent the signals by addition of  $\text{CH}_2\text{O}$ . The peaks at  $m/z = 125$  and  $251$  represent the *n*-heterocycles from the reactions of methylglyoxal with  $\text{NH}_3$ . (b) Formation of *n*-heterocycles from glyoxal and  $\text{NH}_3$ . The  $m/z$  value corresponds to the protonated form. The peaks at  $m/z = 69$ ,  $97$ , and  $115$  represent the *n*-heterocycles from the reactions of glyoxal with  $\text{NH}_3$ . (c) Nucleophilic attack of carbenium ions by  $\text{NH}_3$  facilitated by strong electrostatic attraction (marked by the blue-red arrow). ADL and KDL denote aldehyde diol and ketone diol, respectively.

**Table 1. Peak assignments for oligomeric products detected by TD-ID-CIMS.**

	<i>m/z</i>	Ion	MW	Formula
<b>Methylglyoxal</b>				
Dimers	145	$[\text{C}_6\text{H}_{10}\text{O}_5+\text{H}-\text{H}_2\text{O}]^+$	162	$\text{C}_6\text{H}_{10}\text{O}_5$
	163	$[\text{C}_6\text{H}_{10}\text{O}_5+\text{H}]^+$	162	$\text{C}_6\text{H}_{10}\text{O}_5$
	163	$[\text{C}_6\text{H}_{12}\text{O}_6+\text{H}-\text{H}_2\text{O}]^+$	180	$\text{C}_6\text{H}_{12}\text{O}_6$
	181	$[\text{C}_6\text{H}_{12}\text{O}_6+\text{H}]^+$	180	$\text{C}_6\text{H}_{12}\text{O}_6$
	181	$[\text{C}_6\text{H}_{14}\text{O}_7+\text{H}-\text{H}_2\text{O}]^+$	198	$\text{C}_6\text{H}_{14}\text{O}_7$
	199	$[\text{C}_6\text{H}_{14}\text{O}_7+\text{H}]^+$	198	$\text{C}_6\text{H}_{14}\text{O}_7$
Trimers	217	$[\text{C}_9\text{H}_{12}\text{O}_6+\text{H}]^+$	216	$\text{C}_9\text{H}_{12}\text{O}_6$
	217	$[\text{C}_9\text{H}_{14}\text{O}_7+\text{H}-\text{H}_2\text{O}]^+$	234	$\text{C}_9\text{H}_{14}\text{O}_7$
	235	$[\text{C}_9\text{H}_{14}\text{O}_7+\text{H}]^+$	234	$\text{C}_9\text{H}_{14}\text{O}_7$
	235	$[\text{C}_9\text{H}_{16}\text{O}_8+\text{H}-\text{H}_2\text{O}]^+$	252	$\text{C}_9\text{H}_{16}\text{O}_8$
	253	$[\text{C}_9\text{H}_{16}\text{O}_8+\text{H}]^+$	252	$\text{C}_9\text{H}_{16}\text{O}_8$
	253	$[\text{C}_9\text{H}_{18}\text{O}_9+\text{H}-\text{H}_2\text{O}]^+$	270	$\text{C}_9\text{H}_{18}\text{O}_9$
	271	$[\text{C}_9\text{H}_{18}\text{O}_9+\text{H}]^+$	270	$\text{C}_9\text{H}_{18}\text{O}_9$
	271	$[\text{C}_9\text{H}_{20}\text{O}_{10}+\text{H}-\text{H}_2\text{O}]^+$	288	$\text{C}_9\text{H}_{20}\text{O}_{10}$
	289	$[\text{C}_9\text{H}_{20}\text{O}_{10}+\text{H}]^+$	288	$\text{C}_9\text{H}_{20}\text{O}_{10}$
Tetramers	307	$[\text{C}_{12}\text{H}_{20}\text{O}_9+\text{H}]^+$	306	$\text{C}_{12}\text{H}_{20}\text{O}_9$
	307	$[\text{C}_{12}\text{H}_{22}\text{O}_{10}+\text{H}-\text{H}_2\text{O}]^+$	324	$\text{C}_{12}\text{H}_{22}\text{O}_{10}$
	325	$[\text{C}_{12}\text{H}_{22}\text{O}_{10}+\text{H}]^+$	324	$\text{C}_{12}\text{H}_{22}\text{O}_{10}$
	325	$[\text{C}_{12}\text{H}_{24}\text{O}_{11}+\text{H}-\text{H}_2\text{O}]^+$	342	$\text{C}_{12}\text{H}_{24}\text{O}_{11}$
<b>Glyoxal</b>				
Dimers	117	$[\text{C}_4\text{H}_6\text{O}_5+\text{H}-\text{H}_2\text{O}]^+$	134	$\text{C}_4\text{H}_6\text{O}_5$
	135	$[\text{C}_4\text{H}_6\text{O}_5+\text{H}]^+$	134	$\text{C}_4\text{H}_6\text{O}_5$
	153	$[\text{C}_4\text{H}_8\text{O}_6+\text{H}]^+$	152	$\text{C}_4\text{H}_8\text{O}_6$
	171	$[\text{C}_4\text{H}_{10}\text{O}_7+\text{H}]^+$	170	$\text{C}_4\text{H}_{10}\text{O}_7$
Trimers	175	$[\text{C}_6\text{H}_6\text{O}_6+\text{H}]^+$	174	$\text{C}_6\text{H}_6\text{O}_6$
	193	$[\text{C}_6\text{H}_8\text{O}_7+\text{H}]^+$	192	$\text{C}_6\text{H}_8\text{O}_7$
	211	$[\text{C}_6\text{H}_{10}\text{O}_8+\text{H}]^+$	210	$\text{C}_6\text{H}_{10}\text{O}_8$
	229	$[\text{C}_6\text{H}_{12}\text{O}_9+\text{H}]^+$	228	$\text{C}_6\text{H}_{12}\text{O}_9$
	247	$[\text{C}_6\text{H}_{14}\text{O}_{10}+\text{H}]^+$	246	$\text{C}_6\text{H}_{14}\text{O}_{10}$

**Table 2. Peak assignments for *n*-heterocycles detected by TD-ID-CIMS.**

m/z	MW	Formula	Compound
<b>Methylglyoxal</b>			
83	82	C <sub>4</sub> H <sub>6</sub> N <sub>2</sub>	
119	118		
125	124	C <sub>6</sub> H <sub>8</sub> ON <sub>2</sub>	
251	250	C <sub>6</sub> H <sub>10</sub> O <sub>5</sub>	
<b>Glyoxal</b>			
69	68	C <sub>3</sub> H <sub>4</sub> N <sub>2</sub>	
97	96	C <sub>4</sub> H <sub>4</sub> ON <sub>2</sub>	
115	114	C <sub>4</sub> H <sub>6</sub> O <sub>2</sub> N <sub>2</sub>	

We conducted experiments by exposing seed particles to glyoxal vapor in the presence/absence of NH<sub>3</sub> (Figure 9). In contrast to direct exposure to methylglyoxal vapor, continuous and significant particle growth occurs upon exposure to glyoxal vapor at a mixing ratio of 9 ppb (Figure 9a,b). Exposure of AS particles to glyoxal in the presence of 19 ppb NH<sub>3</sub> exhibits the highest GF of  $2.75 \pm 0.07$  at 90 min, while smaller GF (1.3 to 1.5) occurs for ABS, NaCl, and AS in the absence of NH<sub>3</sub> (Figure 9a,b). Also, the measured GF exhibits a weak dependence on RH from 50 to 90% (Figure 6b). Chemical speciation of the aerosol-phase products by TD-ID-CIMS indicates the highest intensities for dimers and *n*-heterocycles, lower intensities for trimers,

and no measurable tetramers. The maximal intensities for dimers and *n*-heterocycles also correspond to AS with NH<sub>3</sub> (Figures 9c,d, 7b and 8b, and Tables 1 and 2). Similarly, formation of oligomers and *n*-heterocycles involves the glyoxal carbenium ions as the key intermediates (Figure 9e). Our measured size growth of seed particles exposed to glyoxal is consistent with the available experimental results.<sup>45,46</sup> For comparison, a previous study measured a GF value of 1.93 ± 0.04 on 20 nm sulfuric acid nanoparticles exposed to glyoxal at 20% RH and identified the isomeric products of dimers, trimers, tetramers, and pentamers.<sup>45</sup>

Additional experiments of glyoxal and methylglyoxal uptake were performed on AS particles by varying NH<sub>3</sub> from 0 to 46 ppb. The measured GF for both glyoxal and methylglyoxal increases monotonically with increasing NH<sub>3</sub> (Figure 10a,b). The significant particle growth in the presence of NH<sub>3</sub> contrasts with a previous experimental study,<sup>47</sup> showing negligible growth of sulfuric acid nanoparticles exposed to increased gaseous NH<sub>3</sub> (with only acid–base reaction). The increase in GF with NH<sub>3</sub> is explained by inhibited NH<sub>3</sub> evaporation from AS and the reaction of NH<sub>3</sub> with methylglyoxal/glyoxal to yield nonvolatile *n*-heterocycles (Figure 11); the latter is confirmed from the simultaneous increases in GF and the intensities of particle-phase *n*-heterocycles (Figures 4c and 9c).

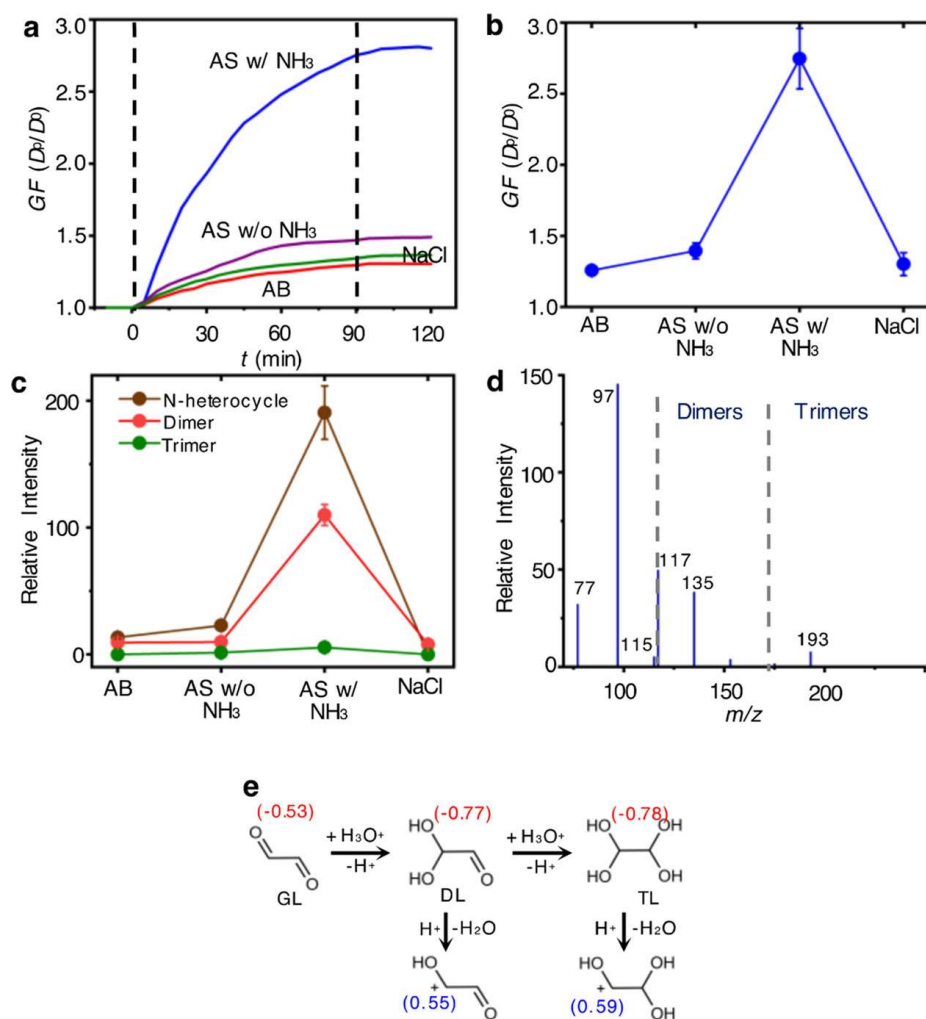


**Figure 9. SOA growth from glyoxal.** (a) Time-dependent GF for AS in the presence (blue) and absence (purple) of 19 ppb NH<sub>3</sub>, NaCl (green), and AB (red) seed particles exposed directly to 9 ppb glyoxal. The vertical dashed line at  $t = 0$  denotes the time of introducing glyoxal vapor, and the vertical dashed line at  $t = 90$  min denotes the time for obtaining GF. (b) Measured GF when directly exposed to 9 ppb glyoxal vapor at  $t = 90$  min. (c) Single-ion monitoring of particle-phase  $n$ -heterocycles at 69, 97, and 115  $m/z$ , dimers at 117, 136, 153, and 171  $m/z$ , and trimers at 175, 193, 211, 229, and 247  $m/z$ . (d) Major mass spectral peaks of particle-phase products on AS in the presence of 19 ppb NH<sub>3</sub>. (e) Carbenium-ion formation from glyoxal (GL). The numbers within parentheses denote the negative (red) or positive (blue) natural charge (in  $e$ ). All experiments were performed at 298 K and RH = 90%. The error corresponds to  $1\sigma$  of at least 3 measurements.

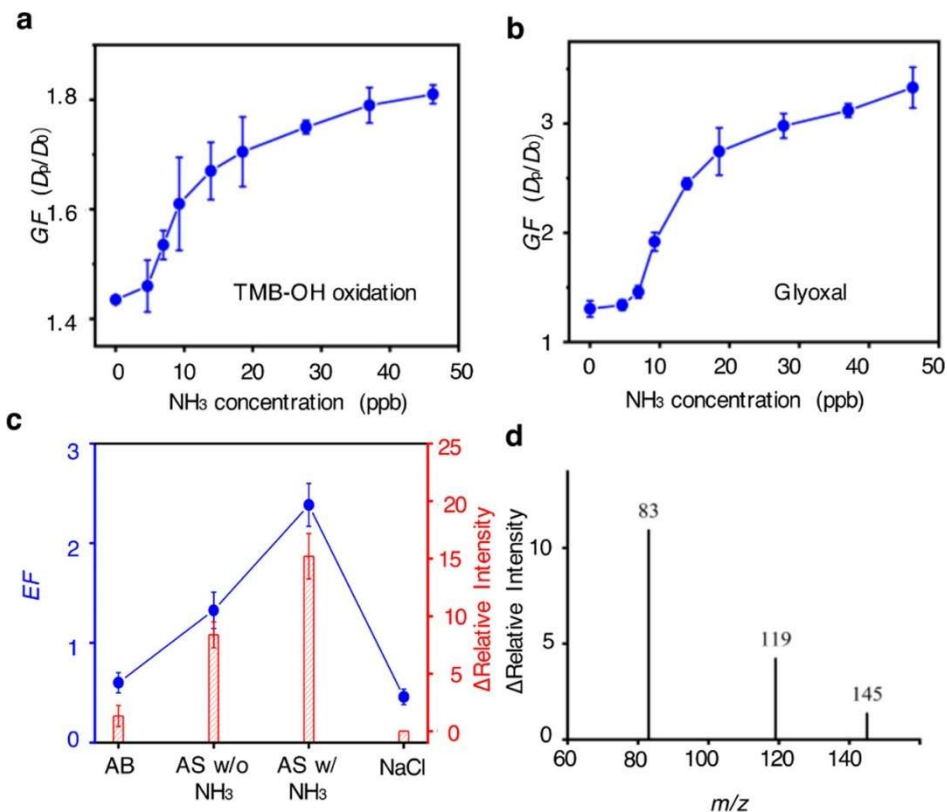


**Figure 10. Synergetic oligomerization in the presence of NH<sub>3</sub> and CH<sub>2</sub>O.** (a) Measured GF of AS particles exposed to TMB-OH oxidation products with varying NH<sub>3</sub> (0–46 ppb). (b) Measured GF of AS particles exposed to glyoxal with varying NH<sub>3</sub> (0–46 ppb). (c) Enhancement factor (EF) by addition of CH<sub>2</sub>O (blue), defined by  $(D_p'^3 - D_p^3)/D_0^3$ , where  $D_p'$  and  $D_p$  denote the particle diameters in the presence and absence of 31 ppb CH<sub>2</sub>O, respectively, and single-ion monitoring of the relative intensity change of the imidazole peak ( $m/z = 83$ ) on particles in the presence and absence of CH<sub>2</sub>O (red) for different seed particles exposed to TMB-OH oxidation products. (d) Change of the relative intensity of imidazole at  $m/z = 83$ , an intermediate at  $m/z = 119$ , and methylglyoxal dimer at  $m/z = 145$  between the presence and absence of CH<sub>2</sub>O on seed particles exposed to the TMB-OH oxidation products. The error bar denotes  $1\sigma$  of 3 repeated measurements.



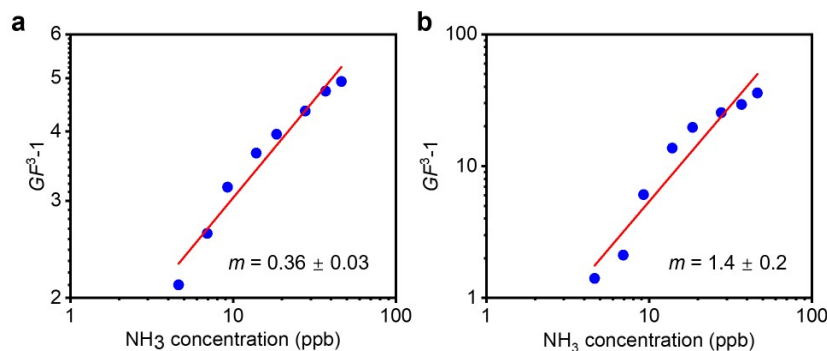


**Figure 11. Dependence of relative volume growth ( $GF^3-1$ ) of AS particles on gas-phase  $NH_3$  concentration exposing to TMB oxidation products.** (a) and glyoxal vapor (b). The relative volume growth is in proportional to the  $NH_3$  concentration (in ppb) to the power of  $m$ :  $(GF^3-1) \propto [NH_3]^m$ . Linear regression of the logarithmic values results in  $m = 0.36 \pm 0.03$  for methylglyoxal and  $m = 1.4 \pm 0.2$  for glyoxal.

We also performed experiments to examine the effects of  $CH_2O$  on particle growth from  $\alpha$ -dicarbonyls. Addition of  $CH_2O$  considerably increases the particle growth from TMB-OH oxidation (Figure 10c), as determined by an enhancement factor,  $EF = (D_p'^3 - D_p^3)/D_o^3$ , where  $D_p'$  and  $D_p$  are the particle diameters in the presence and absence of  $CH_2O$ , respectively. The EF varies with seed particles, reaching a maximum value of  $2.4 \pm 0.2$  for AS with  $NH_3$ . Analysis of particle composition reveals that the enhancement is attributed to the simplest  $n$ -heterocycle-imidazole products ( $m/z = 83$ ), along with an intermediate ( $m/z = 119$ ) and the smallest dimers ( $m/z = 145$ ) (Figure 10c,d). On the other hand, addition of  $CH_2O$  results in a slight decrease of GF for exposure to glyoxal vapor (Figure 12), and no imidazole formation is observed with  $CH_2O$  addition.

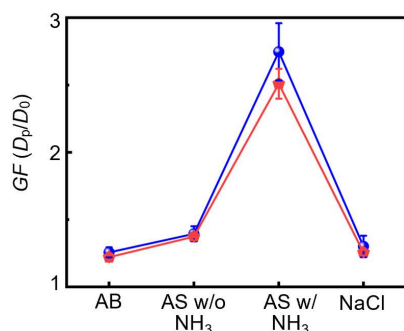


**Figure 12. Particle growth factor when exposure to glyoxal vapor in the presence of CH<sub>2</sub>O.** Growth factors of different seed particles exposed to glyoxal vapor in the absence (blue) and presence (red) of 100 ppb CH<sub>2</sub>O vapor. The error bar denotes 1 $\sigma$  of 3 repeated measurements.

The measured uptake coefficients are higher for methylglyoxal than glyoxal: the  $\gamma$  values on AS seed particles in the presence of NH<sub>3</sub> and CH<sub>2</sub>O are  $(2.4 \pm 0.5) \times 10^{-2}$  and  $(8.1 \pm 1.5) \times 10^{-3}$  for methylglyoxal and glyoxal, respectively (Figure 13a,b, and Table 3). We also measured light extinction and scattering at a wavelength of 532 nm for sub-micrometer particles after exposure to methylglyoxal/glyoxal for 90 min. The measured SSA of  $0.940 \pm 0.015$  for methylglyoxal is lower than that of  $0.985 \pm 0.013$  for glyoxal (Figure 13c), consistent with a previous bulk measurement of stronger light absorption for methylglyoxal than glyoxal from the reactions with amines in bulk solutions.<sup>51</sup>

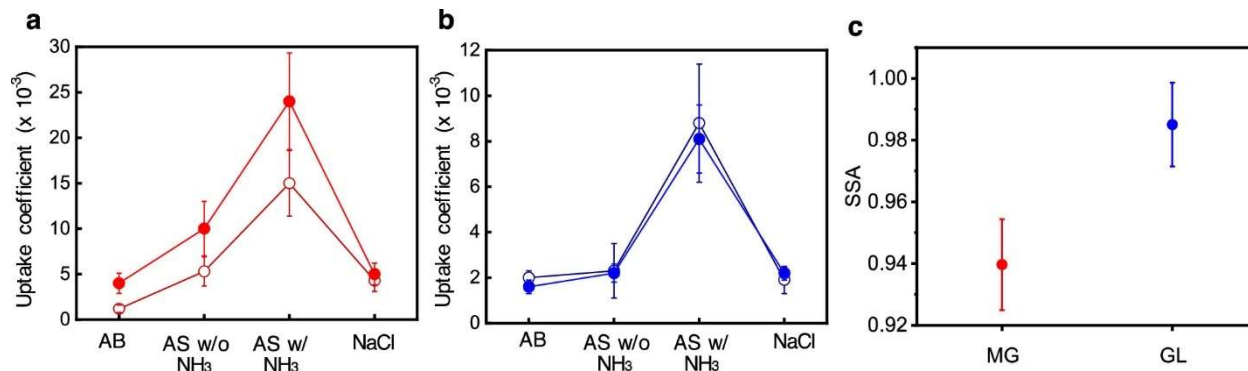


**Figure 13. Distinct reactivity and light absorption between methylglyoxal and glyoxal.** (a) Uptake coefficient for methylglyoxal on different seed particles with 31 ppb CH<sub>2</sub>O (red solid circles) and without CH<sub>2</sub>O (red open circles). (b) Uptake coefficient for glyoxal on different seed particles with 31 ppb CH<sub>2</sub>O (blue solid circles) and without CH<sub>2</sub>O (blue open circles). (c) Measured SSA for AS seed particles exposed to glyoxal and methylglyoxal with 19 ppb NH<sub>3</sub>. The error bar denotes 1 $\sigma$  of 3 repeated measurements.

**Table 3.** Measured uptake coefficient ( $\gamma$ ) for methylglyoxal (MG) and glyoxal (GL) on different seed particles. The uncertainty in the calculated  $\gamma$  reflects the combined random errors in the measured five parameters, i.e.,  $D_o$  = initial diameter,  $D_p$  = final diameter after the exposure time of  $dt$ ,  $N$  = the particle number concentration,  $S$  = particle surface area, and [MG or GL] = concentration for MG or GL. For each parameter, an uncertainty is estimated, corresponding to  $1\sigma$  of at least 3 measurements.

Seed	$D_o$ (nm)	$D_p$ (nm)	$N$ (cm <sup>-3</sup> )	$S$ (10 <sup>-5</sup> cm <sup>2</sup> cm <sup>-3</sup> )	[MG or GL] (10 <sup>10</sup> mole. cm <sup>-3</sup> )	$dt$ (min)	$FR^*$	$\gamma$ (10 <sup>-3</sup> )
<b>MG w/o CH<sub>2</sub>O</b>								
AB	101.5	104.7	40000	4.17	3.7 ± 0.8	19	40.1%	1.2 ± 0.4
AS	121.2	138.1	40000	8.37	3.7 ± 0.8	20	46.4%	5.3 ± 1.6
AS w/NH <sub>3</sub>	116.5	148.0	40000	8.51	3.7 ± 0.8	19	64.2%	15 ± 4
NaCl	119.6	133.8	40000	7.81	3.7 ± 0.8	19	42.1%	4.3 ± 1.2
Sucrose	116.4	161.4	40000	4.79	3.7 ± 0.8	19	34.5%	22 ± 8
<b>MG w/ CH<sub>2</sub>O</b>								
AB	106.2	117.9	40000	5.24	3.7 ± 0.8	19	40.2%	4.0 ± 1.1
AS	112.7	139.5	40000	7.33	3.7 ± 0.8	19	49.3%	10 ± 3
AS w/NH <sub>3</sub>	110.7	157.2	40000	8.39	3.7 ± 0.8	19	69.0%	24 ± 5
NaCl	134.2	156.9	40000	1.23	3.7 ± 0.8	20	38.0%	5.0 ± 1.2
<b>GL w/o CH<sub>2</sub>O</b>								
AB	106.2	116.5	40000	5.16	22 ± 3	19	100%	2.0 ± 0.3
AS	112.5	125.4	40000	6.35	22 ± 3	19	100%	2.3 ± 1.2
AS w/NH <sub>3</sub>	128.7	193.3	40000	14.8	22 ± 3	19	100%	8.8 ± 2.6
NaCl	113.7	124.6	40000	6.43	22 ± 3	19	100%	1.9 ± 0.6
Sucrose	101.2	108.2	40000	2.18	22 ± 3	19	100%	2.8 ± 0.9
<b>GL w/ CH<sub>2</sub>O</b>								
AB	109.2	118.0	40000	5.54	22 ± 3	20	100%	1.6 ± 0.3
AS	112.5	125.2	40000	6.41	22 ± 3	19	100%	2.2 ± 0.4
AS w/NH <sub>3</sub>	123.7	182.4	40000	13.1	22 ± 3	20	100%	8.1 ± 1.5
NaCl	113.2	125.0	40000	6.30	22 ± 3	20	100%	2.2 ± 0.3

\* The fraction ( $FR$ ) of the measured TD-ID-CIMS intensity contributed by MG/GL oligomers and n-heterocycles.

With the measured uptake coefficient, we can derive the dependence of uptake coefficient on NH<sub>3</sub> and CH<sub>2</sub>O concentrations. Considering the presence of gaseous NH<sub>3</sub> and CH<sub>2</sub>O both provide new reaction pathways for methylglyoxal and glyoxal in the aqueous phase, the increase in reactive uptake coefficients in the presence of NH<sub>3</sub> and CH<sub>2</sub>O are expressed as,

$$\gamma - \gamma_0 = A_1[\text{NH}_3]^m + A_2[\text{NH}_3]^m[\text{CH}_2\text{O}]^n \quad (13)$$

where  $\gamma$  and  $\gamma_0$  are uptake coefficients in the presence and absence of NH<sub>3</sub> and CH<sub>2</sub>O, respectively.  $A_1$  and  $A_2$  are two constants.  $m$  and  $n$  are the orders of reactions for NH<sub>3</sub> and CH<sub>2</sub>O, respectively. For methylglyoxal,  $m = 0.36$ ,  $n = 0.25$ , for glyoxal,  $m = 1.4$ ,  $n = 0.48$  (Figure 11). The uptake coefficients of methylglyoxal with various NH<sub>3</sub> and CH<sub>2</sub>O concentrations is calculated by,

$$\gamma \times 10^3 = 5.3 + 9.4 \times \left( \frac{[\text{NH}_3]}{18.5 \text{ ppb}} \right)^{0.36} + [4.8 + 5.0 \times \left( \frac{[\text{NH}_3]}{18.5 \text{ ppb}} \right)^{0.36} \left( \frac{[\text{CH}_2\text{O}]}{31 \text{ ppb}} \right)^{0.25}] \quad (14)$$

The uptake coefficients of glyoxal with various NH<sub>3</sub> and CH<sub>2</sub>O concentrations is calculated by,

$$\gamma \times 10^3 = 2.3 + 6.5 \times \left( \frac{[\text{NH}_3]}{18.5 \text{ ppb}} \right)^{1.4} - [0.1 + 0.6 \times \left( \frac{[\text{NH}_3]}{18.5 \text{ ppb}} \right)^{1.4} \left( \frac{[\text{CH}_2\text{O}]}{31 \text{ ppb}} \right)^{0.48}] \quad (15)$$

Note that 1 ppb can be converted to 41 nmol m<sup>-3</sup> or 2.4 × 10<sup>10</sup> molecules cm<sup>-3</sup> in both equations.

### *Carbenium Ion-Mediated Nucleophilic Addition*

The particle growth from glyoxal and methylglyoxal is regulated by complex aerosol processes (Figure 14), including interfacial interaction as well as liquid-phase diffusion and reaction.<sup>67</sup> We performed molecular dynamics simulations to evaluate the interfacial interaction of

methylglyoxal. A significant decrease in the free energy ( $\sim 4 \text{ kcal mol}^{-1}$ ) occurs when methylglyoxal approaches the air–water interface, indicating a thermodynamically favorable process (Figure 14a). Analysis of the orientation of methylglyoxal reveals that the interfacial interaction is initiated by the carbonyl O-atom, which possesses a prominent negatively charged Natural Bond Orbital (NBO) characteristic ( $-0.57e$ ). Previous experimental studies demonstrated that net charge separation arises from ion distributions at the air–water interface on bulk solutions: the electric field is strongly positive for AS, negligible for ABS, and slightly negative for NaCl.<sup>52</sup> Net charge separation to form the interfacial electric field is likely increased on sub-micrometer aerosols because of high-ionic strength.<sup>68</sup> The interfacial electric attraction on AS is more pronounced for methylglyoxal and  $\text{CH}_2\text{O}$  because of their larger dipole moments ( $1.06 D$  for methylglyoxal and  $3.23 D$  for  $\text{CH}_2\text{O}$ ) and more negative natural charges on the carbonyl O-atom ( $-0.57e$  for methylglyoxal and  $-0.62e$  for  $\text{CH}_2\text{O}$ ) (Figures 4f and 14). On the other hand, interfacial attraction on AS is weaker for glyoxal because of the absence of the dipole moment and smaller negatively charge carbonyl O-atom ( $-0.53e$ ) (Figures 9e and 14). Hence, the ion-induced dipole interaction occurs in a short range for glyoxal but in a long range for methylglyoxal. A recent theoretical study showed a smaller decrease in the free energy ( $\sim 3 \text{ kcal mol}^{-1}$ ) for glyoxal than for methylglyoxal ( $\sim 4 \text{ kcal mol}^{-1}$  in Figure 13a), when approaching the air–water interface.<sup>69</sup>

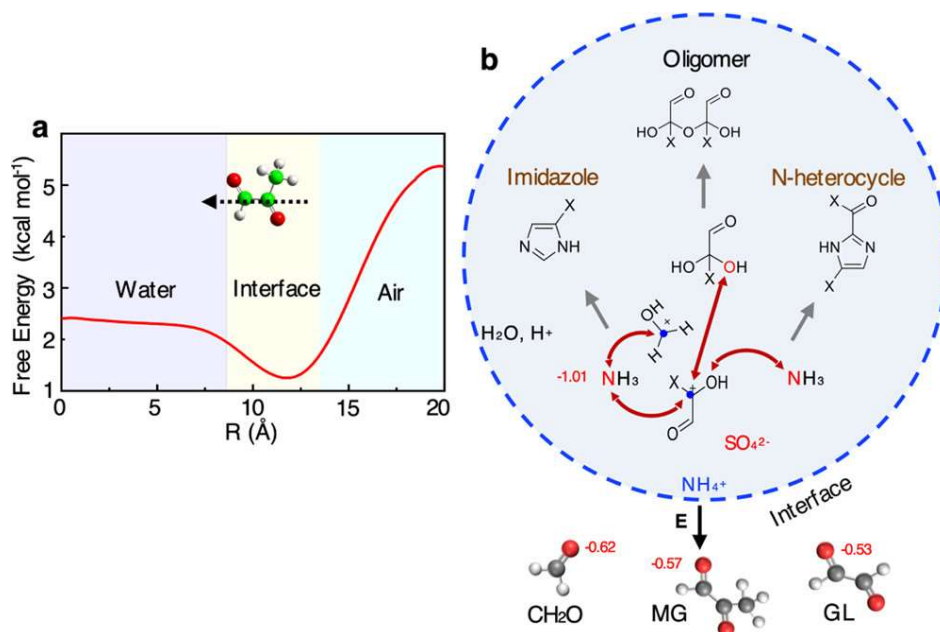


**Figure 14. Carbenium ion-mediated, interfacial electric field-enhanced, and synergetic SOA and BrC formation.** (a) Molecular dynamics simulation of the free energy surface when methylglyoxal approaches the air–water interface. The dashed arrow marks the orientation of methylglyoxal at the interface. (b) Interfacial and cationic enhancement of aerosol formation from carbonyl and hydroxyl organics on AS particles. The numbers denote negative (red) or positive (blue) partial charges in  $e$  for interfacial electronic attraction or nucleophilic addition. The black arrow with the letter E marks a positive electric field (pointing away from the interface) induced from net charge separation of  $\text{NH}_4^+$  and  $\text{SO}_4^{2-}$  distributions at the air–water interface.<sup>(38)</sup> The black-dashed arrows connect the sites for nucleophilic addition. In the molecular structures, X = H or  $\text{CH}_3$  corresponds to glyoxal- or methylglyoxal-derived products, respectively, and the blue dots represent the positively charged carbon atoms of the carbenium ions.

An acid-catalyzed mechanism was speculated for multiphase reactions of organic carbonyls (including glyoxal).<sup>38</sup> Measurements of methylglyoxal and glyoxal on bulk sulfuric acid solutions and of glyoxal on sulfuric acid nanoparticles indicated reduced uptake with acidity,<sup>47,48</sup> invoking hydration-based oligomerization. However, hydration for glyoxal and methylglyoxal to form diols/tetrols is kinetically unfeasible (with an activation energy of 44 kcal mol<sup>-1</sup> for methylglyoxal), and oligomerization is mediated by carbenium ions,<sup>70</sup> which are formed from protonation, hydration, and deprotonation of dicarbonyls (Figures 4e and 9e). Formation of oligomers and *n*-heterocycles includes nucleophilic addition to the carbenium cation by the

negative hydroxyl O-atom ( $-0.77$  to  $-0.80e$ ) of diols/tetrols or the negative N-atom ( $-1.01e$ ) of  $\text{NH}_3$ , respectively (Figures 4e, 8, and 9e). Each step of the cationic oligomerization proceeds without an activation barrier and is enhanced by ion–dipole interaction. Carbenium ions are broadly produced from carbonyls,<sup>70,71</sup> as is also reflected from the large particle growth and formation of imidazole products in the presence of  $\text{CH}_2\text{O}$  (Figure 10c,d). Compared to glyoxal and methylglyoxal, the O-atom in  $\text{CH}_2\text{O}$  has the strongest negative charge, while the C-atom on the  $^+\text{CH}_2\text{OH}$  carbenium ion has the weakest positive charge ( $0.50e$ ), indicating facile protonation but inefficient nucleophilic addition (Figure 14b). The positive natural charges ( $0.55e$  and  $0.59e$ ) on the C-atoms of the glyoxal carbenium ions are slightly larger than that of the formaldehyde carbenium ion ( $0.50e$ ) but are smaller than those of the methylglyoxal carbenium ions ( $0.69e$  and  $0.74e$ ) with the methyl substitution (Figures 4e and 9e). In the presence of  $\text{CH}_2\text{O}$ , there exists a competition between the formaldehyde carbenium ion ( $^+\text{CH}_2\text{OH}$ ) and glyoxal carbenium ions in the reactions with diols, tetrols, or  $\text{NH}_3$ ; the former yields smaller, more volatile oligomers, leading to inhibited particle growth (Figures 13b and 12). In contrast, methylglyoxal carbenium ions react efficiently with  $\text{NH}_3$  to form imines, which subsequently react with the  $\text{CH}_2\text{O}$  carbenium ions to form nonvolatile imidazole products, explaining the higher growth factors and larger uptake coefficients for methylglyoxal in the presence of  $\text{CH}_2\text{O}$  (Figures 10c,d and 13a). To further evaluate the generality of the cationic mechanism, we performed additional experiments using seed particles consisting of sucrose as a surrogate for hydroxycarbonyls (Figure 15). Significant size growth occurs upon exposure of sucrose particles to TMB-OH oxidation, with comparable GF to that measured on AS with  $\text{NH}_3$ . Composition analysis reveals the dominant presence of dimers and sucrose. Sucrose seed particles are neutral and do not involve interfacial charge separation, but the presence of the hydroxy functional groups in sucrose provides the abundant

sites for nucleophilic addition to the carbenium ions for oligomerization. Chemical speciation of the particle-phase composition shows much stronger dimer peaks ( $m/z = 145, 163, 199$ ) and sucrose peak ( $m/z = 325$ ) than that on AS particles, indicating the dominant formation of sucrose-methylglyoxal or sucrose-dimer adducts. In our TD-ID-CIMS measurements, the oligomeric adducts likely decompose to yield dimer and sucrose molecules.

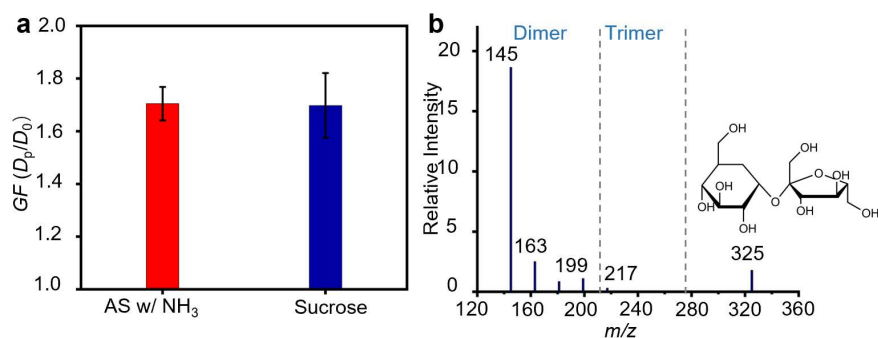


**Figure 15. Oligomerization from multi-functional hydroxycarbonyl.** (a) Seed particles consisting of sucrose were exposed to the oxidation products of TMB by OH, showing comparable  $GF$  to that of AS in the presence of  $\text{NH}_3$ . (b) Relative intensities of dimers at  $m/z = 145, 163, 181,$  and  $199$ , one trimer at  $m/z = 217$ , and sucrose at  $m/z = 325$ . Note that the sucrose and dimer peaks are mainly from the decomposition of sucrose-dimer adducts during the TD-ID-CIMS measurement.

The carbenium ion-mediated oligomerization is distinct from those previously proposed involving an acid catalyst or hydration.<sup>70</sup> Although protonation is favored under acidic conditions, high acidity inhibits hydration and deprotonation to form diols/tetrols and to propagate oligomerization, explaining the highest particle growth under moderate acidic condition (i.e., on AS w/  $\text{NH}_3$ ). The oligomerization pathway occurs in a wide range of acidity and RH, as evident from significant GF and detection of the oligomeric products on all seed particles (i.e., pH from 7 for NaCl and sucrose to  $-0.5$  for ABS). On the other hand, aqueous reactions to yield oligomers



and *n*-heterocycles are likely suppressed at low RH (i.e., below the efflorescent point), because of hindered protonation, hydration, and deprotonation. The multiphase reactions of methylglyoxal and glyoxal increase the particle size by a factor of up to 3 (or the mass by a factor of up to 30) on AS, depending on the abundance of organics or NH<sub>3</sub>. Our observed dependencies of GF and particle-phase product distributions on different seed particles (Figures 4 and 9) are explained by the combined effects of interfacial attraction and liquid-phase reactions. The largest GF and highest formation of nonvolatile products on AS particles are attributed to the strongest interfacial attraction and the most efficient nucleophilic addition involving the carbenium ions. Also, the mechanism established in our work is distinct from previous results of salting-in and salting-out for glyoxal and methylglyoxal, respectively.<sup>72</sup> Instead of varying the solubility of glyoxal and methylglyoxal, ammonium sulfate enhances the SOA formation by providing strongest interfacial electric attraction, the weakly acidic aqueous phase, and involving in aqueous reaction to form *n*-heterocycles. Our measurements of particle chemical compositions show the dominant formation of oligomers and *n*-heterocycles from methylglyoxal and glyoxal, but an absence of other ingredients associated with salting-in and salting-out.

#### *Surface- vs Volume-Limited Oligomerization*

A major distinction in direct exposure of AS seed particles between methylglyoxal and glyoxal vapors lies in significantly different particle growth in our present experiments as well as in previous studies, i.e., a negligibly small growth for methylglyoxal but a large growth for glyoxal.<sup>46,47,50</sup> This disparity is attributed to surface- versus volume-limited reactions on sub-micrometer particles between the two species. Interfacial attraction, protonation, and nucleophilic addition occur more efficiently for methylglyoxal than glyoxal on AS particles (Figure 13). The

negative polarity of the carbonyl O-atom is crucial to providing the protonation site. The methyl substituent increases the carbonyl bond polarization through the inductive electron donating and hyperconjugation effects,<sup>70</sup> as reflected by the more negatively charged O-atom in methylglyoxal than glyoxal (Figures 4e and 13b). In addition, the positive charge on the carbenium ion in methylglyoxal is stronger with methyl substitution, favoring more efficient nucleophilic addition. For glyoxal and methylglyoxal, there is a significant decrease (by a factor of 2–3) in the liquid-phase diffusion coefficients from monomers to trimers (Table 4). The small growth of sub-micrometer particles exposed directly to methylglyoxal vapor (Figures 4a and 5) is explained by surface-limited aqueous reactions (Figure 16a). Efficient formation of oligomers and *n*-heterocycles under elevated methylglyoxal results in rapid oligomerization on the surface and subsequently reduced liquid-phase diffusion. The formation of surface coating is evident from the temporal evolution in the particle growth, i.e., an initial and small GF of 1.03–1.04 (corresponding to a coating thickness of 1.5–2.0 nm), when AS particles are directly exposed to methylglyoxal of 100 ppb to 5 ppm (Figures 4a and 5). The surface coating consisting of nonvolatile products is hydrophobic<sup>73v</sup> and viscous, prohibiting subsequent particle growth and leading to surface-limited reactions. Similarly, surface coating by rapid oligomerization likely explains the negligible size growth of seed particles exposed to increased levels of methylglyoxal vapor (i.e., several hundred ppb to ppm levels) in previous studies.<sup>45–47</sup> On the other hand, formation of a hydrophobic coating is avoided with continuous methylglyoxal production from TMB-OH oxidation at a lower concentration (~2 ppb), as reflected by the continuous and significant particle growth (Figures 4 and 5). Our results of continuous and significant particle growth for methylglyoxal produced from TMB-OH oxidation are consistent with previous measurements of irreversible methylglyoxal uptake on bulk solutions<sup>48</sup> and formation of oligomeric products from the TMB-

OH oxidation experiment.<sup>44</sup> Note that the production of methylglyoxal from TMB-OH oxidation closely mimics that in the atmosphere. Although methylglyoxal represents the dominant product with a molar yield of 90% from TMB-OH oxidation,<sup>44</sup> other oxidation products may play a secondary role in the measured particle growth. Our TD-ID-CIMS measurements confirm that oligomers and *n*-heterocycles from methylglyoxal, NH<sub>3</sub>, and CH<sub>2</sub>O account for the dominant particle-phase products, contributing up to 70% of the measured total intensities (Figure 4e and Table 3). In contrast, oligomerization from glyoxal is clearly volume-limited, as evident from the continuous and significant particle growth in our present experiments as well as in previous studies.<sup>47,50</sup> Inefficient interfacial attraction, protonation, and nucleophilic addition for glyoxal results in less-efficient oligomerization, leading to the absence of surface coating over a wide concentration range (i.e., 9 ppb in our present experiment and from several hundred ppb to ppm levels in previous studies<sup>45,47</sup>). Hence, the considerable differences in aerosol growth and light absorption between methylglyoxal and glyoxal are explainable by surface- or volume-limited reactions, which are governed by their reactivity and gaseous concentrations. Efficient (inefficient) oligomerization for methylglyoxal (glyoxal) results in the formation (absence) of surface coating because of rapid (slow) liquid-phase diffusion and volume-limited (surface-limited) reactions, reconciling the discrepancy in measured particle growth in our present experiments and in previous studies (Figure 16b).

**Table 4. Diffusion coefficients for monomer and trimer of glyoxal and methylglyoxal.**

	solvent	$\eta$ (Pa s)	$k_B$ (J K <sup>-1</sup> )	T (K)	a (m)	$D$ (m <sup>2</sup> s <sup>-1</sup> )
glyoxal monomer	water	$8.9 \times 10^{-4}$	$1.38 \times 10^{-23}$	298	$1.60 \times 10^{-10}$	$1.53 \times 10^{-9}$
methylglyoxal monomer	water	$8.9 \times 10^{-4}$	$1.38 \times 10^{-23}$	298	$1.90 \times 10^{-10}$	$1.29 \times 10^{-9}$
glyoxal trimer	water	$8.9 \times 10^{-4}$	$1.38 \times 10^{-23}$	298	$3.89 \times 10^{-10}$	$6.30 \times 10^{-10}$
methylglyoxal trimer	water	$8.9 \times 10^{-4}$	$1.38 \times 10^{-23}$	298	$4.12 \times 10^{-10}$	$5.95 \times 10^{-10}$

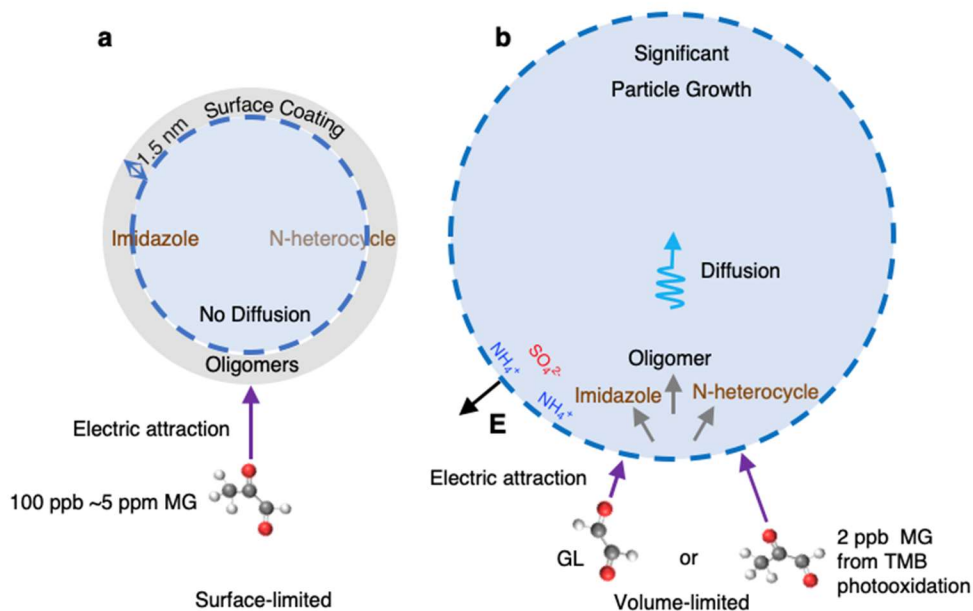


**Figure 16. Surface- and volume-limited uptake of  $\alpha$ -dicarbonyls.** (a) the uptake of methylglyoxal vapor by inhibited by the rapid reaction of methylglyoxal to form surface coating, which results in a surface-limited process. (b) the uptake of glyoxal vapor is a volume-limited process with the free aqueous diffusion of the products.

### Global Perspective for SOA and BrC

Large amounts of oxygenated organics consisting of carbonyl and hydroxyl functional groups are produced from VOC oxidation (Figure 17a), with predicted global budgets of  $223 \pm 34$  Tg a<sup>-1</sup> for methylglyoxal and glyoxal and  $1466 \pm 189$  Tg a<sup>-1</sup> for CH<sub>2</sub>O (Table 5). Also, a major fraction of multifunctional hydroxycarbonyls is produced from biogenic VOC oxidation, e.g.,  $108 \pm 13$  Tg a<sup>-1</sup> for C<sub>4</sub>–C<sub>5</sub> hydroxycarbonyls from isoprene oxidation alone.<sup>54</sup> In comparison, a global budget of  $69 \pm 13$  Tg a<sup>-1</sup> for NH<sub>3</sub> is predicted. Currently, many oxygenated organics are not considered in atmospheric models for SOA and BrC formation because of their high volatility.<sup>37</sup>

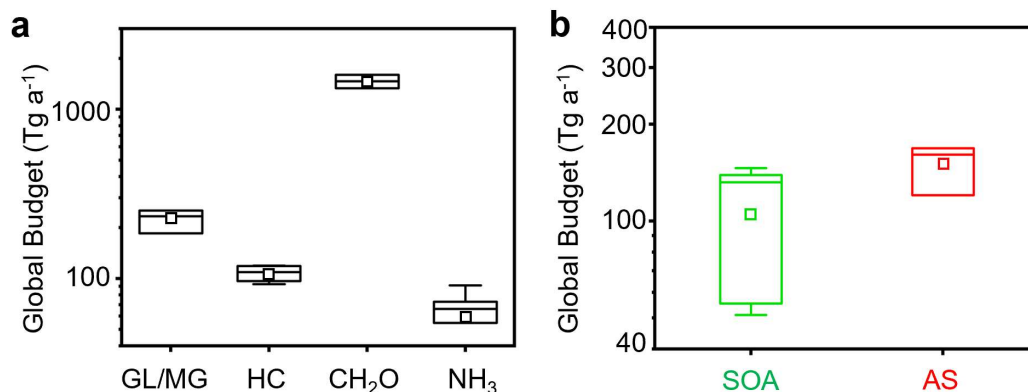


**Figure 17. Unaccounted contributors to global SOA production.** (a) Global budgets of glyoxal/methylglyoxal (GL/MG), hydroxycarbonyls (HC), CH<sub>2</sub>O, and NH<sub>3</sub>. (b) Global SOA (green square) and AS (red square) budgets. See Table S5 for references to the global budget of the various gaseous species.

**Table 5. Global budgets of species involved in cation-mediated, interface-enhanced, and synergistic SOA formation.**

	Global budget (Tg a <sup>-1</sup> )	Average (Tg a <sup>-1</sup> )	STD (Tg a <sup>-1</sup> )	Range (Tg a <sup>-1</sup> )
Methylglyoxal/glyoxal	185 <sup>40</sup> , 233.2 <sup>74</sup> , 252 <sup>a,75</sup>	223	34	185 ~ 252
hydroxycarbonyl	118 <sup>b,76</sup> , 93 <sup>b,77</sup> , 101 <sup>b,78</sup> , 119 <sup>b,79</sup>	108	13	93 ~ 119
CH <sub>2</sub> O	1332 <sup>80</sup> , 1600 <sup>81</sup>	1466	189	1332 ~ 1600
NH <sub>3</sub>	67 <sup>82</sup> , 66 <sup>c,83</sup> , 55 <sup>c,84</sup> , 91 <sup>c,85</sup> , 66 <sup>c,86</sup>	69	13	55 ~ 91
SOA	132 <sup>37</sup> , 91 <sup>74</sup> , 146 <sup>87</sup> , 51 <sup>88</sup> , 139 <sup>89</sup>	112	40	51 ~ 146
AS	120 <sup>d,82</sup> , 161 <sup>d,90</sup> , 168 <sup>d,91</sup>	150	26	120 ~ 168

- a. Estimated from the global budget of GL by assuming a MG/GL ratio of 3.5.
- b. Estimated from the global emission rates of isoprene and a yield of 22.6% for HC.<sup>54</sup>
- c. Converted from the value in TgN a<sup>-1</sup> by multiplying 1.21.
- d. Estimated from global budgets of sulfate aerosols by multiplying the molecular mass ratio of ammonium sulfate/sulfate (1.375).

Our results demonstrate unequivocally that carbonyls (glyoxal/methylglyoxal, CH<sub>2</sub>O, hydroxycarbonyls) contribute significantly to SOA growth on sub-micrometer particles under atmospherically relevant conditions. The mechanism established in the present work explains the ubiquitous coexistence between SOA and AS from global measurements<sup>36</sup> as well as during severe haze formation.<sup>17,29</sup> For example, field measurements showed that the mass fractions of SOA and AS at urban locations worldwide are (29.5 ± 11.7) and (35.0 ± 11.7)% (Figure 18a and Table 6), respectively, representing the two most abundant ingredients in secondary aerosols.<sup>36</sup> Also, severe haze formation in China is consistently characterized by concurrent increases in the mass concentrations of SOA and AS (Figure 18b,c). In particular, explosive secondary aerosol growth

was observed under polluted urban conditions, which is dominated by SOA formation.<sup>92</sup> These field measurements are consistent with synergetic aerosol formation from interacting carbonyls and NH<sub>3</sub>/AS. Specifically, hygroscopic AS aerosols promote SOA formation by inducing interfacial attraction<sup>52</sup> and protonation for carbonyls and nucleophilic addition to form nonvolatile oligomers and *n*-heterocycles.<sup>70</sup> Also, the multiphase chemistry represents an important pathway for sulfate formation from anthropogenic sulfur dioxide (SO<sub>2</sub>) emissions, and an increasing organic content enhances aqueous sulfate production. Furthermore, the synergetic aerosol formation involving carbonyls and NH<sub>3</sub>/AS implies a larger-than-recognized biogenic–anthropogenic interaction,<sup>93</sup> which is critical to assessing anthropogenic influences on varying atmospheric compositions and radiative forcing. Our experimental results show a 30-fold increase in the SOA mass growth on AS particles, implying that changes in anthropogenic (NH<sub>3</sub> and SO<sub>2</sub>) emissions inevitably amplify the global SOA budget, which is dominated by biogenic sources. Currently, the total global SOA and AS budgets are estimated to be 112 ± 40 and 150 ± 26 Tg a<sup>-1</sup>, respectively (Figure 17b and Table 5). Our measured uptake coefficients for glyoxal and methylglyoxal, which account for the carbenium ion-mediated nucleophilic addition, interfacial electric field attraction, and organic–inorganic interaction, are applicable to atmospheric models. Future studies are necessary to reassess secondary aerosol formation from the interaction between natural (BVOC) and anthropogenic (NH<sub>3</sub> and SO<sub>2</sub>) emissions, by implementing the fundamental chemical mechanisms in global chemical transport models.<sup>5,40</sup>

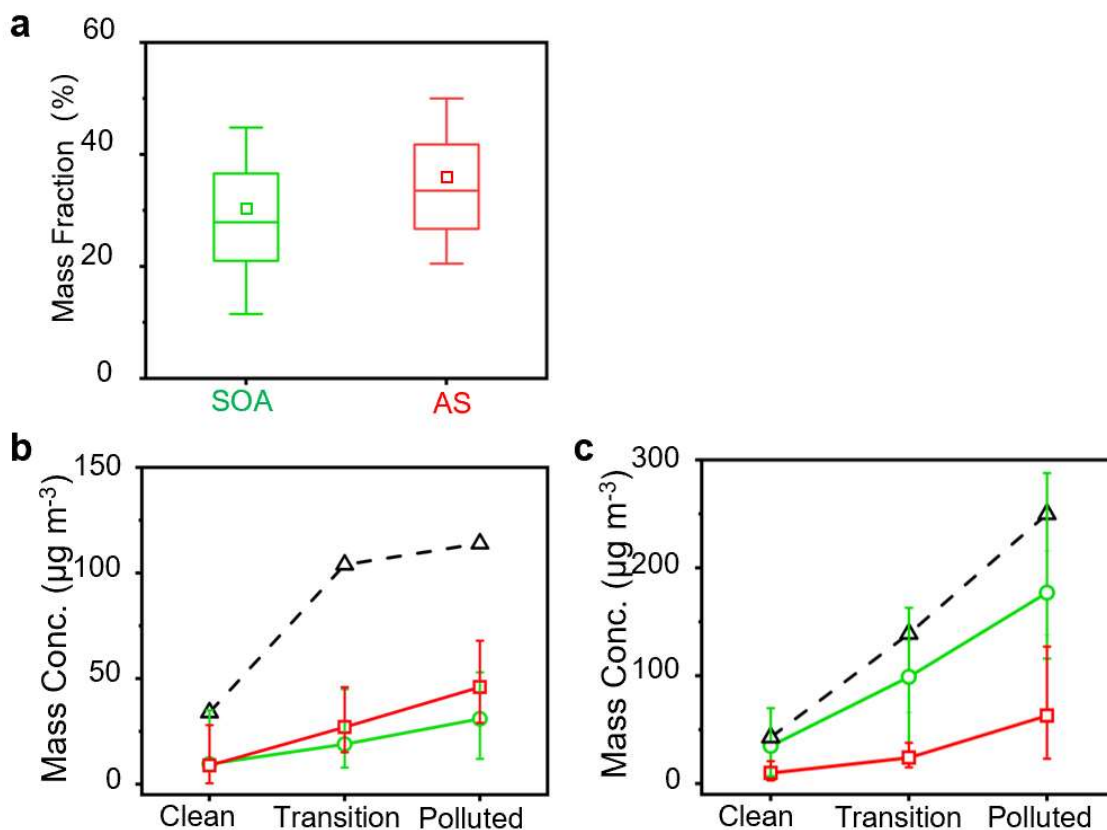


**Figure 18. Mutually promoted inorganic and organic aerosol formation.** (a) Coexistence between SOA and AS from global aerosol measurements.<sup>36</sup> (b) Measured concurrent increases in mass concentrations for PM<sub>2.5</sub> (black), SOA (green), and AS (red) during severe haze formation in Beijing.<sup>29</sup> (c) Measurements of PM<sub>2.5</sub> (black), organic matter (green), and SA (red) during a 2012 winter haze event in Xi'an, China.<sup>68</sup>



**Table 6. Measured mass fractions of SOA and AS in major urban cities.<sup>36</sup>**

		SOA (%)	AS (%)
Beijing		20.8	41.8
Tokyo	Summer	35.6	38.6
Tokyo	Winter	14.2	27.8
Pittsburgh, PA		21.1	63.9
Mexico City		30.2	20.9
Riverside, CA		36.6	29.8
Houston, TX		21.1	50.0
Boulder, CO		56.8	20.5
New York City	Summer	39.3	45.9
New York City	Winter	22.4	35.3
Vancouver		35.7	22.9
Edinburgh		40.0	26.7
Manchester	Summer	21.0	39.9
Manchester	Winter	11.5	26.9
Mainz		25.6	39.5
Zurich	Summer	44.8	22.9
Zurich	Winter	20.0	31.8
Chelmsford		34.0	45.3
Average (%)		29.5	35.0
STD (%)		11.7	11.7
Range (%)		11.5 ~ 56.8	20.5 ~ 63.9

### **Atmospheric Implications**

Our work provides direct experimental evidence for carbenium ion-mediated, interface electric field-enhanced, and synergetic oligomerization involving ubiquitous glyoxal, methylglyoxal,  $\text{CH}_2\text{O}$ , hydroxycarbonyls,  $\text{NH}_3$ , and ammonium sulfate. We show that methylglyoxal is more reactive than glyoxal because of (i) significantly more efficient growth and

larger uptake coefficient on seed particles under atmospherically relevant concentrations, (ii) lower SSA on AS seed particles, (iii) higher formation of imidazole in the presence of  $\text{CH}_2\text{O}$ , and (iv) more rapid formation of surface coating for methylglyoxal than glyoxal. The largest size growth on AS seed particles with  $\text{NH}_3$  corroborates the mechanisms of interfacial electric field-enhanced(38) and carbenium ion-mediated(39) oligomerization. Our findings resolve an outstanding discrepancy concerning the multiphase chemistry of glyoxal and methylglyoxal in previous experimental studies, which are attributable to surface- versus volume-limited reactions. The multiphase chemistry leading to SOA and BrC formation is dependent on the reactivity and gaseous concentrations of the aerosol precursors as well as the physicochemical properties of seed particles (i.e., size, pH, phase state, chemical composition, etc.), highlighting the necessity to closely mimic the atmospheric conditions in future laboratory studies to investigate aerosol chemistry.<sup>94,95</sup>

Aerosol formation involving atmospherically abundant carbonyls (i.e., glyoxal, methylglyoxal,  $\text{CH}_2\text{O}$ , hydroxycarbonyls) and ammonia/ammonium sulfate established here occurs widely on aqueous aerosols and cloud/fog droplets under typically tropospheric conditions, providing an explanation for ubiquitous coexistence between SOA and AS from global aerosol measurements and during severe haze formation in Asia. Recognition of this aerosol formation mechanism from natural and anthropogenic emissions also implies larger-than-expected biogenic–anthropogenic interaction and a major missing source for SOA and BrC formation on urban, regional, and global scales.

CHAPTER III  
MULTI-GENERATION PRODUCTION OF SECONDARY ORGANIC AEROSOL FROM  
TOLUENE PHOTOOXIDATION\*

**Introduction**

SOA produced from photochemical oxidation of anthropogenic and biogenic VOCs represents a dominant constituent of tropospheric fine aerosols,<sup>1,4</sup> with profound implications for air quality, human health, weather, and climate.<sup>10,11,96–100</sup> Photochemical oxidation of VOCs yields various condensable oxidized organics with distinct functionality, volatility, and reactivity. Current available mechanisms of VOC oxidation leading to SOA formation include condensation of low- or non-volatile products, equilibrium gas-particle partitioning of intermediate-volatile products, and aerosol-phase reactions of volatile products to form non-volatile compounds.<sup>23,101</sup> Understanding the chemical mechanisms leading to SOA formation represents a significant challenge in atmospheric chemistry research. Atmospheric models consistently underestimate SOA mass concentrations measured in field studies.<sup>27,37,92</sup> Moreover, light-absorbing BrC represents one type of organic aerosol that scatters and absorbs solar radiation and is produced from various primary and secondary sources. Secondary BrC is formed by a variety of atmospheric chemical processes, including multiphase reactions and cloud processing.<sup>51,102,103</sup>

Aromatic hydrocarbons account for about 20 to 30% of VOCs under urban environments and are emitted primarily from anthropogenic sources, i.e., from motor vehicles and industrial activities.<sup>29,104,105</sup> Toluene is the most abundant aromatic hydrocarbon in the urban atmosphere, for

---

\* This chapter is reprinted with permission from Li, Y.; Zhao, J.; Wang, Y.; Seinfeld, J. H.; Zhang, R. Multi-generation production of secondary organic aerosol from toluene photooxidation. *Environ. Sci. Technol.* **2021**, *55*, doi/10.1021/acs.est.1c02026. Copyright 2021 American Chemical Society.

which its photochemical oxidation is mainly initiated by the hydroxyl radical (OH) via multiple reaction stages/pathways.<sup>106–108</sup> An experimental-theoretical study showed that the most favorable pathway for toluene oxidation corresponds to OH addition to the aromatic ring to yield the OH-toluene adduct, which subsequently react via H-extraction by O<sub>2</sub> to form cresol, rather than with O<sub>2</sub> addition to form the primary peroxy radicals (RO<sub>2</sub>).<sup>109</sup> Typically, SOA formation from toluene photooxidation is believed to be dominated by condensation/partitioning of the oxidation products,<sup>1</sup> including organic acids and low-volatility polyhydroxy organics (LVO) such as polyhydroxy methyl benzoquinones and polyhydroxy toluenes.<sup>110</sup> Also, multistage autoxidation of RO<sub>2</sub> from aromatics likely yields highly-oxidized organic molecules (HOMs) with low volatility and a high ratio of oxygen to carbon atoms (O/C), and previous studies detected HOMs in the gas-phase.<sup>111–113</sup> However, the reported yield for HOMs from toluene oxidation is small (about 0.1%),<sup>111</sup> and HOMs have yet to be detected in the aerosol-phase to confirm their contribution to SOA formation. Note that LVOs differ from HOMs in terms of the oxidation pathways (i.e., OH addition versus RO<sub>2</sub> autoxidation) and O/C, while both possess low volatility. In addition, toluene-derived SOA formation involves aqueous chemistry relevant to cloud processing and aqueous aerosols.<sup>114</sup> A recent experimental study found that NH<sub>3</sub> enhances the SOA mass loading from toluene photooxidation in the presence of nitrogen oxides (NO<sub>x</sub> = NO + NO<sub>2</sub>) especially under wet conditions, attributable to formation of carboxylates and organic nitrates.<sup>115</sup> Another recent smog chamber study on toluene photooxidation observed an increasing SOA yield with increasing NO<sub>x</sub> under low-NO<sub>x</sub> conditions but a suppressed SOA yield under high-NO<sub>x</sub> conditions.<sup>116</sup> Also, the latter study showed an increase in the particle number concentration, diameter, and extinction/scattering coefficients relevant to the formation of ammonium nitrate and nitrogen-containing compounds by adding NH<sub>3</sub>.<sup>116</sup> Several studies revealed that small  $\alpha$ -dicarbonyls (i.e.,

glyoxal and methylglyoxal), which are the major products of toluene oxidation, produce low-volatility oligomers and light-absorbing BrC via aqueous reactions.<sup>50,51</sup> Moreover, a recent theoretical study established a carbenium ion-mediated oligomerization mechanism for methylglyoxal to produce SOA.<sup>70</sup> In addition, increased light absorption was detected when toluene-derived SOA was exposed to gas-phase NH<sub>3</sub>, indicative of BrC formation.<sup>117,118</sup>

However, previous studies have been unable to assess temporally resolved SOA production from multi-generation VOC oxidation. For example, no previous work has measured time-dependent production of condensable oxidized organics and variations in the aerosol properties, and there lacks chemical speciation for the aerosol-phase products from toluene oxidation. The available chemical mechanisms have yet to explain explosive secondary aerosol growth observed under polluted conditions, which is dominated by SOA formation.<sup>92</sup> In this work, we elucidate the fundamental chemical mechanisms leading to SOA formation from toluene oxidation by simultaneously tracking the temporal evolutions in the gaseous products and aerosol properties.

## Experimental

A 1 m<sup>3</sup> environmental chamber (Teflon® PFA) with eighteen black light lamps (18 × 30W, F30T8/350BL, Sylvania) was used in our experiments (Figure 19), similar to our previous studies.<sup>53,119</sup> Briefly, monodispersed seed particles were exposed to the products from OH-toluene oxidation in the reaction chamber. Photooxidation of toluene was initiated by turning on the black light lamps, when OH radicals were produced from photolysis of hydrogen peroxide (H<sub>2</sub>O<sub>2</sub>). The initial concentration for toluene and the steady-state concentration for OH were estimated to be 6.6 ppm and  $2.7 \times 10^6$  molecules cm<sup>-3</sup>, respectively. A water bubbler at a temperature of 30°C was used to humidify the chamber from 10% to 90% RH, and all experiments were performed at 298

K. A  $N_2$  flow of 5 slpm was used to atomize 0.06 M solution of ammonium sulfate -  $(NH_4)_2SO_4$  or AS, ammonium bisulfate -  $NH_4HSO_4$  or ABS, and sodium chloride - NaCl to produce monodispersed seed particles. Seed particles were dried to RH of 2% by a Nafion Gas Dryer, charged by a bipolar charger, and analyzed by an integrated aerosol analytical system. Monodispersed seed particles with an initial size of 100 nm were size-selected by a DMA with an initial particle concentration of  $1.5 \times 10^4 \text{ cm}^{-3}$  measured by a condensation particle counter (CPC). The three different types of seed particles, i.e.,  $(NH_4)_2SO_4$ ,  $NH_4HSO_4$ , and NaCl, were selected to represent distinct particle acidity and interfacial electric fields.<sup>52</sup> The acidity of seed particles was estimated using a thermodynamic model,<sup>120</sup> with the pH value of 3~5 in the presence of gaseous  $NH_3$  and 0~1 in the absence of gaseous  $NH_3$  for  $(NH_4)_2SO_4$ , -0.5 for  $NH_4HSO_4$ , and 7 for NaCl. Also, there likely exists an electric field induced from net charge separation of soluble ions at the air-water interface, which is strongly positive for  $(NH_4)_2SO_4$ , negligible for  $NH_4HSO_4$ , and slightly negative for NaCl.<sup>52</sup> For experiments in the presence of  $NH_3$  or  $NO_x$ ,  $NH_3$  or  $NO_x$  were introduced prior to toluene and the concentration of  $NH_3$  and  $NO_x$  after correction for wall loss is calculated similar to those in Chapter II. The particle size growth, density, light scattering/absorption were simultaneously and continuously monitored, after monodispersed seed particles were exposed to the products of toluene-OH oxidation in the reaction chamber. The particle size increase was quantified by a growth factor,  $GF$ , which is defined by  $D_p/D_0$ , where  $D_p$  is the diameter after exposure and  $D_0 = 100 \text{ nm}$  is the initial diameter measured by DMA. Note both  $D_p$  and  $D_0$  correspond to the dry particle diameter measured after passing through the Nafion dryer (about 2% RH). An Aerosol Particle Mass (APM) Analyzer was used to derive the particle density. The density for the SOA materials ( $\rho_{SOA}$ ) is calculated by,

$$\rho_{SOA} = \frac{\rho GF^3 - \rho_0}{GF^3 - 1} \quad (16)$$

where  $\rho$  and GF are measured particle density ( $\text{g cm}^{-3}$ ) and growth factor at  $t$  (min), respectively.  $\rho_0$  is the density of  $(\text{NH}_4)_2\text{SO}_4$  ( $1.77 \text{ g cm}^{-3}$ ),  $\text{NH}_4\text{HSO}_4$  ( $1.78 \text{ g cm}^{-3}$ ), or  $\text{NaCl}$  ( $2.16 \text{ g cm}^{-3}$ ). The uncertainty in the density measurements was estimated to be  $\pm 0.03 \text{ g cm}^{-3}$ . An ID-CIMS and a TD-ID-CIMS using  $\text{H}_3\text{O}^+$  analyzed and quantified gases and aerosol-phase chemical composition, respectively. An integrating nephelometer and a cavity ring-down spectrometer were employed to measure  $b_{\text{sca}}$  and  $b_{\text{ext}}$  at 532 nm, respectively. The  $b_{\text{abs}}$  was determined from  $(b_{\text{ext}} - b_{\text{sca}})$ , and the SSA was calculated from  $b_{\text{sca}}/b_{\text{ext}}$ . Measurements of gaseous concentrations of the oxidation products and aerosol properties (i.e.,  $GF$ ,  $SSA$ , density, and chemical composition) were made simultaneously throughout the experiments. While the gaseous concentrations of the oxidation products,  $GF$ ,  $SSA$ , and density were temporally resolved in our experiments, the particle chemical composition was analyzed after seed particles were exposed for 20 mins to toluene photooxidation and collected for 2 additional hours by TD-ID-CIMS, reflecting an overall aerosol chemical makeup during an experiment. Similar to  $GF$ ,  $SSA$ , density, and chemical composition were measured under dry conditions, whereas measurements of the oxidation products were made directly by analyzing gases from the chamber by ID-CIMS. To assess the effects of different seed particles, RH, and  $\text{NH}_3$  on SOA and BrC formation, we compared the measured  $GF$  and  $SSA$  values after 90-min exposure to the OH-toluene oxidation.

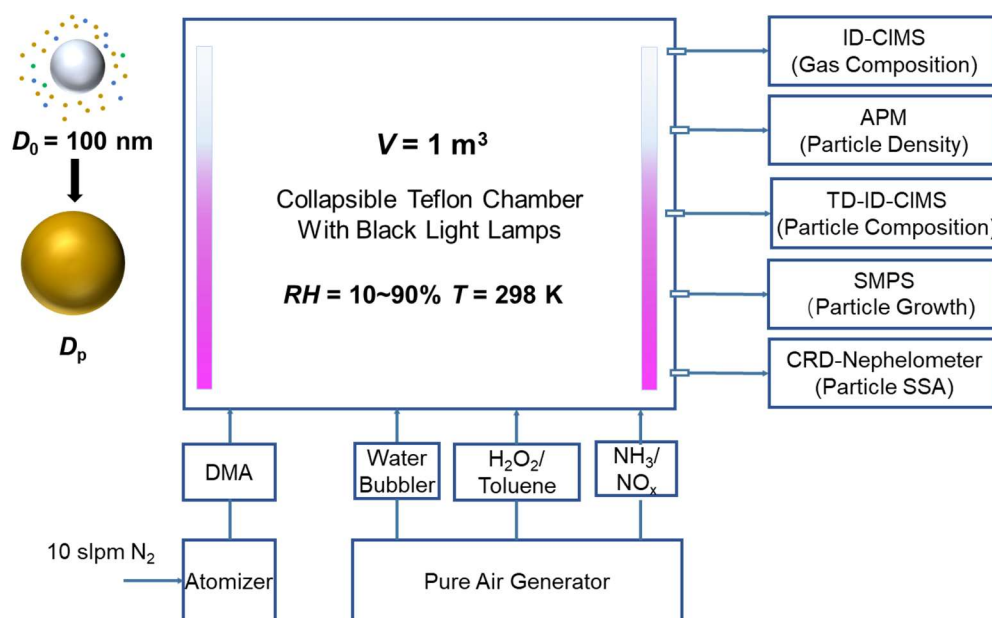


**Figure 19. Schematic representation of the experimental setup.** DMA for differential mobility analyzer; ID-CIMS for ion drift – chemical ionization mass spectrometry; APM for aerosol particle mass analyzer, TD-ID-CIMS for thermal desorption - ion drift – chemical ionization mass spectrometry; SMPS for scanning mobility particle sizer; and CRD for cavity ring-down spectroscopy. Monodispersed seed particles consisting of ammonium bisulfate, ammonium sulfate, and sodium chloride were exposed to oxidation products between toluene by OH and in the absence/presence of NH<sub>3</sub> vapors inside a 1 m<sup>3</sup> reaction chamber. RH was regulated between 10% and 90%, and T was maintained at 298 K. The gaseous concentrations of the oxidation products and particle properties, such as density, chemical composition, growth, and single scattering albedo, were simultaneously quantified by ID-CIMS, APM, TD-ID-CIMS, SMPS, and CRD-Nephelometer, respectively.

### *Vapor Wall Loss*

Wall-loss of reactive gases represents a major challenge in investigating SOA formation from VOC oxidation using environmental chambers.<sup>21,58,121,122</sup> For example, previous studies typically determined the SOA yield in the absence/presence of polydisperse seed particles, which is largely subject to the effect of wall-loss. However, such a deficiency was remedied from synchronized measurements of the gas-phase products and the changes in the aerosol properties (i.e., size, density, and optical properties), when monodisperse seed particles were exposed to



toluene-OH oxidation. While wall-loss results in reduced concentrations of gaseous oxidation products and particles, the variations in the measured particle properties directly reflect gas-to-particle conversion from toluene oxidation, which is linked to the production of condensable oxidized organics, the interfacial process (accommodation), equilibrium partitioning (solubility), and aerosol-phase diffusion and reactions. Specifically, we derived the uptake coefficient ( $\gamma$ ) for condensable oxidized organics from the measured gaseous concentrations and particle size growth similar to that described in Chapter II, which is independent on wall-loss and commonly employed to represent SOA formation in atmospheric models. Also, we quantified wall-loss of reactive gases at different RH from the measured concentrations of the oxidation products by ID-CIMS.

## Results and Discussion

### *Temporally resolved SOA production*

To assess the formation of condensable oxidized organics contributing to SOA formation, we measured the evolution of the gaseous products from toluene-OH photooxidation using ID-CIMS. Formation of multi-generation products, typically delineated by the sequence of reactions with OH, is identifiable from their temporal variations (Figure 20a and Figure 21). The first-generation products (G1) include cresol ( $m/z = 109$ ) and benzaldehyde ( $m/z = 107$ ), which are produced via OH addition (about 90%) to the aromatic ring and H-extraction (10%) from the methyl group, respectively (Figure 21b).<sup>106,107,21,22</sup> The second-generation (G2) products consist of  $\alpha$ -dicarbonyls, i.e., glyoxal ( $m/z = 59$ ) and methylglyoxal ( $m/z = 73$ ),  $\gamma$ -dicarbonyls (butenedial and methylbutenedial at  $m/z = 99$ ), benzoic acid ( $m/z = 123$ ), epoxide, and dihydroxy toluene (Figures 21c and 23), which are produced from the subsequent reactions of the G1 products with OH. The third generation (G3) products contain mainly multi-functional organic acids (Figure 1d),

including pyruvic acid ( $m/z = 89$ ) and 4-oxo-2-pentenoic acid ( $m/z = 115$ ), which are formed from the reactions of the G2 products with OH. The G1 products appear shortly upon the initiation of photooxidation by ultraviolet light, reaching peak mixing ratios of  $\sim 16$  ppb for cresol and  $\sim 5$  ppb for benzaldehyde (Figure 20b). The G2 products rise subsequently after the G1 products, with the peak mixing ratios from 1 to 5 ppb (Figure 20c and Figure 22a). Note that benzoic acid exhibits a much slower growth than those of other G2 products, because of a smaller branching ratio for the H-extraction pathway.<sup>107</sup> The G3 products start to increase at around 20 min and reach peak mixing ratios ranging from sub-ppb to 2 ppb (Figure 20d and Figure 22b). Cresol exhibits the highest mixing ratio among all products, consistent with its dominant yield from toluene oxidation,<sup>109</sup> and the peak concentrations of the oxidation products decrease consecutively from G1, G2, to G3 (Figure 20b-d). The time-dependent concentrations of the earlier generational products (G1 and G2) exhibit a decline at longer reaction times, reflecting the conversion from the earlier to later generational (G2 and G3) products (Fig. 20b,c,d). In contrast, the toluene concentration shows a continuous decay throughout the experiments (Figure 22c).

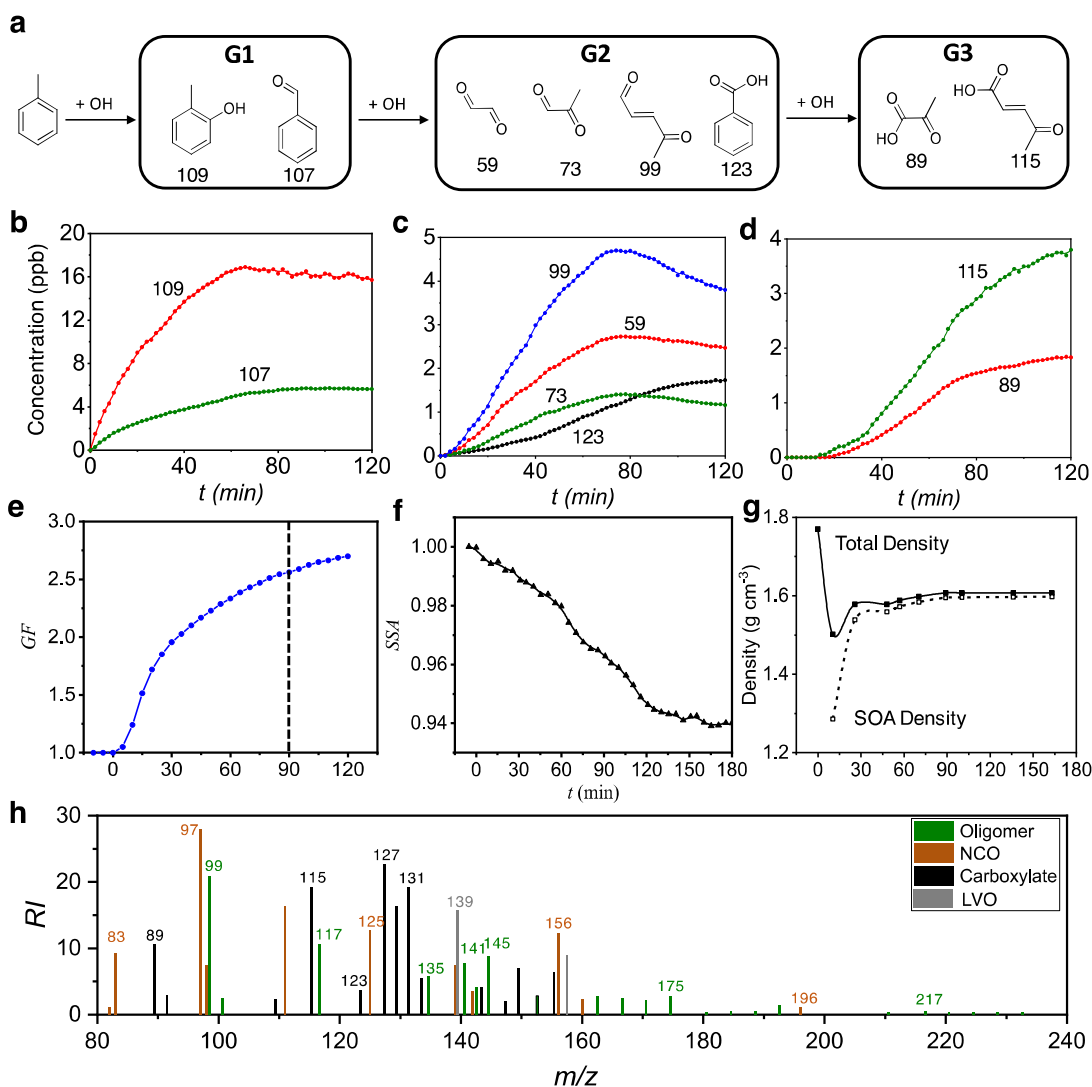


**Figure 20. Temporal evolution of gaseous products and particle properties.** (a) Three-generation (G1, G2, and G3) oxidation products of toluene-OH photooxidation. The numbers denote the mass to charge ratio ( $m/z$ ). (b-d) Time-dependent gas-phase concentrations of G1 (b), G2 (c), and G3 (d) oxidation products. (e-g) Time-dependent growth factor ( $GF = D_p/D_0$ , e), single scattering albedo ( $SSA$ , f), and densities (g, black solid line) of seed particles exposed to toluene oxidation products. The dashed line in (g) displays the calculated density for the SOA materials. (h) Relative intensity ( $RI$ ) of aerosol-phase products detected by TD-ID-CIMS. Initiation of photooxidation by ultraviolet light occurred at  $t = 0$ . All experiments were carried out for  $(NH_4)_2SO_4$  seed particles with 19 ppb  $NH_3$  at 298 K and  $RH = 90\%$ .

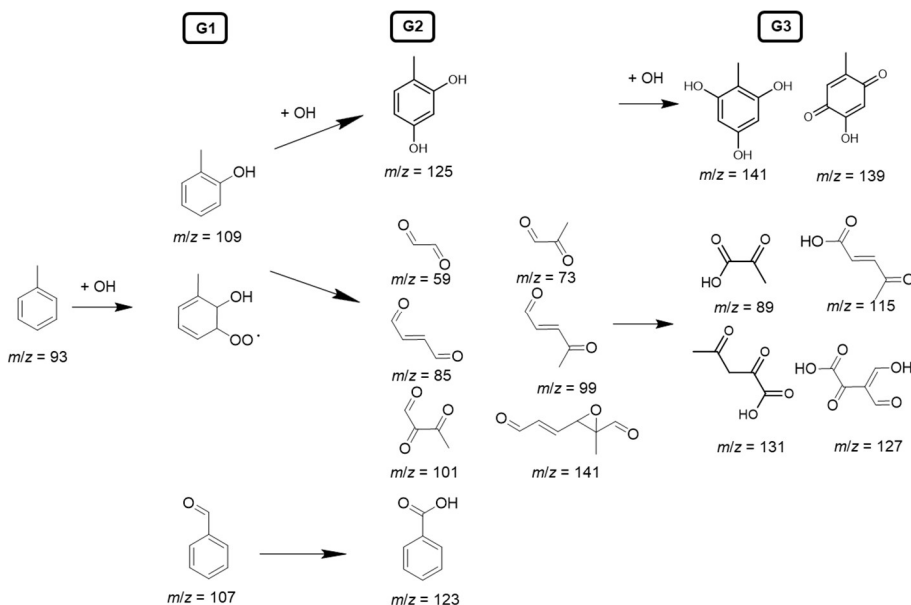


**Figure 21. Multi-generation products from toluene-OH photooxidation.** The letters of G1, G2, and G3 denote the sequence of reactions with OH, and the numbers denote the mass to charge ratio ( $m/z$ ).

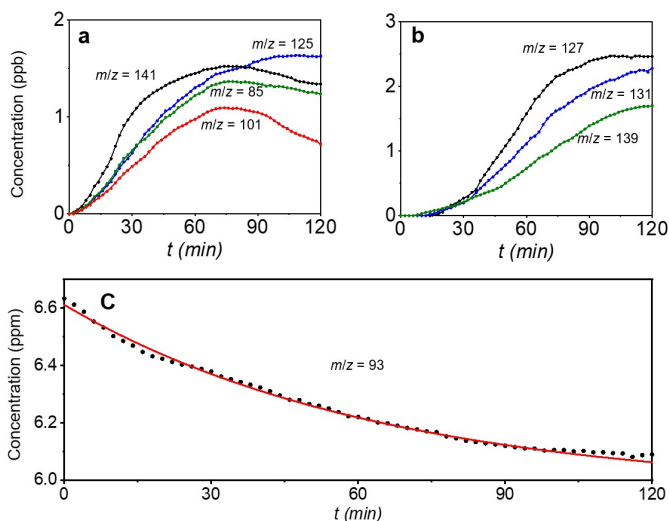


**Figure 22. Temporal evolutions in products and reactants from toluene oxidation.** The gaseous concentrations of G2 products (a), G3 products (b), and toluene (c). The red solid line in (c) corresponds to kinetic simulation of the toluene concentration. The initial concentration for toluene and the steady-state concentration for OH were  $6.6 \text{ ppm}$  and  $2.7 \times 10^6 \text{ molecules cm}^{-3}$ , respectively, with a bimolecular rate constant of  $5.5 \times 10^{-12} \text{ cm}^3 \text{ molecule}^{-1} \text{ s}^{-1}$ . The experiments were carried out on  $(\text{NH}_4)_2\text{SO}_4$  seed particles with  $19 \text{ ppb NH}_3$  and at  $298 \text{ K}$  and  $\text{RH} = 90\%$ . Initiation of photooxidation by ultraviolet light occurred at  $t = 0$ .

The temporal evolution of the  $GF$ ,  $SSA$ , and density of  $(\text{NH}_4)_2\text{SO}_4$  seed particles exposed to toluene-OH oxidation in the presence of 19 ppb  $\text{NH}_3$  and at 90% RH is depicted in Figure 20e-g. The size growth factor,  $GF$ , exhibits an initial delay ( $\sim 5$  min) and then increases monotonically, reaching 2.56 at 90 min (Figure 20e). The initial hysteresis in  $GF$  is consistent with delayed formation of the G2/G3 products (Figure 20c,d), which are mainly responsible for the measured particle growth. While the low-volatility G2/G3 products engage in gas-particle conversion (for epoxide and dihydroxy toluene) or ionic dissociation/acid-base reaction to form carboxylates (for organic acids), the volatile G2 products (i.e.,  $\alpha$ -dicarbonyls and  $\gamma$ -dicarbonyls) undergo aerosol-phase reactions to form oligomers (Figure 23). In addition,  $\alpha$ -dicarbonyls and  $\gamma$ -dicarbonyls react with  $\text{NH}_3$  to yield nitrogen-containing organics (NCO), including nitrogen-heterocycles and nitrogen-heterochains (Figure 24), which are characteristic of light-absorbing BrC.<sup>26,70</sup> The measurement of  $SSA$  shows a steady decline throughout the exposure and reaches 0.94 at 180 min (Figure 20g), confirming BrC production. Our measured  $SSA$  is consistent with another study of toluene-derived SOA, which showed a decrease of  $SSA$  from 0.97 to 0.85 within 2 hours in the presence of  $\text{NH}_3$ .<sup>116</sup> The total density decreases from  $1.77 \text{ g cm}^{-3}$  to  $1.50 \text{ g cm}^{-3}$  within the initial 10 min (with a corresponding  $GF$  of 1.31) and then increases steadily to  $1.61 \text{ g cm}^{-3}$  at 160 min. We derived the density for the SOA component on  $(\text{NH}_4)_2\text{SO}_4$  particles, which increases from  $1.28 \text{ g cm}^{-3}$  at 10 min to  $1.60 \text{ g cm}^{-3}$  at 160 min (Figure 20g). The evolution in density clearly reflects variation in the chemical composition during particle growth, because of the distinct material densities for the condensable oxidized organics from G2/G3 products as well as the aerosol-phase oligomeric products (Table 7). For example, the densities of benzoic acid, monomers of glyoxal and methylglyoxal, and imidazoles are 1.27, 1.05-1.27, and 1.03-1.23  $\text{g cm}^{-3}$ , respectively, while the densities for the oligomers of glyoxal and methylglyoxal reach 1.71-1.90  $\text{g cm}^{-3}$ . The initial

decline in the total density corresponds to a chemical composition dominated by organic acids and smaller oligomers from the G2 products, while the continuous increase in the SOA density is characteristic of increasing aqueous-phase reactions to yield larger oligomeric products (Figure 20g). In addition, the evolutions in the measured *GF* and density correlate closely with those of the G2 products (including benzoic acid and dicarbonyls) (Fig. 20c,e,g), confirming their role in the initial decline of the total particle density.

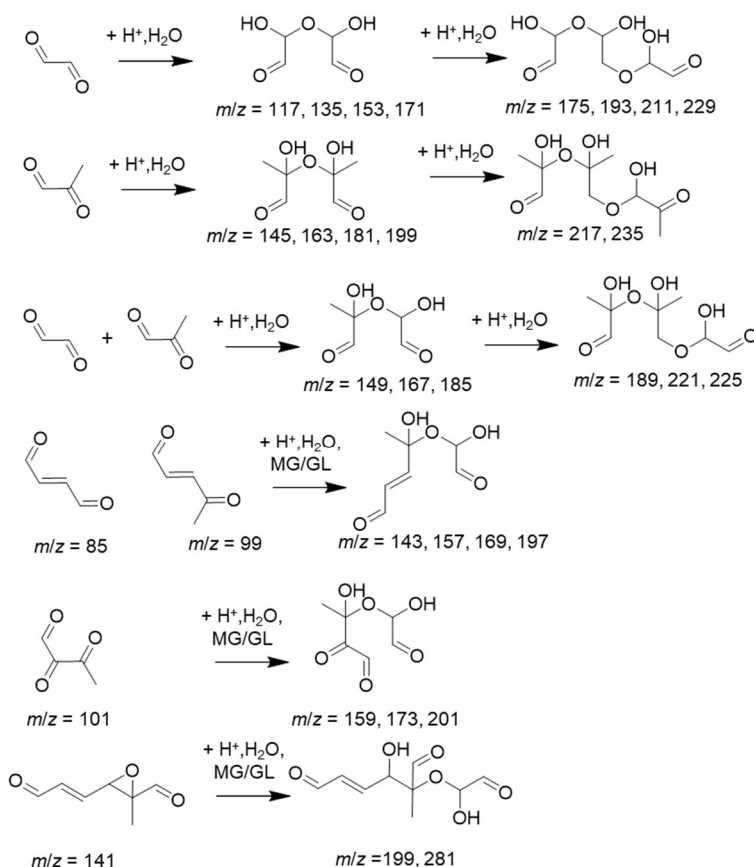


**Figure 23. Pathways for oligomerization.** The mechanisms leading to formation of particle-phase oligomers from  $\alpha$ -dicarbonyls,  $\gamma$ -dicarbonyls, tricarbonyls, and epoxide detected by TD-ID-CIMS.

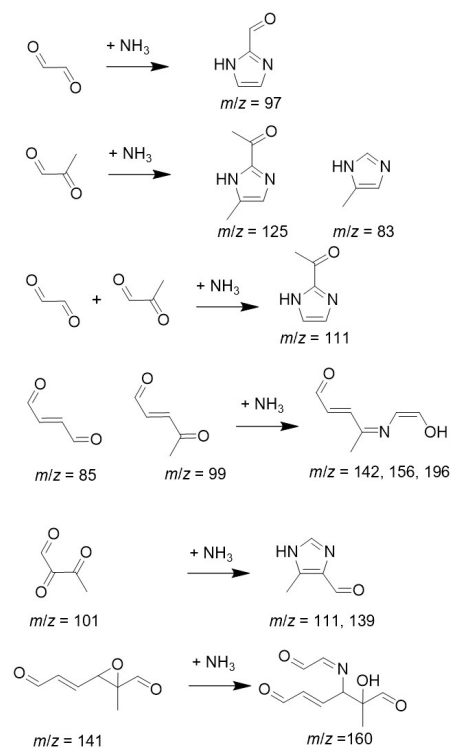


**Figure 24. Pathway for BrC formation.** The mechanisms leading to formation of particle-phase nitrogen-containing organics (NCO) from  $\alpha$ -dicarbonyls,  $\gamma$ -dicarbonyls, tricarbonyls, and epoxide.

**Table 7. Density of identified major SOA components by TD-ID-CIMS.**

Compounds	$m/z$	Density ( $\text{g cm}^{-3}$ )
Methylimidazole	83	1.03
Methylglyoxal	73	1.05
butenedial	85	1.06
4-Oxo-2-pentenoic acid	115	1.2
Imidazole	69	1.23
Pyruvic acid	89	1.25
Benzoic acid	123	1.27
Glyoxal	59	1.27
Dihydroxy toluene	125	1.29
Acetylpyruvic acid	131	1.3
Glyoxylic acid	75	1.38
Trihydroxy toluene	141	1.4
Glyoxal oligomers	175	1.71
2-hydroxy-5-methylquinone	139	1.4
Oxalic acid	91	1.9
Methylglyoxal oligomers	127	1.9

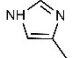
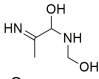
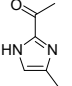
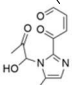
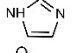
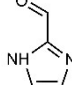
To further unravel the identity of the condensable oxidized organics responsible for the measured *GF*, *SSA*, and density, we analyzed the chemical compositions by collecting particles after exposure to toluene-OH oxidation using TD-ID-CIMS (Figure 20h). The composition measurements reveal the dominant abundances of three functional groups in the aerosol-phase, i.e., oligomers, NCO, and carboxylates, along with a trace amount of LVO (including hydroxyl toluene/benzoquinone). Assuming comparable sensitivity to proton-transfer reactions for the aerosol-phase organics,<sup>123</sup> we estimated the contributions of oligomers, NCO, carboxylates, and LVO to the total SOA formation from the measured mass intensities, with the values of 26%, 26%, 40%, and 8%, respectively (Table 8). The identified mass peaks shown in Figure 1h are summarized in Tables 9 to 11, and the corresponding reaction pathways leading to the formation of oligomers and NCO are illustrated in Figures 23 and 24, respectively.

**Table 8. The percent contributions of condensable organic species from toluene-OH oxidation to the particle-phase mass intensity.** GL: glyoxal, MG: methylglyoxal, GL+MG: cross-reaction of glyoxal and methylglyoxal. Note that the cross-reaction products of  $\gamma$ -carbonyls/tricarbonyls with  $\alpha$ -dicarbonyls are summed into the contribution of  $\gamma$ -carbonyls/tricarbonyls. The experiments were carried on  $(\text{NH}_4)_2\text{SO}_4$  seed particle with 19 ppb of  $\text{NH}_3$  and with the initial concentrations of toluene and OH of 6.6 ppm and  $2.7 \times 10^6$  molecules  $\text{cm}^{-3}$ , respectively.

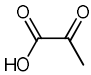
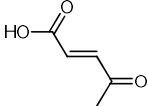
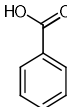
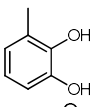
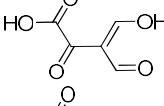
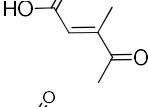
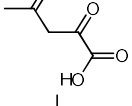
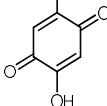
Condensable oxidized organics	Contribution		
	Oligomerization	NCO formation	Total
GL	6%	7%	13%
MG	4%	6%	10%
GL+MG	6%	3%	9%
$\gamma$ -dicarbonyls	5%	5%	10%
tricarbonyls	2%	4%	6%
epoxide	3%	1%	4%
Sum	26%	26%	52%
Carboxylates			40%
LVO			8%



**Table 9. Mass peak assignments for nitrogen-containing organics (NCO) from  $\alpha$ -dicarbonyls n-heterocycles and  $\gamma$ -carbonyls n-chains detected by TD-ID-CIMS.**

m/z	MW	Formula	Compound
Methylglyoxal n-heterocycles			
83	82	C <sub>4</sub> H <sub>6</sub> N <sub>2</sub>	
119	118	C <sub>4</sub> H <sub>10</sub> O <sub>2</sub> N <sub>2</sub>	
125	124	C <sub>6</sub> H <sub>8</sub> ON <sub>2</sub>	
251	250	C <sub>6</sub> H <sub>10</sub> O <sub>5</sub>	
Glyoxal n-heterocycles			
69	68	C <sub>3</sub> H <sub>4</sub> N <sub>2</sub>	
97	96	C <sub>4</sub> H <sub>4</sub> ON <sub>2</sub>	
tricarboxyl n-heterocycles			
111	110	C <sub>5</sub> H <sub>6</sub> ON <sub>2</sub>	
139	138	C <sub>6</sub> H <sub>6</sub> O <sub>2</sub> N <sub>2</sub>	
$\gamma$ -carbonyls n-chains			
142	141	C <sub>6</sub> H <sub>7</sub> O <sub>2</sub> N	
156	155	C <sub>7</sub> H <sub>9</sub> O <sub>2</sub> N	
196	195	C <sub>4</sub> H <sub>6</sub> O <sub>2</sub> N <sub>2</sub>	

**Table 10. Mass peak assignments for organic acids and low-volatile organics (LVO) detected by TD-ID-CIMS.**

m/z	MW	Formula	Compound
89	88	C <sub>3</sub> H <sub>4</sub> O <sub>3</sub>	
115	114	C <sub>5</sub> H <sub>6</sub> O <sub>3</sub>	
123	122	C <sub>7</sub> H <sub>6</sub> O <sub>2</sub>	
125	124	C <sub>7</sub> H <sub>8</sub> O <sub>2</sub>	
127	126	C <sub>5</sub> H <sub>4</sub> O <sub>5</sub>	
129	128	C <sub>6</sub> H <sub>8</sub> O <sub>3</sub>	
131	130	C <sub>5</sub> H <sub>6</sub> O <sub>4</sub>	
139	138	C <sub>7</sub> H <sub>6</sub> O <sub>3</sub>	

**Table 11. Mass peak assignments for oligomeric products detected by TD-ID-CIMS.**

	<i>m/z</i>	Ion	MW	Formula
<b>Methylglyoxal</b>				
Dimers	145	[C <sub>6</sub> H <sub>10</sub> O <sub>5</sub> +H-H <sub>2</sub> O] <sup>+</sup>	162	C <sub>6</sub> H <sub>10</sub> O <sub>5</sub>
	163	[C <sub>6</sub> H <sub>10</sub> O <sub>5</sub> +H] <sup>+</sup>	162	C <sub>6</sub> H <sub>10</sub> O <sub>5</sub>
	163	[C <sub>6</sub> H <sub>12</sub> O <sub>6</sub> +H-H <sub>2</sub> O] <sup>+</sup>	180	C <sub>6</sub> H <sub>12</sub> O <sub>6</sub>
	181	[C <sub>6</sub> H <sub>12</sub> O <sub>6</sub> +H] <sup>+</sup>	180	C <sub>6</sub> H <sub>12</sub> O <sub>6</sub>
	181	[C <sub>6</sub> H <sub>14</sub> O <sub>7</sub> +H-H <sub>2</sub> O] <sup>+</sup>	198	C <sub>6</sub> H <sub>14</sub> O <sub>7</sub>
	199	[C <sub>6</sub> H <sub>14</sub> O <sub>7</sub> +H] <sup>+</sup>	198	C <sub>6</sub> H <sub>14</sub> O <sub>7</sub>
Trimers	217	[C <sub>9</sub> H <sub>12</sub> O <sub>6</sub> +H] <sup>+</sup>	216	C <sub>9</sub> H <sub>12</sub> O <sub>6</sub>
	217	[C <sub>9</sub> H <sub>14</sub> O <sub>7</sub> +H-H <sub>2</sub> O] <sup>+</sup>	234	C <sub>9</sub> H <sub>14</sub> O <sub>7</sub>
	235	[C <sub>9</sub> H <sub>14</sub> O <sub>7</sub> +H] <sup>+</sup>	234	C <sub>9</sub> H <sub>14</sub> O <sub>7</sub>
	235	[C <sub>9</sub> H <sub>16</sub> O <sub>8</sub> +H-H <sub>2</sub> O] <sup>+</sup>	252	C <sub>9</sub> H <sub>16</sub> O <sub>8</sub>
	253	[C <sub>9</sub> H <sub>16</sub> O <sub>8</sub> +H] <sup>+</sup>	252	C <sub>9</sub> H <sub>16</sub> O <sub>8</sub>
	253	[C <sub>9</sub> H <sub>18</sub> O <sub>9</sub> +H-H <sub>2</sub> O] <sup>+</sup>	270	C <sub>9</sub> H <sub>18</sub> O <sub>9</sub>
	271	[C <sub>9</sub> H <sub>18</sub> O <sub>9</sub> +H] <sup>+</sup>	270	C <sub>9</sub> H <sub>18</sub> O <sub>9</sub>
	271	[C <sub>9</sub> H <sub>20</sub> O <sub>10</sub> +H-H <sub>2</sub> O] <sup>+</sup>	288	C <sub>9</sub> H <sub>20</sub> O <sub>10</sub>
	289	[C <sub>9</sub> H <sub>20</sub> O <sub>10</sub> +H] <sup>+</sup>	288	C <sub>9</sub> H <sub>20</sub> O <sub>10</sub>
<b>Glyoxal</b>				
Dimers	117	[C <sub>4</sub> H <sub>6</sub> O <sub>5</sub> +H-H <sub>2</sub> O] <sup>+</sup>	134	C <sub>4</sub> H <sub>6</sub> O <sub>5</sub>
	135	[C <sub>4</sub> H <sub>6</sub> O <sub>5</sub> +H] <sup>+</sup>	134	C <sub>4</sub> H <sub>6</sub> O <sub>5</sub>
	153	[C <sub>4</sub> H <sub>8</sub> O <sub>6</sub> +H] <sup>+</sup>	152	C <sub>4</sub> H <sub>8</sub> O <sub>6</sub>
	171	[C <sub>4</sub> H <sub>10</sub> O <sub>7</sub> +H] <sup>+</sup>	170	C <sub>4</sub> H <sub>10</sub> O
Trimers	175	[C <sub>6</sub> H <sub>6</sub> O <sub>6</sub> +H] <sup>+</sup>	174	C <sub>6</sub> H <sub>6</sub> O <sub>6</sub>
	193	[C <sub>6</sub> H <sub>8</sub> O <sub>7</sub> +H] <sup>+</sup>	192	C <sub>6</sub> H <sub>8</sub> O <sub>7</sub>
	211	[C <sub>6</sub> H <sub>10</sub> O <sub>8</sub> +H] <sup>+</sup>	210	C <sub>6</sub> H <sub>10</sub> O <sub>8</sub>
	229	[C <sub>6</sub> H <sub>12</sub> O <sub>9</sub> +H] <sup>+</sup>	228	C <sub>6</sub> H <sub>12</sub> O <sub>9</sub>
	247	[C <sub>6</sub> H <sub>14</sub> O <sub>10</sub> +H] <sup>+</sup>	246	C <sub>6</sub> H <sub>14</sub> O <sub>10</sub>
<b>tricarbonyl</b>				
Monomers	101	[C <sub>4</sub> H <sub>4</sub> O <sub>3</sub> +H] <sup>+</sup>	100	C <sub>4</sub> H <sub>4</sub> O <sub>3</sub>
	159	[C <sub>6</sub> H <sub>6</sub> O <sub>5</sub> +H] <sup>+</sup>	158	C <sub>6</sub> H <sub>6</sub> O <sub>5</sub>
Dimers	173	[C <sub>7</sub> H <sub>8</sub> O <sub>5</sub> +H] <sup>+</sup>	172	C <sub>7</sub> H <sub>8</sub> O <sub>5</sub>
	201	[C <sub>8</sub> H <sub>8</sub> O <sub>6</sub> +H] <sup>+</sup>	200	C <sub>8</sub> H <sub>8</sub> O <sub>6</sub>
<b>γ-dicarbonyls</b>				
Monomers	85	[C <sub>4</sub> H <sub>4</sub> O <sub>2</sub> +H] <sup>+</sup>	84	C <sub>4</sub> H <sub>4</sub> O <sub>2</sub>
	99	[C <sub>5</sub> H <sub>6</sub> O <sub>2</sub> +H] <sup>+</sup>	98	C <sub>5</sub> H <sub>6</sub> O <sub>2</sub>
Dimers	143	[C <sub>6</sub> H <sub>6</sub> O <sub>4</sub> +H] <sup>+</sup>	142	C <sub>6</sub> H <sub>6</sub> O <sub>4</sub>
	157	[C <sub>7</sub> H <sub>8</sub> O <sub>4</sub> +H] <sup>+</sup>	156	C <sub>7</sub> H <sub>8</sub> O <sub>4</sub>
	169	[C <sub>8</sub> H <sub>8</sub> O <sub>4</sub> +H] <sup>+</sup>	168	C <sub>8</sub> H <sub>8</sub> O <sub>4</sub>
	197	[C <sub>10</sub> H <sub>12</sub> O <sub>4</sub> +H] <sup>+</sup>	196	C <sub>10</sub> H <sub>12</sub> O <sub>4</sub>
<b>epoxide</b>	141	[C <sub>7</sub> H <sub>8</sub> O <sub>3</sub> +H] <sup>+</sup>	140	C <sub>7</sub> H <sub>8</sub> O <sub>3</sub>

### *SOA formation on different seed particles*

The temporal evolution of *GF* on different types of seed particles shows similarly a rapid, continuous increase in *GF*, after a short initial hysteresis (Figure 25a). Among the different seed particles,  $(\text{NH}_4)_2\text{SO}_4$  in the presence of  $\text{NH}_3$  exhibits the largest *GF* and lowest *SSA* at 90 min (Figure 25b), because of efficient oligomer and NCO production. The calculated SOA density ranges from  $1.19 \text{ g cm}^{-3}$  to  $1.28 \text{ g cm}^{-3}$  at 10 min (Figure 25c), which are characteristic of an initial composition dominated by organic acids and smaller oligomers from the G2 products (Table 7), and increases throughout the experiment, consistent with increasing oligomerization.  $(\text{NH}_4)_2\text{SO}_4$  particles with  $\text{NH}_3$  exhibit the highest density ( $1.60 \text{ g cm}^{-3}$ ), similar as the measured *GF*. The density of  $1.60 \text{ g cm}^{-3}$  for the toluene-derived SOA is higher than that of common organics reported previously ( $1.4 \text{ g cm}^{-3}$ ).<sup>57</sup> Comparison of the chemical composition on the different seed particles reveals increased carboxylates from  $\text{NH}_4\text{HSO}_4$ ,  $(\text{NH}_4)_2\text{SO}_4$  without  $\text{NH}_3$ ,  $(\text{NH}_4)_2\text{SO}_4$  with  $\text{NH}_3$ , to NaCl seed particles, consistent with an increasing acid-base reaction. Additionally, the reaction between NaCl and organic acids yields sodium carboxylates and leads to evaporation of hydrogen chloride (HCl), explaining the largest carboxylate intensity on NaCl seed particles (Fig. 25d). Among the different types of seed particles, the intensities for oligomers and NCO reach the highest for  $(\text{NH}_4)_2\text{SO}_4$  particles with  $\text{NH}_3$  (Figure 25d). No NCO compounds are identified on NaCl seed particles in the absence of  $\text{NH}_3$ . The density trends among the different seed particles are similar to that in oligomer intensity (Figure 25c,d), indicating an essential role of oligomerization in regulating the particle density.

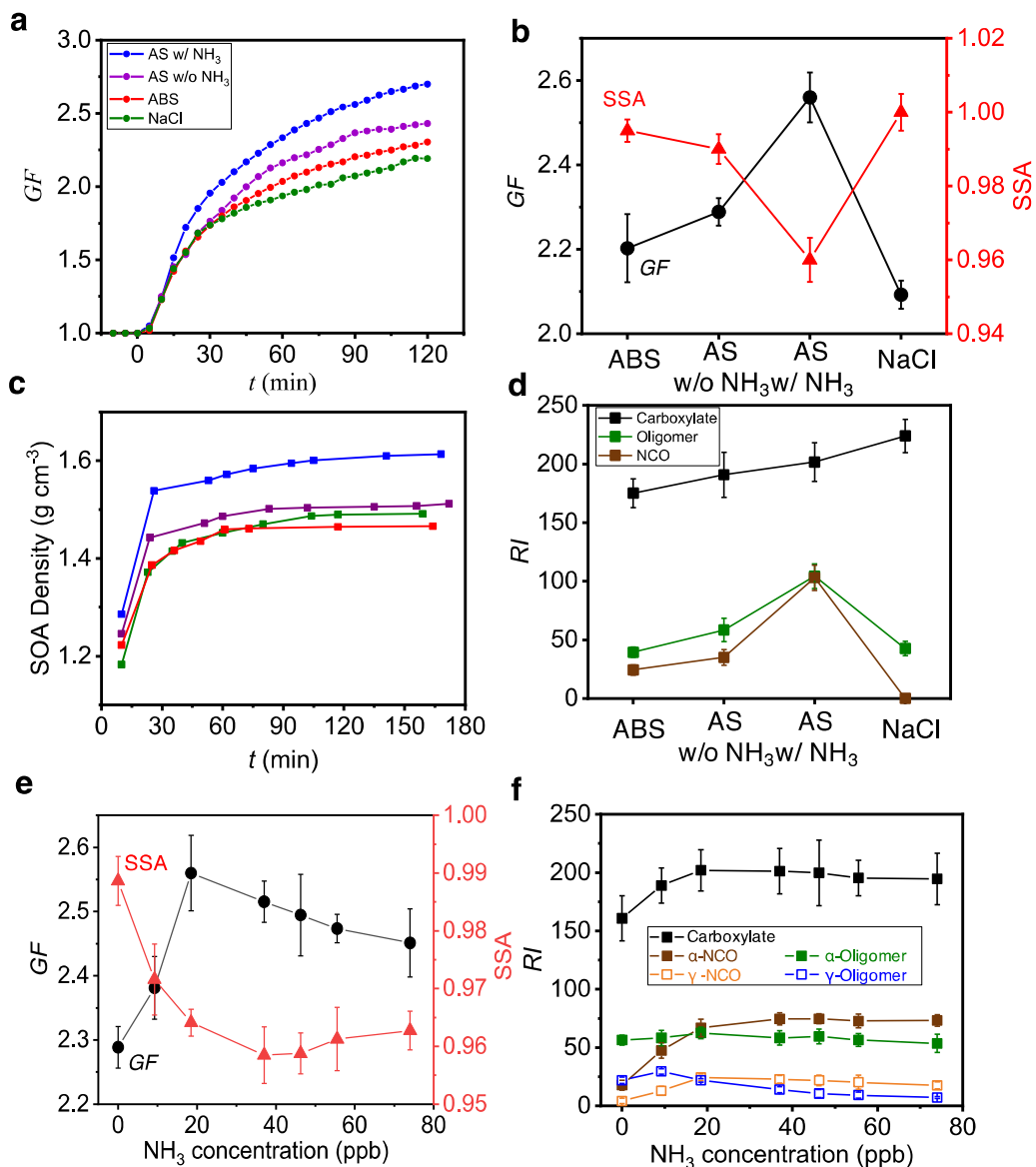


**Figure 25. Variation in SOA growth with seed particles.** (a) Time-dependent growth for  $(\text{NH}_4)_2\text{SO}_4$  particles in the presence (AS w/  $\text{NH}_3$ , blue) and absence (AS w/o  $\text{NH}_3$ , purple) of 19 ppb  $\text{NH}_3$  and for  $\text{NH}_4\text{HSO}_4$  (ABS, red) and NaCl (green) particles in the absence of  $\text{NH}_3$ . (b)  $GF$  (black) and SSA (red) at 90 mins of exposure. (c) SOA density for seed particles of  $(\text{NH}_4)_2\text{SO}_4$  in the presence (blue) and absence (purple) of 19 ppb  $\text{NH}_3$ , ABS (red), and NaCl (green). The color legend is similar to that in (a). (d) Aerosol-phase relative intensity ( $RI$ ) for carboxylates (black), oligomers (green), and NCO (brown) on different seed particles. (e)  $GF$  (black) and SSA (red) at  $t = 90$  min with varying  $\text{NH}_3$  concentrations between 0 and 74 ppb. (f) Aerosol-phase relative intensities ( $RI$ ) for carboxylates (black square), oligomers (green square), N-heterocycles (brown square) from  $\alpha$ -dicarbonyls, oligomers (blue open square), and N-chains (brown open square) from  $\gamma$ -carbonyl with varying  $\text{NH}_3$  concentrations between 0 and 74 ppb. Initiation of photooxidation by ultraviolet light occurred at  $t = 0$ . The error bar denotes  $1\sigma$  of 3 replicated measurements.

The dependences of the measured  $GF$ ,  $SSA$ , and density on the different seed particles are explainable by the mechanisms leading to the formation of the observed aerosol-phase products (Figure 25d). Gas-particle conversion of organic acids from the G2/G3 products likely includes ionic dissociation to form carboxylates or acid-base reactions to form ammonium (sodium) carboxylates in the presence of  $\text{NH}_3$  ( $\text{NaCl}$ ), as evident from the increasing carboxylate intensity (Figure 25d). On the other hand, di-carbonyls engage in oligomerization, which is mediated by carbenium ions.<sup>70</sup> Protonation, hydration, and deprotonation of di-carbonyls produce carbenium ions and diols/tetrols, and subsequent nucleophilic addition to the carbenium cation by the negative hydroxyl O-atom of diols/tetrols or the negative N-atom of  $\text{NH}_3$  results in the formation of oligomers and NCO, respectively. While protonation is favored under acidic conditions, high proton concentration inhibits hydration and deprotonation to form diols/tetrols, resulting in most efficient oligomerization under moderate acidic condition, i.e., on  $(\text{NH}_4)_2\text{SO}_4$  particles with  $\text{NH}_3$ . Also, oligomerization is likely promoted by an electric field on  $(\text{NH}_4)_2\text{SO}_4$ , because of net charge separation from ion distributions at the interface.<sup>52</sup> The interfacial electric field is strongly positive for  $(\text{NH}_4)_2\text{SO}_4$  solutions and is likely enhanced on sub-micrometer particles due to high ionic strength.<sup>68</sup> A positive electric field exerts interfacial attraction to the carbonyl and carboxylic functional groups, which possess negatively charged characteristics. Hence, the most efficient nucleophilic addition involving the carbenium ions and the strongest interfacial attraction jointly explain the largest  $GF$  and highest intensities for oligomers and NCO on  $(\text{NH}_4)_2\text{SO}_4$  particles with  $\text{NH}_3$ . Recent measurements of SOA and BrC formation from glyoxal and methylglyoxal showed that the formation of oligomers and NCOs occurs over a wide acidity range and is most efficient on  $(\text{NH}_4)_2\text{SO}_4$  particles with  $\text{NH}_3$ , consistent with our present results.<sup>26</sup>

We further examined the dependence of  $GF$ ,  $SSA$ , and chemical composition on gaseous  $NH_3$  (Figure 25e). For  $(NH_4)_2SO_4$  particles,  $GF$  initially increases with  $NH_3$  but decreases when the  $NH_3$  concentration exceeds 19 ppb. On the other hand,  $SSA$  decreases with  $NH_3$  but increases slightly when the  $NH_3$  concentration exceeds 37 ppb. These dependences of  $GF$  and  $SSA$  on  $NH_3$  reflect the competition in the formation between oligomers and NCO from  $\alpha$ - and  $\gamma$ -dicarbonyls.  $NH_3$  is involved in the aerosol-phase reactions with dicarbonyls to form NCO and with organic acids to form ammonium carboxylates, responsible for the increasing  $GF$  and decreasing  $SSA$  with initially increasing  $NH_3$ . However, an elevated  $NH_3$  concentration likely converts dicarbonyls to di-imine compounds, resulting in fewer carbonyl functional groups to form larger NCO. Small NCO is subjected to evaporation back to the gas-phase, leading to a reduced  $GF$  and slightly increased  $SSA$  at subsequently increasing  $NH_3$ . Analysis of the particle composition confirms that NCO and carboxylates initially increase with  $NH_3$  but become invariant when  $NH_3$  exceeds 19 ppb, while there are slightly decreasing oligomers when  $NH_3$  exceeds 19 ppb. We performed additional experiments by exposing  $NH_4HSO_4$  and NaCl seed particles to toluene-OH oxidation products by varying  $NH_3$ . For  $NH_4HSO_4$  seed particles, addition of  $NH_3$  converts  $NH_4HSO_4$  to  $(NH_4)_2SO_4$ , resulting in similar  $GF$  as that of  $(NH_4)_2SO_4$  (Figure 26). For NaCl seed particles,  $GF$  increases considerably with  $NH_3$  and becomes independent on  $NH_3$  at a concentration exceeding 19 ppb (Figure 27a), similar to the measured carboxylate intensity (Figure 27b). Also, the intensities for oligomer and NCO decrease and increase, respectively, with increasing  $NH_3$ , consistent with the competition in the formation between oligomers and NCO (Figure 27b).

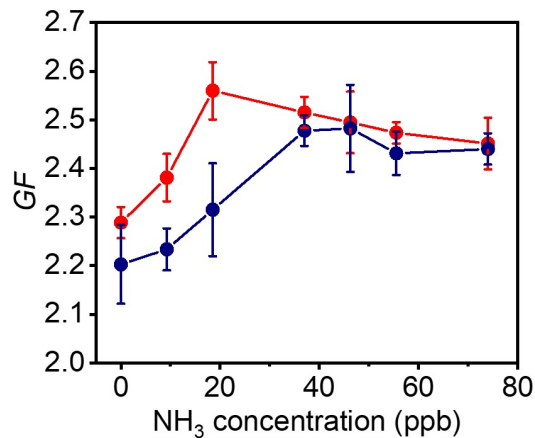


**Figure 26. Size growth with NH<sub>3</sub>.** Comparison of measured  $GF$  at  $t = 90$  mins between NH<sub>4</sub>HSO<sub>4</sub> (blue) and (NH<sub>4</sub>)<sub>2</sub>SO<sub>4</sub> (red) seed particles exposed to toluene-OH oxidation products at varying NH<sub>3</sub> concentrations between 0 and 74 ppb. The error bar denotes  $1\sigma$  of 3 repeated measurements. All experiments were carried out at 298 K and RH = 90%.

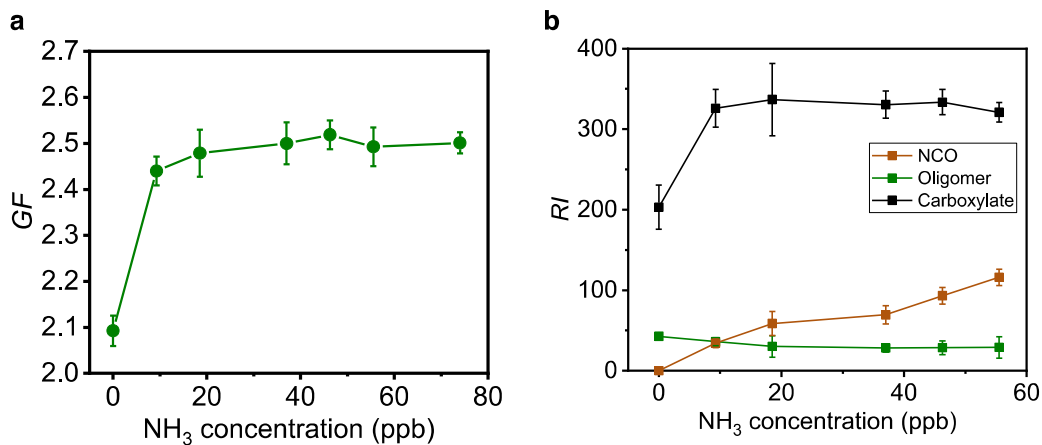


**Figure 27. Variations in size growth and composition with NH<sub>3</sub>.** Measurements of  $GF$  and chemical compositions on NaCl seed particles exposed to toluene-OH oxidation products with varying NH<sub>3</sub>. (a)  $GF$  at  $t = 90$  mi with varying NH<sub>3</sub> concentrations between 0 and 74 ppb. (b) Particle-phase mass relative intensity ( $RI$ ) for carboxylates (black), oligomers (green), and NCO (brown). The error bar denotes  $1\sigma$  of 3 repeated measurements.



### *Effects of RH and gaseous reactants*

We carried out additional experiments by varying RH from 10% to 90% (Figure 28). Comparison of the measured evolutions in *GF*, SSA, and density shows noticeable RH effects. At low RH (10%), the particle growth exhibits an elongated hysteresis, as evident from the evolution in the *GF*. Compared to 90% RH with a delay of ~5 min, the increase in *GF* only occurs after a hysteresis of 10-15 min at 10% RH (Figure 28a), relevant to delayed formation of later (i.e., G3) generation products. Specifically, the G2 products (i.e., dicarbonyls) mainly contribute to the particle growth via the formation of oligomers and NCOs at high RH, while the G3 products (i.e., as pyruvic acid and 4-oxo-2-pentenic acid) are mainly responsible for the particle growth via the formation of carboxylates at low RH. These multifunctional organic acids are produced from further oxidation of the G2 products, i.e., dicarbonyls, by OH radicals. In contrast to an initial decrease but subsequent increase in total density at 90% RH, the total density decreases monotonically at 10% RH (Figure 28b). The calculated density for the SOA materials increases slightly with reaction time at 10% RH, i.e., from 1.33 to 1.43 g cm<sup>-3</sup>, compared to a much larger increase from 1.28 to 1.60 g cm<sup>-3</sup> at 90% RH (Figure 29). These differences in the particle density imply that condensable oxidized organics contributes distinctly to the particle growth under high and low RH conditions. Also, measured SSA at 90 min is equal to unity at 10% RH and decreases with increasing RH (Figure 28c), indicating that NCO formation is negligible at low RH and occurs only at high RH.

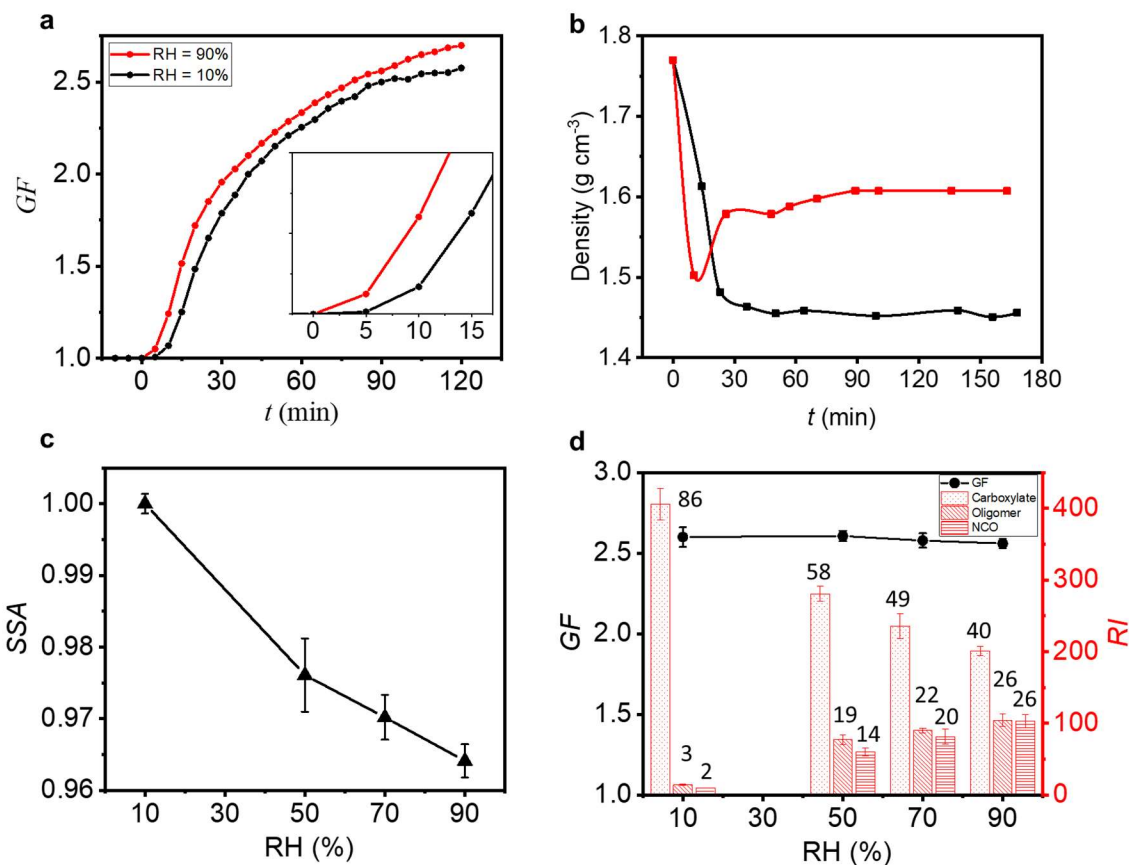


**Figure 28. RH dependence of SOA formation.** (a) Time-dependent growth at RH = 90% (red) and RH = 10% (black) for (NH<sub>4</sub>)<sub>2</sub>SO<sub>4</sub> seed particles with 19 ppb NH<sub>3</sub>. The insert displays an enlarged portion of the figure during the initial 15 min. (b) Time-dependent particle density at RH = 90% (red) and RH = 10% (black) for (NH<sub>4</sub>)<sub>2</sub>SO<sub>4</sub> seed particles with 19 ppb NH<sub>3</sub>. (c) SSA with varying RH between 10% and 90% for (NH<sub>4</sub>)<sub>2</sub>SO<sub>4</sub> seed particle with 19 ppb NH<sub>3</sub>. (d) *GF* (black circle) and aerosol-phase intensities of carboxylates (left column), oligomers (middle column), and NCO (right column) with varying RH between 10% and 90%. The number corresponds to the percent contribution (%) to the total observed mass intensity. All experiments correspond to (NH<sub>4</sub>)<sub>2</sub>SO<sub>4</sub> seed particles with 19 ppb NH<sub>3</sub>. Initiation of photooxidation by ultraviolet light occurred at  $t = 0$ . The error bar denotes the standard deviation of 3 repeated measurements.

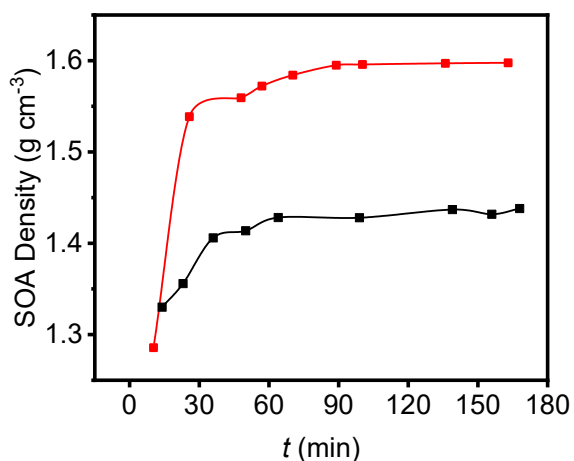


**Figure 29. Temporal evolution in SOA density.** SOA density at RH = 90% (red) and 10% (black). All experiments were carried out on  $(\text{NH}_4)_2\text{SO}_4$  seed particles with 19 ppb  $\text{NH}_3$ . Initiation of photooxidation by ultraviolet light occurred at  $t = 0$ .

To gain further understanding on the cause for the variability in  $GF$ ,  $SSA$ , and density, we performed measurements of the chemical composition at varying RH. At low RH (10%), carboxylates represent dominantly the aerosol-phase products (about 86%), while the contributions of oligomers, NCO, and LVO to the total SOA formation are estimated as 3%, 2%, and 9%, respectively (Table 12). With increasing RH from 10% to 90%, the contributions to the total SOA formation consecutively increase and decrease for oligomers/NCO and carboxylates, respectively, while the fraction for LVO is nearly invariant. These dependences of  $GF$ ,  $SSA$ , and density on RH are relevant to the aerosol-phase chemistry to form carboxylates, oligomers, and NCO. For  $(\text{NH}_4)_2\text{SO}_4$  particles, the deliquescent and efflorescent points occur, respectively, at 80% and 36% RH.<sup>124</sup> At low RH (10%), aqueous reactions to yield oligomers/NCO are considerably suppressed below the efflorescent point, attributable to hindered protonation, hydration, and deprotonation of di-carbonyls. Also, the measured gaseous concentrations of sub-ppb to a few ppb levels for organic acids are much smaller than their corresponding equilibrium vapor pressures (Table 13), rendering implausible gas-to-particle conversion by condensation alone. On the other hand, the equilibrium vapor pressures of organic acids are likely reduced in a multi-component system via the analogous Raoult's Law. In addition, water molecules inevitably play a key role in stabilizing carboxylates in the aerosol-phase, because of its dominant abundance even at 10% RH,

i.e., with a gaseous concentration of  $6 \times 10^{16}$  molecules  $\text{cm}^{-3}$  or  $3.3 \times 10^3$  ppm. Particles consisting of organic acids retain water even at very low RH (i.e., with a  $\text{H}_2\text{O}$  mass fraction of 17% at 5% RH), which facilitates the formation of carboxylates via ionic dissociation or acid-base reactions below the efflorescent point. The equilibrium vapor pressures of hydroxyl toluene/benzoquinone are much lower than those for organic acids (Table 13), favoring efficient gas-to-particle conversion for LVOs.

**Table 12. Relative contributions of condensable oxidized organics with each type of functionality to SOA formation.** Experimental conditions:  $(\text{NH}_4)_2\text{SO}_4$  seed particles with 19 ppb  $\text{NH}_3$  and at 10% - 90% RH.

Functionality	SOA Contribution (%)			
	RH (%)			
	10	50	70	90
Di-carbonyls	3	19	22	26
Di-carbonyls+ $\text{NH}_3$	2	14	20	26
Carboxylates	86	58	49	40
LVO	9	9	9	8

**Table 13. Oxygen to carbon (O/C) ratio for identified SOA components and saturation vapor pressures ( $P_s$ ) of condensable oxidized organics.**

Compound	O/C	$p_s$ (atm, 298 K)
<b>Oligomers</b>		
Glyoxal	1	$2.3 \times 10^{-2}$
Glyoxal dimers	1~1.75	
Glyoxal trimers	1~1.67	
Methylglyoxal	0.67	$1.6 \times 10^{-1}$
Methylglyoxal dimers	0.67~1.17	
Methylglyoxal trimers	0.67~1.11	
Butenedial	0.5	$7.9 \times 10^{-4}$
Butenedial dimers	0.5~0.87	
Methylbutenedial	0.4	$3.9 \times 10^{-4}$
Methylbutenedial dimers	0.4~0.7	
Tricarbonyl	0.75	$1.6 \times 10^{-3}$
Tricarbonyl dimers	0.75~0.9	
Epoxide	0.43	
<b>NCO</b>		
Glyoxal N-heterocycles	0~0.25	
Methylglyoxal N-heterocycles	0~0.17	
Butenedial N-heterochains	0~0.25	
Methylbutenedial N-heterochains	0~0.2	
Tricarbonyl N-heterocycles	0.2~0.4	
Epoxide N-heterochains	0~0.44	
<b>Organic acids</b>		
Benzoic acid	0.29	$1.1 \times 10^{-5}$
4-Oxo-2-pentenoic acid	0.6	$6.6 \times 10^{-6}$
Acetylpyruvic acid	0.8	
Pyruvic acid	1.2	$6.1 \times 10^{-4}$
Glyoxylic acid	1.5	$1.9 \times 10^{-3}$
<b>Others</b>		
	1.25	
Dihydroxy toluene	0.29	
Trihydroxy toluene	0.43	$1.1 \times 10^{-8}$
2-Hydroxy-5-methylquinone	0.43	$5.3 \times 10^{-7}$

Interestingly, the particle growth is weakly dependent on (slightly decreasing with) RH from 10% to 90% (Figure 28d). Such a RH dependence is related to gas-particle conversion, aqueous reactions, and wall-loss of the oxidation products. Specifically, wall-loss of the precursors for oligomers, NCO, and carboxylates are more pronounced at high RH, as evident from the measured concentrations of the various condensable oxidized organics. Wall-loss is 1.3 to 4.3

times more efficient at 90% RH than at 10% RH, leading to reduced gaseous concentrations of the condensable oxidized organics at high RH (Table 14). The larger wall loss at higher RH is explained by increasing aqueous reactions of the condensable oxidized organics onto the Teflon chamber wall via oligomerization (for dicarbonyls) and ionic dissociation/acid-base reaction (for organic acids). Hence, the weak dependence of  $GF$  on RH is attributed to a canceling effect between increased aqueous reactions to form oligomers, NCO, and carboxylates but decreased gaseous concentrations of the condensable oxidized organics due to larger wall-loss at higher RH. At 10% RH,  $GF$  increases slightly (i.e., from 2.53 to 2.65) with  $\text{NH}_3$ , and the  $GF$  increase correlates with increased carboxylates in the aerosol-phase (Figure 30). The  $GF$  increase with  $\text{NH}_3$  at low RH is smaller than that at high RH (Figures 26 and 27), indicating a hindered acid-base reaction. Furthermore, the evidence for the occurrence of oligomerization and acid-base reaction at low RH (10%) unambiguously indicates an indispensable role of  $\text{H}_2\text{O}$  to form oligomers, NCO, and carboxylates (Figure 28d and Table 12), albeit to a lesser extent.

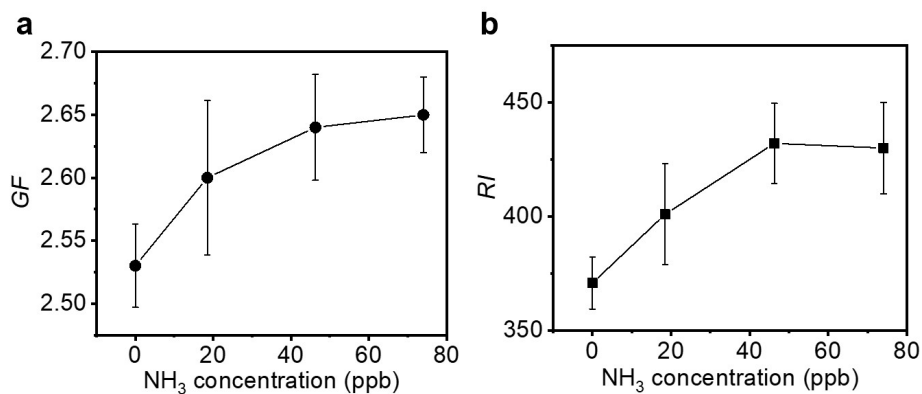


**Figure 30. Variations in size growth and composition with  $\text{NH}_3$ .**  $GF$  (a) and particle-phase mass relative intensity ( $RI$ ) for carboxylates (b) on  $(\text{NH}_4)_2\text{SO}_4$  seed particles at varying  $\text{NH}_3$  concentrations between 0 and 74 ppb and at RH = 10%. The error bar denotes  $1\sigma$  of 3 repeated measurements.

**Table 14. Comparison of measured gaseous concentrations of condensable oxidized organics from toluene-OH oxidation between 10% and 90% RH.**

<i>m/z</i>	Average Concentration (ppb)		Ratio (10% to 90% RH)
	10% RH	90% RH	
59	5.4	1.9	2.8
73	3.2	0.9	3.4
85	2.6	0.7	3.7
89	3.6	0.9	4.0
91	5.2	2.9	1.8
99	9.6	3.1	3.1
101	3.0	0.7	4.3
107	6.5	4.2	1.5
109	22.6	13.3	1.7
111	5.9	3.1	1.9
115	6.8	1.9	3.6
123	2.0	0.9	2.2
125	1.3	1	1.3
127	2.5	1.3	1.9
131	2.3	1.1	2.0
139	2.3	0.9	2.5
141	2.4	1.1	2.1
155	0.7	0.2	3.2
157	0.5	0.13	3.8

The measured size growth of particles and the corresponding gas-phase concentrations of the condensable oxidized organics were employed to derive the uptake coefficient on ammonium sulfate in the presence of 19 ppb NH<sub>3</sub> at 10% and 90% RH (Table 15). The  $\gamma$  value for dicarbonyls is the highest at 90% RH (from  $3 \times 10^{-3}$  to  $1.2 \times 10^{-2}$ ) but is significantly reduced (from  $3.4 \times 10^{-4}$  to  $9.0 \times 10^{-4}$ ) at 10% RH, while the  $\gamma$  value for organic acids and LVOs is only slightly higher at higher RH (90%). The measured  $\gamma$  appears to correlate with the acid dissociation constant ( $K_a$ ) and solubility among the organic acids, i.e., being the highest for pyruvic acid and the lowest for benzoic acid. For comparison, our derived  $\gamma$  values for glyoxal and methylglyoxal are consistent with those recently reported at 90% RH (within 20%).<sup>26</sup>

**Table 15. Measured uptake coefficient ( $\gamma$ ) for condensable oxidized organics on ammonium sulfate seed particles in the presence of ammonia.** The uncertainty in the calculated  $\gamma$  reflects the combined random errors in the measured five parameters, i.e.,  $D_o$  = initial diameter,  $D_p$  = final diameter after the exposure time of  $dt$ ,  $N$  = the particle number concentration,  $S$  = average particle surface area, and  $[A]$  = average concentration of species A. FR = percent contributions to the particle-phase mass intensity. For each parameter, an uncertainty is estimated, corresponding to  $1\sigma$  of at least 3 measurements.

Species	$D_o$ (nm)	$D_p$ (nm)	$N$ ( $\text{cm}^{-3}$ )	$S$ ( $10^{-5} \text{cm}^2$ $\text{cm}^{-3}$ )	$[A]$ (ppb)	FR	$\gamma$ ( $10^{-3}$ )
<b>RH = 90%</b>							
Glyoxal	100.0	256.0	15000	1.55	1.9	13%	$8.3 \pm 2.0$
Methylglyoxal	100.0	256.0	15000	1.55	0.9	10%	$12 \pm 2.8$
$\gamma$ -Dicarbonyls	100.0	256.0	15000	1.55	3.1	10%	$3.0 \pm 0.6$
Benzoic acid	100.0	256.0	15000	1.55	0.9	0.9%	$0.84 \pm 0.11$
4-Oxo-2-pentenoic acid	100.0	256.0	15000	1.55	1.9	4.8%	$2.2 \pm 0.4$
Pyruvic acid	100.0	256.0	15000	1.55	0.9	2.6%	$2.9 \pm 0.3$
LVO	100.0	256.0	15000	1.55	1.2	8.0%	$5.0 \pm 1.5$
Nitrophenol <sup>a</sup>	100.0	246.0	15000	1.46	1.4	3.1%	$1.6 \pm 0.3$
<b>RH = 10%</b>							
Glyoxal	100.0	260.0	15000	0.85	5.4	1.9%	$0.75 \pm 0.18$
Methylglyoxal	100.0	260.0	15000	0.85	3.2	1.5%	$0.90 \pm 0.20$
$\gamma$ -Dicarbonyls	100.0	260.0	15000	0.85	9.6	2.0%	$0.34 \pm 0.07$
Benzoic acid	100.0	260.0	15000	0.85	2.0	1.1%	$0.80 \pm 0.14$
4-Oxo-2-pentenoic acid	100.0	260.0	15000	0.85	6.8	9.1%	$2.0 \pm 0.5$
Pyruvic acid	100.0	260.0	15000	0.85	3.6	5.3%	$2.5 \pm 0.4$
LVO	100.0	260.0	15000	0.85	2.9	9.4%	$4.2 \pm 1.5$
Nitrophenol*	100.0	253.5	15000	0.82	2.3	3.0%	$1.6 \pm 0.3$

<sup>a</sup> Measured in the presence of 100 ppb  $\text{NO}_x$



To evaluate the effects of  $\text{NO}_x$  on SOA formation from toluene oxidation, we performed additional experiments using  $(\text{NH}_4)_2\text{SO}_4$  seed particles in the presence of  $\text{NH}_3$  by varying  $\text{NO}_x$  concentrations from 0 to 300 ppb (Figure 31a-c). Measurements of the time-dependent gas-phase concentrations show the formation of three major nitrophenols from  $\text{NO}_2$  addition to the OH-toluene adduct in the presence of  $\text{NO}_x$ , i.e., 2-nitrophenol ( $m/z = 140$ ), methyl nitrophenol ( $m/z = 154$ ), and dihydroxy nitrotoluene ( $m/z = 170$ ) (Figure 31d). The evolution in the gas-phase concentrations clearly illustrates multi-generation production of nitrophenols. The concentrations of the first-generation nitrophenols (i.e., 2-nitrophenol and methyl nitrophenol) increase instantaneously upon initiation of photooxidation, while the second generation nitrophenol (i.e., dihydroxy nitrotoluene) appears with a significant delay of about 30 min. The decrease in the concentrations of 2-nitrophenol and methyl nitrophenol at longer reaction time ( $> 60$  min) reflects their consumption to form dihydroxy nitrotoluene. The production of nitrophenols is much smaller than those for dicarbonyls and organic acids from toluene oxidation (Figures 20 and 31), consistent with a small yield of less than 7% under high- $\text{NO}_x$  conditions.<sup>110</sup> Addition of 100 ppb  $\text{NO}_x$  causes a slight decrease in the measured  $GF$  (at 90 min) compared to that without  $\text{NO}_x$  in the RH range of 10-90% (Figure 31a). At a constant RH level (70%), the  $GF$  value decreases monotonically from  $2.58 \pm 0.04$  to  $2.40 \pm 0.05$  from 0 to 300 ppb  $\text{NO}_x$  (Figure 31b). Analysis of the particle composition reveals that the decreasing size growth correlates with simultaneous decreases of carboxylates, oligomers, and NCOs but an increase of nitrophenols in the aerosol-phase (Figure 31c). The contribution of nitrophenols to SOA formation is estimated to range from 3% to 6% and is the largest from methyl nitrophenol. The production of the gas-phase nitrophenols and their corresponding volatility decrease and increase, respectively, with increasing functionality, explaining the largest contribution to SOA formation from methyl nitrophenol. The effects of  $\text{NO}_x$

on toluene oxidation include the production of nitrophenols and the cycling between RO<sub>2</sub> and alkoxy (RO) radicals, impacting the product distributions for the condensable oxidized organics. Specifically, the presence of NO<sub>x</sub> alters the competing RO<sub>2</sub> reactions, and the formation of nitrophenols decreases the production of dicarbonyls and organic acids, as reflected by decreased oligomers, NCOs, and carboxylates in the aerosol-phase with increasing NO<sub>x</sub>.

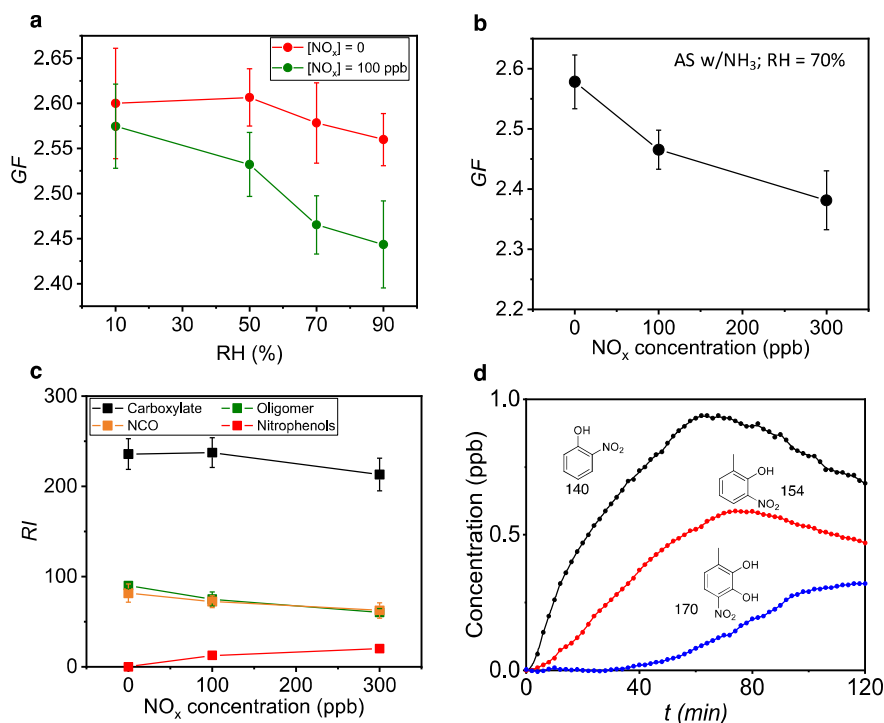


**Figure 31. The effects of NO<sub>x</sub> on SOA formation from toluene oxidation.** (a) Dependence of *GF* at 90 min on RH for (NH<sub>4</sub>)<sub>2</sub>SO<sub>4</sub> seed particles with 19 ppb NH<sub>3</sub> in the presence/absence of NO<sub>x</sub>. (b) Dependence of *GF* at 90 min on the initial NO<sub>x</sub> concentration for (NH<sub>4</sub>)<sub>2</sub>SO<sub>4</sub> seed particles with 19 ppb NH<sub>3</sub> and at RH = 70%. (c) Aerosol-phase relative intensities (*RI*) for carboxylates (black), oligomers (green), NCO (brown), and nitrophenols (red) with varying initial NO<sub>x</sub> concentration for (NH<sub>4</sub>)<sub>2</sub>SO<sub>4</sub> seed particles with 19 ppb NH<sub>3</sub> and at RH = 70%. (d) Time-dependent gas-phase concentrations of 2-nitrophenol (black), methyl nitrophenol (red), and dihydroxy nitrotoluene (blue). The numbers denote the mass to charge ratio (*m/z*). Initiation of photooxidation by ultraviolet light occurred at *t* = 0. The error bar denotes 1σ of 3 replicated measurements.

We further examined SOA growth by varying concentrations of the gaseous reactants, i.e., toluene and OH (Figure 32). The particle volume growth rate, defined by  $GR_v = (D_2^3 - D_1^3)/(D_0^3 \Delta t)$  where  $D_2$  and  $D_1$  are the diameters after 30 and 10 min of exposure, increases with the concentrations of toluene (Figure 32a). Measurements of the chemical compositions show increased carboxylates, oligomers, and NCOs with increasing toluene concentrations (Figure S10b), consistent with increasing production of condensable oxidized organics to contribute to increasing particle growth. Similarly, there is increased SOA formation, when OH concentration is increased by a factor of up to 6 (Figure 32c). The measured oligomers and NCO increase initially but then decrease with increasing OH, while there is a monotonic increase for carboxylates (Figure 32d). While increasing photochemical oxidation generally favors the production of condensable oxidized organics, an excessive OH level oxidizes gaseous dicarbonyls to organic acids to shift oligomerization to carboxylate formation, impacting multi-generational SOA formation. The trends in the aerosol-phase carboxylates, oligomers, and NCOs with OH are attributed to an increased formation of organic acids at the expense of dicarbonyls because of multi-generational photooxidation (Figure 32d).

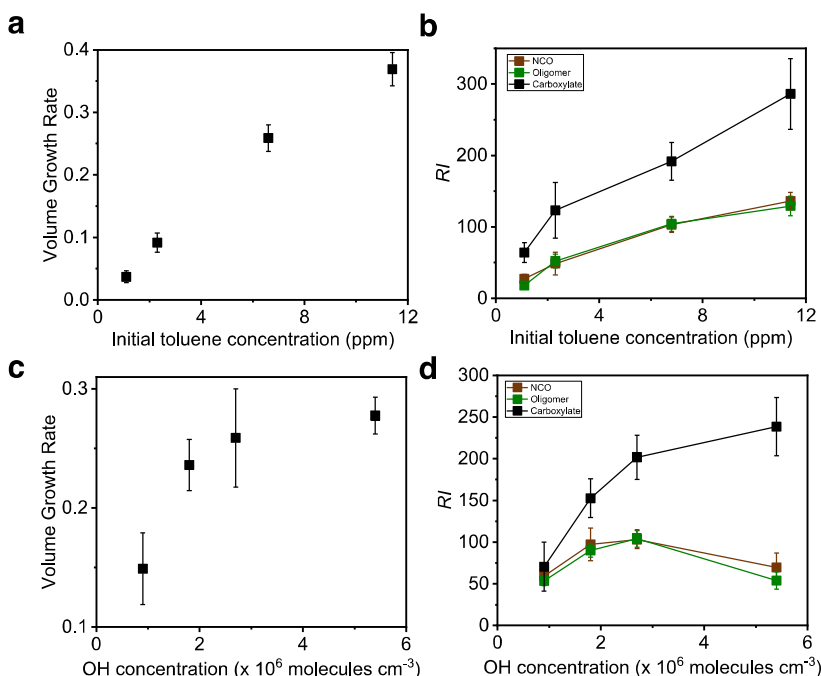


**Figure 32. Variations in particle growth with reactants.** Particle growth under different concentrations of toluene and OH. (a) Particle volume growth rate (defined as  $GR_V = (D_2^3 - D_1^3) / (D_0^3 \Delta t)$ , where  $D_2$  and  $D_1$ , are the diameter of dry particles after 30 min and 10 min of exposure, respectively.  $\Delta t = 20$  min is the time duration) with initial toluene concentration from 1.1 to 11.4 ppm. (b) Particle-phase mass intensity ( $RI$ ) for carboxylates (black), oligomers (green), and NCO (brown) with initial toluene concentration from 1.1 to 11.4 ppm. The OH concentration in (a) and (b) is  $2.7 \times 10^6$  molecules  $\text{cm}^{-3}$ . (c) Measured  $GR_V$  with OH concentration from  $0.9 \times 10^6$  to  $5.4 \times 10^6$  molecules  $\text{cm}^{-3}$ . (d) Particle-phase mass intensity for carboxylates (black), oligomers (green), and NCO (brown) with varying OH concentrations from  $0.9 \times 10^6$  to  $5.4 \times 10^6$  molecules  $\text{cm}^{-3}$ . The initial toluene concentration in (c) and (d) is 6.6 ppm. The error bar denotes  $1\sigma$  of 3 repeated measurements.

### *Linking multi-generation oxidation to SOA formation*

The experimental methodology developed here allows for differentiation of the contributions of multi-generation products from VOC oxidation to SOA formation. By simultaneously monitoring the concentrations of gaseous products and particle properties (i.e., size, density, optical properties, and chemical composition), we elucidate the chemical mechanisms for multi-generation SOA production from toluene-OH oxidation (Figure 33). Exposure to the oxidation products results in rapid size growth and browning of seed particles

(Figures 20e,f and 25a,b). Two major types of condensable oxidized organics consisting of the di-carbonyl and carboxylic functional groups are identified from toluene oxidation, along with a small amount of LVOs (Figures 20h, 25d,f, and 28d and Table 8). The dominant contribution of oligomers, NCOs, and carboxylates to SOA formation is verified from the evolutions in *GF*, SSA, and density as well as from direct measurements of the aerosol-phase compositions (Figures 20 and 25). In particular, measurements of SSA and density provide further insight into chemical speciation of condensable oxidized organics relevant to BrC and SOA formation.

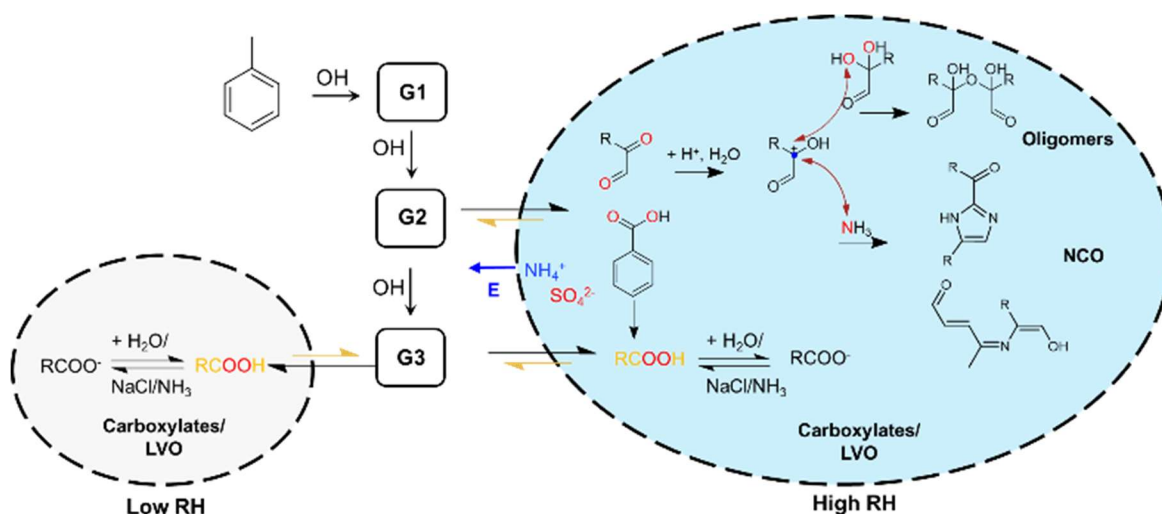


**Figure 33. Multi-generation SOA and BrC formation from toluene-OH oxidation.** The letters G1, G2, and G3 denote the sequence of reactions with OH. The red arrows connect the sites for nucleophilic addition, and the blue arrow labels the electric field arising from interfacial charge separation between NH<sub>4</sub><sup>+</sup> and SO<sub>4</sub><sup>2-</sup>, which exerts attraction to the negatively charged O-atom (marked by red) of dicarbonyls and organic acids.

Multi-generation photooxidation is clearly illustrated from the temporally resolved evolution in gaseous and aerosol-phase products. There exist multiple unimolecular (i.e., isomerization and ring-opening) and bimolecular (i.e., with OH and O<sub>2</sub>) reactions leading to condensable oxidized organics (Figure 21). Typically, unimolecular reactions occur on much

shorter timescales than bimolecular reactions, and bimolecular reactions with O<sub>2</sub> are faster than those with OH, because of high O<sub>2</sub> abundance.<sup>106–108</sup> Our results demonstrate prompt SOA and BrC formation from the G2 (two OH reaction steps) and G3 (three OH reaction steps) products, along with one-two additional steps of reactions with O<sub>2</sub>. Also, our results show negligible contribution to SOA formation for HOMs, which are proposed from multi-generation oxidation, i.e., involving three-four OH and two-four O<sub>2</sub> reaction sequences.<sup>112</sup> Specifically, we detected no measurable signals associated with HOMs both in the gas and aerosol-phases. The formation of primary RO<sub>2</sub> from initial OH addition to the aromatic ring is thermodynamically and kinetically unfavorable,<sup>109</sup> consistent with the large yield of cresols detected by ID-CIMS in our experiments (Figure 20b). The dominant formation of cresols but negligible formation of primary RO<sub>2</sub> explain a small yield for HOMs from toluene oxidation, which are proposed to be produced from autoxidation of RO<sub>2</sub> via intramolecular rearrangement.

Our experiments show that the condensable oxidized organics with different functionalities contribute distinctly to SOA formation. While organic acids from the G2/G3 products engage in ionic dissociation or acid-base reactions to yield carboxylates, di-carbonyls from the G2 products undergo aqueous reactions to form oligomers and NCOs. Gas-particle conversion for organic acids occurs over a wide RH range (i.e., from 10 to 90%), though to a lesser extent at low RH. Condensation of organic acids is implausible because of their high equilibrium vapor pressures (Table 13), and the occurrence of gas-particle conversion implicates a critical role of H<sub>2</sub>O in stabilizing organic acids,<sup>122</sup> by facilitating carboxylate formation. Formation of oligomers and NCO from dicarbonyls takes place efficiently above the efflorescent point at high RH, corroborating an aqueous mechanism involving carbenium ion-mediated and interfacial electric field-enhanced oligomerization to form oligomers and NCOs. Such a mechanism also explains

inefficient formation of oligomers and NCOs at low RH, because of significantly inhibited protonation, hydration, and deprotonation of dicarbonyls.

The conventional view for SOA formation is that multi-generation photooxidation of VOCs yields products with successively decreasing volatility. The extent of VOC oxidation is commonly expressed by the O/C ratio, which is also correlated to the volatility of the products. For example, HOMs, which likely consist of a range of chemical functional groups such as peroxides, hydroperoxides, and peroxy-carboxylic acids with a high O/C ratio (close to unity), are believed to possess sufficiently-low volatility and to represent an important category of oxidation products for SOA formation.<sup>111-113</sup> From chemical composition measurements using TD-ID-CIMS, we determined the O/C ratio for the SOA components consisting of carboxylates, oligomers, NCOs, and LVO, which varies between 0 and 1.75 (Table 13). Notably, there is little correlation between the O/C ratio and SOA contribution for the abundance of aerosol-phase products (normalized by their gaseous concentrations), with a correlation coefficient of  $R^2 = 0.015$  (Figure 34a). Also, the volatility of organic acids and dicarbonyls is sufficiently high to preclude condensation (Table 13). Similarly, there exists no correlation between the equilibrium vapor pressure and SOA formation for the condensable oxidized organics (i.e., dicarbonyls, organic acids, and LVO), with a correlation coefficient of  $R^2 = 0.052$  (Figure 34b). Hence, neither the O/C ratio of the SOA components nor the equilibrium vapor pressure of the condensable oxidized organics accurately reflects SOA formation from toluene oxidation.

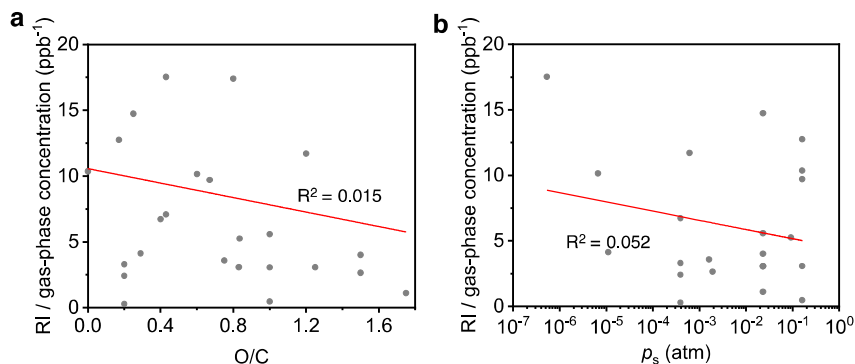


**Figure 34. SOA formations versus O/C ratio and volatility.** Correlation of the particle-phase mass intensity ( $RI$ ) of identified SOA components normalized by the gaseous concentrations of the condensable oxidized organic to the oxygen-carbon ( $O/C$ ) ratio (a) and the saturation vapor pressure at 298K (b). The experiments were performed on  $(NH_4)_2SO_4$  seed particles with 19 ppb  $NH_3$  at  $RH = 90\%$ , similar to Figure 1h. The red solid line represents linear fitting through the data.

### *Atmospheric Implications*

In our work, the OH concentration is comparable to the ambient level, while the toluene concentration is much higher than those of urban conditions, which range widely from sub ppb to several hundred ppb.<sup>104,105</sup> Production of the condensable oxidized organics in the atmosphere is dependent on the types/abundances of VOCs as well as the extent of oxidation (i.e., the intensity of solar radiation and the reaction time). A latest experimental work showed up to 70% of SOA formation by oligomeric products from the OH-initiated oxidation of trimethylbenzene (at 90% RH),<sup>26</sup> which has a molar yield of 90% for methylglyoxal. Our experimental results provide plausible explanation for large SOA formation under polluted environments.<sup>92</sup> Recent measurements revealed that the hygroscopicity for the SOA component resembles those of organic acids, alkylammonium carboxylates, and ammonium carboxylates on clean days with low RH but those of glyoxal and methylglyoxal oligomers on polluted days with high RH,<sup>125</sup> consistent with our observed trends for the contributions of organic acids and oligomers/NCOs to SOA formation



at low and high RH conditions, respectively. Another recent study suggested a dominant role of uptake of gas-phase oxidation products in SOA formation in Beijing, which is attributable to non-equilibrium dissolution of simple carbonyls and organic acids and increases with RH.<sup>126</sup> Since the aerosol physiochemical properties (i.e., size, mass, density, light absorbing/scattering, etc.) are dependent on RH, the change in the aerosol properties from field measurements is typically referenced to dry particles at low RH.<sup>29,92</sup> For example, measurements of the mass concentration for fine particulate matter (size smaller than 2.5  $\mu\text{m}$  or  $\text{PM}_{2.5}$ ) are conducted after 48-h equilibration of sample filters below 35-45% RH in an air-conditioned setting.<sup>68</sup> Drying of aerosols inevitably leads to evaporation of volatile and water-soluble species. Hence, SOA formation or growth in field studies is dominantly contributed by non-volatile aerosol-phase products, similar to our present work.

In summary, we show that dicarbonyls and organic acids contribute dominantly to SOA and BrC formation from toluene oxidation, because of their prompt production and large yields. The functionality of the condensable oxidized organics largely regulates their participation in aerosol-phase reactions, i.e., ionic dissociation or acid-base reaction for organic acids to form the carboxylates and oligomerization for dicarbonyls to form oligomers/NCO. Our findings of SOA formation from toluene oxidation reconcile atmospheric measurements of explosive SOA growth under polluted urban conditions and underscore the importance for understanding multi-generation production of condensable oxidized organics and the relationship between the functionality and aerosol-phase reactivity. Future studies are necessary to identify and quantify condensable oxidized organics from photooxidation of different VOC types, including the production from gaseous oxidation, relationship between functionality and reactivity in the aerosol-phase, and contributions to SOA and BrC formation. In addition, our results corroborate that the synergetic

interaction between toluene oxidation and  $\text{NH}_3$  contributes to BrC formation, which impacts the radiative transfer in the atmosphere. The optical properties of ambient BrC aerosols are dependent on the abundance of the precursor gases, the timescale and extent of their photooxidation, production of NCOs, and the mixing state among various aerosol ingredients.

## CHAPTER IV

# FUNCTIONALITY-BASED SECONDARY ORGANIC AEROSOL FORMATION FROM *m*-XYLENE PHOTOOXIDATION

### Introduction

Aromatic hydrocarbons (e.g., benzene, toluene, xylenes, and trimethylbenzene) account for 20-30% of the total VOCs in urban atmosphere and are considered as the major anthropogenic SOA precursors.<sup>29,104,105</sup> *m*-Xylene is an important constituent of aromatic hydrocarbons, with its mean concentration up to 140.8  $\mu\text{g m}^{-3}$  in the urban atmosphere.<sup>127</sup> The photooxidation of *m*-xylene is typically initiated by the OH, with a rate constant of  $2.4 \times 10^{-11}$   $\text{cm}^3 \text{ molecule}^{-1} \text{ s}^{-1}$  and nearly four times higher than that of toluene.<sup>128</sup> Traditionally, SOA formation from *m*-xylene is considered to be from the gas-particle partitioning of semi-volatile and intermediate volatility products from photooxidation.<sup>129</sup> Also, autoxidation chain reaction of RO<sub>2</sub> from aromatics photooxidation likely yields HOMs with low volatility and a high O/C. However, the reported yield for HOMs from xylene oxidation is small (1.0% to 1.7%).<sup>111</sup> On the other hand, some key oxidation products of *m*-xylene were found to be involved in multiphase reactions and contribute to SOA formation.<sup>70</sup> Recently, an experimental study showed that SOA formation from toluene photooxidation is mainly contributed by volatile dicarbonyls and low-volatility organic acids due to their unique functionalities and aerosol-phase reactivities. A series of studies found that O-H, C=O, C-O-C, and C-OH were the main functional groups in aromatic-derived SOA using a Fourier-transform infrared spectrometer (FTIR), indicating a dominant contribution of SOA by dicarbonyls and carboxylic acid via aqueous reactions.<sup>130,131</sup> In these studies, the intensities for the functional groups of aqueous reaction products increased with

increasing RH. Another study found that the SOA yield from *m*-xylene-OH oxidation decrease significantly (from 14% to 0.8%) with increasing RH (from 14% to 74%) but intensity for C-O-C group of oligomers on FTIR was higher at high RH.<sup>132</sup> Currently, aerosol-phase reactions of VOC oxidation products are parameterized by assuming certain branching ratios for functionalization/fragmentation in atmospheric models.<sup>133,134</sup> However, previous studies have been unable to assess the temporal evolution of SOA production from *m*-xylene oxidation.<sup>113,114</sup> The volatility-based partitioning approach has yet to explain explosive secondary aerosol growth observed under polluted urban conditions.<sup>92</sup>

In this work, we investigate the contribution of condensable oxidized organics with different functionalities to SOA formation from *m*-xylene oxidation. Monodispersed sub micrometer seed particles were exposed to *m*-xylene-OH oxidation products, and evolutions of the gaseous products and aerosol properties were simultaneously measured. Furthermore, a functionality-based approach to assess the SOA formation from *m*-xylene photooxidation is identified.

## Experimental

A 1 m<sup>3</sup> environmental chamber (Teflon® PFA) with eighteen black light lamps (18 × 30W, F30T8/350BL, Sylvania) was used in our experiments, same with that in Chapter III. Briefly, seed particles were exposed to the oxidation products from OH-*m*-xylene reactions in the reaction chamber. Photooxidation of toluene was initiated by turning on the black light lamps, when OH radicals were produced from photolysis of H<sub>2</sub>O<sub>2</sub>. The initial concentration for *m*-xylene and the steady-state concentration for OH were estimated to be 1.9 ppm and 2.1 × 10<sup>6</sup> molecules cm<sup>-3</sup>, respectively. A water bubbler at a temperature of 30°C was used to humidify the

chamber from 10% to 90% RH, and all experiments were performed at 298 K. A 5-slp<sub>m</sub> N<sub>2</sub> flow was used to atomize 0.06 M solution of ammonium sulfate - (NH<sub>4</sub>)<sub>2</sub>SO<sub>4</sub>, ammonium bisulfate - NH<sub>4</sub>HSO<sub>4</sub>, and sodium chloride - NaCl to produce mono-dispersed seed particles. Seed particles were dried to RH of ~2% by a Nafion drier, charged by a bipolar charger, and analyzed by an integrated aerosol analytical system. Seed particles with an initial size of 100 nm were size-selected by a DMA with an initial particle concentration of  $1.5 \times 10^4 \text{ cm}^{-3}$  measured by a CPC. The three different types of seed particles, i.e., (NH<sub>4</sub>)<sub>2</sub>SO<sub>4</sub>, NH<sub>4</sub>HSO<sub>4</sub>, and NaCl, were selected to represent distinct particle acidity and interfacial electric fields.<sup>52</sup> The particle size growth, density, light scattering/absorption were simultaneously and continuously monitored, after monodispersed seed particles were exposed to the products of *m*-xylene-OH oxidation in the reaction chamber. The particle size increase was quantified by a growth factor, *GF*, which is defined by  $D_p/D_0$ , where  $D_p$  is the diameter after exposure and  $D_0 = 100 \text{ nm}$  is the initial diameter measured by DMA. Note both  $D_p$  and  $D_0$  correspond to the dry particle diameter measured after passing through a Nafion Gas Dryer. An APM Analyzer was used to derive the particle density. An ID-CIMS and a TD-ID-CIMS using H<sub>3</sub>O<sup>+</sup> analyzed and quantified gases and particle-phase chemical composition, respectively. An integrating nephelometer and a cavity ring-down spectrometer were employed to measure  $b_{\text{sca}}$  and  $b_{\text{ext}}$  coefficients at 532 nm, respectively. The  $b_{\text{abs}}$  was determined from  $(b_{\text{ext}} - b_{\text{sca}})$ , and the SSA was calculated from  $b_{\text{sca}}/b_{\text{ext}}$ . Measurements of gaseous concentrations of the oxidation products and aerosol properties (i.e., *GF*, *SSA*, density, and chemical composition) were made simultaneously throughout the experiments. While the gaseous concentrations of the oxidation products, *GF*, *SSA*, and density were temporally resolved in our experiments, the particle chemical composition was analyzed after seed particles were exposed for 20 mins to toluene photooxidation and collected for 2 additional

hours by TD-ID-CIMS, reflecting an overall aerosol chemical makeup during an experiment. To assess the effects of different seed particles, RH, and NH<sub>3</sub> on SOA and BrC formation, we compared the measured *GF* and *SSA* values after 90-min exposure to the OH-*m*-xylene oxidation.

Wall loss estimation, SOA density, and uptake coefficient calculations are similar to those described in Chapter III.

#### *SOA yield calculation*

SOA yield is calculated by,

$$Y = \frac{\Delta M_{\text{SOA}}}{\Delta M_{\text{VOC}}} \quad (17)$$

where  $\Delta M_{\text{SOA}}$  and  $\Delta M_{\text{VOC}}$  are the mass of SOA formed and VOC consumed till 120 min, respectively.  $\Delta M_{\text{SOA}}$  is calculated by the mass growth of the particles,

$$\Delta M_{\text{SOA}} = \frac{\pi(D_p^3 - D_0^3)\rho\bar{N}}{6} \quad (18)$$

where  $\bar{N} = \frac{15000 \text{ cm}^{-3} + 7500 \text{ cm}^{-3}}{2} = 11250 \text{ cm}^{-3}$  is the average particle number concentration,

$\Delta M_{\text{VOC}}$  is measured by the ID-CIMS.

#### *Kinetic Branching Ratio*

The kinetic branching ratio for *m*-xylene oxidation products with AS seed particle and 19 ppb NH<sub>3</sub> at 70% RH is calculated by,

$$\text{BR}_i = \frac{T_i}{T_1 + T_2 + T_3} \quad (19)$$

where  $i = 1, 2, \text{ or } 3$ ,  $T_1$ ,  $T_2$ , and  $T_3$  denote the first-order rate constant for wall loss ( $= k_w$ ), reactive uptake ( $= \frac{1}{4}\gamma\bar{c}S$ ), and OH oxidation ( $= k_{OH}[OH]_{ss}$ ).

## Results and Discussion

### *Multi-generation SOA formation*

To evaluate the SOA formation from the oxidation products of *m*-xylene, we first measured the time-dependent concentrations of condensable oxidized organics in the gas-phase using an ID-CIMS. The formation of the gas-phase products follows the sequence of oxidation by OH with three major generations (Figure 35a and Figure 36). The first-generation products (P1) include dimethylphenol ( $m/z = 123$ ) and methylbenzaldehyde ( $m/z = 121$ ), which are produced from OH addition to the aromatic ring ( $\sim 96\%$ ) and hydrogen extraction ( $\sim 4\%$ ) from the methyl group, respectively.<sup>135</sup> The concentrations of P1 ascend immediately upon the initiation of photooxidation by ultraviolet light, reaching peak mixing ratios of 20 ppb for dimethylphenol and 8.8 ppb for methylbenzaldehyde (Figure 35b). The concentrations of P1 start to decrease after 70 min to 100 min, which reflects the conversion of P1 to later generation products as well as the loss to the chamber wall. The second-generation products (P2) consist of methylglyoxal ( $m/z = 73$ ), methylbutenedial ( $m/z = 99$ ), toluic acid ( $m/z = 137$ ), epoxide, and dimethylresorcinol (Figure 35c and Figure 36), which are produced from the subsequent reactions of the P1 with OH/HO<sub>2</sub>. The concentrations of P2 rise after those of P1, with peak mixing ratios ranging from 0.4 to 4 ppb (Figure 35c and Figure 37). The concentration of toluic acid rises later than those of dicarbonyls due to the slower rates for OH reacting with side chain than addition to the aromatic ring. The third-generation products (P3) contain mainly multi-functional organic acids, including pyruvic acid ( $m/z = 89$ ), 4-oxo-2-pentenic acid ( $m/z = 115$ ),

and 3-methyl-4-oxo-2-pentenoic acid ( $m/z = 129$ ), which are formed from the reactions of the P2 with OH. The concentrations of P3 increase monotonically after delays of around 10 min and reach mixing ratios ranging from sub-ppb to 4 ppb at  $t = 120$  min (Figure 1d). On the other hand, the concentration of *m*-xylene shows a continuous and exponential decay throughout the experiments from 1.94 to 1.36 ppm, and the steady-state concentration of OH is calculated to be  $2.1 \times 10^6$  molecules  $\text{cm}^{-3}$  (Figure 38).

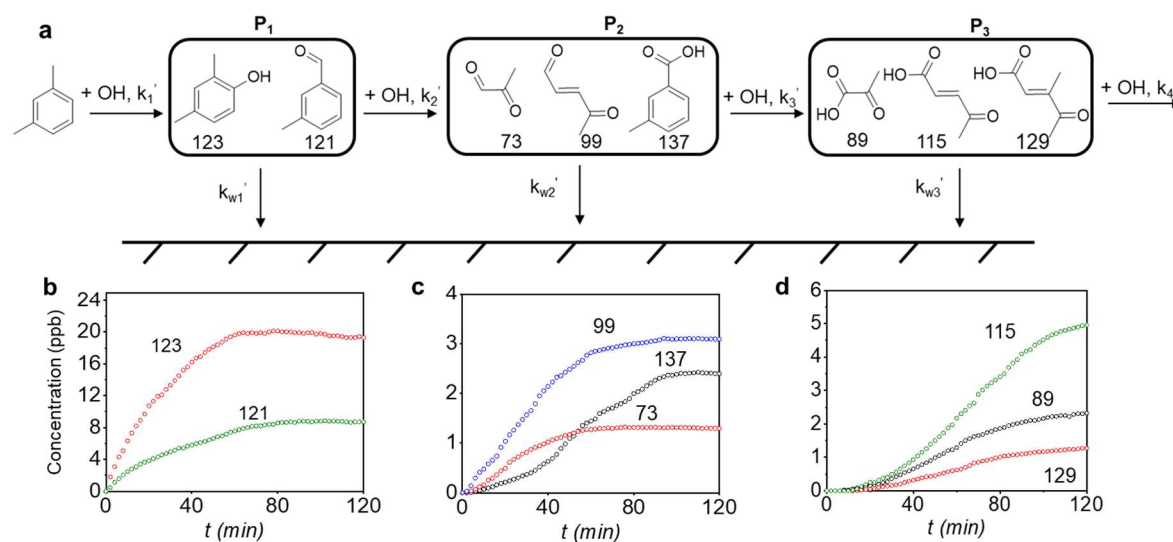


**Figure 35. Temporal evolution of gaseous products.** (a) Three-generation oxidation products (P1, P2, and P3) of *m*-xylene-OH photooxidation. The numbers denote the mass to charge ratio ( $m/z$ ). (b-d) Time-dependent gas-phase concentrations of P1 (b), P2 (c), and P3 (d) oxidation products. All experiments were carried out for  $(\text{NH}_4)_2\text{SO}_4$  seed particles with 19 ppb  $\text{NH}_3$  at 298 K and  $\text{RH} = 70\%$ .



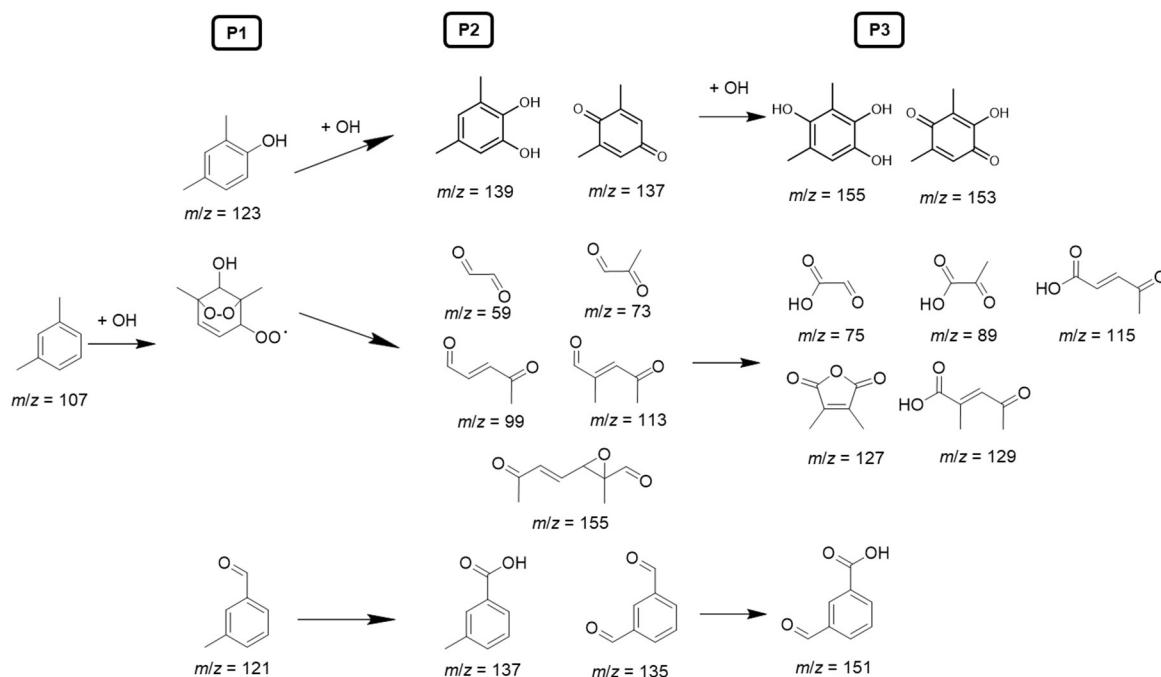


**Figure 36. Multi-generation products from *m*-xylene-OH photooxidation.** The letters of P1, P2, and P3 denote the products of first, second, and third generation of reactions with OH, respectively. The numbers denote the mass to charge ratio ( $m/z$ ).

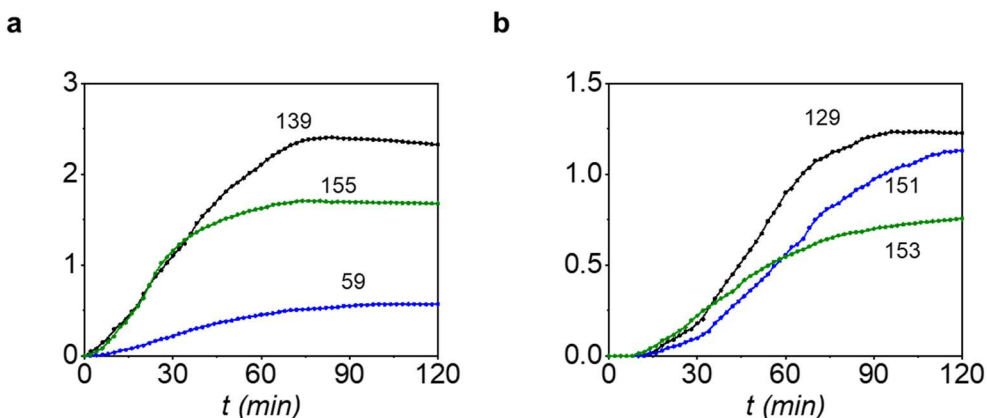


**Figure 37. Temporal evolutions of P2 (a) and P3 (b) concentrations from *m*-xylene oxidation.** The experiments were carried out on  $(\text{NH}_4)_2\text{SO}_4$  seed particles with 19 ppb  $\text{NH}_3$  and at 298 K and RH = 90%. Initiation of photooxidation by ultraviolet light occurred at  $t = 0$ .

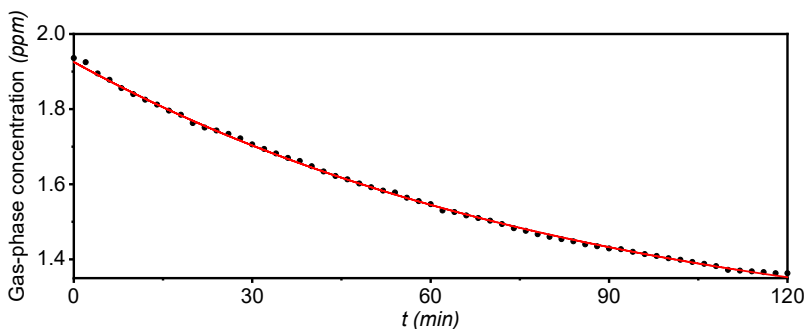


**Figure 38. Temporal evolutions of *m*-xylene under photooxidation.** The red solid line corresponds to exponential fitting of the *m*-xylene concentration. The initial concentration for *m*-xylene and the steady-state concentration for OH were 1.9 ppm and  $2.1 \times 10^6$  molecules  $\text{cm}^{-3}$ , respectively, with a bimolecular rate constant of  $2.4 \times 10^{-11}$   $\text{cm}^3$  molecule $^{-1}$  s $^{-1}$ . The experiments were carried out on  $(\text{NH}_4)_2\text{SO}_4$  seed particles with 19 ppb  $\text{NH}_3$  and at 298 K and RH = 90%. Initiation of photooxidation by ultraviolet light occurred at  $t = 0$ .

Furthermore, we measured time-dependent *GF*, *SSA*, and density of  $(\text{NH}_4)_2\text{SO}_4$  seed particles when exposed to *m*-xylene-OH oxidation products in the presence of 19 ppb  $\text{NH}_3$  (Figure 39a-c). The size growth factor, *GF*, increases monotonically upon initiation of photooxidation and reaches 2.41 at  $t = 120$  min (Figure 39a). The measurement of *SSA* shows a steady decline throughout the exposure and reaches  $(0.91 \pm 0.01)$  at  $t = 120$  min (Figure 39b), indicating the production of BrC. The total density decreases from  $1.77$   $\text{g cm}^{-3}$  to  $1.53$   $\text{g cm}^{-3}$  within the initial 10 min (with a corresponding *GF* of 1.24) and then increases steadily to  $1.7$   $\text{g cm}^{-3}$  at  $t = 120$  min. We derived the density for the SOA components on  $(\text{NH}_4)_2\text{SO}_4$  particles, which increases from  $1.28$   $\text{g cm}^{-3}$  at  $t = 10$  min to  $1.55$   $\text{g cm}^{-3}$  at  $t = 120$  min (Figure 39c). This density for *m*-xylene-derived SOA is higher than that of common organics reported previously ( $1.4$   $\text{g cm}^{-3}$ ).<sup>136</sup> The evolution in density clearly reflects variation in the chemical composition during particle growth, because of distinct material densities for the condensable oxidized organics from P2/P3 as well as the particle-phase oligomeric products. For example, the densities

of toluic acid, monomers of glyoxal and methylglyoxal, and imidazoles are 1.06, 1.05-1.27, and 1.03-1.23 g cm<sup>-3</sup>, respectively, while the densities for the oligomers of glyoxal and methylglyoxal reach 1.71-1.90 g cm<sup>-3</sup> (Table 7). The initial decline in the total density corresponds to a chemical composition dominated by organic acids and smaller oligomers from the P2, while the continuous increase in the SOA density is characteristic of increasing aqueous-phase reactions to yield larger oligomeric products (Figure 39d). In addition, the evolutions in the measured *GF* and density correlate closely with those of the P2 (including toluic acid and dicarbonyls) (Fig. 35c and Fig. 39a-c), confirming their contributions to the initial decline in the total particle density.

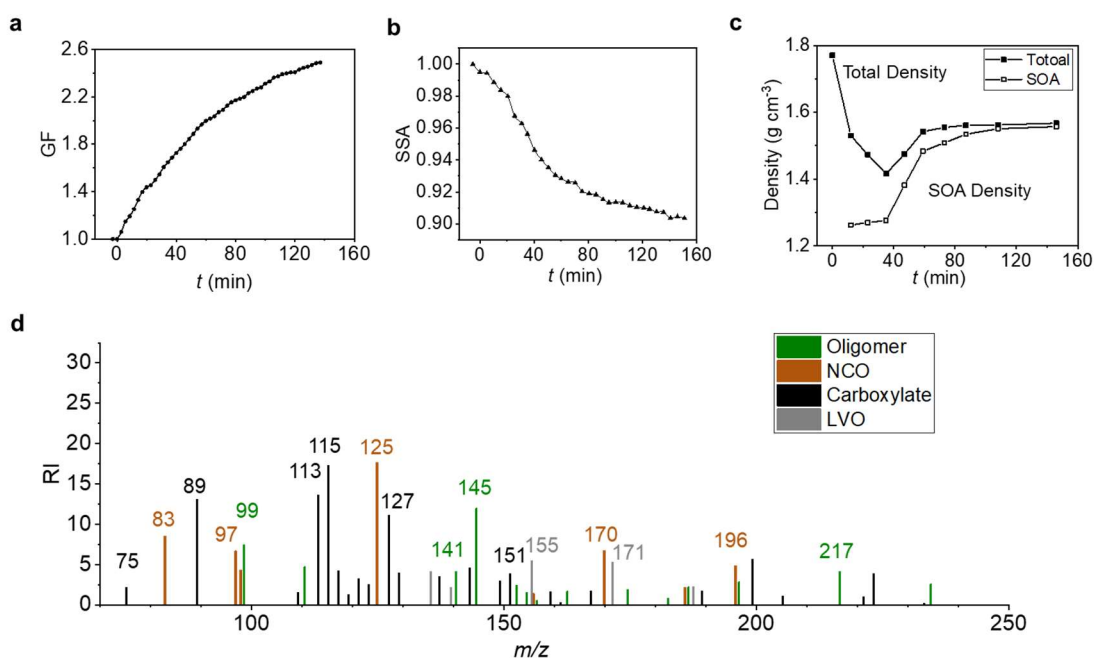


**Figure 39. Multigeneration SOA formation from *m*-xylene photooxidation.** (a-c) Time-dependent growth factor ( $GF = D_p/D_0$ , a), single scattering albedo (SSA, b), and densities (c, black solid line) of seed particles exposed to toluene oxidation products. The dashed line in (c) displays the calculated density for the SOA materials. (d) Chemical speciation of particle-phase products by TD-ID-CIMS. All experiments were carried out for  $(\text{NH}_4)_2\text{SO}_4$  seed particles with 19 ppb  $\text{NH}_3$  at 298 K and  $\text{RH} = 90\%$ .

To further unravel the identity of the condensable oxidized organics responsible for the measured  $GF$ ,  $SSA$ , and density, we analyzed the chemical compositions by collecting particles after 20-min exposure to *m*-xylene-OH oxidation using TD-ID-CIMS (Figure 39d). The composition measurements reveal the dominant abundances of three functional groups in the particle-phase, i.e., carboxylates, oligomers, and NCO, along with a small amount of LVO including dimethylresorcinol/benzoquinone. While the volatile P2 (i.e.,  $\alpha$ -dicarbonyls and  $\gamma$ -dicarbonyls) undergo particle-phase reactions to form oligomers (Figure 23), the P2/P3 (e.g., organic acids, epoxide, and dimethylresorcinol) engage in gas-particle partitioning or acid-base reaction to form carboxylates. In addition,  $\alpha$ -dicarbonyls and  $\gamma$ -dicarbonyls react with  $\text{NH}_3$  to yield NCO, including nitrogen-heterocycles and nitrogen-heterochains (Figure 24), which are light-absorbing BrC. Our measured SSA (0.91 at  $t = 120$  min) is lower than another study of toluene-derived SOA, showing a decrease of SSA from 1 to 0.94 within 180 min of in the presence of  $\text{NH}_3$ . This is explained by the higher yield of methylglyoxal from *m*-xylene photooxidation (52%) than that of toluene (21%),<sup>137</sup> and methylglyoxal has been found to produce BrC more efficiently via aqueous reaction than glyoxal.<sup>51</sup> Assuming comparable sensitivity to proton-transfer reactions for the particle-phase organics,<sup>123</sup> we estimated the contributions of oligomers, NCO, carboxylates, and LVO to the total SOA formation from the measured mass intensities, with the values of 22%, 23%, 47%, and 8%, respectively (Table 16).

**Table 16. The percent contributions of condensable organic species from *m*-xylene-OH oxidation to the particle-phase mass intensity.** GL: glyoxal, MG: methylglyoxal, GL+MG: cross-reaction of glyoxal and methylglyoxal. Note that the cross-reaction products of  $\gamma$ -carbonyls/tricarbonyls with  $\alpha$ -dicarbonyls are summed into the contribution of  $\gamma$ -carbonyls/tricarbonyls. The experiments were carried on  $(\text{NH}_4)_2\text{SO}_4$  seed particle with 19 ppb of  $\text{NH}_3$ .

Condensable oxidized organics	Contribution		
	Oligomerization	NCO formation	Total
GL	3%	3%	6%
MG	10%	12%	22%
$\gamma$ -dicarbonyls	7%	8%	15%
epoxide	2%	0.3%	2%
Carboxylates			47%
LVO			8%

#### *Effects of Seed Particles and $\text{NH}_3$ Concentration*

Among the different seed particles,  $(\text{NH}_4)_2\text{SO}_4$  in the presence of  $\text{NH}_3$  exhibits the largest *GF* and lowest *SSA* at  $t = 120$  min (Figure 40a), because of efficient oligomer and NCO production. The dependences of the measured *GF*, *SSA*, and density on the different seed particles are explainable by the mechanisms leading to the formation of the observed particle-phase products (Figure 40d). Di-carbonyls engage in oligomerization, which is mediated by carbenium ions.<sup>70</sup> Protonation, hydration, and deprotonation of di-carbonyls produce carbenium ions and diols/tetrols, and subsequent nucleophilic addition to the carbenium cation by the negative hydroxyl O-atom of diols/tetrols or the negative N-atom of  $\text{NH}_3$  results in the formation of oligomers and NCO, respectively. While carbenium ion formation is favored under acidic conditions, high proton concentration inhibits hydration and deprotonation to form diols/tetrols, resulting in most efficient oligomerization under moderate acidic condition (i.e., on  $(\text{NH}_4)_2\text{SO}_4$  particles with  $\text{NH}_3$ ). Also, oligomerization is likely promoted by an electric field on  $(\text{NH}_4)_2\text{SO}_4$ , because of net charge

separation from ion distributions at the interface.<sup>52</sup> The interfacial electric field is positive and the strongest for  $(\text{NH}_4)_2\text{SO}_4$  solutions and is likely enhanced on sub-micrometer particles due to high ionic strength. A positive electric field exerts interfacial attraction to the carbonyl and carboxylic functional groups, which possess negatively charged characteristics.<sup>52</sup> Hence, the most efficient nucleophilic addition involving the carbenium ions and the strongest interfacial attraction jointly explain the largest  $GF$  and highest intensities for oligomers and NCO on  $(\text{NH}_4)_2\text{SO}_4$  particles with  $\text{NH}_3$ . Recent measurements of SOA and BrC formation from glyoxal and methylglyoxal showed that the formation of oligomers and NCOs occurs over a wide acidity range,<sup>26</sup> consistent with our present results. On the other hand, gas-particle partitioning of organic acids likely includes ionic dissociation to form carboxylates or acid-base reactions to form ammonium/sodium carboxylates in the presence of  $\text{NH}_3/\text{NaCl}$ , as evident from the increasing carboxylate intensity.

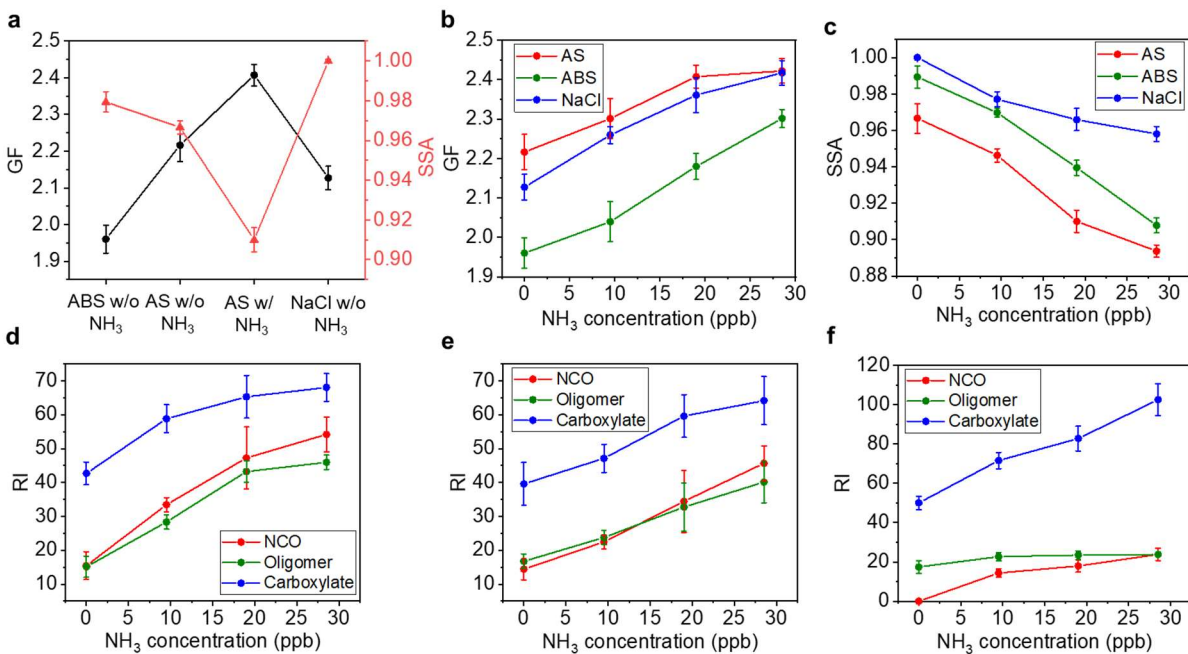


**Figure 40. Variation in SOA growth with seed particles and  $\text{NH}_3$  concentration.** (a)  $GF$  (black) and  $SSA$  (red) at 90 mins of exposure for  $(\text{NH}_4)_2\text{SO}_4$  particles in the presence (AS w/  $\text{NH}_3$ ) and absence (AS w/o  $\text{NH}_3$ ) of 19 ppb  $\text{NH}_3$  and for  $\text{NH}_4\text{HSO}_4$  (ABS) and NaCl particles in the absence of  $\text{NH}_3$ . (b,c) growth factor (b) and  $SSA$  (c) at  $t = 120$  min with varying  $\text{NH}_3$  concentration between 0 and 27 ppb for AS (red), ABS (green), and NaCl (blue) seed particles. (d-f) Particle-phase mass relative intensity (RI) for NCO (red), oligomers (green), and carboxylates (blue) on AS (d), ABS (e), and NaCl (f) seed particles. The error bar denotes  $1\sigma$  of 3 replicated measurements.

**Table 17. SOA mass yield (%) from *m*-xylene-OH oxidation.**

$\text{NH}_3$ (ppb)	RH (%)	Aerosol mass yield (%)		
		AS	ABS	NaCl
0	70	3.6	2.4	3.2
9.5	70	4.2	2.8	3.9
19	10	10.7	6.6	15.7
19	30	6.5	4.9	7.2
19	50	6.5	4	5.7
19	70	4.8	3.5	4.5
28.5	70	4.8	4.2	4.8

We further examined the dependence of  $GF$ ,  $SSA$ , and chemical composition on gaseous  $NH_3$  (Figure 40b-f). For all three types of seed particles,  $GF$  increases while  $SSA$  decreases with  $NH_3$  concentration from 0 to 27 ppb (Figure 40b,c). These dependences of  $GF$  and  $SSA$  on  $NH_3$  are explained by aqueous reactions of  $NH_3$  with dicarbonyls to form NCO and with organic acids to form ammonium carboxylates. The calculated SOA mass yields at 70% RH increase from 3.6% to 4.8% for AS, from 2.4% to 4.2% for ABS, and 3.2% to 4.8% for NaCl with increasing  $NH_3$  concentration from 0 to 28.5 ppb. Analysis of the particle composition confirms that oligomers, NCO and carboxylates increase with  $NH_3$  (Figure 40d-f). For AS and ABS, gaseous  $NH_3$  increase the pH of seed particles by shifting the equilibrium  $NH_3(g) \leftrightarrow NH_3 \cdot H_2O(aq) \leftrightarrow NH_4^+(aq) + OH^-(aq)$  to the right side, which results in weakly acid solution favoring oligomerization (Figure 40d,e). In addition,  $NH_3$  involves in the aqueous reaction with dicarbonyls to form NCO, which further increase the SOA yield and light absorption. On the other hand, increasing  $NH_3$  significantly increases the carboxylate formation on NaCl particles due to the reaction between carboxylic acid with  $NH_3 \cdot H_2O$  under alkaline condition (Figure 40f).

### *Effects of RH*

Since RH is one of the most significant physical parameters affecting SOA formation especially multiphase reactions, we carried out additional experiments by varying RH from 10% to 70% (Figure 41). Comparison of the measured evolutions in  $GF$ , particle-phase composition,  $SSA$ , and density shows noticeable RH effects. The particle growth factor decreases with increasing RH from  $(3.10 \pm 0.06)$  at RH = 10% to  $(2.41 \pm 0.03)$  at RH = 70% (Figure 41a). The impact of RH on SOA formation is further depicted by the calculated SOA yields (Table 17). SOA mass yield



decreases from 10.7% to 4.8% for AS, 6.6% to 3.5% for ABS, 15.7% to 4.5% for NaCl with increasing RH from 10% to 70% in the presence of 19 ppb NH<sub>3</sub>. The decreasing SOA yield at increasing RH is consistent with previous studies showing that SOA yield decreases from 16.5% to 3.2% with increasing RH from 14% to 79%.<sup>132</sup> For the particle-phase chemical composition, carboxylates represent the dominant particle-phase products (85% to 47%), while the contributions of oligomers and NCO become significant under high RH (Figure 41a). With increasing RH from 10% to 70%, the contributions to the total SOA formation consecutively increase and decrease for oligomers/NCO and carboxylates, respectively, while the fraction for LVO is nearly invariant (Table 18). Such a RH dependence is related to gas-particle partitioning, aqueous reactions, and wall-loss of the oxidation products. For (NH<sub>4</sub>)<sub>2</sub>SO<sub>4</sub> particles, the deliquescent and efflorescent points occur, respectively, at 80% and 36% RH.<sup>1</sup> At low RH (10% and 30%), aqueous reactions to yield oligomers/NCO are considerably suppressed below the efflorescent point, attributable to hindered protonation, hydration, and deprotonation of di-carbonyls. On the other hand, particles consisting of organic acids retain water even at very low RH,<sup>138</sup> which facilitates the formation of carboxylates via ionic dissociation or acid-base reactions below the efflorescent point. The equilibrium vapor pressures for LVOs are much lower than those for organic acids (Table 13), indicating efficient condensation for LVOs. Additionally, wall-loss of the precursors for oligomers, NCO, and carboxylates are more pronounced at high RH, as evident from the measured concentrations of the various condensable oxidized organics. Wall-loss is 1.3 to 4.3 times more efficient at 90% RH than at 10% RH, leading to reduced gaseous concentrations of the condensable oxidized organics at high RH (Table 14). The larger wall loss at higher RH is explained by increasing aqueous reactions of reactive gases onto the Teflon chamber wall via oligomerization

(for dicarbonyls) and acid-base reaction (for organic acids). As a result, the measured GF decreases with increasing RH.

**Table 18. Relative contributions of condensable oxidized organics to SOA formation on (NH<sub>4</sub>)<sub>2</sub>SO<sub>4</sub> seed particles with 19 ppb NH<sub>3</sub> and at 10% - 70% RH.**

Functionality	SOA Contribution (%)			
	RH (%)			
	10	30	50	70
Di-carbonyls	2	5	15	20
Di-carbonyls+NH <sub>3</sub>	2	4	16	23
Carboxylates	85	80	58	47
LVO	8	8	8	8

The measured SSA at  $t = 120$  min is equal to unity at 10% and 30% RH and decreases with increasing RH (Figure 41b), which is in accordance with the negligible formation of NCO at low RH but increasing formation of NCO with increasing RH above 50% in the aerosol phase. Also, in contrast to an initial decrease but subsequent increase in total density at 70% RH, the total density decreases monotonically at 10% RH (Figure 41c). The calculated density for the SOA materials increases slightly with reaction time at 10% RH, i.e., from 1.27 to 1.39 g cm<sup>-3</sup> (Figure 4c), compared to a much larger increase from 1.26 to 1.55 g cm<sup>-3</sup> at 90% RH (Figure 39c). These differences in the particle agree with the fact that high density oligomer contribute negligibly while carboxylic acid contribute dominantly to SOA at low RH. The normalized particle growth exhibits a significant initial hysteresis of about 15 min compared to that at 90% RH (Figure 41d). This is explained by the delayed formation of later generation products (i.e., P3). Specifically, SOA formation at high RH is contributed by both P2 (e.g., dicarbonyls) and P3 (i.e., as pyruvic acid and 4-oxo-2-pentenic acid) from *m*-xylene photooxidation. Seed particles start to growth with the rise of P2 concentration. In contrast, SOA formation at low RH is dominantly contributed by P3, whose

concentration starts to increase after around 10 min. As a result, the growth of particles is delayed for about 15 min at low RH.

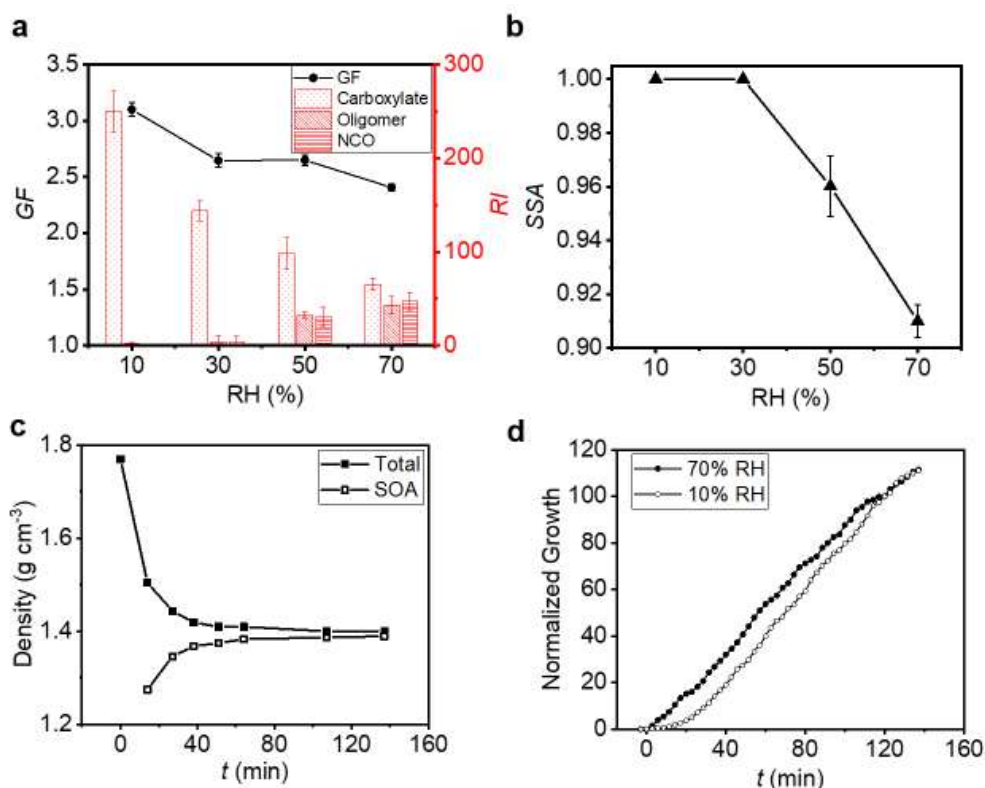


**Figure 41. RH dependence of SOA formation.** (a) *GF* (black circle) and particle-phase intensities of carboxylates (left column), oligomers (middle column), and NCO (right column) with varying RH between 10% and 70%. The number corresponds to the percent contribution (%) to the total observed mass intensity. (b) SSA with varying RH between 10% and 70% for  $(\text{NH}_4)_2\text{SO}_4$  seed particle with 19 ppb  $\text{NH}_3$ . (c) Time-dependent particle density (solid square) and SOA density (open square) at RH = 10% for  $(\text{NH}_4)_2\text{SO}_4$  seed particles with 19 ppb  $\text{NH}_3$ . (d) Comparison between time-dependent normalized growth at RH = 70% (solid circle) and RH = 10% (open circle) for  $(\text{NH}_4)_2\text{SO}_4$  seed particles with 19 ppb  $\text{NH}_3$ . All experiments correspond to  $(\text{NH}_4)_2\text{SO}_4$  seed particles with 19 ppb  $\text{NH}_3$ . Initiation of photooxidation by ultraviolet light occurred at  $t = 0$ . The error bar denotes the standard deviation of 3 repeated measurements.

### *Effects of NO<sub>x</sub> concentration*

To evaluate the effects of NO<sub>x</sub> on SOA formation from toluene oxidation, we performed additional experiments by using (NH<sub>4</sub>)<sub>2</sub>SO<sub>4</sub> seed particles and varying initial NO<sub>x</sub> concentrations from 0 to 500 ppb (Figure 42). Measurements of the time-dependent gas-phase concentrations show the formation of three major nitrophenols from NO<sub>2</sub> addition to OH-toluene adduct in the presence of NO<sub>x</sub>, i.e., 4-methyl-2-nitrophenol ( $m/z = 154$ ), dimethyl nitrophenol ( $m/z = 168$ ), and dimethyl 4-nitrocatechol ( $m/z = 184$ ) (Figure 42a). The evolution in the gas-phase concentrations clearly illustrates multi-generation production of nitrophenols. The concentrations of the first-generation nitrophenols (i.e., 4-methyl-2-nitrophenol and dimethyl nitrophenol) increase instantaneously upon initiation of photooxidation, while the second generation nitrophenol (i.e., dimethyl 4-nitrocatechol) appears with a significant delay of about 20 min. The production of nitrophenols is much smaller than those for dicarbonyls and organic acids from toluene oxidation, consistent with a small yield of less than 7% under high-NO<sub>x</sub> conditions.<sup>56</sup> At a constant RH level (70%), the *GF* values on (NH<sub>4</sub>)<sub>2</sub>SO<sub>4</sub> seed particles in the presence of NH<sub>3</sub> decreases monotonically from  $2.41 \pm 0.03$  to  $2.18 \pm 0.03$  with the NO<sub>x</sub> concentrations from 0 to 500 ppb (Figure 42b). The SSA decreases significantly from  $0.911 \pm 0.006$  to  $0.839 \pm 0.003$  with increasing NO<sub>x</sub> concentration from 0 to 500 ppb, which is explained by the formation of light absorbing nitrophenol species. Analysis of the particle composition reveals that the decreasing size growth with increasing NO<sub>x</sub> concentration correlates with simultaneous decreases of carboxylates, oligomers, and NCOs but an increase of nitrophenols in the particle-phase (Figure 42d). The contribution of nitrophenols to SOA formation is estimated to range from 3% to 6% and is the largest from dimethyl nitrophenol. The effects of NO<sub>x</sub> on toluene oxidation include the production of nitrophenols and cycling between RO<sub>2</sub> and RO radicals, impacting the product distributions for

the condensable oxidized organics. Specifically, the presence of  $\text{NO}_x$  alters the competing  $\text{RO}_2$  reactions, and formation of nitrophenols decreases the production of dicarbonyls and organic acids, as reflected by decreased oligomers, NCOs, and carboxylates in the particle-phase with increasing  $\text{NO}_x$ .

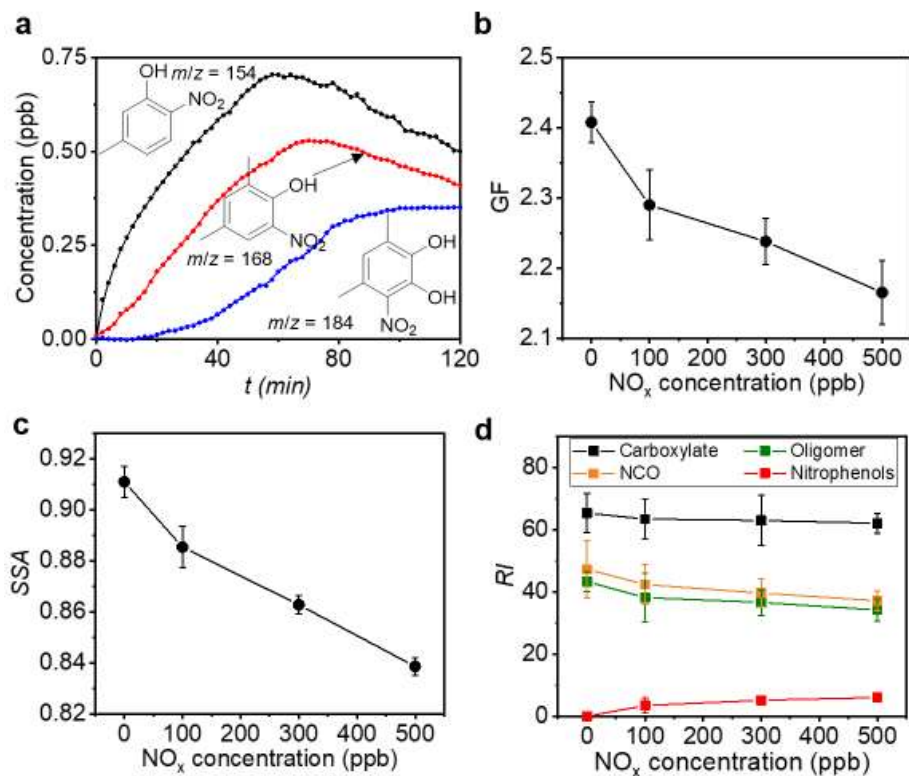


**Figure 42. The effects of  $\text{NO}_x$  on SOA formation from toluene oxidation.** (a) Time-dependent gas-phase concentrations of 5-methyl-2-nitrophenol (black,  $m/z = 154$ ), dimethyl nitrophenol (red,  $m/z = 168$ ), and dihydroxy nitrotoluene (blue,  $m/z = 184$ ). The numbers denote the mass to charge ratio ( $m/z$ ). (b,c) Dependence of  $GF$  (b) and  $SSA$  (c) at  $t = 90$  min on  $\text{NO}_x$  concentration for  $(\text{NH}_4)_2\text{SO}_4$  seed particles with 19 ppb  $\text{NH}_3$  at  $\text{RH} = 70\%$ . (d) Particle-phase relative mass intensities ( $RI$ ) for carboxylates (black), oligomers (green), NCO (brown), and nitrophenols (red) with varying initial  $\text{NO}_x$  concentration for  $(\text{NH}_4)_2\text{SO}_4$  seed particles with 19 ppb  $\text{NH}_3$  at  $\text{RH} = 70\%$ . Initiation of photooxidation by ultraviolet light occurred at  $t = 0$ . The error bar denotes  $1\sigma$  of 3 replicated measurements.

### *Functionality-based SOA formation*

Our results show that the condensable oxidized organics from *m*-xylene photooxidation contribute distinctly to SOA formation based on their functionalities (Figure 43a). The photooxidation of *m*-xylene yields multigeneration products (P1~Pn) with diverse and increasing functionalities. P1 consists of COOs with phenol or aldehyde functionality which are not engaged in aerosol-phase reactions and readily evaporate into the gas-phase. P2 consists of mainly dicarbonyls as well as a small amount of carboxylic acid and epoxide. Dicarbonyls contain two negatively charged carbonyl O-atoms to provide the protonation sites. The conjugated carbonyl functional groups of dicarbonyls allow for efficient resonance stabilization of carbenium ions after protonation. Carbenium ions readily undergo nucleophilic addition to yield large oligomers or NCO (Figure 43a). Formation of oligomers and NCO from dicarbonyls takes place efficiently above the efflorescent point at high RH. P3 consists of primarily carboxylic acids. Carboxylic acids possess a carbonyl group and a hydroxyl group. Deprotonation of the hydroxy group of carboxylic acids occurs via ionic dissociation or acid-base reactions (with NH<sub>3</sub>, amines, or Cl<sup>-</sup>) under weakly acidic to neutral conditions to yield carboxylates. Gas-particle partitioning for organic acids occurs over a wide RH range (i.e., from 10 to 70%), though to a lesser extent at low RH. Condensation of organic acids is implausible because of their high equilibrium vapor pressures (Table 13), and the occurrence of gas-particle partitioning implicates a critical role of H<sub>2</sub>O in stabilizing organic acids, by facilitating carboxylate formation. Further oxidation of P3 produces COOs with multifunctional groups including hydroxy, carbonyl, and carboxylic acid functionalities. For example, LVOs contains multiple hydroxy groups have very low volatilities and tend to condense to the aerosol phase. Also, there is negligible contribution to SOA formation

from HOMs, likely due to its negligible yield from *m*-xylene photooxidation.<sup>111</sup> Specifically, we detected no measurable signals associated with HOMs both in the gas and particle phases.

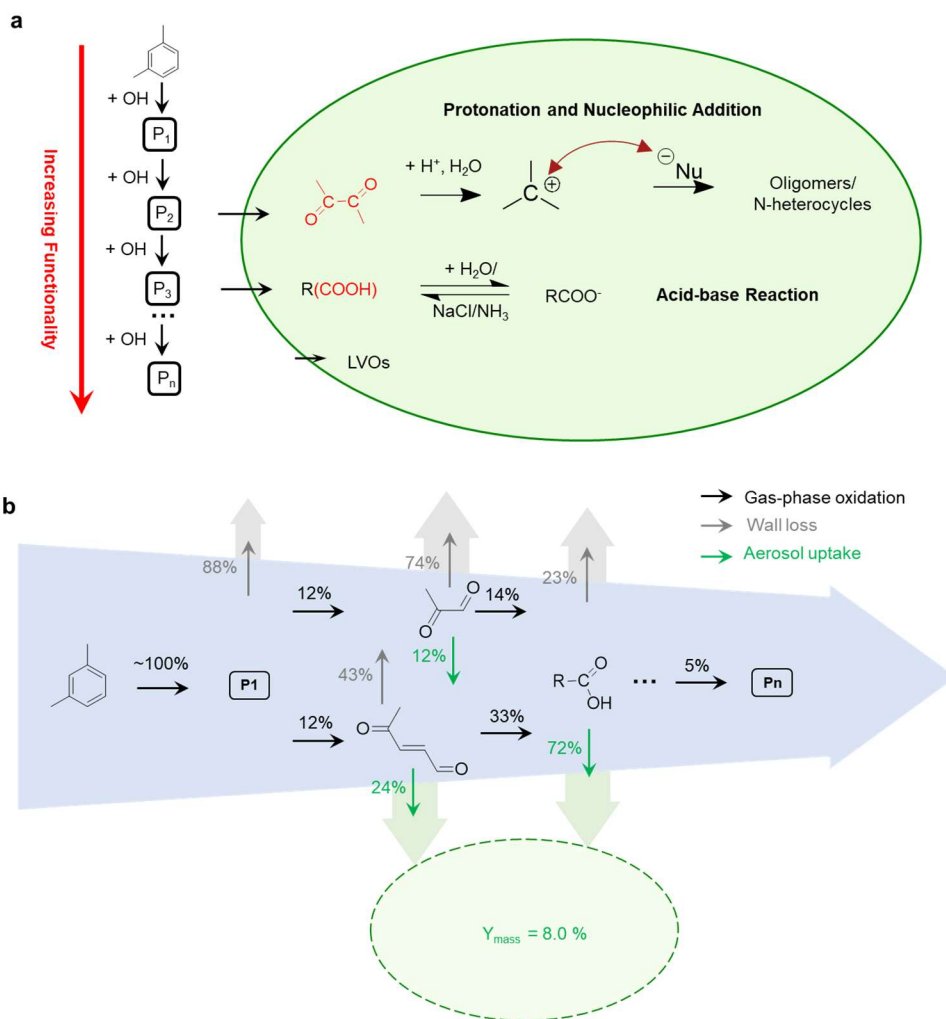


**Figure 43. Functionality-based SOA formation from *m*-xylene photooxidation.** (a) Multi-generation SOA formation from toluene-OH oxidation. The red arrow connects the sites for nucleophilic addition. Initiation of photooxidation by ultraviolet light occurred at  $t = 0$ . (b) Kinetic branching ratio of representative oxidation products. The black, gray, and green arrows stand for the pathways for gas-phase oxidation, wall loss, and uptake to aerosols, respectively. The number denotes the branching ratio to each pathway.

The measured size growth of particles and the corresponding gas-phase concentrations of the condensable oxidized organics were employed to derive the uptake coefficient on ammonium sulfate in the presence of 19 ppb NH<sub>3</sub> at 10% and 90% RH (Table 19). The  $\gamma$  values for dicarbonyls are the highest (from  $3 \times 10^{-3}$  to  $1.2 \times 10^{-2}$ ) at 90% RH but are significantly reduced (from  $3.4 \times 10^{-4}$  to  $9.0 \times 10^{-4}$ ) at 10% RH, while the  $\gamma$  values for organic acids and LVOs are only slightly higher at 90% RH. The measured  $\gamma$  appears to correlate with the acid dissociation constant ( $K_a$ ) and solubility among the organic acids, i.e., being the highest for pyruvic acid and the lowest for benzoic acid.

To simulate SOA yields with the measured uptake coefficients, we calculated the kinetic branching ratio for P1, P2, and P3 with AS seed particle in the presence of 19 ppb NH<sub>3</sub> at 70% RH. 88% of P1 is subjected to wall loss while 12% of P1 is further oxidized to produce P2. Methylglyoxal and methylbutenedial are taken as two surrogates for P2. For methylglyoxal, 74% is lost to the chamber wall, 12% contributes to SOA formation via reactive uptake, and 14% goes towards further oxidation. For methylbutenedial, 43% is subjected to wall loss, 24% contributes to SOA formation, and 33% is further oxidized. 4-Oxo-2-pentenoic acid is taken as the surrogate for P3, of which 23% is lost to the chamber wall, 72% forms SOA, and 5% is oxidized. Assuming that all the gas-phase COOs are completely converted (i.e., by wall loss, reactive uptake or oxidation), the overall SOA yield is 8.0%. In our study, the remaining gas-phase COOs at 120 min is 28 ppb, 6.4 ppb (0.9 ppb for methylglyoxal and 5.5 ppb for methylbutenedial), 8.6 ppb for P1, P2, and P3, respectively, which correspond to 41% of reacted *m*-xylene not completely converted. As a result, the estimated SOA yield is 4.7% on AS in the presence of 19 ppb NH<sub>3</sub> at 70% RH, which is comparable to the measured yield of 4.8% (by  $\pm 6\%$ ).



**Table 19. Measured uptake coefficient ( $\gamma$ ) for condensable oxidized organics on ammonium sulfate seed particles in the presence of ammonia.** The uncertainty in the calculated  $\gamma$  reflects the combined random errors in the measured five parameters, i.e.,  $D_o$  = initial diameter,  $D_p$  = final diameter after the exposure time of  $dt$ ,  $N$  = the particle number concentration,  $S$  = average particle surface area, and  $[A]$  = average concentration of species A. FR = percent contributions to the particle-phase mass intensity (Table S2). For each parameter, an uncertainty is estimated, corresponding to  $1\sigma$  of at least 3 measurements.

Species	$D_o$ (nm)	$D_p$ (nm)	$N$ (cm <sup>-3</sup> )	$S$ (10 <sup>-5</sup> cm <sup>2</sup> cm <sup>-3</sup> )	$[A]$ (ppb)	FR	$\gamma$ (10 <sup>-3</sup> )
<b>RH = 90%</b>							
Glyoxal	100.0	256.0	15000	1.55	1.9	13%	8.3 ± 2.0
Methylglyoxal	100.0	256.0	15000	1.55	0.9	10%	12 ± 2.8
$\gamma$ -Dicarbonyls	100.0	256.0	15000	1.55	3.1	10%	3.0 ± 0.6
Benzoic acid	100.0	256.0	15000	1.55	0.9	0.9%	0.84 ± 0.11
4-Oxo-2-pentenoic acid	100.0	256.0	15000	1.55	1.9	4.8%	2.2 ± 0.4
Pyruvic acid	100.0	256.0	15000	1.55	0.9	2.6%	2.9 ± 0.3
LVO	100.0	256.0	15000	1.55	1.2	8.0%	5.0 ± 1.5
Nitrophenol*	100.0	246.0	15000	1.46	1.4	3.1%	1.6 ± 0.3
<b>RH = 10%</b>							
Glyoxal	100.0	260.0	15000	0.85	5.4	1.9%	0.75 ± 0.18
Methylglyoxal	100.0	260.0	15000	0.85	3.2	1.5%	0.90 ± 0.20
$\gamma$ -Dicarbonyls	100.0	260.0	15000	0.85	9.6	2.0%	0.34 ± 0.07
Benzoic acid	100.0	260.0	15000	0.85	2.0	1.1%	0.80 ± 0.14
4-Oxo-2-pentenoic acid	100.0	260.0	15000	0.85	6.8	9.1%	2.0 ± 0.5
Pyruvic acid	100.0	260.0	15000	0.85	3.6	5.3%	2.5 ± 0.4
LVO	100.0	260.0	15000	0.85	2.9	9.4%	4.2 ± 1.5
Nitrophenol*	100.0	253.5	15000	0.82	2.3	3.0%	1.6 ± 0.3

\* Measured in the presence of 100 ppb NO<sub>x</sub>

### *Comparison between SOA Formation from Toluene and m-Xylene*

There exist notable similarities and differences between the SOA formation from photooxidation of *m*-xylene and toluene (in Chapter III). The SOA formations from both precursors are contributed mainly by dicarbonyls at high RH and carboxylic acids as well as LVOs in a wide RH range. The measured uptake coefficients for the condensable oxidized organics from two precursors are comparable (within  $\pm 20\%$ ). This indicates that the measured uptake coefficients are applicable to assess the SOA formation from various aromatic VOCs.

On the other hand, the photooxidation of *m*-xylene is much faster than that of toluene (with the rate constant for *m*-xylene with OH nearly four times higher than that of toluene).<sup>128</sup> Higher photooxidation rate leads to more rapid formation of P2/P3, resulting in an earlier increase of particle diameters (Figure 39a) for *m*-xylene oxidation compared to the 5-min delay of particle growth for toluene oxidation. Also, the faster oxidation rate of *m*-xylene photooxidation leads to more production of later generation products (i.e., carboxylic acids) and higher contribution of carboxylates (47%) to SOA formation than that of toluene (40%). In addition, the yield of methylglyoxal is significantly higher from *m*-xylene photooxidation (~52%) than that of toluene oxidation (~21%).<sup>137</sup> Methylglyoxal is more reactive than glyoxal in aqueous reaction to form oligomers and NCO.<sup>26</sup> Higher yield of methylglyoxal from *m*-xylene oxidation results in more efficient SOA formation and browning than that of toluene under comparable precursor and oxidant concentrations (Figure 39).

### *Atmospheric Implications*

In summary, we show that SOA formation from *m*-xylene-OH oxidation is primarily from COOs with dicarbonyls and carboxylic acid functionalities, due to their prompt production and

large yields from *m*-xylene oxidation. The functionality of COOs largely determines their reactivity in the aerosol-phase. Dicarboxyls undergo oligomerization to form oligomers/NCO at RH above efflorescence point and carboxylic acids engage in ionic dissociation or acid-base reaction to form the carboxylates at wide RH range. The measured reactive uptake coefficients for COOs are dependent on their functionalities and consistent with those derived from SOA formation by toluene-OH oxidation. The measured uptake coefficients for each functionality allow for quantifying the contribution of multiphase reactions to SOA formation and likely applicable to the various VOCs precursors.

In our work, the OH concentration is comparable to the ambient level, while the *m*-xylene concentration and the reaction time are higher and shorter, respectively, than those of typical atmospheric conditions. Production of the condensable oxidized organics in the atmosphere is dependent on the types/abundances of VOCs as well as the extent of oxidation (i.e., the intensity of solar radiation and the reaction time).<sup>110</sup> Our experimental results provide explanations for large SOA formation under polluted environments.<sup>92</sup> For example, recent measurements revealed that hygroscopicity for the SOA component resembles those of organic acids, alkylammonium carboxylates, and ammonium carboxylates on clean days with low RH but those of glyoxal and methylglyoxal oligomers on polluted days with high RH,<sup>125</sup> consistent with our observed trends for the contributions of organic acids and oligomers/NCOs to SOA formation at low and high RH conditions, respectively. Our findings of SOA formation from *m*-xylene oxidation reconcile atmospheric measurements of explosive SOA growth under polluted urban conditions<sup>17</sup> and underscore the importance for understanding multi-generation production of condensable oxidized organics and the relationship between the functionality and particle-phase reactivity.

CHAPTER V  
UNDERSTANDING THE ROLE OF AEROSOL IN THE TRANSMISSION FOR THE  
COVID-19 PANDEMIC\*

**Introduction**

The novel coronavirus outbreak, coronavirus disease 2019 (COVID-19), which was declared a pandemic by the World Health Organization (WHO) on March 11, 2020, has infected over 160 million people and caused nearly 3.5 million fatalities globally.<sup>139</sup> Intensive effort is ongoing worldwide to establish effective treatments and develop a vaccine for the disease. The novel coronavirus, named as severe acute respiratory syndrome coronavirus 2 (SARS-CoV-2), belongs to the family of the pathogen that is responsible for respiratory illness linked to the 2002–2003 outbreak (SARS-CoV-1).<sup>140</sup> The enveloped virus contains a positive-sense single-stranded RNA genome and a nucleocapsid of helical symmetry of ~120 nm. There exist several plausible pathways for viruses to be transmitted from person to person. Human atomization of virus-bearing particles occurs from coughing/sneezing and even from normal breathing/talking by an infected person.<sup>141–143</sup> These mechanisms of viral shedding produce large droplets and small aerosols, which are conventionally delineated at a size of 5 µm to characterize their distinct dispersion efficiencies and residence times in air as well as the deposition patterns along the human respiratory tract.<sup>4,141</sup> Virus transmission occurs via direct (deposited on persons) or indirect (deposited on objects) contact and airborne (droplets and aerosols) routes. Large droplets readily

---

\* Part of this chapter is reprinted with permission from Li, Y.; Zhang, R.; Zhao, J.; Molina, M. J. Understanding Transmission, and Intervention for the COVID-19 Pandemic in the United States. *Sci. Total Environ.* **2020**, *748*, 141560. Copyright 2020 Elsevier B.V. Part of this chapter is reprinted with permission from Zhang, R.; Li, Y.; Zhang, A. L.; Wang, Y.; Molina, M. J. Identifying Airborne Transmission as the Dominant Route for the Spread of COVID-19. *Proc. Natl. Acad. Sci.* **2020**, *117* (26), 14857 – 14863. Copyright 2020 National Academy of Sciences.

settle out of air to cause person/object contamination; in contrast, aerosols are efficiently dispersed in air. While transmission via direct or indirect contact occurs in a short range, airborne transmission via aerosols can occur over an extended distance and time. Inhaled virus-bearing aerosols deposit directly along the human respiratory tract.

Previous experimental and observational studies on interhuman transmission have indicated a significant role of aerosols in the transmission of many respiratory viruses, including influenza virus, SARS-CoV-1, and MERS-CoV.<sup>12-14</sup> For example, airborne coronavirus MERS-CoV exhibited strong capability of surviving, with about 64% of microorganisms remaining infectious 60 min after atomization at 25 °C and 79% RH.<sup>13</sup> On the other hand, rapid virus decay occurred, with only 5% survival over a 60-min procedure at 38 °C and 24% RH, indicative of inactivation. Recent experimental studies have examined the stability of SARS-CoV-2, showing that the virus remains infectious in aerosols for hours and on surfaces up to days.<sup>144</sup>

Several parameters likely influence the microorganism survival and delivery in air, including temperature, humidity, microbial resistance to external physical and biological stresses, and solar ultraviolet (UV) radiation.<sup>12</sup> Transmission and infectivity of airborne viruses are also dependent on the size and number concentration of inhaled aerosols, which regulate the amount (dose) and pattern for respiratory deposition. With typical nasal breathing (i.e., at a velocity of  $\sim 1 \text{ m} \cdot \text{s}^{-1}$ ),<sup>142</sup> inhalation of airborne viruses leads to direct and continuous deposition into the human respiratory tract. In particular, fine aerosols penetrate deeply into the respiratory tract and even reach other vital organs.<sup>11</sup> In addition, viral shedding is dependent on the stages of infection and varies between symptomatic and asymptomatic carriers. A recent finding showed that the highest viral load in the upper respiratory tract occurs at the symptom onset, suggesting the peak of infectiousness on or before the symptom onset and substantial asymptomatic transmission for

SARS-CoV-2.<sup>145</sup> A study built on models of airborne disease transmission to derive the indoor airborne transmission rate of SARS-CoV-2 based on the rates of ventilation and air filtration, dimensions of the room, breathing rate, respiratory activity and face mask use of its occupants, and infectiousness of the respiratory aerosols.<sup>146</sup> Another epidemiologic modeling study showed that surgical masks are effective at preventing the transmission of SARS-CoV-2 as most environments and contacts are under conditions of low virus abundance and the respiratory particles can be largely reduced by masks.<sup>147</sup>

The COVID-19 outbreak is significantly more pronounced than that of the 2002/2003 SARS, and the disease continues to spread at an alarming rate worldwide, despite extreme measures taken by many countries to constrain the pandemic.<sup>139</sup> The enormous scope and magnitude of the COVID-19 outbreak reflect not only a highly contagious nature but also exceedingly efficient transmission for SARS-CoV-2. Currently, the mechanisms to spread the virus remain uncertain, particularly considering the relative contribution of the contact vs. airborne transmission routes to this global pandemic.

To gain insight into the role of aerosols in infectious virus transmission and assess the effectiveness of mitigation measures, we analyzed the trend of the pandemic and mitigation measures in Wuhan, Italy, NYC, and fifteen U.S. states from January 23 to May 18, 2020. Wuhan, Italy, and NYC represent the early epicenters for the pandemic and the cumulative confirmed infections and daily new confirmed cases in the fifteen states collectively account for about 78% of the total confirmed infections in the U.S. on May 18, 2020.

## Methods

### *Statistical analysis*

Statistical analysis was performed for the data of cumulative infections and daily new infections during each period using linear regression. The significance of the sub-exponential growth and subsequent linearity in the cumulative infections after stay-at-home orders for all fifteen states is reflected by the high correlation coefficients ( $R^2$  ranging from 0.935 to 0.995 for the sub-exponential growth and from 0.986 to 0.999 for the linear growth). While the  $R^2$  values in the daily new infections are low because of large fluctuations in the data, the slope of the regression reflects the trend in the data.

### *Projection of the difference in the total infections by face covering*

Projection of the pandemic trend without face covering was performed by establishing the linear correlation between the total confirmed cases ( $y$ ) and date ( $x$ ) prior to implementing this measure for each state, with the onset date as  $x = 0$ . We considered the data ranging from 15 to 30 days prior to implementing mandated face covering, dependent on the regression to achieve the highest correlation coefficients. The derived regression was used for the projections, considering the high correlation coefficients for the data prior to the onset of mandated face covering.

### *Estimation of the basic reproduction rate ( $R_0$ )*

The number of cumulative confirmed cases ( $N$ ) during the initial sub-exponential period (8 March to 12 April) is expressed as,

$$N = N_0 R_0^{t/\tau} \quad (20)$$

where  $N_0$  is the initial confirmed cases,  $t$  is the time in day, and  $\tau$  is the serial interval for COVID-19, which is determined to be  $(3.96 \pm 0.43)$  days.<sup>148</sup> In the logarithmic plot, this equation is expressed as,

$$\log_{10} N = \log_{10} N_0 + \frac{\log_{10} R_0}{\tau} t \quad (21)$$

The basic reproduction rate ( $R_0$ ) is calculated from,

$$R_0 = 10^{S\tau} \quad (22)$$

where  $S$  is the slope of exponential fitting of the initial period.

### *Data Sources*

The data for accumulative confirmed infections and fatalities in Wuhan, Italy, and NYC were taken from the reports by Wuhan Municipal Health Commission (<http://wjw.wuhan.gov.cn/>), European CDC (<https://www.ecdc.europa.eu/en>), and NYC government (<https://www1.nyc.gov/site/doh/covid/covid-19-data.page>), respectively. The data of accumulative confirmed infections and fatalities worldwide were taken from WHO COVID-19 situation report (<https://www.who.int/emergencies/diseases/novel-coronavirus-2019/situation-reports>),<sup>139</sup> and the numbers in China, Italy, and United States were from taken from European CDC.

The COVID-19 confirmed cases for California (CA), Florida (FL), Georgia (GA), Ohio (OHs), Texas (TX), Virginia (VA), Connecticut (CT), Massachusetts (MA), Michigan (MI), New Jersey (NJ), New York (NY), Pennsylvania (PA), Illinois (IL), Louisiana (LA), and Maryland (MD) were recorded from California Department of Public Health (<https://www.cdph.ca.gov/Programs/CID/DCDC/pages/immunization/ncov2019.aspx#COVID->



19%20by%20the%20Numbers), Florida Department of Health (<https://floridahealthcovid19.gov/#latest-stats>), Georgia Department of Public Health (<https://dph.georgia.gov/covid-19-daily-status-report>), Ohio Department of Health (<https://coronavirus.ohio.gov/wps/portal/gov/covid-19/dashboards/overview>), Texas Department of State Health Services (<https://dshs.texas.gov/coronavirus/>), Virginia Health Department (<https://www.vdh.virginia.gov/coronavirus/>), Connecticut government (<https://data.ct.gov/stories/s/COVID-19-data/wa3g-tfvc/>), Massachusetts Department of Public Health (<https://www.mass.gov/info-details/covid-19-response-reporting>), US CDC COVID Data Tracker (<https://www.cdc.gov/covid-data-tracker/#trends>), US CDC COVID Data Tracker (<https://www.cdc.gov/covid-data-tracker/#trends>), New York State Department of Health (<https://covid19tracker.health.ny.gov/views/NYS-COVID19-Tracker/NYSDOHCOVID-19Tracker-Map?%3Aembed=yes&%3Atoolbar=no&%3Atabs=n>), Pennsylvania Department of Health (<https://www.health.pa.gov/topics/disease/coronavirus/Pages/Coronavirus.aspx>), Illinois Department of Health (<https://www.dph.illinois.gov/covid19/covid19-statistics>), Louisiana Department of Health (<http://ldh.la.gov/Coronavirus/>), and Maryland Department of Health (<https://coronavirus.maryland.gov/>) daily at 6 pm ET.

Ground-based measurements of PM<sub>2.5</sub> and RH in Wuhan were taken from the China National Environmental Monitoring Centre (<http://beijingair.sinaapp.com/>). The PM<sub>2.5</sub> data in NYC were taken from US Environmental Protection Agency (<https://www.epa.gov/outdoor-air-quality-data>). The PM<sub>2.5</sub> data in Rome were taken were from Centro Regionale della Qualità dell'aria (<http://www.arpalazio.net/main/aria/>). The RH data in Rome and NYC were taken from the 6-hourly interim reanalysis of the European Centre for Medium-range Weather Forecasts (<https://www.ecmwf.int/en/forecasts/datasets/reanalysis-datasets/era5>).

## **Results and Discussion**

### *Distinct Pandemic Trends*

To gain insight into the mechanism of the virus transmission routes and assess the effectiveness of mitigation measures, we first analyzed the trend of the pandemic worldwide from January 23 to May 9, 2020 (Figure 1). The COVID-19 outbreak initially emerged during December 2019 in Wuhan, China. The numbers of confirmed infections and fatalities in China dominated the global trend during January and February 2020 (Figure 44a,b), but the increases in the newly confirmed cases and fatalities in China have exhibited sharp declines since February (Figure 44b). In contrast to the curve flattening in China, those numbers in other countries have increased sharply since the beginning of March. The epicenter shifted from Wuhan to Italy in early March and to NYC in early April. By April 30, the numbers of confirmed COVID-19 cases and deaths, respectively, reached over 200,000 and 27,000 in Italy and over 1,000,000 and 52,000 in the United States, compared to about 84,000 and 4,600 in China (Figure 44b). Notably, the curves in Italy exhibit a slowing trend since mid-April, while the numbers in the world and the United States continue to increase. Remarkably, the recent trends in the numbers of infections and fatalities in the world and in the United States exhibit striking linearity since the beginning of April (Figure 44c).

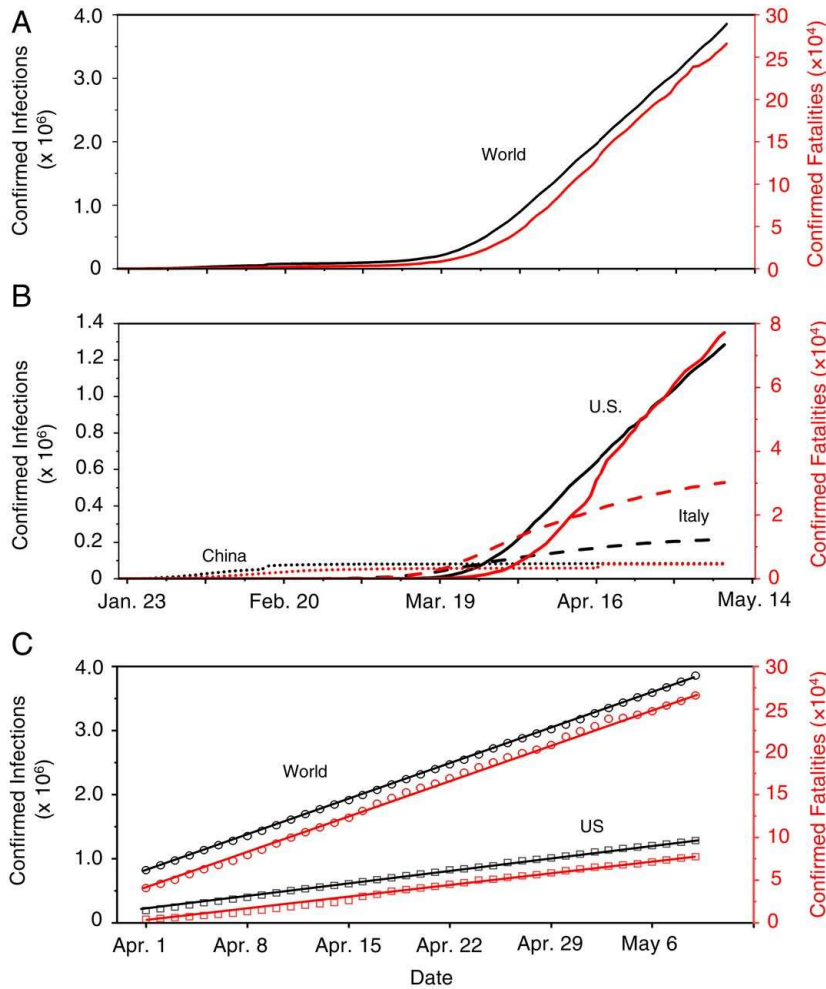


**Figure 44. Distinct global trends of the COVID-19 pandemic.** (a) Confirmed infections and fatalities worldwide. (b) Comparison of the confirmed infections and fatalities between China, Italy, and United States. (c) Linear regression of the confirmed infections and fatalities worldwide and in United States from April 1 to May 9, 2020; the linear regression is, respectively,  $y = 79,398x + 810,167$  ( $R^2 = 0.999$ ) for infections and  $y = 6,075x + 39,409$  ( $R^2 = 0.998$ ) for fatalities worldwide and  $y = 28,971x + 201,187$  ( $R^2 = 0.999$ ) for infections and  $y = 2,059x + 243$  ( $R^2 = 0.995$ ) for fatalities in the United States. The left axis and black color correspond to the numbers of confirmed infections, and the right axis and red color represent the confirmed fatalities.

We interpreted the differences in the pandemic trends by considering the mitigation measures implemented worldwide. The curve flattening in China can be attributed to extensive testing, quarantine, and contact tracing; other aggressive measures implemented in China include lockdown of all cities and rural areas in the whole country, isolation of residents having close

contact with infected people, and mandated wearing of face masks in public. However, the effectiveness of those mitigation measures has yet to be rigorously evaluated. Differentiation of the effects of those mitigation measures in China is challenging,<sup>149</sup> since the implementation occurred almost simultaneously in January 2020. While similar quarantine, isolation, and city lockdown measures were also implemented on March 9 in Italy after the country became the second epicenter, the curve of infections has yet to show complete flattening. In the United States, guidelines for social distancing, quarantine, and isolation were issued by the federal government on March 16, and stay-at-home orders were implemented by many state and local governments starting, for example, between March 19 and April 3 and on March 22 in NYC. The social distancing measures implemented in the United States include staying at least 6 feet (~2 m) away from other people, no gathering in groups, staying out of crowded places, and avoiding mass gatherings. Obviously, the continuous rise in the US infected number casts doubt on the effectiveness of those preventive measures alone (Figure 44b,c).

In contrast to China, wearing of face masks was not mandated and was unpopular in most of the western world during the early outbreak of the pandemic. Advice on the use of face masks was not issued until April 6, 2020 by the WHO, claiming that it is important only to prevent infected persons from viral transmission by filtering out droplets but that it is unimportant to prevent uninfected persons from breathing virus-bearing aerosols. The regions heavily plagued by COVID-19 in northern Italy, such as Lombard, ordered face covering in public starting on April 6, and the Italian authorities required nationwide mandatory use of face masks on May 4. All New Yorkers were mandated to use face covering in public starting on April 17, when social distancing was not possible. With measures implemented in the United States seemingly comparable to those in China, social distancing, quarantine, and isolation exhibited little impact on stopping the

spreading of the disease in the United States, as reflected by the linearity from April 1 to May 9 (Figure 44c). It is possible, however, that these measures alter the slope of the infection curve, that is, by reducing the rate of infections during the early stage of the pandemic. Notably, the recommended physical separation for social distancing is beneficial to prevent direct contact transmission but is insufficient (without face masks) to protect inhalation of virus-bearing aerosols (or even small droplets at intermediate proximity), owing to rapid air mixing.

Second, we analyze the pandemic trends in fifteen top-infected states of the U.S. The initial outbreak in the fifteen U.S. states exhibits a sub-exponential growth in the number of total confirmed infections (Figures 45 and 45), which is characteristic of the COVID-19 pandemic worldwide.<sup>150,151</sup> This distinct sub-exponential increase lasted over a period of two to four weeks, i.e., from 15 March to 12 April (Table 20). The onset of the sub-exponential growth coincided with the issuing of the federal guidelines for social distancing on 16 March. In addition, all fifteen states implemented stay-at-home orders during the initial outbreak between 19 March and 3 April, which also overlapped with the period of the sub-exponential growth.

**Table 20 COVID-19 pandemic trend and projection of the difference in total infections by face covering in the fifteen top-infected states of U.S.**

	Daily confirmed cases trend			Total confirmed cases projection			Projected difference <sup>c</sup>
	Stay-at-home order <sup>a</sup>	$S_1^b$ (d <sup>-1</sup> )	Mandated face covering <sup>a</sup>	$S_2^b$ (d <sup>-1</sup> )	Sub-exp range	Linear range	
States without mandated face covering							
CA	3/19	24	n/a		3/8~4/2	4/3~5/18	
FL	4/3	-12	n/a		3/8~4/9	4/10~5/18	
GA	4/3	-4	n/a		3/8~4/5	4/6~5/18	
OHs	3/24	7	n/a		3/8~4/2	4/3~5/18	
TX	4/2	11	n/a		3/8~4/10	4/11~5/18	
VA	3/30	15	n/a		3/8~4/11	4/12~5/18	
States with mandated face covering							
CT	3/24	34	4/21	-11	3/8~4/4	4/5~4/20	5835 (15%)
MA	3/24	31	5/6	-70	3/8~4/8	4/9~5/5	13634 (16%)
MI	3/24	2·5	4/27	-13	3/8~3/27	3/28~4/26	8452 (16%)
NJ	3/22	127	4/14	-86	3/8~3/29	3/30~4/13	40529 (27%)
NY	3/23	123	4/18	-181	3/8~3/27	3/28~4/17	168884 (48%)
PA	4/1	-15	4/20	-21	3/8~4/2	4/2~4/19	13086 (21%)
IL	3/22	50	5/1	-30	3/8~4/11	4/12~4/30	-12113 (-12%)
LA	3/24	-18	5/1	-2	3/8~4/11	4/12~4/30	1122 (3·2%)
MD	3/31	23	4/18	12	3/8~4/2	4/3~4/17	-8546 (-20%)

<sup>a</sup> orders that took effect after 5 pm are considered to start from the next day

<sup>b</sup>  $S_1$ ,  $S_2$ , and  $S_3$  (d<sup>-1</sup>) denote the slopes of linear regression of daily cases between stay-at-home order and mandated face covering and after mandated face covering.

<sup>c</sup> Projected difference between the reported total cases on May 18 and the corresponded projected number of cases based on the data prior to implementing mandated face covering. The percentage is relative to the reported total cases on May 18.

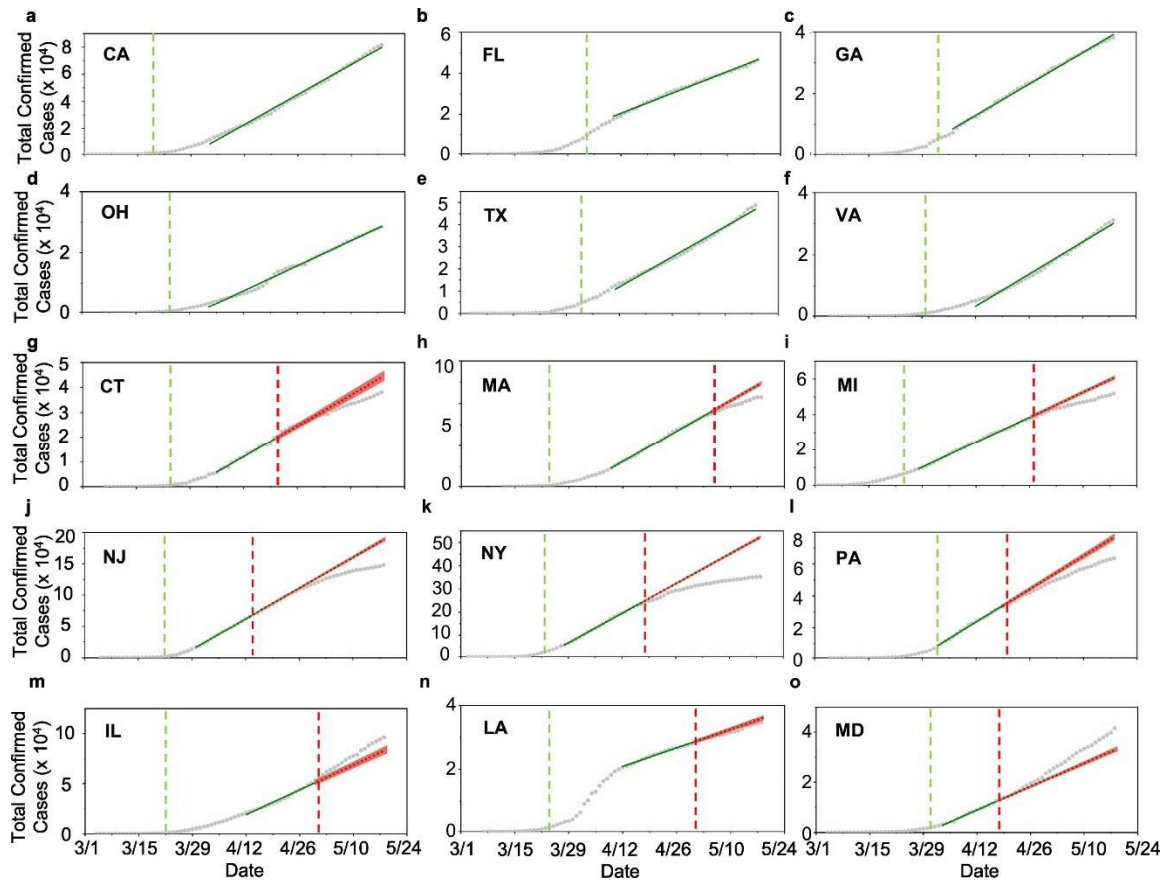


**Figure 45. Cumulative confirmed COVID-19 cases in the top-fifteen infected states of the U.S.** (a-f) For states without mandated face covering, a – California (CA), b – Florida (FL), c- Georgia (GA), d – Ohio (OHs), e – Texas (TX), and f – Virginia (VA), (g-o) for states with mandated face covering, g – Connecticut (CT), h – Massachusetts (MA), i – Michigan (MI), j – New Jersey (NJ), k – New York (NY), l – Pennsylvania (PA), m – Illinois (IL), n – Louisiana (LA), and o – Maryland (MD). The vertical green and red dashed lines label the onsets for stay-at-home orders and mandated face covering, respectively. For comparison, guidelines for social distancing were issued by the federal government on March 16, 2020. The solid green line denotes linear regression through the data, and the dotted green line denotes projection of infections without face covering based on linear regression for the data prior to the onset of mandated face covering. The red shade (g-o) represents 95% confidence interval for the projection.

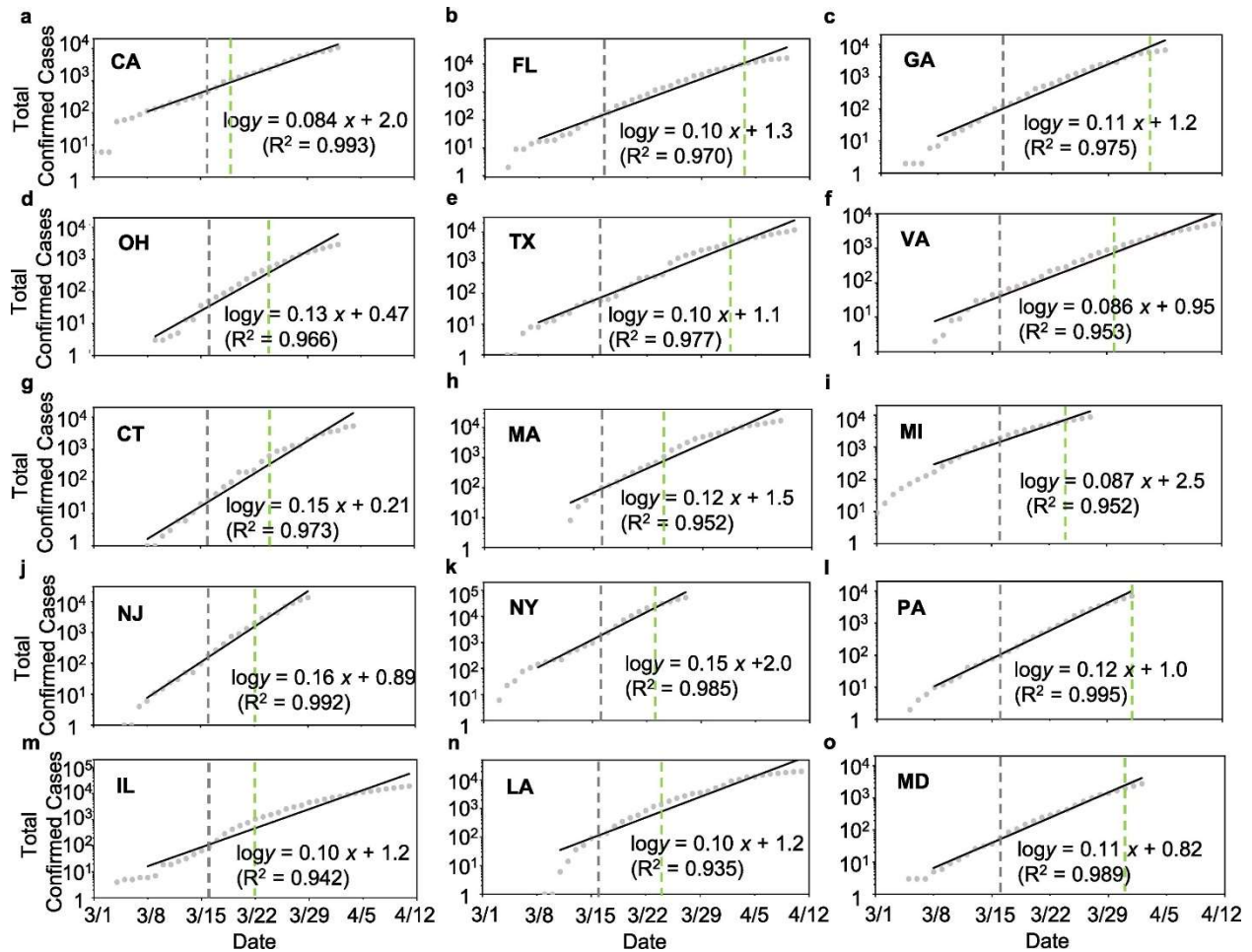


**Figure 46. Initial sub-exponential growth in the total infections.** (a-f) For states without mandated face covering, a – CA, b – FL, c – GA, d – OHs, e – TX, and f – VA, (g-o) for states with mandated face covering, g – CT, h – MA, i – MI, j – NJ, k – NY, l – PA, m – IL, n – LA, and o – MD. The vertical grey and green dashed lines label the beginning of social distancing and stay-at-home orders, respectively.

Another key feature in the total infection curve is reflected by a remarkable linearity immediately following the initial sub-exponential growth (Figures. 45 and 47). The onsets of the linear growth of the total infections are between 0 to 20 days after the implementation of stay-at-home orders among the fifteen states. This linearity in the infection curve represents a dynamic equilibrium between transmission and mitigation measures. For the six states without implementing mandated face covering, the linearity extends one to two months until the end of our



analysis period (18 May) (Figure 45a-f and 47a-f). For example, the number of the total infections increases linearly from early April to 18 May for the states without mandated face covering, with the correlation coefficients ranging from 0.991 to 0.998. Nine states subsequently mandated face covering during the period of 14 April to 6 May, and this implementation occurred 18 to 43 days later than those of the stay-at-home orders. For seven states with mandated face covering, deviation from the linearity and curve flattening appear after the onset of mandated face covering (Figure 45g-l,n). Significant curve flattening is most evident in NY and NJ, occurring shortly after implementing this measure. Only two exceptions (IL and MD) show an unexpected upward trend in the number of total infections after mandated face covering (Figure 45m,o).

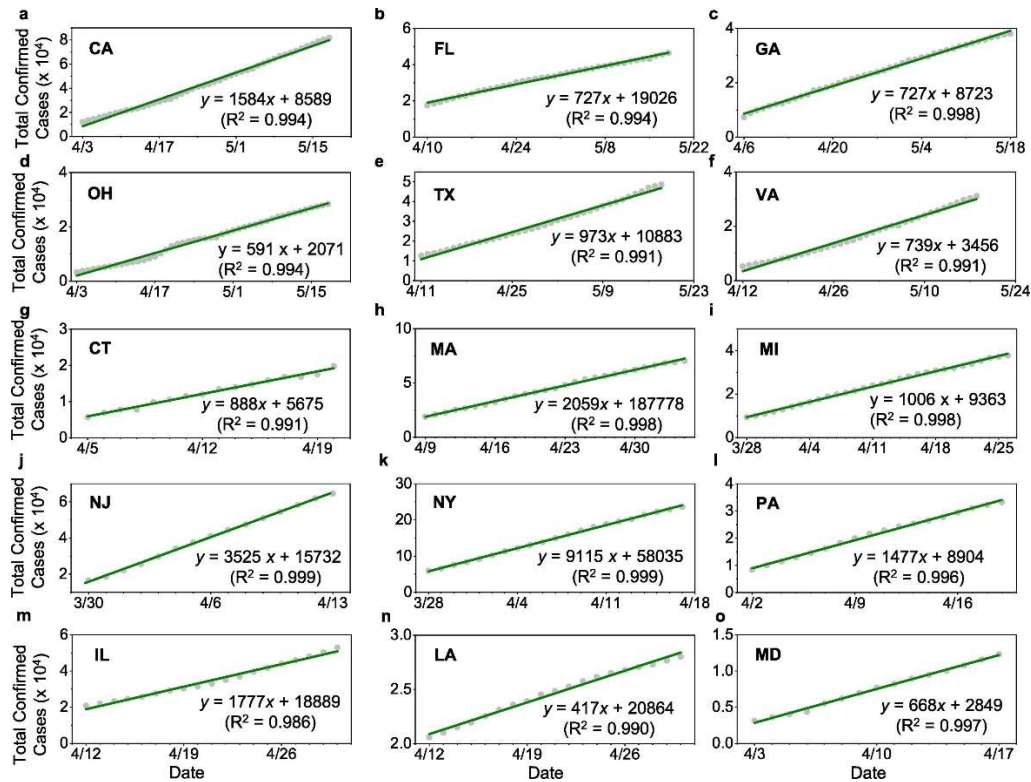


**Figure 47. Linear increase in the total infections following the initial sub-exponential growth.** (a-f) For states without mandated face covering, a – CA, b –FL, c – GA, d – OHs, e –TX, and f –VA, (g-o) for states with mandated face covering, g – CT, h – MA, i – MI, j – NJ, k – NY, l – PA, m – IL, n – LA, and o – MD. The dates cover the range from the end of the sub-exponential growth period to 18 May for a-f or to the onset of mandated face covering for g-o.

### *Understanding the Impacts of Face Covering*

Compared to the simultaneous implementation of measures in China, intervention measures were successively implemented in the western world (Figure 48a), providing an opportunity for assessing their relative effectiveness. We quantified the effects of face covering by projecting the number of infections based on the data prior to implementing the use of face masks in Italy on April 6 and NYC on April 17 (Figure 48a). Such projections are reasonable considering the excellent linear correlation for the data prior to the onset of mandated face covering (Figures 48b,c and 49). Our analysis indicates that face covering reduced the number of infections by over 75,000 in Italy from April 6 to May 9 and by over 66,000 in NYC from April 17 to May 9. In addition, varying the correlation from 15 d to 30 d prior to the onset of the implementation reveals little difference in the projection for both places, because of the high correlation coefficients (Figure 49). Notably, the trends of the infection curves in Italy and NYC contrast to those in the world and in the United States (Figure 44c), which show little deviation from the linearity due to the non-implementation of face-covering measures globally and nationally, respectively. The inability of social distancing, quarantine, and isolation alone to curb the spread of COVID-19 is also evident from the linearity of the infection curve prior to the onset of the face-covering rule in Italy on April 6 and in NYC on April 17 (Figure 48b,c). Hence, the difference made by implementing face covering significantly shapes the pandemic trends worldwide.

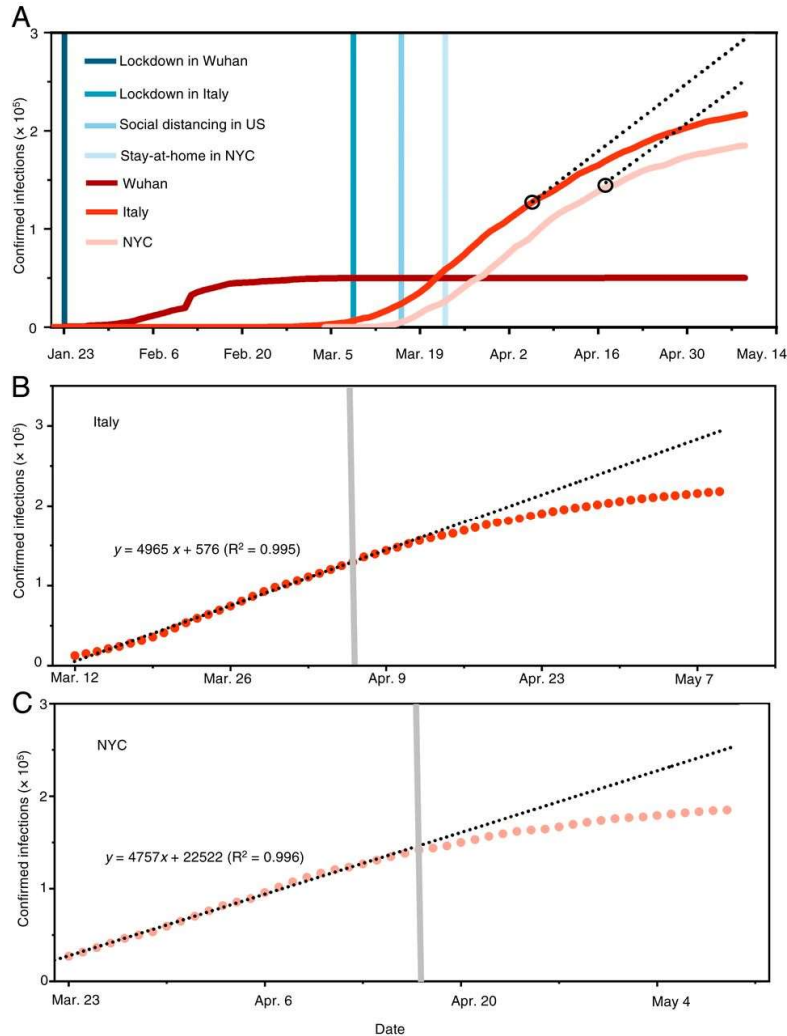


**Figure 48. The evolving epicenter from Wuhan, to Italy, to NYC.** (a) Comparison of the trends and mitigation measures between Wuhan, Italy, and NYC in 2020. The vertical lines mark the date for implementing mitigation measures. The two black circles label the dates when face covering was implemented: April 6 in northern Italy and April 17 in NYC. The black dashed lines represent the projection without face covering based on linear regression of 26-d data prior to implementing this measure. (b) Linear regression of the number of confirmed infections for 26-d data prior to implementing face covering in Italy. The shaded vertical line denotes the date when face covering was implemented on April 6 in northern Italy. (c) Linear regression of the number of confirmed infections for 26-d data prior to implementing face covering in NYC. The shaded vertical line denotes the date when face covering was implemented on April 17 in NYC. In b and c, the circles are reported values, and the dotted line represents fitting and projection of the confirmed infections before and after face-covering, respectively.

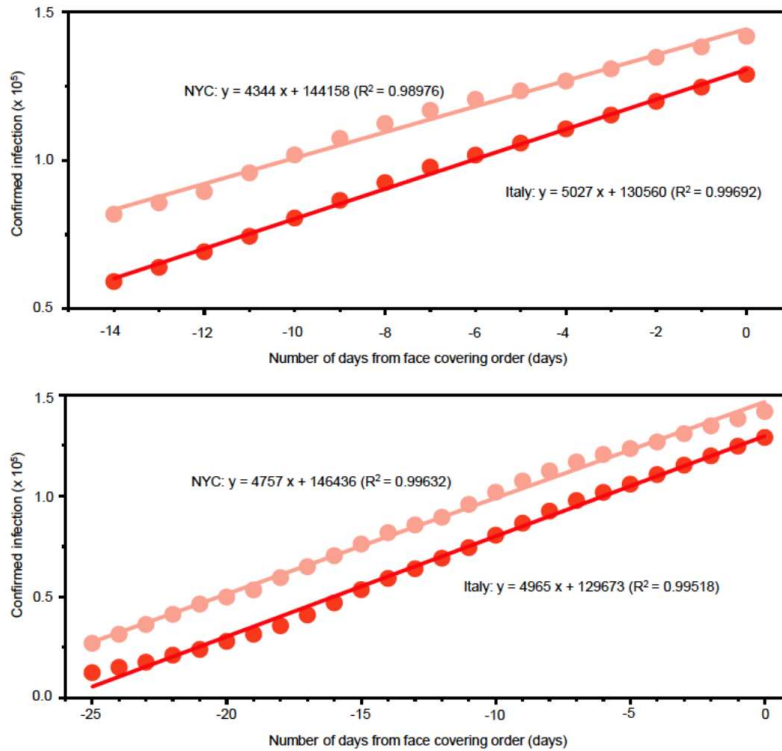


**Figure 49. Linear correlation of the number of confirmed infections for using 15-day. (a) and 26- day (b) data prior to implementing face-covering in Italy and NYC.**

Additionally, we assessed the effects of face covering on the numbers of total infections by calculating the difference between projected and reported numbers in the total infections. This estimation is justifiable considering the high correlation coefficients ( $R^2$  from 0.986 to 0.999) (Fig. 47g-o). The projection yields a range of total infections prevented by face covering for the nine states, with the two largest differences of ~168,000 (48%) in New York and ~41,000 (27%) in New Jersey (Table 20). Overall, the total number of prevented infections with this measure is estimated to reach ~252,000 on 18 May in the seven states (Table 20), which is equivalent to ~17% of the total infections in the nation. For Illinois and Maryland, however, the projected values are lower than the reported numbers, by about 12% and 20%, respectively.

### *Insights into the Transmission Mechanism*

We further elucidated the contribution of airborne transmission to the COVID-19 outbreak by comparing the trends and mitigation measures during the pandemic worldwide and by considering the virus transmission routes (Figure 50). Face covering prevents both airborne transmission by blocking atomization and inhalation of virus-bearing aerosols and contact transmission by blocking viral shedding of droplets. On the other hand, social distancing, quarantine, and isolation, in conjunction with hand sanitizing, minimize contact (direct and indirect) transmission but do not protect against airborne transmission. With social distancing, quarantine, and isolation in place worldwide and in the United States since the beginning of April, airborne transmission represents the only viable route for spreading the disease, when mandated face covering is not implemented. Similarly, airborne transmission also contributes dominantly to the linear increase in the infection prior to the onset of mandated face covering in Italy and NYC. Hence, the unique function of face covering to block atomization and inhalation of virus-bearing aerosols accounts for the significantly reduced infections in China, Italy, and NYC, indicating that airborne transmission of COVID-19 represents the dominant route for infection.

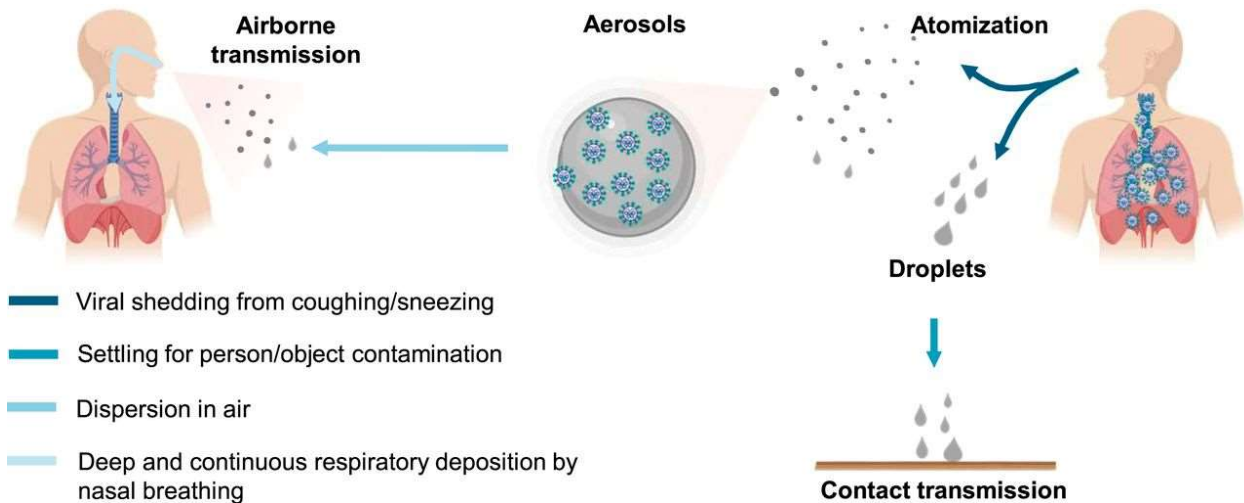


**Figure 50. Transmission of COVID-19.** Human atomization of viruses arises from coughing or sneezing of an infected person, producing virus-containing droplets ( $>5 \mu\text{m}$ ) and aerosols ( $<5 \mu\text{m}$ ). Virus transmission from person to person occurs through direct/indirect contact and airborne aerosol/droplet routes. Large droplets mainly settle out of air to cause person/object contamination, while aerosols are efficiently dispersed in air. Direct and airborne transmissions occur in short range and extended distance/time, respectively. Inhaled airborne viruses deposit directly into the human respiration tract.

Recent measurements identified SARS-Cov-2 RNA on aerosols in Wuhan's hospitals<sup>152</sup> and outdoor in northern Italy,<sup>153</sup> unraveling the likelihood of indoor and outdoor airborne transmission. Within an enclosed environment, virus-bearing aerosols from human atomization are readily accumulated, and elevated levels of airborne viruses facilitate transmission from person to person. Transmission of airborne viruses in open air is subject to dilution, although virus accumulation still occurs due to stagnation under polluted urban conditions. Removal of virus-bearing particles from human atomization via deposition is strongly size dependent, with the settling velocities ranging from  $2.8 \times 10^{-5} \text{ m} \cdot \text{s}^{-1}$  to  $1.4 \times 10^{-3} \text{ m} \cdot \text{s}^{-1}$  for the sizes of 1 and 10  $\mu\text{m}$ , respectively. For comparison, typical wind velocity is about  $1 \text{ m} \cdot \text{s}^{-1}$  to  $3 \text{ m} \cdot \text{s}^{-1}$  indoors<sup>154</sup> and is  $\sim 1 \text{ m} \cdot \text{s}^{-1}$  horizontally and  $0.1 \text{ m} \cdot \text{s}^{-1}$  vertically in stable air. Under those indoor and outdoor conditions, the residence time of virus-bearing aerosols reaches hours, due to air mixing.

We also examined ambient conditions relevant to the outbreaks in Wuhan, Italy, and NYC. The initial outbreak of COVID-19 in Wuhan coincided with the winter haze season in China, during which high levels of PM<sub>2.5</sub> were prevalent in air (Figures 51 and 52). On the other hand, the daily average PM<sub>2.5</sub> concentrations were much lower during the outbreaks in Rome, Italy, and in NYC. The airborne transmission pathways (i.e., indoor or outdoor) as well as the effects of ambient PM<sub>2.5</sub> levels on virus transmission may be variable among urban cities. For example, the winter haze conditions in China likely exacerbated outdoor virus spreading,<sup>155</sup> because of low UV radiation, air stagnation (lacking ventilation on the city scale), and low temperature. Also, there may exist a synergetic effect of simultaneous exposure to the virus and PM<sub>2.5</sub> to enhance the infectivity, severity, and fatalities of the disease.<sup>156</sup> In addition, nascent virus-bearing aerosols produced from human atomization likely undergo transformation in air, including coagulation with ambient preexisting PM and/or growth on a time scale of a few hours in typical urban air. Such transformation, as recently documented on coarse PM in Italy,<sup>153</sup> may mitigate virus inactivation, by providing a medium to preserve its biological properties and elongating its lifetimes. However, key questions remain concerning transformation and transmission of virus-bearing aerosols from human atomization in air. Specifically, what are the impacts of transformation of human-atomized aerosols on viral surviving and infectivity in air?

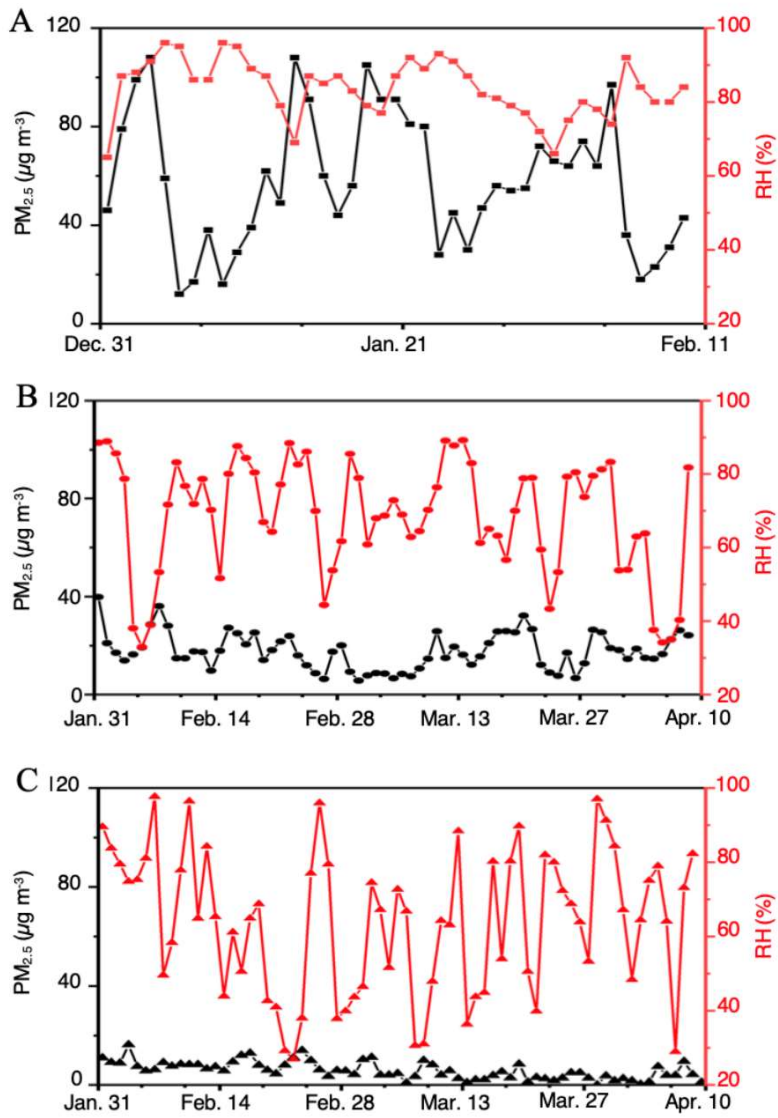
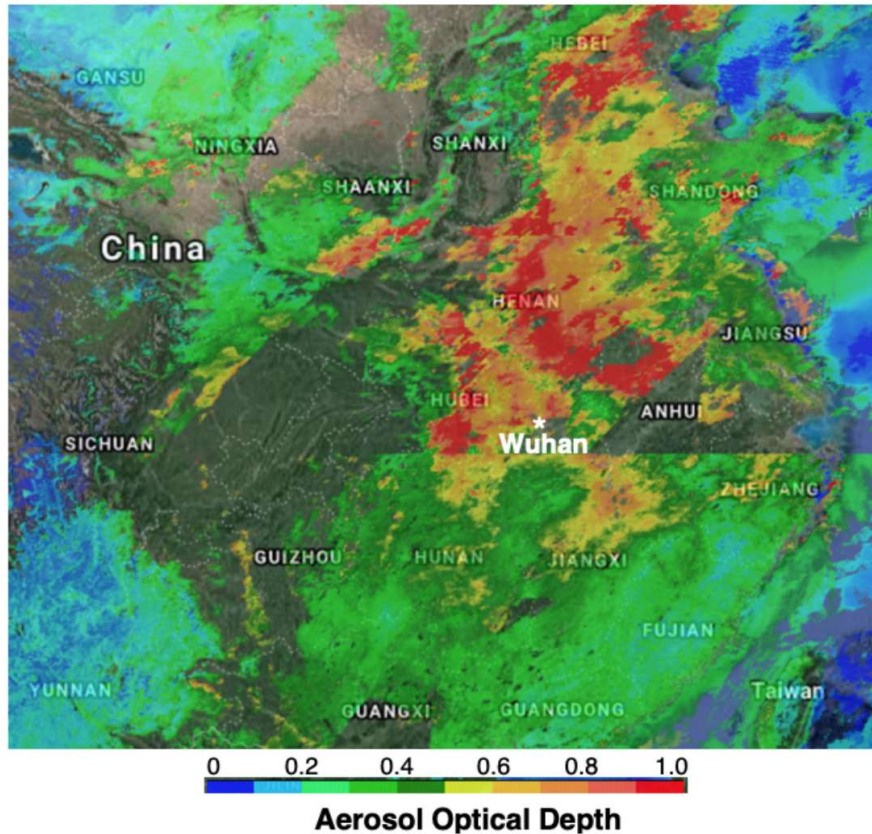


Figure 51. RH and PM<sub>2.5</sub> amid COVID-19 outbreaks in Wuhan (a), Rome (b), and NYC (c).





**Figure 52. Mingling of coronavirus COVID-19 with regional haze in Wuhan, China.** Aerosol optical depth over Eastern China from the Tropospheric Monitoring Instrument (TROPOMI). The data are averaged over January 10 to February 10, 2020. The red (blue) color indicates high (low) aerosol concentration. The city of Wuhan is marked by the white asterisk.

While the humidity effect on viral surviving is uncertain, the conditions during the outbreaks in Wuhan, Rome, and NYC correspond to high RH yet low absolute humidity because of low temperature (Figure 52). Early experimental work showed remarkable survival for the analogous coronavirus MERS-CoV at the RH level characteristic of the COVID-19 outbreaks in Wuhan, Rome, and NYC.<sup>13</sup> For comparison, indoor temperature and RH typically range from 21 °C to 27 °C and 20 to 70%, respectively.

Of particular importance are the considerations that render airborne SARS-CoV-2 the most efficient among all transmission routes. Even with normal nasal breathing, inhalation of virus-bearing aerosols results in deep and continuous deposition into the human respiratory tract, and

this transmission route typically requires a low dose. Also, airborne viruses have great mobility and sufficiently long surviving time for dispersion, and residents situated in densely populated environments are highly vulnerable. In addition, nascent micrometer-size aerosols produced from coughing/sneezing of infected people have the potential of containing many viruses, particularly for asymptomatic carriers.

Future research is critically needed to assess the transmission, transformation, and dispersion of virus-bearing aerosols from human atomization under different environmental conditions, as well as the related impacts on virus infectivity. It is equally important to understand human atomization of airborne viruses: What are the number and size distributions of nascent aerosols as well as the viral load per particle from coughing/sneezing? It is also imperative to evaluate human inhalation of airborne viruses: How are aerosols deposited along the respiratory tract, and what is the minimum dose of airborne viruses required for infection? It is also important to evaluate the performance of face masks to quantify the efficiency to filtrate airborne viruses relevant to human atomization and inhalation. Elucidation of these mechanisms requires an interdisciplinary effort.

#### *A Policy Perspective on Mitigation Measures*

The governments' responses to the COVID-19 pandemic have so far differed significantly worldwide. Swift actions to the initial outbreak were undertaken in China, as reflected by nearly simultaneous implementation of various aggressive mitigation measures. On the other hand, the response to the pandemic was generally slow in the western world, and implementation of the intervention measures occurred only consecutively. Clearly, the responsiveness of the mitigation measures governed the evolution, scope, and magnitude of the pandemic globally.

Curbing the COVID-19 relies not only on decisive and sweeping actions but also, critically, on the scientific understanding of the virus transmission routes, which determines the effectiveness of the mitigation measures (Figure 53). In the United States, social distancing and stay-at-home measures, in conjunction with hand sanitizing (Figure 53, path A), were implemented during the early stage of the pandemic. These measures minimized short-range contact transmission but did not prevent long-range airborne transmission, responsible for the inefficient containing of the pandemic in the United States. Mandated face covering, such as those implemented in China, Italy, and NYC, effectively prevented airborne transmission by blocking atomization and inhalation of virus-bearing aerosols and contact transmission by blocking viral shedding of droplets. While the combined face-covering and social distancing measures offered dual protection against the virus transmission routes, the timing and sequence in implementing the measures also exhibited distinct outcomes during the pandemic. For example, social distancing measures, including city lockdown and stay-at-home orders, were implemented well before face covering was mandated in Italy and NYC (Figure 53, path B), and this sequence left an extended window (28 d in Italy and 32 d in NYC) for largely uninterrupted airborne transmission to spread the disease. The simultaneous implementation of face covering and social distancing (Figure 53, path C), such as that undertaken in China, was most optimal, and this configuration, in conjunction with extensive testing and contact tracing, was responsible for the curve flattening in China. Also, there likely existed remnants of virus transmission after the implementation of regulatory measures, because of circumstances when the measures were not practical or were disobeyed and/or imperfection of the measures. Such limitations, which have been emphasized by the WHO, spurred on controversial views on the validity of wearing face masks to prevent the virus transmission during the pandemic.

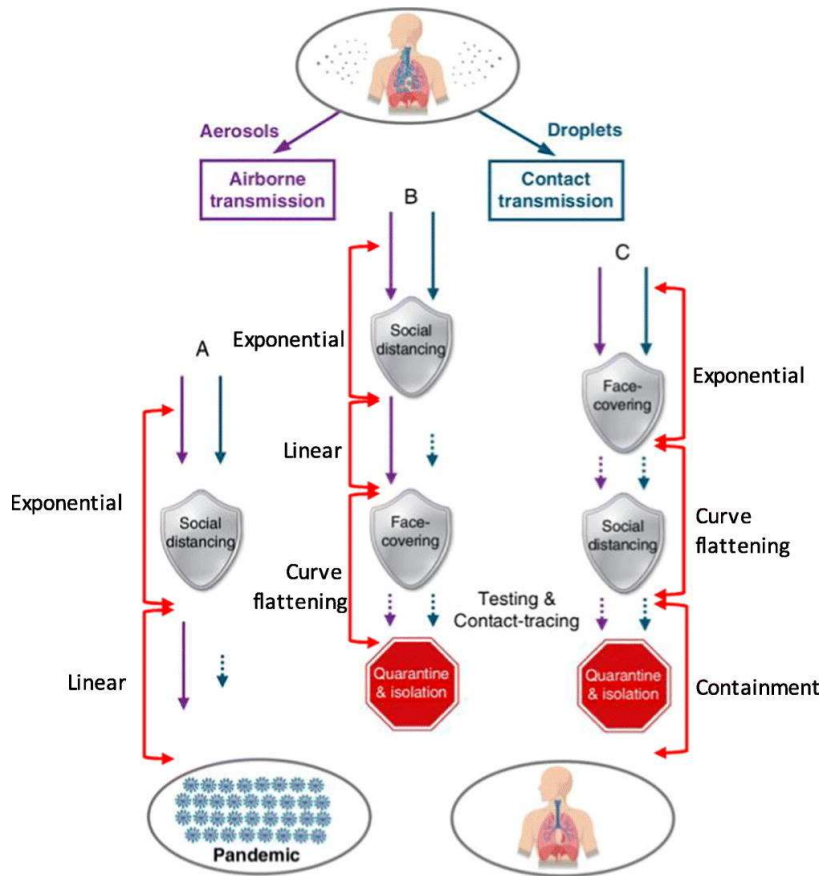


**Figure 53. Mitigation paradigm.** Scenarios of virus transmission under the distancing/quarantine/isolation measure only (path A), the measures with distancing/quarantine/isolation followed by face covering (path B), and the measures with simultaneous face covering and distancing/quarantine/isolation (path C). The short-dashed arrows label possible remnants of virus transmission due to circumstances when the measure is not possible or disobeyed and/or imperfection of the measure.

Social distancing, in conjunction with hand sanitizing, minimizes contact transmission but does not prevent airborne transmission. Compared to social distancing, the stay-at-home measure in principle limits both contact and airborne exposures. However, there exist many exceptions to the stay-at-home measure, including essential activities such as shopping for food and groceries and providing crucial services. These exceptions render airborne transmission as the most likely route to drive the disease spreading, when social distancing and hand-hygiene are still effective. In contrast, face covering prevents airborne transmission by blocking viral shedding and inhalation

of virus-bearing aerosols as well as contact transmission by blocking viral shedding of droplets. The combined face-covering, social distancing, and stay-at-home measures offered maximal protections against contact and airborne exposures. Also, there exist plausible remnants of the mitigation measures, which arise from circumstances when the practices are not possible or are disobeyed and/or imperfection of the measures. In addition, other second-order factors likely impact the pandemic trends, including the incubation period required from exposure to SARS-CoV-2 to development of symptoms, testing conducted, and uncertainties in data reporting. The incubation period has been widely documented from epidemiological studies.<sup>157</sup>

The changes in the total infection rate (defined as  $R_N = \frac{dN}{dt}$ , where  $N$  is the total confirmed infections), is regulated by several forcing terms,

$$\frac{dR_N}{dt} = \sum_{i=1}^2 T_i - \sum_{j=1}^3 I_j + \sum_{k=1}^n S_k \quad (23)$$

where  $T_i$  is the transmission related to the contact ( $i = 1$ ) and airborne ( $i = 2$ ) routes,  $I_j$  is intervention ( $j = 1$  for social distancing,  $j = 2$  for stay-at-home order, and  $j = 3$  for mandated face covering),  $S_k$  denotes all second-order processes, and  $t$  is time in days.

For the initial sub-exponential period in the absence of intervention and secondary forcing, the change in the infection rate is expressed as,

$$\frac{dR_N}{dt} = \sum_{i=1}^2 T_i > 0 \quad (24)$$

This equation is conventionally transformed to the following form, in which the infection rate is proportional to the number of the total confirmed cases,

$$\frac{dN}{dt} = N(\beta - \gamma) \quad (25)$$

$$\frac{dR_N}{dt} = N(\beta - \gamma)^2 \quad (26)$$

where  $\beta$  is the estimated number of people that an infected person infects per day ( $\beta = \frac{\ln R_0}{\tau}$ ). For the fifteen states, the average value of  $R_0$  is estimated to be  $2.8 \pm 0.8$ , and the average value of  $\beta$  is calculated to be  $0.26 \pm 0.10 \text{ d}^{-1}$  for the initial sub-exponential period, consistent with other previous.<sup>150,151</sup>

The containment of the initial sub-exponential growth and subsequent conversion to the linear growth in the total infections during the early outbreak are attributable to social distancing and stay-at-home measures, because of reduced contact transmission ( $T_1$ ). In addition, the duration of two to five weeks for the sub-exponential growth is relevant to the timing for implementation of social distancing and stay-at-home measures, the incubation period required from exposure to SARS-CoV-2 to development of symptoms, testing conducted, and data reporting for the COVID-19 confirmed cases.

Although the combined social distancing (in conjunction with hand sanitizing) and stay-at-home measures reduce contact transmission ( $T_1$ ), they are ineffective in protecting against airborne transmission ( $T_2$ ), as reflected by the linear growth in the total infection curve after implementing social distancing/stay-at-home measures. Specifically, the exceptions to the stay-at-home measure, such as shopping for food and groceries and providing crucial services, render airborne transmission as the only viable route for the disease spreading, when social distancing and hand-hygiene are exercised. Hence, the linear growth in the total infection curve is primarily driven by airborne transmission ( $T_2$ ). The linearity in the total infection curve after social distancing/stay-at-home measures is regulated by the dynamic equilibrium between first-order

airborne transmission and intervention as well as the combined second-order effects, including face covering prior to and/or without the mandated measure. The change in the infection rate after implementation of social distancing/stay-at-home orders is  $\frac{dR_N}{dt} = 0$ , corresponding to an overall canceling effect among the forcing terms. After implementing the social distancing/stay-at-home measures, airborne transmission ( $T_2$ ) remains as the first-order process, while contact transmission ( $T_1$ ) is reduced to a second-order process (remnant).

The subsequent implementation of mandated face covering disrupts the dynamic equilibrium between airborne transmission and social distancing/stay-at-home measures. The effects of face covering on reducing both contact and airborne transmissions result in an overall negative forcing term, i.e.,  $\frac{dR_N}{dt} < 0$ , explaining the departure from the linearity and curve flattening in most states with mandated face covering. Hence, the combined social distancing/stay-at-home measures and face covering provide additional prevention against airborne transmission. The onset of the curve flattening is relevant to the timing of implementation of mandated face covering, the incubation period, testing conducted, and data reporting for COVID-19. In addition, the second-order effect of face covering among citizens prior to the mandated measure also exerts an impact on curve flattening, likely explaining the earlier onset in New York. Advice of using face masks was made on 3 April by the U.S. Centers for Disease Control and Prevention (CDC) and on 6 April by the World Health Organization (WHO). Those various factors jointly explain the differences in the onsets of the curve flattening among the seven states. The continuous increase in the total confirmed cases after face covering is attributed to the remnants of the mitigation measures as well as inadequate testing, lacking contact tracing, and asymptomatic transmission. Also, the timing and sequence in implementing the mitigation measures exert distinct outcomes on the pandemic. The implementation of mandated face covering was delayed by 18-43 days than

those of the stay-at-home orders, allowing an extended period for uninterrupted airborne transmission to spread the disease.

The uncertainty in assessing the effectiveness of face covering is relevant to several factors, including the remnants of this measure and other second-order effects. For example, the curve flattening in the total infections is most pronounced in New York and New Jersey, likely due to strict enforcement of this measure after both emerging as the most infected states of COVID-19 in the nation. In addition, variations in the number of COVID-19 testing conducted, data reporting, and mass gatherings also contribute to the anomalies of the pandemic trends, such as the large spikes in Florida, Georgia, Pennsylvania, and Louisiana in early April (Fig. 4). Also, the upward trend in Illinois after mandated face covering is likely related to reported mass gathering of house parties (with more than 1000 people) on 25 April and protests around 1 May. For Maryland, the upward trend is likely related to reported gathering of protests demanding reopening the economy on 18 April as well as obtaining 500,000 coronavirus tests from South Korea on 20 April.

Under loosened mitigation measures, both contact and airborne transmission routes are re-invigorated, and reduced mitigation measures result in an overall positive effect among the forcing terms. Hence, the change in the infection rate is  $\frac{dR_N}{dt} > 0$  under relaxed social distancing, stay-at-home, and face-covering measures, leading to an upward trend. This scenario likely corresponds to those in Illinois and Maryland after the onset of mandated face covering and to those in Texas and Florida after reopening the economy on 1 May and 4 May, respectively. Large spikes in the daily new cases are evident after re-opening for both states.

Notably, the uncertainties of face covering in protecting inter-human transmission, which have been emphasized by the WHO, have resulted in intensive debates on wearing face masks to prevent inter-human transmission during the pandemic and inconsistent recommendations by U.S.



CDC and WHO. Evidence for the effectiveness of face covering has been recently recognized, showing reduced emissions of respiratory droplets and aerosols when worn by infected individuals and prevented inter-human transmission.<sup>158</sup>

There exist many first-order and second-order processes that regulate the transmission and intervention, posing enormous challenges for understanding and modeling the pandemic trends.<sup>159</sup> While detailed modeling for the COVID-19 pandemic trend is beyond the scope of our work, the framework developed in our study provides the guidance to understand and model the COVID-19 pandemic, by emphasizing the first-order processes for viral transmission mechanisms, interventions, and their interactions. Specifically, our approach captures and represents the essential first-order processes, i.e., the transmission routes of SARS-CoV-2 (contact vs airborne transmission), the interventions (social distancing/stay-at-home and mandated face-covering), and the interaction between transmission routes and interventions. Furthermore, our work explains the pandemic trend at multiple locations and provides insight to development of intervention policies to constrain the spread of COVID-19 pandemic.

## **Conclusions**

In this study, we analyzed the cumulative confirmed infections from Jan 21 to May 18, 2020 for Wuhan, Italy, NYC, and the top-fifteen states heavily plagued in the U.S. During this period, unique intervention measures, such as social distancing, stay-at-home, and mandated face covering, were undertaken, and our results illustrate that these measures have contributed to the distinct trends in the total infections as well as the daily new infections.

Our analysis reveals that there exists an initial sub-exponential and a subsequent linear growth in the trends of total confirmed infections for most places. The linearity in the total

confirmed infections emerges between 0 and 20 days after implementing stay-at-home orders and extends one to two months without mandated face covering or to the onset of mandated face covering orders. This remarkable linearity reflects a dynamic equilibrium among the first-order forcing terms, i.e., transmission, intervention, and the interaction between transmission and intervention as well as combined (addition or canceling) second-order effects. Deviation from this linearity and curve flattening occur after the onset of mandated face covering for seven states. We estimate that the number of the total infections prevented by face covering reaches over 75,000 in Italy from April 6 to May 9, over 66,000 in New York City from April 17 to May 9, and about 252,000 on May 18 in seven states.

The inadequacy of social distancing and stay-at-home measures alone in preventing inter-human transmission is illustrated by the continuous linear growth in the total infection curve after implementing these measures. The combined social distancing, hand sanitizing, and stay-at-home measures reduce contact transmission, but are ineffective in protecting airborne transmission without face covering. The linear growth in the total infection curve after implementing the social distancing/stay-at-home measures is mainly driven by airborne transmission. The dominant role of airborne transmission in spreading the COVID-19 pandemic is jointly explainable by several facts relevant to virus-laden aerosols, i.e., direct and deep deposition into the respiratory tract by inhalation, great mobility and sufficiently long surviving-time for dispersion in air, and high viral contents from asymptomatic carriers. The subsequent implementation of mandated face covering disrupts the dynamic equilibrium between airborne transmission and social distancing/stay-at-home measures. The addition of face covering results in an overall negative forcing term, leading to the departure from the linearity and curve flattening in most states with mandated face covering. Under relaxed social distancing, stay-at-home, and face-covering measures, the overall effect

among the forcing terms becomes positive, leading to an upward pandemic trend after reopening the economy.

In summary, our results corroborate the importance of airborne transmission in spreading the disease and face covering in preventing inter-human transmission. Our findings highlight the necessity of face covering in curbing the spread of the disease. In particular, universal face covering, in conjunction with social distancing and hand hygiene, provides the maximal protection against inter-human transmission and the combination of these intervention measures with rapid and extensive testing as well as contact tracing represents the key in containing the COVID-19 pandemic.

## CHAPTER VI

### SUMMARY AND CONCLUSIONS

In this dissertation, we have investigated the mechanism for the formation of SOA from VOC oxidation products and the role of aerosol in the transmission of infectious diseases. Using novel environmental chamber methodology, we simultaneously track the evolutions of gas-phase oxidation and aerosol properties (i.e., size, density, optical properties, and chemical composition) when monodisperse sub-micrometer seed particles are exposed to SOA precursors from VOC oxidation under various conditions (i.e.,  $\text{NH}_3$ ,  $\text{CH}_2\text{O}$ ,  $\text{NO}_x$  concentrations, seed particle compositions, and RH).

Our experimental study on SOA formation from small  $\alpha$ -dicarbonyls provide direct experimental evidence for carbenium ion-mediated, interface electric field-enhanced, and synergetic oligomerization involving ubiquitous glyoxal, methylglyoxal,  $\text{CH}_2\text{O}$ , hydroxycarbonyls,  $\text{NH}_3$ , and ammonium sulfate. Our results show that methylglyoxal engages in multiphase reactions more efficiently than glyoxal. The higher reactivity of methylglyoxal is evident by its larger uptake coefficient on seed particles under atmospherically relevant concentrations, lower SSA on AS seed particles, higher formation of imidazole in the presence of  $\text{CH}_2\text{O}$ , and more rapid formation of surface coating at high concentrations. Also, our findings reconcile an outstanding discrepancy concerning the multiphase chemistry of glyoxal and methylglyoxal in previous experimental studies, i.e., negligible size growth upon exposure to methylglyoxal vapor but large size growth upon exposure to glyoxal vapor under similar experimental conditions. We show that this discrepancy is attributable to surface- versus volume-limited reactions, where elevated levels of methylglyoxal rapidly form viscous surface coating

and inhibit further growth of seed particles. Our results indicate that the multiphase chemistry of small  $\alpha$ -dicarbonyls leading to SOA and BrC formation is dependent on the reactivity and gaseous concentrations of the aerosol precursors as well as the physicochemical properties of seed particles (i.e., size, pH, phase state, chemical composition, etc.), highlighting the necessity to closely mimic the atmospheric conditions in future laboratory studies to investigate aerosol chemistry.

Additionally, we elucidate the fundamental chemical mechanism of multi-generation photooxidation of volatile organic compounds to yield SOA, revealing significant contributions of dicarbonyls and organic acids to SOA formation because of their unique functionality to engage in aerosol-phase reactions and prompt, high yields from toluene and *m*-xylene oxidation. We show large size-increase and browning of monodisperse sub-micrometer seed particles occur shortly after initiating photooxidation at 10-90% RH, which is attributed to earlier generation products consisting dominantly of dicarbonyl and carboxylic functional groups. While volatile dicarbonyls engage in aqueous reactions to yield non-volatile oligomers and light-absorbing nitrogen-heterocycles/heterochains (in the presence of  $\text{NH}_3$ ) at high RH, organic acids contribute to aerosol carboxylates via ionic dissociation or acid-base reaction in a wide RH range. The measured uptake coefficients for COOs produced from toluene/*m*-xylene oxidation depend strongly on their functionality and show good consistency between those from toluene and *m*-xylene. Our findings of SOA formation from toluene oxidation reconcile atmospheric measurements of explosive SOA growth under polluted urban conditions and underscore the importance for understanding multi-generation production of condensable oxidized organics and the relationship between the functionality and aerosol-phase reactivity. Future studies are necessary to identify and quantify condensable oxidized organics from photooxidation of

different VOC types, including the production from gaseous oxidation, relationship between functionality and reactivity in the aerosol-phase, and contributions to SOA and BrC formation. In addition, our results corroborate that the synergetic interaction between toluene oxidation and  $\text{NH}_3$  contributes to BrC formation, which impacts the radiative transfer in the atmosphere.

Furthermore, we assess the role of aerosol in transmission of infectious diseases and the effectiveness of face covering in preventing inter-human transmission for the several epicenters of COVID-19 pandemic during Jan 21 and May 18, 2020 by analyzing the pandemic trend and mitigation measures. We show that the curve of total confirmed infections exhibits an initial sub-exponential growth and a subsequent linear growth after implementing social distancing/stay-at-home orders. The linearity extends one to two months for the six states without mandated face covering and to the onset of mandated face covering for the other nine states with this measure, reflecting a dynamic equilibrium between first-order transmission kinetics and intervention. With mandated face covering, the pandemic trends show significant deviation from this linearity. The inadequacy of social distancing and stay-at-home measures alone in preventing inter-human transmission is reflected by the continuous linear growth in the total infection curve after implementing these measures, which is mainly driven by airborne transmission. We conclude that airborne transmission and face covering play the dominant role in spreading the disease and flattening the total infection curve, respectively. Our findings provide policymakers and the public with compelling evidence that universal face covering, in conjunction with social distancing and hand hygiene, represents the maximal protection against inter-human transmission and the combination of these intervention measures with rapid and extensive testing as well as contact tracing is crucial in containing the COVID-19 pandemic.

## REFERENCES

- (1) Seinfeld, J. H.; Pandis, S. N. *Atmospheric Chemistry and Physics: From Air Pollution to Climate Change*; John Wiley & Sons, 2016.
- (2) Esworthy, R. *Air Quality: EPA'S 2013 Changes to the Particulate Matter (PM) Standard*; 2014.
- (3) HEI Review Panel on Ultrafine Particles. *Understanding the Health Effects of Ambient Ultrafine Particles*; Health Effects Institute: Boston, MA, 2013.
- (4) Zhang, R.; Wang, G.; Guo, S.; Zamora, M. L.; Ying, Q.; Lin, Y.; Wang, W.; Hu, M.; Wang, Y. Formation of Urban Fine Particulate Matter. *Chem. Rev.* **2015**, *115* (10), 3803–3855. <https://doi.org/10.1021/acs.chemrev.5b00067>.
- (5) IPCC. *Climate Change 2013: The Physical Science Basis. Contribution of Working Group I to the Fifth Assessment Report of the Intergovernmental Panel on Climate Change*. Cambridge University Press, Cambridge, United Kingdom and New York, NY, USA, 1535; Cambridge University Press, 2013.
- (6) World Health Organization. Air pollution. <https://www.who.int/airpollution/en/> (accessed May 20, 2021).
- (7) Valavanidis, A.; Fiotakis, K.; Vlachogianni, T. Airborne Particulate Matter and Human Health: Toxicological Assessment and Importance of Size and Composition of Particles for Oxidative Damage and Carcinogenic Mechanisms. *J. Environ. Sci. Heal. Part C* **2008**, *26* (4), 339–362. <https://doi.org/10.1080/10590500802494538>.
- (8) Mukherjee, A.; Agrawal, M. A Global Perspective of Fine Particulate Matter Pollution and Its Health Effects BT - Reviews of Environmental Contamination and Toxicology Volume 244; de Voogt, P., Ed.; Springer International Publishing: Cham, 2018; pp 5–51.

[https://doi.org/10.1007/398\\_2017\\_3](https://doi.org/10.1007/398_2017_3).

- (9) Burnett, R.; Chen, H.; Szyszkowicz, M.; Fann, N.; Hubbell, B.; Pope, C. A.; Apte, J. S.; Brauer, M.; Cohen, A.; Weichenthal, S.; Coggins, J.; Di, Q.; Brunekreef, B.; Frostad, J.; Lim, S. S.; Kan, H.; Walker, K. D.; Thurston, G. D.; Hayes, R. B.; Lim, C. C.; Spadaro, J. V; et al. Global Estimates of Mortality Associated with Long-Term Exposure to Outdoor Fine Particulate Matter. *Proc. Natl. Acad. Sci.* **2018**, *115* (38), 9592 LP – 9597. <https://doi.org/10.1073/pnas.1803222115>.
- (10) Wu, G.; Brown, J.; Zamora, M. L.; Miller, A.; Satterfield, M. C.; Meininger, C. J.; Steinhäuser, C. B.; Johnson, G. A.; Burghardt, R. C.; Bazer, F. W.; Li, Y.; Johnson, N. M.; Molina, M. J.; Zhang, R. Adverse Organogenesis and Predisposed Long-Term Metabolic Syndrome from Prenatal Exposure to Fine Particulate Matter. *Proc. Natl. Acad. Sci. U. S. A.* **2019**, *116* (24), 11590–11595. <https://doi.org/10.1073/pnas.1902925116>.
- (11) Rychlik, K. A.; Secrest, J. R.; Lau, C.; Pulczynski, J.; Zamora, M. L.; Leal, J.; Langley, R.; Myatt, L. G.; Raju, M.; Chang, R. C.-A.; Li, Y.; Golding, M. C.; Rodrigues-Hoffmann, A.; Molina, M. J.; Zhang, R.; Johnson, N. M. In Utero Ultrafine Particulate Matter Exposure Causes Offspring Pulmonary Immunosuppression. *Proc. Natl. Acad. Sci.* **2019**, *116* (9), 3443–3448. <https://doi.org/10.1073/pnas.1816103116>.
- (12) Tellier, R. Aerosol Transmission of Influenza A Virus: A Review of New Studies. *J. R. Soc. Interface* **2009**, *6* (SUPPL. 6). <https://doi.org/10.1098/rsif.2009.0302.focus>.
- (13) Pyankov, O. V.; Bodnev, S. A.; Pyankova, O. G.; Agranovski, I. E. Survival of Aerosolized Coronavirus in the Ambient Air. *J. Aerosol Sci.* **2018**, *115* (September 2017), 158–163. <https://doi.org/10.1016/j.jaerosci.2017.09.009>.
- (14) Weber, T. P.; Stilianakis, N. I. Inactivation of Influenza A Viruses in the Environment and



- Modes of Transmission: A Critical Review. *J. Infect.* **2008**, *57* (5), 361–373.  
<https://doi.org/https://doi.org/10.1016/j.jinf.2008.08.013>.
- (15) Zhang, R.; Suh, I.; Zhao, J.; Zhang, D.; Fortner, E. C.; Tie, X.; Molina, L. T.; Molina, M. J. Atmospheric New Particle Formation Enhanced by Organic Acids. *Science* (80-. ). **2004**, *304* (5676), 1487 LP – 1490. <https://doi.org/10.1126/science.1095139>.
- (16) Lee, S. H.; Gordon, H.; Yu, H.; Lehtipalo, K.; Haley, R.; Li, Y.; Zhang, R. New Particle Formation in the Atmosphere: From Molecular Clusters to Global Climate. *J. Geophys. Res. Atmos.* **2019**. <https://doi.org/10.1029/2018JD029356>.
- (17) An, Z.; Huang, R.-J.; Zhang, R.; Tie, X.; Li, G.; Cao, J.; Zhou, W.; Shi, Z.; Han, Y.; Gu, Z.; Ji, Y. Severe Haze in Northern China: A Synergy of Anthropogenic Emissions and Atmospheric Processes. *Proc. Natl. Acad. Sci.* **2019**, *116* (18), 8657 LP – 8666.  
<https://doi.org/10.1073/pnas.1900125116>.
- (18) Atkinson, R.; Arey, J. Atmospheric Degradation of Volatile Organic Compounds. *Chem. Rev.* **2003**, *103* (12), 4605–4638. <https://doi.org/10.1021/cr0206420>.
- (19) Gilman, J. B.; Lerner, B. M.; Kuster, W. C.; de Gouw, J. A. Source Signature of Volatile Organic Compounds from Oil and Natural Gas Operations in Northeastern Colorado. *Environ. Sci. Technol.* **2013**, *47* (3), 1297–1305. <https://doi.org/10.1021/es304119a>.
- (20) Finlayson-Pitts, B. J.; Pitts, J. N. Chemistry of the Upper and Lower Atmosphere; Finlayson-Pitts, B. J., Pitts, J. N. B. T.-C. of the U. and L. A., Eds.; Academic Press: San Diego, 2000; pp 1–14. <https://doi.org/https://doi.org/10.1016/B978-012257060-5/50003-4>.
- (21) Hallquist, M.; Wenger, J. C.; Baltensperger, U.; Rudich, Y.; Simpson, D.; Claeys, M.; Dommen, J.; Donahue, N. M.; George, C.; Goldstein, A. H.; Hamilton, J. F.; Herrmann, H.; Hoffmann, T.; Iinuma, Y.; Jang, M.; Jenkin, M. E.; Jimenez, J. L.; Kiendler-Scharr,

- A.; Maenhaut, W.; McFiggans, G.; Mentel, T. F.; Monod, A.; Prévôt, A. S. H.; Seinfeld, J. H.; Surratt, J. D.; Szmigielski, R.; Wildt, J. The Formation, Properties and Impact of Secondary Organic Aerosol: Current and Emerging Issues. *Atmos. Chem. Phys.* **2009**, *9* (14), 5155–5236. <https://doi.org/10.5194/acp-9-5155-2009>.
- (22) Zhang, R.; Khalizov, A.; Wang, L.; Hu, M.; Xu, W. Nucleation and Growth of Nanoparticles in the Atmosphere. *Chem. Rev.* **2012**, *112* (3), 1957–2011. <https://doi.org/10.1021/cr2001756>.
- (23) Shrivastava, M.; Cappa, C. D.; Fan, J.; Goldstein, A. H.; Guenther, A. B.; Jimenez, J. L.; Kuang, C.; Laskin, A.; Martin, S. T.; Ng, N. L.; Petaja, T.; Pierce, J. R.; Rasch, P. J.; Roldin, P.; Seinfeld, J. H.; Shilling, J.; Smith, J. N.; Thornton, J. A.; Volkamer, R.; Wang, J.; Worsnop, D. R.; Zaveri, R. A.; Zelenyuk, A.; Zhang, Q. Recent Advances in Understanding Secondary Organic Aerosol: Implications for Global Climate Forcing. *Rev. Geophys.* **2017**, *55* (2), 509–559. <https://doi.org/10.1002/2016RG000540>.
- (24) Laskin, A.; Laskin, J.; Nizkorodov, S. A. Chemistry of Atmospheric Brown Carbon. *Chem. Rev.* **2015**, *115* (10), 4335–4382. <https://doi.org/10.1021/cr5006167>.
- (25) Curry, L. A.; Tsui, W. G.; McNeill, V. F. Technical Note: Updated Parameterization of the Reactive Uptake of Glyoxal and Methylglyoxal by Atmospheric Aerosols and Cloud Droplets. *Atmos. Chem. Phys.* **2018**, *18* (13), 9823–9830. <https://doi.org/10.5194/acp-18-9823-2018>.
- (26) Li, Y.; Ji, Y.; Zhao, J.; Wang, Y.; Shi, Q.; Peng, J.; Wang, Y.; Wang, C.; Zhang, F.; Wang, Y.; Seinfeld, J. H.; Zhang, R. Unexpected Oligomerization of Small  $\alpha$ -Dicarbonyls for Secondary Organic Aerosol and Brown Carbon Formation. *Environ. Sci. Technol.* **2021**, *55* (8), 4430–4439. <https://doi.org/10.1021/acs.est.0c08066>.

- (27) Heald, C. L.; Jacob, D. J.; Park, R. J.; Russell, L. M.; Huebert, B. J.; Seinfeld, J. H.; Liao, H.; Weber, R. J. A Large Organic Aerosol Source in the Free Troposphere Missing from Current Models. *Geophys. Res. Lett.* **2005**, *32* (18), 1–4.  
<https://doi.org/10.1029/2005GL023831>.
- (28) Tan, Y.; Lim, Y. B.; Altieri, K. E.; Seitzinger, S. P.; Turpin, B. J. Mechanisms Leading to Oligomers and SOA through Aqueous Photooxidation: Insights from OH Radical Oxidation of Acetic Acid and Methylglyoxal. *Atmos. Chem. Phys.* **2012**, *12* (2), 801–813.  
<https://doi.org/10.5194/acp-12-801-2012>.
- (29) Guo, S.; Hu, M.; Zamora, M. L.; Peng, J.; Shang, D.; Zheng, J.; Du, Z.; Wu, Z.; Shao, M.; Zeng, L.; Molina, M. J.; Zhang, R. Elucidating Severe Urban Haze Formation in China. *Proc. Natl. Acad. Sci. U. S. A.* **2014**, *111* (49), 17373–17378.  
<https://doi.org/10.1073/pnas.1419604111>.
- (30) Herrmann, H.; Schaefer, T.; Tilgner, A.; Styler, S. A.; Weller, C.; Teich, M.; Otto, T. Tropospheric Aqueous-Phase Chemistry: Kinetics, Mechanisms, and Its Coupling to a Changing Gas Phase. *Chem. Rev.* **2015**, *115* (10), 4259–4334.  
<https://doi.org/10.1021/cr500447k>.
- (31) Alfarra, M. R.; Hamilton, J. F.; Wyche, K. P.; Good, N.; Ward, M. W.; Carr, T.; Barley, M. H.; Monks, P. S.; Jenkin, M. E.; Lewis, A. C.; McFiggans, G. B. The Effect of Photochemical Ageing and Initial Precursor Concentration on the Composition and Hygroscopic Properties of  $\beta$ -Caryophyllene Secondary Organic Aerosol. *Atmos. Chem. Phys.* **2012**, *12* (14), 6417–6436. <https://doi.org/10.5194/acp-12-6417-2012>.
- (32) Deng, W.; Liu, T.; Zhang, Y.; Situ, S.; Hu, Q.; He, Q.; Zhang, Z.; Lü, S.; Bi, X.; Wang, X.; Boreave, A.; George, C.; Ding, X.; Wang, X. Secondary Organic Aerosol Formation

- from Photo-Oxidation of Toluene with NO<sub>x</sub> and SO<sub>2</sub>: Chamber Simulation with Purified Air versus Urban Ambient Air as Matrix. *Atmos. Environ.* **2017**, *150*, 67–76.  
<https://doi.org/10.1016/j.atmosenv.2016.11.047>.
- (33) Shilling, J. E.; Chen, Q.; King, S. M.; Rosenoern, T.; Kroll, J. H.; Worsnop, D. R.; DeCarlo, P. F.; Aiken, A. C.; Sueper, D.; Jimenez, J. L.; Martin, S. T. Loading-Dependent Elemental Composition of  $\alpha$ -Pinene SOA Particles. *Atmos. Chem. Phys.* **2009**, *9* (3), 771–782. <https://doi.org/10.5194/acp-9-771-2009>.
- (34) Molina, L. T. Introductory Lecture: Air Quality in Megacities. *Faraday Discuss.* **2021**, *226* (0), 9–52. <https://doi.org/10.1039/D0FD00123F>.
- (35) National Academies of Sciences Engineering and Medicine. *The Future of Atmospheric Chemistry Research: Remembering Yesterday, Understanding Today, Anticipating Tomorrow*; The National Academies Press: Washington, DC, 2016.  
<https://doi.org/10.17226/23573>.
- (36) Jimenez, J. L.; Canagaratna, M. R.; Donahue, N. M.; Prevot, A. S. H.; Zhang, Q.; Kroll, J. H.; DeCarlo, P. F.; Allan, J. D.; Coe, H.; Ng, N. L.; Aiken, A. C.; Docherty, K. S.; Ulbrich, I. M.; Grieshop, A. P.; Robinson, A. L.; Duplissy, J.; Smith, J. D.; Wilson, K. R.; Lanz, V. A.; Hueglin, C.; Worsnop, D. R.; et al. Evolution of Organic Aerosols in the Atmosphere. *Science* (80-. ). **2009**, *326* (5959), 1525 LP – 1529.  
<https://doi.org/10.1126/science.1180353>.
- (37) Hodzic, A.; Kasibhatla, P. S.; Jo, D. S.; Cappa, C. D.; Jimenez, J. L.; Madronich, S.; Park, R. J. Rethinking the Global Secondary Organic Aerosol (SOA) Budget: Stronger Production, Faster Removal, Shorter Lifetime. *Atmos. Chem. Phys.* **2016**, *16* (12), 7917–7941. <https://doi.org/10.5194/acp-16-7917-2016>.

- (38) Jang, M.; Czoschke, N. M.; Lee, S.; Kamens, R. M.; Fortner, E. C.; Tie, X.; Molina, L. T.; Molina, M. J. Heterogeneous Atmospheric Aerosol Production by Acid-Catalyzed Particle-Phase Reactions. *Science* (80-. ). **2002**, *298* (5594), 814–817. <https://doi.org/10.1126/science.1075798>.
- (39) Rudich, Y.; Donahue, N. M.; Mentel, T. F. Aging of Organic Aerosol: Bridging the Gap Between Laboratory and Field Studies. *Annu. Rev. Phys. Chem.* **2007**, *58* (1), 321–352. <https://doi.org/10.1146/annurev.physchem.58.032806.104432>.
- (40) Fu, T. M.; Jacob, D. J.; Wittrock, F.; Burrows, J. P.; Vrekoussis, M.; Henze, D. K. Global Budgets of Atmospheric Glyoxal and Methylglyoxal, and Implications for Formation of Secondary Organic Aerosols. *J. Geophys. Res. Atmos.* **2008**, *113* (15). <https://doi.org/10.1029/2007JD009505>.
- (41) Ji, Y.; Zheng, J.; Qin, D.; Li, Y.; Gao, Y.; Yao, M.; Chen, X.; Li, G.; An, T.; Zhang, R. OH-Initiated Oxidation of Acetylacetone: Implications for Ozone and Secondary Organic Aerosol Formation. **2018**, *52* (19), 11169–11177. <https://doi.org/10.1021/acs.est.8b03972>.
- (42) Loeffler, K. W.; Koehler, C. A.; Paul, N. M.; De Haan, D. O. Oligomer Formation in Evaporating Aqueous Glyoxal and Methyl Glyoxal Solutions. *Environ. Sci. Technol.* **2006**, *40* (20), 6318–6323. <https://doi.org/10.1021/es060810w>.
- (43) Volkamer, R.; Jimenez, J. L.; San Martini, F.; Dzepina, K.; Zhang, Q.; Salcedo, D.; Molina, L. T.; Worsnop, D. R.; Molina, M. J. Secondary Organic Aerosol Formation from Anthropogenic Air Pollution: Rapid and Higher than Expected. *Geophys. Res. Lett.* **2006**, *33* (17). <https://doi.org/10.1029/2006GL026899>.
- (44) Kalberer, M.; Paulsen, D.; Sax, M.; Steinbacher, M.; Dommen, J.; Prevot, A. S. H.; Fisseha, R.; Weingartner, E.; Frankevich, V.; Zenobi, R.; Baltensperger, U. Identification

- of Polymers as Major Components of Atmospheric Organic Aerosols. *Science* (80-. ). **2004**, *303* (5664), 1659 LP – 1662. <https://doi.org/10.1126/science.1092185>.
- (45) Kroll, J. H.; Ng, N. L.; Murphy, S. M.; Varutbangkul, V.; Flagan, R. C.; Seinfeld, J. H. Chamber Studies of Secondary Organic Aerosol Growth by Reactive Uptake of Simple Carbonyl Compounds. *J. Geophys. Res. Atmos.* **2005**, *110* (D23). <https://doi.org/10.1029/2005JD006004>.
- (46) Wang, L.; Xu, W.; Khalizov, A. F.; Zheng, J.; Qiu, C.; Zhang, R. Laboratory Investigation on the Role of Organics in Atmospheric Nanoparticle Growth. *J. Phys. Chem. A* **2011**, *115* (32), 8940–8947. <https://doi.org/10.1021/jp1121855>.
- (47) Wang, L.; Khalizov, A. F.; Zheng, J.; Xu, W.; Ma, Y.; Lal, V.; Zhang, R. Atmospheric Nanoparticles Formed from Heterogeneous Reactions of Organics. *Nat. Geosci.* **2010**, *3* (4), 238–242. <https://doi.org/10.1038/ngeo778>.
- (48) Zhao, J.; Levitt, N. P.; Zhang, R.; Chen, J. Heterogeneous Reactions of Methylglyoxal in Acidic Media: Implications for Secondary Organic Aerosol Formation. *Environ. Sci. Technol.* **2006**, *40* (24), 7682–7687. <https://doi.org/10.1021/es060610k>.
- (49) Gomez, M. E.; Lin, Y.; Guo, S.; Zhang, R. Heterogeneous Chemistry of Glyoxal on Acidic Solutions. An Oligomerization Pathway for Secondary Organic Aerosol Formation. *J. Phys. Chem. A* **2015**, *119* (19), 4457–4463. <https://doi.org/10.1021/jp509916r>.
- (50) De Haan, D. O.; Hawkins, L. N.; Welsh, H. G.; Pednekar, R.; Casar, J. R.; Pennington, E. A.; de Loera, A.; Jimenez, N. G.; Symons, M. A.; Zauscher, M.; Pajunoja, A.; Caponi, L.; Cazaunau, M.; Formenti, P.; Gratien, A.; Pangui, E.; Doussin, J.-F. Brown Carbon Production in Ammonium- or Amine-Containing Aerosol Particles by Reactive Uptake of

- Methylglyoxal and Photolytic Cloud Cycling. *Environ. Sci. Technol.* **2017**, *51* (13), 7458–7466. <https://doi.org/10.1021/acs.est.7b00159>.
- (51) Marrero-Ortiz, W.; Hu, M.; Du, Z.; Ji, Y.; Wang, Y. Y.; Guo, S.; Lin, Y.; Gomez-Hernandez, M.; Peng, J.; Li, Y.; Secrest, J.; Zamora, M. L.; Wang, Y. Y.; An, T.; Zhang, R. Formation and Optical Properties of Brown Carbon from Small  $\alpha$ -Dicarbonyls and Amines. **2019**, *53* (1), 117–126. <https://doi.org/10.1021/acs.est.8b03995>.
- (52) Hua, W.; Jubb, A. M.; Allen, H. C. Electric Field Reversal of  $\text{Na}_2\text{SO}_4$ ,  $(\text{NH}_4)_2\text{SO}_4$ , and  $\text{Na}_2\text{CO}_3$  Relative to  $\text{CaCl}_2$  and  $\text{NaCl}$  at the Air/Aqueous Interface Revealed by Heterodyne Detected Phase-Sensitive Sum Frequency. *J. Phys. Chem. Lett.* **2011**, *2* (20), 2515–2520. <https://doi.org/10.1021/jz200888t>.
- (53) Khalizov, A. F.; Lin, Y.; Qiu, C.; Guo, S.; Collins, D.; Zhang, R. Role of OH-Initiated Oxidation of Isoprene in Aging of Combustion Soot. *Environ. Sci. Technol.* **2013**, *47* (5), 2254–2263. <https://doi.org/10.1021/es3045339>.
- (54) Zhao, J.; Zhang, R.; Fortner, E. C.; North, S. W. Quantification of Hydroxycarbonyls from OH-Isoprene Reactions. *J. Am. Chem. Soc.* **2004**, *126* (9), 2686–2687. <https://doi.org/10.1021/ja0386391>.
- (55) Fortner, E. C.; Zhao, J.; Zhang, R. Development of Ion Drift-Chemical Ionization Mass Spectrometry. *Anal. Chem.* **2004**, *76* (18), 5436–5440. <https://doi.org/10.1021/ac0493222>.
- (56) Dotan, I.; Albritton, D. L.; Lindinger, W.; Pahl, M. Mobilities of  $\text{CO}_2^+$ ,  $\text{N}_2\text{H}^+$ ,  $\text{H}_3\text{O}^+$ ,  $\text{H}_3\text{O}^+\cdot\text{H}_2\text{O}$ , and  $\text{H}_3\text{O}^+\cdot(\text{H}_2\text{O})_2$  Ions in  $\text{N}_2$ . *The Journal of Chemical Physics*. 1976, pp 5028–5030. <https://doi.org/10.1063/1.432943>.
- (57) Khalizov, A. F.; Xue, H.; Wang, L.; Zheng, J.; Zhang, R. Enhanced Light Absorption and Scattering by Carbon Soot Aerosol Internally Mixed with Sulfuric Acid. *J. Phys. Chem. A*

- 2009**, *113* (6), 1066–1074. <https://doi.org/10.1021/jp807531n>.
- (58) Zhang, X.; Cappa, C. D.; Jathar, S. H.; McVay, R. C.; Ensberg, J. J.; Kleeman, M. J.; Seinfeld, J. H. Influence of Vapor Wall Loss in Laboratory Chambers on Yields of Secondary Organic Aerosol. *Proc. Natl. Acad. Sci. U. S. A.* **2014**, *111* (16), 5802–5807. <https://doi.org/10.1073/pnas.1404727111>.
- (59) McMurry, P. H.; Rader, D. J. Aerosol Wall Losses in Electrically Charged Chambers. *Aerosol Sci. Technol.* **1985**, *4* (3), 249–268. <https://doi.org/10.1080/02786828508959054>.
- (60) Bongartz, A.; Schweighoefer, S.; Roose, C.; Schurath, U. The Mass Accommodation Coefficient of Ammonia on Water. *J. Atmos. Chem.* **1995**, *20* (1), 35–58. <https://doi.org/10.1007/BF01099917>.
- (61) Tang, M. J.; Cox, R. A.; Kalberer, M. Compilation and Evaluation of Gas Phase Diffusion Coefficients of Reactive Trace Gases in the Atmosphere: Volume 1. Inorganic Compounds. *Atmos. Chem. Phys.* **2014**, *14* (17), 9233–9247. <https://doi.org/10.5194/acp-14-9233-2014>.
- (62) Jones, R.; Lehr, W.; Simecek-Beatty, D.; Reynolds, M. ALOHA® (Areal Locations of Hazardous Atmospheres) 5.4.4 : Technical Documentation. 2013.
- (63) Jayne, J. T.; Worsnop, D. R.; Kolb, C. E.; Swartz, E.; Davidovits, P. Uptake of Gas-Phase Formaldehyde by Aqueous Acid Surfaces. *J. Phys. Chem.* **1996**, *100* (19), 8015–8022. <https://doi.org/10.1021/jp953196b>.
- (64) Phillips, J. C.; Braun, R.; Wang, W.; Gumbart, J.; Tajkhorshid, E.; Villa, E.; Chipot, C.; Skeel, R. D.; Kalé, L.; Schulten, K. Scalable Molecular Dynamics with NAMD. *J. Comput. Chem.* **2005**, *26* (16), 1781–1802. <https://doi.org/10.1002/jcc.20289>.
- (65) Martins-Costa, M. T. C.; Anglada, J. M.; Francisco, J. S.; Ruiz-Lopez, M. F. Reactivity of



- Volatile Organic Compounds at the Surface of a Water Droplet. *J. Am. Chem. Soc.* **2012**, *134* (28). <https://doi.org/10.1021/ja304971e>.
- (66) Lu, T.; Chen, F. Multiwfn: A Multifunctional Wavefunction Analyzer. *J. Comput. Chem.* **2012**, *33* (5), 580–592. <https://doi.org/https://doi.org/10.1002/jcc.22885>.
- (67) Ravishankara, A. R. Heterogeneous and Multiphase Chemistry in the Troposphere. *Science* (80-. ). **1997**, *276* (5315), 1058 LP – 1065. <https://doi.org/10.1126/science.276.5315.1058>.
- (68) Wang, G.; Zhang, R.; Gomez, M. E.; Yang, L.; Levy Zamora, M.; Hu, M.; Lin, Y.; Peng, J.; Guo, S.; Meng, J.; Li, J.; Cheng, C.; Hu, T.; Ren, Y.; Wang, Y. Y.; Gao, J.; Cao, J.; An, Z.; Zhou, W.; Li, G.; Molina, M. J.; et al. Persistent Sulfate Formation from London Fog to Chinese Haze. *Proc. Natl. Acad. Sci.* **2016**, *113* (48), 13630–13635.
- (69) Shi, Q.; Zhang, W.; Ji, Y.; Wang, J.; Qin, D.; Chen, J.; Gao, Y.; Li, G.; An, T. Enhanced Uptake of Glyoxal at the Acidic Nanoparticle Interface: Implications for Secondary Organic Aerosol Formation. *Environ. Sci. Nano* **2020**, *7* (4), 1126–1135. <https://doi.org/10.1039/D0EN00016G>.
- (70) Ji, Y.; Shi, Q.; Li, Y.; An, T.; Zheng, J.; Peng, J.; Gao, Y.; Chen, J.; Li, G.; Wang, Y.; Zhang, F.; Zhang, A. L.; Zhao, J.; Molina, M. J.; Zhang, R. Carbenium Ion-Mediated Oligomerization of Methylglyoxal for Secondary Organic Aerosol Formation. *Proc. Natl. Acad. Sci.* **2020**, *117* (24), 13294 LP – 13299. <https://doi.org/10.1073/pnas.1912235117>.
- (71) Zhao, J.; Levitt, N. P.; Zhang, R. Heterogeneous Chemistry of Octanal and 2, 4-Hexadienal with Sulfuric Acid. *Geophys. Res. Lett.* **2005**, *32* (9). <https://doi.org/https://doi.org/10.1029/2004GL022200>.
- (72) Waxman, E. M.; Elm, J.; Kurtén, T.; Mikkelsen, K. V.; Ziemann, P. J.; Volkamer, R.

- Glyoxal and Methylglyoxal Setschenow Salting Constants in Sulfate, Nitrate, and Chloride Solutions: Measurements and Gibbs Energies. *Environ. Sci. Technol.* **2015**, *49* (19), 11500–11508. <https://doi.org/10.1021/acs.est.5b02782>.
- (73) Xu, W.; Guo, S.; Gomez-Hernandez, M.; Zamora, M. L.; Secretst, J.; Marrero-Ortiz, W.; Zhang, A. L.; Collins, D. R.; Zhang, R. Cloud Forming Potential of Oligomers Relevant to Secondary Organic Aerosols. *Geophys. Res. Lett.* **2014**, *41* (18), 6538–6545. <https://doi.org/10.1002/2014GL061040>.
- (74) Lin, G.; Penner, J. E.; Sillman, S.; Taraborrelli, D.; Lelieveld, J. Global Modeling of SOA Formation from Dicarbonyls, Epoxides, Organic Nitrates and Peroxides. *Atmos. Chem. Phys.* **2012**, *12* (10), 4743–4774. <https://doi.org/10.5194/acp-12-4743-2012>.
- (75) Myriokefalitakis, S.; Vrekoussis, M.; Tsigaridis, K.; Wittrock, F.; Richter, A.; Brühl, C.; Volkamer, R.; Burrows, J. P.; Kanakidou, M. The Influence of Natural and Anthropogenic Secondary Sources on the Glyoxal Global Distribution. *Atmos. Chem. Phys.* **2008**, *8* (16), 4965–4981. <https://doi.org/10.5194/acp-8-4965-2008>.
- (76) Lathièrè, J.; Hauglustaine, D. A.; Friend, A. D.; De Noblet-Ducoudré, N.; Viovy, N.; Folberth, G. A. Impact of Climate Variability and Land Use Changes on Global Biogenic Volatile Organic Compound Emissions. *Atmos. Chem. Phys.* **2006**, *6* (8), 2129–2146. <https://doi.org/10.5194/acp-6-2129-2006>.
- (77) Müller, J.-F. F.; Stavroukou, T.; Wallens, S.; De Smedt, I.; Van Roozendael, M.; Potosnak, M. J.; Rinne, J.; Munger, B.; Goldstein, A.; Guenther, A. B. Global Isoprene Emissions Estimated Using MEGAN, ECMWF Analyses and a Detailed Canopy Environment Model. *Atmos. Chem. Phys.* **2008**, *8* (5), 1329–1341. <https://doi.org/10.5194/acp-8-1329-2008>.

- (78) Stadtler, S.; Kühn, T.; Schröder, S.; Taraborrelli, D.; Schultz, M. G.; Kokkola, H. Isoprene Derived Secondary Organic Aerosol in a Global Aerosol Chemistry Climate Model. *Geosci. Model Dev. Discuss.* **2017**, No. October, 1–35. <https://doi.org/10.5194/gmd-2017-244>.
- (79) Messina, P.; Lathièrè, J.; Sindelarova, K.; Vuichard, N.; Granier, C.; Ghattas, J.; Cozic, A.; Hauglustaine, D. A. Global Biogenic Volatile Organic Compound Emissions in the ORCHIDEE and MEGAN Models and Sensitivity to Key Parameters. *Atmos. Chem. Phys.* **2016**, *16* (22), 14169–14202. <https://doi.org/10.5194/acp-16-14169-2016>.
- (80) Fortems-Cheiney, A.; Chevallier, F.; Pison, I.; Bousquet, P.; Saunois, M.; Szopa, S.; Cressot, C.; Kurosu, T. P.; Chance, K.; Fried, A. The Formaldehyde Budget as Seen by a Global-Scale Multi-Constraint and Multi-Species Inversion System. *Atmos. Chem. Phys.* **2012**, *12* (15), 6699–6721. <https://doi.org/10.5194/acp-12-6699-2012>.
- (81) Stavroukou, T.; Müller, J. F.; De Smedt, I.; Van Roozendaal, M.; Van Der Werf, G. R.; Giglio, L.; Guenther, A. Global Emissions of Non-Methane Hydrocarbons Deduced from SCIAMACHY Formaldehyde Columns through 2003-2006. *Atmos. Chem. Phys.* **2009**, *9* (11), 3663–3679. <https://doi.org/10.5194/acp-9-3663-2009>.
- (82) Pye, H. O. T.; Liao, H.; Wu, S.; Mickley, L. J.; Jacob, D. J.; Henze, D. J.; Seinfeld, J. H. Effect of Changes in Climate and Emissions on Future Sulfate-Nitrate-Ammonium Aerosol Levels in the United States. *J. Geophys. Res. Atmos.* **2009**, *114* (1), 1–18. <https://doi.org/10.1029/2008JD010701>.
- (83) Feng, Y.; Penner, J. E. Global Modeling of Nitrate and Ammonium: Interaction of Aerosols and Tropospheric Chemistry. *J. Geophys. Res. Atmos.* **2007**, *112* (1), 1–24. <https://doi.org/10.1029/2005JD006404>.

- (84) Dentener, F. J.; Crutzen, P. J. A Three-Dimensional Model of the Global Ammonia Cycle. *J. Atmos. Chem.* **1994**, *19* (4), 331–369. <https://doi.org/10.1007/BF00694492>.
- (85) Schlesinger, W. H.; Hartley, A. E. A Global Budget for Atmospheric NH<sub>3</sub>. *Biogeochemistry* **1992**, *15* (3), 191–211. <https://doi.org/10.1007/BF00002936>.
- (86) Bouwman, A. F.; Van Der Hoek, K. W. Scenarios of Animal Waste Production and Fertilizer Use and Associated Ammonia Emission for the Developing Countries. *Atmos. Environ.* **1997**. [https://doi.org/10.1016/S1352-2310\(97\)00288-4](https://doi.org/10.1016/S1352-2310(97)00288-4).
- (87) Shrivastava, M.; Easter, R. C.; Liu, X.; Zelenyuk, A.; Singh, B.; Zhang, K.; Ma, P. L.; Chand, D.; Ghan, S.; Jimenez, J. L.; Zhang, Q.; Fast, J.; Rasch, P. J.; Tiitta, P. Global Transformation and Fate of SOA: Implications of Low-Volatility SOA and Gas-Phase Fragmentation Reactions. *J. Geophys. Res.* **2015**. <https://doi.org/10.1002/2014JD022563>.
- (88) Tsigaridis, K.; Daskalakis, N.; Kanakidou, M.; Adams, P. J.; Artaxo, P.; Bahadur, R.; Balkanski, Y.; Bauer, S. E.; Bellouin, N.; Benedetti, A.; Bergman, T.; Berntsen, T. K.; Beukes, J. P.; Bian, H.; Carslaw, K. S.; Chin, M.; Curci, G.; Diehl, T.; Easter, R. C.; Ghan, S. J.; Zhang, X.; et al. The AeroCom Evaluation and Intercomparison of Organic Aerosol in Global Models. *Atmos. Chem. Phys.* **2014**, *14* (19), 10845–10895. <https://doi.org/10.5194/acp-14-10845-2014>.
- (89) Spracklen, D. V.; Jimenez, J. L.; Carslaw, K. S.; Worsnop, D. R.; Evans, M. J.; Mann, G. W.; Zhang, Q.; Canagaratna, M. R.; Allan, J.; Coe, H.; McFiggans, G.; Rap, A.; Forster, P. Aerosol Mass Spectrometer Constraint on the Global Secondary Organic Aerosol Budget. *Atmos. Chem. Phys.* **2011**, *11* (23), 12109–12136. <https://doi.org/10.5194/acp-11-12109-2011>.
- (90) Chin, M.; Rood, R. B.; Lin, S. J.; Müller, J. F.; Thompson, A. M. Atmospheric Sulfur

- Cycle Simulated in the Global Model GOCART: Model Description and Global Properties. *J. Geophys. Res. Atmos.* **2000**, *105* (D20), 24671–24687.  
<https://doi.org/10.1029/2000JD900384>.
- (91) Alexander, B.; Park, R. J.; Jacob, D. J.; Gong, S. Transition Metal-Catalyzed Oxidation of Atmospheric Sulfur: Global Implications for the Sulfur Budget. *J. Geophys. Res. Atmos.* **2009**, *114* (2), 1–13. <https://doi.org/10.1029/2008JD010486>.
- (92) Peng, J.; Hu, M.; Shang, D.; Wu, Z.; Du, Z.; Tan, T.; Wang, Y.; Zhang, F.; Zhang, R. Explosive Secondary Aerosol Formation during Severe Haze in the North China Plain. *Environ. Sci. Technol.* **2021**, *55* (4), 2189–2207.
- (93) Goldstein, A. H.; Koven, C. D.; Heald, C. L.; Fung, I. Y. Biogenic Carbon and Anthropogenic Pollutants Combine to Form a Cooling Haze over the Southeastern United States. *Proc. Natl. Acad. Sci.* **2009**, *106* (22), 8835 LP – 8840.  
<https://doi.org/10.1073/pnas.0904128106>.
- (94) Guo, S.; Hu, M.; Peng, J.; Wu, Z.; Zamora, M. L.; Shang, D.; Du, Z.; Zheng, J.; Fang, X.; Tang, R.; Wu, Y.; Zeng, L.; Shuai, S.; Zhang, W.; Wang, Y.; Ji, Y.; Li, Y.; Zhang, A. L.; Wang, W.; Zhang, F.; Zhao, J.; Gong, X.; Wang, C.; Molina, M. J.; Zhang, R. Remarkable Nucleation and Growth of Ultrafine Particles from Vehicular Exhaust. *Proc. Natl. Acad. Sci.* **2020**, *117* (7), 3427–3432. <https://doi.org/10.1073/pnas.1916366117>.
- (95) Zhang, F.; Wang, Y.; Peng, J.; Chen, L.; Sun, Y.; Duan, L.; Ge, X.; Li, Y.; Zhao, J.; Liu, C.; Zhang, X.; Zhang, G.; Pan, Y.; Wang, Y.; Zhang, A. L.; Ji, Y.; Wang, G.; Hu, M.; Molina, M. J.; Zhang, R. An Unexpected Catalyst Dominates Formation and Radiative Forcing of Regional Haze. *Proc. Natl. Acad. Sci.* **2020**, *117* (8), 3960–3966.  
<https://doi.org/10.1073/pnas.1919343117>.

- (96) Stocker, T. F.; Qin, D.; Plattner, G. K.; Tignor, M. M. B.; Allen, S. K.; Boschung, J.; Nauels, A.; Xia, Y.; Bex, V.; Midgley, P. M. Climate Change 2013 the Physical Science Basis: Working Group I Contribution to the Fifth Assessment Report of the Intergovernmental Panel on Climate Change. *Clim. Chang. 2013 Phys. Sci. Basis Work. Gr. I Contrib. to Fifth Assess. Rep. Intergov. Panel Clim. Chang.* **2013**, 9781107057, 1–1535. <https://doi.org/10.1017/CBO9781107415324>.
- (97) Pope III, C. A.; Burnett, R. T.; Thun, M. J.; Calle, E. E.; Krewski, D.; Ito, K.; Thurston, G. D. Lung Cancer, Cardiopulmonary Mortality, and Long-Term Exposure to Fine Particulate Air Pollution. *JAMA* **2002**, 287 (9), 1132–1141. <https://doi.org/10.1001/jama.287.9.1132>.
- (98) Wang, Y.; Wang, M.; Zhang, R.; Ghan, S. J.; Lin, Y.; Hu, J.; Pan, B.; Levy, M.; Jiang, J. H.; Molina, M. J. Assessing the Effects of Anthropogenic Aerosols on Pacific Storm Track Using a Multiscale Global Climate Model. *Proc. Natl. Acad. Sci.* **2014**, 111 (19), 6894 LP – 6899. <https://doi.org/10.1073/pnas.1403364111>.
- (99) Fan, J.; Zhang, R.; Tao, W.-K.; Mohr, K. I. Effects of Aerosol Optical Properties on Deep Convective Clouds and Radiative Forcing. *J. Geophys. Res. Atmos.* **2008**, 113 (D8). <https://doi.org/https://doi.org/10.1029/2007JD009257>.
- (100) Wang, Y.; Khalizov, A.; Levy, M.; Zhang, R. New Directions: Light Absorbing Aerosols and Their Atmospheric Impacts. *Atmos. Environ.* **2013**, 81, 713–715. <https://doi.org/https://doi.org/10.1016/j.atmosenv.2013.09.034>.
- (101) Donahue, N. M.; Kroll, J. H.; Pandis, S. N.; Robinson, A. L. A Two-Dimensional Volatility Basis Set – Part 2: Diagnostics of Organic-Aerosol Evolution. *Atmos. Chem. Phys.* **2012**, 12 (2), 615–634. <https://doi.org/10.5194/acp-12-615-2012>.

- (102) Moise, T.; Flores, J. M.; Rudich, Y. Optical Properties of Secondary Organic Aerosols and Their Changes by Chemical Processes. *Chem. Rev.* **2015**, *115* (10), 4400–4439.  
<https://doi.org/10.1021/cr5005259>.
- (103) Powelson, M. H.; Espelien, B. M.; Hawkins, L. N.; Galloway, M. M.; De Haan, D. O. Brown Carbon Formation by Aqueous-Phase Carbonyl Compound Reactions with Amines and Ammonium Sulfate. *Environ. Sci. Technol.* **2014**, *48* (2), 985–993.  
<https://doi.org/10.1021/es4038325>.
- (104) Fortner, E. C.; Zheng, J.; Zhang, R.; Berk Knighton, W.; Volkamer, R. M.; Sheehy, P.; Molina, L.; André, M. Measurements of Volatile Organic Compounds Using Proton Transfer Reaction – Mass Spectrometry during the MILAGRO 2006 Campaign. *Atmos. Chem. Phys.* **2009**, *9* (2), 467–481. <https://doi.org/10.5194/acp-9-467-2009>.
- (105) Wang, M.; Zhu, T.; Zheng, J.; Zhang, R. Y.; Zhang, S. Q.; Xie, X. X.; Han, Y. Q.; Li, Y. Use of a Mobile Laboratory to Evaluate Changes in On-Road Air Pollutants during the Beijing 2008 Summer Olympics. *Atmos. Chem. Phys.* **2009**, *9* (21), 8247–8263.  
<https://doi.org/10.5194/acp-9-8247-2009>.
- (106) Andino, J. M.; Smith, J. N.; Flagan, R. C.; Goddard, W. A.; Seinfeld, J. H. Mechanism of Atmospheric Photooxidation of Aromatics: A Theoretical Study. *J. Phys. Chem.* **1996**, *100* (26), 10967–10980. <https://doi.org/10.1021/jp9529351>.
- (107) Suh, I.; Zhang, D.; Zhang, R.; Molina, L. T.; Molina, M. J. Theoretical Study of OH Addition Reaction to Toluene. *Chem. Phys. Lett.* **2002**, *364* (5), 454–462.  
[https://doi.org/https://doi.org/10.1016/S0009-2614\(02\)01364-7](https://doi.org/https://doi.org/10.1016/S0009-2614(02)01364-7).
- (108) Suh, I.; Zhang, R.; Molina, L. T.; Molina, M. J. Oxidation Mechanism of Aromatic Peroxy and Bicyclic Radicals from OH–Toluene Reactions. *J. Am. Chem. Soc.* **2003**, *125* (41),

- 12655–12665. <https://doi.org/10.1021/ja0350280>.
- (109) Ji, Y.; Zhao, J.; Terazono, H.; Misawa, K.; Levitt, N. P.; Li, Y.; Lin, Y.; Peng, J.; Wang, Y.; Duan, L.; Pan, B.; Zhang, F.; Feng, X.; An, T.; Marrero-Ortiz, W.; Secret, J.; Zhang, A. L.; Shibuya, K.; Molina, M. J.; Zhang, R. Reassessing the Atmospheric Oxidation Mechanism of Toluene. *Proc. Natl. Acad. Sci.* **2017**, *114* (31), 8169–8174. <https://doi.org/10.1073/pnas.1705463114>.
- (110) Schwantes, R. H.; Schilling, K. A.; McVay, R. C.; Lignell, H.; Coggon, M. M.; Zhang, X.; Wennberg, P. O.; Seinfeld, J. H. Formation of Highly Oxygenated Low-Volatility Products from Cresol Oxidation. *Atmos. Chem. Phys.* **2017**, *17* (5), 3453–3474. <https://doi.org/10.5194/acp-17-3453-2017>.
- (111) Molteni, U.; Bianchi, F.; Klein, F.; El Haddad, I.; Frege, C.; Rossi, M. J.; Dommen, J.; Baltensperger, U. Formation of Highly Oxygenated Organic Molecules from Aromatic Compounds. *Atmos. Chem. Phys.* **2018**, *18* (3), 1909–1921. <https://doi.org/10.5194/acp-18-1909-2018>.
- (112) Garmash, O.; Rissanen, M. P.; Pullinen, I.; Schmitt, S.; Kausiala, O.; Tillmann, R.; Zhao, D.; Percival, C.; Bannan, T. J.; Priestley, M.; Hallquist, Å. M.; Kleist, E.; Kiendler-Scharr, A.; Hallquist, M.; Berndt, T.; McFiggans, G.; Wildt, J.; Mentel, T. F.; Ehn, M. Multi-Generation OH Oxidation as a Source for Highly Oxygenated Organic Molecules from Aromatics. *Atmos. Chem. Phys.* **2020**, *20* (1), 515–537. <https://doi.org/10.5194/acp-20-515-2020>.
- (113) Wang, M.; Chen, D.; Xiao, M.; Ye, Q.; Stolzenburg, D.; Hofbauer, V.; Ye, P.; Vogel, A. L.; Mauldin, R. L.; Amorim, A.; Baccharini, A.; Baumgartner, B.; Brilke, S.; Dada, L.; Dias, A.; Duplissy, J.; Finkenzeller, H.; Garmash, O.; He, X.-C.; Hoyle, C. R.; Kim, C.;



- Kvashnin, A.; Lehtipalo, K.; Fischer, L.; Molteni, U.; Petäjä, T.; Pospisilova, V.; Quéléver, L. L. J.; Rissanen, M.; Simon, M.; Tauber, C.; Tomé, A.; Wagner, A. C.; Weitz, L.; Volkamer, R.; Winkler, P. M.; Kirkby, J.; Worsnop, D. R.; Kulmala, M.; Baltensperger, U.; Dommen, J.; El-Haddad, I.; Donahue, N. M. Photo-Oxidation of Aromatic Hydrocarbons Produces Low-Volatility Organic Compounds. *Environ. Sci. Technol.* **2020**, *54* (13), 7911–7921. <https://doi.org/10.1021/acs.est.0c02100>.
- (114) Faust, J. A.; Wong, J. P. S.; Lee, A. K. Y.; Abbatt, J. P. D. Role of Aerosol Liquid Water in Secondary Organic Aerosol Formation from Volatile Organic Compounds. *Environ. Sci. Technol.* **2017**, *51* (3), 1405–1413. <https://doi.org/10.1021/acs.est.6b04700>.
- (115) Chen, L.; Bao, Z.; Wu, X.; Li, K.; Han, L.; Zhao, X.; Zhang, X.; Wang, Z.; Azzi, M.; Cen, K. The Effects of Humidity and Ammonia on the Chemical Composition of Secondary Aerosols from Toluene/NO<sub>x</sub> Photo-Oxidation. *Sci. Total Environ.* **2020**, *728*, 138671. <https://doi.org/https://doi.org/10.1016/j.scitotenv.2020.138671>.
- (116) Qi, X.; Zhu, S.; Zhu, C.; Hu, J.; Lou, S.; Xu, L.; Dong, J.; Cheng, P. Smog Chamber Study of the Effects of NO<sub>x</sub> and NH<sub>3</sub> on the Formation of Secondary Organic Aerosols and Optical Properties from Photo-Oxidation of Toluene. *Sci. Total Environ.* **2020**, *727*, 138632. <https://doi.org/https://doi.org/10.1016/j.scitotenv.2020.138632>.
- (117) Updyke, K. M.; Nguyen, T. B.; Nizkorodov, S. A. Formation of Brown Carbon via Reactions of Ammonia with Secondary Organic Aerosols from Biogenic and Anthropogenic Precursors. *Atmos. Environ.* **2012**, *63*, 22–31. <https://doi.org/https://doi.org/10.1016/j.atmosenv.2012.09.012>.
- (118) Wang, Y.; Liu, P.; Li, Y. J.; Bateman, A. P.; Martin, S. T.; Hung, H.-M. The Reactivity of Toluene-Derived Secondary Organic Material with Ammonia and the Influence of Water

- Vapor. *J. Phys. Chem. A* **2018**, *122* (38), 7739–7747.  
<https://doi.org/10.1021/acs.jpca.8b06685>.
- (119) Qiu, C.; Khalizov, A. F.; Zhang, R. Soot Aging from OH-Initiated Oxidation of Toluene. *Environ. Sci. Technol.* **2012**, *46* (17), 9464–9472. <https://doi.org/10.1021/es301883y>.
- (120) Fountoukis, C.; Nenes, A. ISORROPIA II: A Computationally Efficient Thermodynamic Equilibrium Model for  
 $\text{K}^+$ – $\text{Ca}^{2+}$ – $\text{Mg}^{2+}$ – $\text{NH}_4^+$ – $\text{Na}^+$   
 $^+$ – $\text{SO}_4^{2-}$ – $\text{NO}_3^-$ – $\text{Cl}^-$   
 $^-$ – $\text{HSO}_2$  Aerosols. *Atmos. Chem. Phys.* **2007**, *7* (17), 4639–4659.  
<https://doi.org/10.5194/acp-7-4639-2007>.
- (121) Yeh, G. K.; Ziemann, P. J. Gas-Wall Partitioning of Oxygenated Organic Compounds: Measurements, Structure–Activity Relationships, and Correlation with Gas Chromatographic Retention Factor. *Aerosol Sci. Technol.* **2015**, *49* (9), 727–738.  
<https://doi.org/10.1080/02786826.2015.1068427>.
- (122) Krechmer, J. E.; Day, D. A.; Jimenez, J. L. Always Lost but Never Forgotten: Gas-Phase Wall Losses Are Important in All Teflon Environmental Chambers. *Environ. Sci. Technol.* **2020**, *54* (20), 12890–12897. <https://doi.org/10.1021/acs.est.0c03381>.
- (123) Zhao, J.; Zhang, R. Proton Transfer Reaction Rate Constants between Hydronium Ion ( $\text{H}_3\text{O}^+$ ) and Volatile Organic Compounds. *Atmos. Environ.* **2004**, *38* (14), 2177–2185.  
<https://doi.org/https://doi.org/10.1016/j.atmosenv.2004.01.019>.
- (124) Onasch, T. B.; Siefert, R. L.; Brooks, S. D.; Prenni, A. J.; Murray, B.; Wilson, M. A.; Tolbert, M. A. Infrared Spectroscopic Study of the Deliquescence and Efflorescence of Ammonium Sulfate Aerosol as a Function of Temperature. *J. Geophys. Res. Atmos.* **1999**,

- 104 (D17), 21317–21326. <https://doi.org/https://doi.org/10.1029/1999JD900384>.
- (125) Liu, J.; Zhang, F.; Xu, W.; Sun, Y.; Chen, L.; Li, S.; Ren, J.; Hu, B.; Wu, H.; Zhang, R. Hygroscopicity of Organic Aerosols Linked to Formation Mechanisms. *Geophys. Res. Lett.* **2021**, *48* (4), e2020GL091683. <https://doi.org/https://doi.org/10.1029/2020GL091683>.
- (126) Gkatzelis, G. I.; Papanastasiou, D. K.; Karydis, V. A.; Hohaus, T.; Liu, Y.; Schmitt, S. H.; Schlag, P.; Fuchs, H.; Novelli, A.; Chen, Q.; Cheng, X.; Broch, S.; Dong, H.; Holland, F.; Li, X.; Liu, Y.; Ma, X.; Reimer, D.; Rohrer, F.; Shao, M.; Tan, Z.; Taraborrelli, D.; Tillmann, R.; Wang, H.; Wang, Y.; Wu, Y.; Wu, Z.; Zeng, L.; Zheng, J.; Hu, M.; Lu, K.; Hofzumahaus, A.; Zhang, Y.; Wahner, A.; Kiendler-Scharr, A. Uptake of Water-Soluble Gas-Phase Oxidation Products Drives Organic Particulate Pollution in Beijing. *Geophys. Res. Lett.* **2021**, *n/a* (n/a), e2020GL091351. <https://doi.org/https://doi.org/10.1029/2020GL091351>.
- (127) Khoder, M. I. Ambient Levels of Volatile Organic Compounds in the Atmosphere of Greater Cairo. *Atmos. Environ.* **2007**, *41* (3), 554–566. <https://doi.org/https://doi.org/10.1016/j.atmosenv.2006.08.051>.
- (128) Zhao, J.; Zhang, R.; Misawa, K.; Shibuya, K. Experimental Product Study of the OH-Initiated Oxidation of m-Xylene. *J. Photochem. Photobiol. A Chem.* **2005**, *176* (1), 199–207. <https://doi.org/https://doi.org/10.1016/j.jphotochem.2005.07.013>.
- (129) Song, C.; Na, K.; Cocker, D. R. Impact of the Hydrocarbon to NO<sub>x</sub> Ratio on Secondary Organic Aerosol Formation. *Environ. Sci. Technol.* **2005**, *39* (9), 3143–3149. <https://doi.org/10.1021/es0493244>.
- (130) Jia, L.; Xu, Y. Different Roles of Water in Secondary Organic Aerosol Formation from

- Toluene and Isoprene. *Atmos. Chem. Phys.* **2018**, *18* (11), 8137–8154.  
<https://doi.org/10.5194/acp-18-8137-2018>.
- (131) Jia, L.; Xu, Y. Effects of Relative Humidity on Ozone and Secondary Organic Aerosol Formation from the Photooxidation of Benzene and Ethylbenzene. *Aerosol Sci. Technol.* **2014**, *48* (1), 1–12. <https://doi.org/10.1080/02786826.2013.847269>.
- (132) Zhang, Q.; Xu, Y.; Jia, L. Secondary Organic Aerosol Formation from OH-Initiated Oxidation of m-Xylene: Effects of Relative Humidity on Yield and Chemical Composition. *Atmos. Chem. Phys.* **2019**, *19* (23), 15007–15021.  
<https://doi.org/10.5194/acp-19-15007-2019>.
- (133) Donahue, N. M.; Robinson, A. L.; Stanier, C. O.; Pandis, S. N. Coupled Partitioning, Dilution, and Chemical Aging of Semivolatile Organics. *Environ. Sci. Technol.* **2006**, *40* (8), 2635–2643. <https://doi.org/10.1021/es052297c>.
- (134) Xing, L.; Shrivastava, M.; Fu, T.-M.; Roldin, P.; Qian, Y.; Xu, L.; Ng, N. L.; Shilling, J.; Zelenyuk, A.; Cappa, C. D. Parameterized Yields of Semivolatile Products from Isoprene Oxidation under Different NO<sub>x</sub> Levels: Impacts of Chemical Aging and Wall-Loss of Reactive Gases. *Environ. Sci. Technol.* **2018**, *52* (16), 9225–9234.  
<https://doi.org/10.1021/acs.est.8b00373>.
- (135) Jenkin, M. E.; Saunders, S. M.; Wagner, V.; Pilling, M. J. Protocol for the Development of the Master Chemical Mechanism, MCM v3 (Part B): Tropospheric Degradation of Aromatic Volatile Organic Compounds. *Atmos. Chem. Phys.* **2003**, *3* (1), 181–193.  
<https://doi.org/10.5194/acp-3-181-2003>.
- (136) Song, C.; Na, K.; Warren, B.; Malloy, Q.; Cocker, D. R. Secondary Organic Aerosol Formation from M-Xylene in the Absence of NO<sub>x</sub>. *Environ. Sci. Technol.* **2007**, *41* (21),

- 7409–7416. <https://doi.org/10.1021/es070429r>.
- (137) Nishino, N.; Arey, J.; Atkinson, R. Formation Yields of Glyoxal and Methylglyoxal from the Gas-Phase OH Radical-Initiated Reactions of Toluene, Xylenes, and Trimethylbenzenes as a Function of NO<sub>2</sub> Concentration. *J. Phys. Chem. A* **2010**, *114* (37), 10140–10147. <https://doi.org/10.1021/jp105112h>.
- (138) Xue, H.; Khalizov, A. F.; Wang, L.; Zheng, J.; Zhang, R. Effects of Coating of Dicarboxylic Acids on the Mass–Mobility Relationship of Soot Particles. *Environ. Sci. Technol.* **2009**, *43* (8), 2787–2792. <https://doi.org/10.1021/es803287v>.
- (139) World Health Organization. Coronavirus disease (COVID-2019) situation reports <https://www.who.int/emergencies/diseases/novel-coronavirus-2019/situation-reports/> (accessed May 22, 2021).
- (140) Fe, A. R.; Perlman, S. Coronaviruses: An Overview of Their Replication and Pathogenesis. *Methods in Molecular Biology*. **2015**, *1282*, 1–23. <https://doi.org/10.1007/978-1-4939-2438-7>.
- (141) Kutter, J. S.; Spronken, M. I.; Fraaij, P. L.; Fouchier, R. A.; Herfst, S. Transmission Routes of Respiratory Viruses among Humans. *Curr. Opin. Virol.* **2018**, *28*, 142–151. <https://doi.org/10.1016/j.coviro.2018.01.001>.
- (142) Tang, J. W.; Nicolle, A. D.; Klettner, C. A.; Pantelic, J.; Wang, L.; Suhaimi, A. Bin; Tan, A. Y. L.; Ong, G. W. X.; Su, R.; Sekhar, C.; Cheong, D. D. W.; Tham, K. W. Airflow Dynamics of Human Jets: Sneezing and Breathing - Potential Sources of Infectious Aerosols. *PLoS One* **2013**, *8* (4), e59970–e59970. <https://doi.org/10.1371/journal.pone.0059970>.
- (143) Leung, N. H. L.; Chu, D. K. W.; Shiu, E. Y. C.; Chan, K.-H.; McDevitt, J. J.; Hau, B. J.

- P.; Yen, H.-L.; Li, Y.; Ip, D. K. M.; Peiris, J. S. M.; Seto, W.-H.; Leung, G. M.; Milton, D. K.; Cowling, B. J. Respiratory Virus Shedding in Exhaled Breath and Efficacy of Face Masks. *Nat. Med.* **2020**, *26* (5), 676–680. <https://doi.org/10.1038/s41591-020-0843-2>.
- (144) van Doremalen, N.; Bushmaker, T.; Morris, D. H.; Holbrook, M. G.; Gamble, A.; Williamson, B. N.; Tamin, A.; Harcourt, J. L.; Thornburg, N. J.; Gerber, S. I.; Lloyd-Smith, J. O.; de Wit, E.; Munster, V. J. Aerosol and Surface Stability of SARS-CoV-2 as Compared with SARS-CoV-1. *N. Engl. J. Med.* **2020**, *382* (16), 1564–1567. <https://doi.org/10.1056/NEJMc2004973>.
- (145) He, X.; Lau, E. H. Y.; Wu, P.; Deng, X.; Wang, J.; Hao, X.; Lau, Y. C.; Wong, J. Y.; Guan, Y.; Tan, X.; Mo, X.; Chen, Y.; Liao, B.; Chen, W.; Hu, F.; Zhang, Q.; Zhong, M.; Wu, Y.; Zhao, L.; Zhang, F.; Cowling, B. J.; Li, F.; Leung, G. M. Temporal Dynamics in Viral Shedding and Transmissibility of COVID-19. *Nat. Med.* **2020**, *26* (5), 672–675. <https://doi.org/10.1038/s41591-020-0869-5>.
- (146) Bazant, M. Z.; Bush, J. W. M. A Guideline to Limit Indoor Airborne Transmission of COVID-19. *Proc. Natl. Acad. Sci.* **2021**, *118* (17), e2018995118. <https://doi.org/10.1073/pnas.2018995118>.
- (147) Cheng, Y.; Ma, N.; Witt, C.; Rapp, S.; Wild, P. S.; Andreae, M. O.; Pöschl, U.; Su, H. Face Masks Effectively Limit the Probability of SARS-CoV-2 Transmission. *Science* (80-). **2021**, eabg6296. <https://doi.org/10.1126/science.abg6296>.
- (148) Du, Z.; Xu, X.; Wu, Y.; Wang, L.; Cowling, B. J.; Meyers, L. A. Serial Interval of COVID-19 among Publicly Reported Confirmed Cases. *Emerg. Infect. Dis.* **2020**, *26* (6), 1341–1343. <https://doi.org/10.3201/eid2606.200357>.
- (149) Ferretti, L.; Wymant, C.; Kendall, M.; Zhao, L.; Nurtay, A.; Abeler-Dörner, L.; Parker,

- M.; Bonsall, D.; Fraser, C. Quantifying SARS-CoV-2 Transmission Suggests Epidemic Control with Digital Contact Tracing. *Science* (80-. ). **2020**, *368* (6491), eabb6936.  
<https://doi.org/10.1126/science.abb6936>.
- (150) Kucharski, A. J.; Russell, T. W.; Diamond, C.; Liu, Y.; Edmunds, J.; Funk, S.; Eggo, R. M.; Sun, F.; Jit, M.; Munday, J. D.; Davies, N.; Gimma, A.; van Zandvoort, K.; Gibbs, H.; Hellewell, J.; Jarvis, C. I.; Clifford, S.; Quilty, B. J.; Bosse, N. I.; Abbott, S.; Klepac, P.; Flasche, S. Early Dynamics of Transmission and Control of COVID-19: A Mathematical Modelling Study. *Lancet Infect. Dis.* **2020**, *20* (5), 553–558.  
[https://doi.org/https://doi.org/10.1016/S1473-3099\(20\)30144-4](https://doi.org/https://doi.org/10.1016/S1473-3099(20)30144-4).
- (151) Li, Q.; Guan, X.; Wu, P.; Wang, X.; Zhou, L.; Tong, Y.; Ren, R.; Leung, K. S. M.; Lau, E. H. Y.; Wong, J. Y.; Xing, X.; Xiang, N.; Wu, Y.; Li, C.; Chen, Q.; Li, D.; Liu, T.; Zhao, J.; Liu, M.; Tu, W.; Chen, C.; Jin, L.; Yang, R.; Wang, Q.; Zhou, S.; Wang, R.; Liu, H.; Luo, Y.; Liu, Y.; Shao, G.; Li, H.; Tao, Z.; Yang, Y.; Deng, Z.; Liu, B.; Ma, Z.; Zhang, Y.; Shi, G.; Lam, T. T. Y.; Wu, J. T.; Gao, G. F.; Cowling, B. J.; Yang, B.; Leung, G. M.; Feng, Z. Early Transmission Dynamics in Wuhan, China, of Novel Coronavirus–Infected Pneumonia. *N. Engl. J. Med.* **2020**, *382* (13), 1199–1207.  
<https://doi.org/10.1056/NEJMoa2001316>.
- (152) Liu, Y.; Ning, Z.; Chen, Y.; Guo, M.; Liu, Y.; Gali, N. K.; Sun, L.; Duan, Y.; Cai, J.; Westerdahl, D.; Liu, X.; Xu, K.; Ho, K.; Kan, H.; Fu, Q.; Lan, K. Aerodynamic Analysis of SARS-CoV-2 in Two Wuhan Hospitals. *Nature* **2020**, *582* (7813), 557–560.  
<https://doi.org/10.1038/s41586-020-2271-3>.
- (153) Setti, L.; Passarini, F.; De Gennaro, G.; Barbieri, P.; Perrone, M. G.; Borelli, M.; Palmisani, J.; Di Gilio, A.; Torboli, V.; Fontana, F.; Clemente, L.; Pallavicini, A.; Ruscio,

- M.; Piscitelli, P.; Miani, A. SARS-Cov-2RNA Found on Particulate Matter of Bergamo in Northern Italy: First Evidence. *Environ. Res.* **2020**, *188*, 109754.  
<https://doi.org/10.1016/j.envres.2020.109754>.
- (154) WALLACE, L. A.; EMMERICH, S. J.; HOWARD-REED, C. Continuous Measurements of Air Change Rates in an Occupied House for 1 Year: The Effect of Temperature, Wind, Fans, and Windows. *J. Expo. Sci. Environ. Epidemiol.* **2002**, *12* (4), 296–306.  
<https://doi.org/10.1038/sj.jea.7500229>.
- (155) Gong, Z.; Gu, S.; Zhang, Y.; Sun, J.; Wu, X.; Ling, F.; Shi, W.; Zhang, P.; Li, D.; Mao, H.; Zhang, L.; Wen, D.; Zhou, B.; Zhang, H.; Huang, Y.; Zhang, R.; Jiang, J.; Lin, J.; Xia, S.; Chen, E.; Chen, Z. Probable Aerosol Transmission of Severe Fever with Thrombocytopenia Syndrome Virus in Southeastern China. *Clin. Microbiol. Infect.* **2015**, *21* (12), 1115–1120. <https://doi.org/https://doi.org/10.1016/j.cmi.2015.07.024>.
- (156) Wu, X.; Nethery, R. C.; Sabath, B. M.; Braun, D.; Dominici, F. Exposure to Air Pollution and COVID-19 Mortality in the United States: A Nationwide Cross-Sectional Study. *medRxiv* **2020**, 2020.04.05.20054502. <https://doi.org/10.1101/2020.04.05.20054502>.
- (157) Guan, W.; Ni, Z.; Hu, Y.; Liang, W.; Ou, C.; He, J.; Liu, L.; Shan, H.; Lei, C.; Hui, D. S. C.; Du, B.; Li, L.; Zeng, G.; Yuen, K.-Y.; Chen, R.; Tang, C.; Wang, T.; Chen, P.; Xiang, J.; Li, S.; Wang, J.; Liang, Z.; Peng, Y.; Wei, L.; Liu, Y.; Hu, Y.; Peng, P.; Wang, J.; Liu, J.; Chen, Z.; Li, G.; Zheng, Z.; Qiu, S.; Luo, J.; Ye, C.; Zhu, S.; Zhong, N. Clinical Characteristics of Coronavirus Disease 2019 in China. *N. Engl. J. Med.* **2020**, *382* (18), 1708–1720. <https://doi.org/10.1056/NEJMoa2002032>.
- (158) Cheng, K. K.; Lam, T. H.; Leung, C. C. Wearing Face Masks in the Community during the COVID-19 Pandemic: Altruism and Solidarity. *Lancet* **2020**.



[https://doi.org/10.1016/S0140-6736\(20\)30918-1](https://doi.org/10.1016/S0140-6736(20)30918-1).

(159) Siegenfeld, A. F.; Taleb, N. N.; Bar-Yam, Y. Opinion: What Models Can and Cannot Tell

Us about COVID-19. *Proc. Natl. Acad. Sci.* **2020**, 202011542.

<https://doi.org/10.1073/pnas.2011542117>.